Felix Johannes Flomm

Investigating the spatio-temporal organization of human cytomegalovirus secondary envelopment and egress

Leibniz Institute of Virology
Dissertation submitted to the faculty of mathematics, informatics and natural sciences of the University of Hamburg, Department of chemistry

Hamburg in 2022

Reviewer 1: Prof. Dr. Jens Bosse
Reviewer 2: Prof. Dr. Wolfram Brune
Reviewer 3: Prof. Dr. Paul Walther

Date of disputation: 18.11.2022

Examination Committee:

Chair: Prof. Dr. Kay Grünewald
Co-Chair: Prof. Dr. Wolfgang Maison
Members: Prof. Dr. Jens Bosse, Prof. Dr. Wolfram Brune, Jan Kosiński PhD

The experimental work presented here and the authoring of this dissertation was performed in Hamburg between October 2017 and July 2022 at the Leibniz Institute of Virology, formerly Heinrich Pette Institute for Experimental Virology, under the supervision of Prof. Kay Grünewald, and Prof. Jens Bosse from the Hannover Medical School at the Centre for Structural Systems Biology.

Investigating the spatio-temporal organization of human cytomegalovirus secondary envelopment and egress

Felix Johannes Flomm

I PUBLICATION LIST

Parts of the work presented here have been published in:
Flomm FJ, Soh TK, Schneider C, Wedemann L, Britt HM, Thalassinos K, Pfitzner S, Reimer R, Grünewald K, Bosse JB Intermittent Bulk Release of Human Cytomegalovirus. Plos Pathog. 2022;*in production*

Data related to this work are deposited in:
Flomm FJ, Soh TK, Schneider C, Wedemann L, Britt HM, Thalassinos K, Pfitzner S, Reimer R, Grünewald K, Bosse JB. "Intermittent Bulk Release of Human Cytomegalovirus" Associated Data; 2022 [cited 2022 July 26]. Database: Dryad [Internet]. Available from: https://doi.org/10.5061/dryad.gtht76hpt

Flomm FJ, Soh TK, Schneider C, Wedemann L, Britt HM, Thalassinos K, Pfitzner S, Reimer R, Grünewald K, Bosse JB. "Intermittent Bulk Release of Human Cytomegalovirus" Correlative 3D SBFSEM Data; 2022 [cited 2022 July 26]. Database: Dryad [Internet]. Available from: https://doi.org/10.5061/dryad.5dv41ns7z

II ABBREVIATIONS

Abbreviation	*Meaning*
AC	Assembly Complex/Compartment
AIDS	Acquired Immunodeficiency Syndrome
ALIX	ALG-2-interacting protein X
AP	Assembly precursor
ATCC	American Type Culture Collection
ATP	Adenosine triphosphate
BAC	Bacterial artificial chromosome
BSA	Bovine serum albumin
CD	Cluster of differentiation
CHMP	Charged multivesicular body protein
CNS	Central nervous system
cos	Cosine
CPE	Cytopathic effect
ctr	Control
CVSC	Capsid vertex specific components
Daxx	Death domain associated protein
ddH_2O	Double distilled water
DDSA	Dodecenylsuccinic anhydride
DMEM	Dulbecco's modified Eagle's medium
DMP-30	2,4,6-Tris(dimethylaminomethyl)phenol
DMSO	Dimethyl sulfoxide
DNA	Deoxyribonucleic acid
dNTP	Deoxynucleoside triphosphate
D-PBS	Dulbecco's phosphate buffered saline
dpi	Days post infection
E	Early
E. coli	*Escherichia coli*
EBV	Epstein-Barr virus
EC	Endothelial cell
EDTA	Ethylenediaminetetraacetic acid
EGFP	Enhanced green fluorescent protein
EM	Electron microscopy
EMCCD	Electron-multiplying charge-coupled device
ER	Endoplasmic reticulum
ERGIC	Endoplasmic reticulum Golgi intermediate compartment
ESCRT	Endosomal sorting complexes required for transport
EVA	Extracellular viral accumulation
FB	Fibroblast
FBS	Fetal bovine serum
FGF	Fibroblast growth factor
Fiji	Fiji is just ImageJ
fps	Frames per second

Abbreviation	*Meaning*
g	Gravitational force on earth
GaAsP	Gallium arsenide phosphide
GCV	Ganciclovir/Valganciclovir
GHS	Globally Harmonized System of Classification and Labelling of Chemicals
GM130	Golgi matrixprotein 130
Grasp	Golgi reassembly stacking protein
gX	Glycoprotein X as in gB
h	Hour
HCMV	Human cytomegalovirus
HDAC	Histone deacetylase
HEK	Human embryonal kidney cells
HFF	Human foreskin fibroblast
HMVEC	Human microvascular endothelial cells
hpi	Hours post infection
HRP	Horseradish peroxidase
HSP	Heat shock protein
HSV-1	Herpes simplex virus 1
IE	Immediate early
IF	Immunofluorescence
IRL	Internal repeat long
IRS	Internal repeat short
kV	Kilovolt
L	Late
LAMP1	Lysosomal-associated membrane protein 1
MCP	Major capsid protein
min	Minute
MNA	Methylnorbornene-2,3-dicarboxylic acid anhydride
MOI	Multiplicity of infection
MSD	Mean squared displacement
MT	Microtubule
MTOC	Microtubule organizing center
MVB	Multivesicular body
MViB	Multiviral body
NA	Numerical aperture
NEB	New England Biolabs
NEC	Nuclear egress complex
NP1C	C-terminal fragment of HCMV pUL80 after autoproteolysis
OD600	Optical density at 600 nm
pac	Packaging signal sequence
PAGE	Polyacrylamide gel electrophoresis
PCR	Polymerase chain reaction
PEI	Polyethylenimine

Abbreviation	*Meaning*
PFA	Paraformaldehyde
PFU	Plaque forming units
PKM2	Pyruvate kinase M2
PLT	Progressive lowering of temperature
PML-NB	Promyelocytic leukemia nuclear bodies
PMT	Photomultiplier tube
pp	Phosphoprotein, as in pp150
PRV	Pseudorabies virus
pTRL	Protein from a gene in the HCMV terminal repeat long (TRL) region
pUL	Protein from a gene in the HCMV unique long (UL) region
pUS	Protein from a gene in the HCMV unique short (US) region
Rab	Ras-associated binding
Ras	Rat sarcoma virus (protein family)
RNA	Ribonucleic acid
ROI	Region of interest
RT	Room temperature (20-25°C)
s	Second
SBF-SEM	Serial block-face scanning electron microscopy
sCMOS	Scientific complementary metal-oxide-semiconductor
SCP	Small capsid protein
SDS	Sodium dodecyl sulfate
sin	Sine
SiR	Silicon rhodamine
siRNA	Small interfering RNA
SNARE	Soluble N-ethylmaleimide-sensitive-factor attachment receptor
Snap	Synaptosomal associated protein
SNAP	SNAP-tag
ssDNA	Single stranded DNA
TAE	Tris-acetate-EDTA
TE	Tris-EDTA
Taq	*Thermus aquaticus*
TEM	Transmission electron microscopy
TGN	Trans-Golgi network
TRI	Triplex
Tris	Tris(hydroxymethyl)aminomethane
TrISS	Tracking information segmentation and search tool
TRL	Terminal repeat long
TRS	Terminal repeat short
TSG101	Tumor susceptibility gene 101
UL	Unique long
US	Unique short
VAMP	Vesicle-associated membrane protein

Abbreviation	*Meaning*
Vps4	Vacuolar protein sorting-associated protein 4
WB	Western blot
WT	Wild type

1 Zusammenfassung

Das humane Zytomegalievirus (HCMV) ist ein Pathogen von hoher klinischer Relevanz. Insbesondere für Kleinkinder und Menschen mit einem geschwächten Immunsystem stellt HCMV eine große Gefahr dar, da es in diesen Patientengruppen zu opportunistischen Infektionen mit schweren Verläufen führen kann. Obwohl HCMV seit mehr als 60 Jahren der Wissenschaft bekannt ist, gelang es bisher nicht, einen wirksamen Impfstoff gegen dieses Virus zu entwickeln. Darüber hinaus gibt es nur wenige zugelassene Medikamente, die häufig schwere Nebenwirkungen auslösen. Alle zugelassenen Wirkstoffe gegen HCMV zielen auf Prozesse der Virusreplikation im Zellkern ab. Es gibt jedoch noch keinen Wirkstoff, der spätere zytoplasmatische Phasen der viralen Morphogenese inhibiert. Bevor infektiöse Viruspartikel die infizierte Zelle verlassen, um die nächste Wirtszelle zu infizieren, müssen sie in einem finalen Morphogeneseschritt im Zytoplasma behüllt werden. Dieser Schritt wird im Falle von Herpesviren sekundäre Behüllung (eng. *secondary envelopment*) genannt und ist essentiell, da nur Viruspartikel mit einer intakten und vollständigen Membranhülle infektiös sind. Um dies zu ermöglichen, führt eine HCMV Infektion zu tiefgehenden Veränderungen im zellulären Membrantransportsystem und reorganisiert Membranen von zellulären Kompartimenten, um ein spezialisiertes Assemblierungskompartiment (eng. *assembly compartment*, kurz: *AC*) zu erzeugen.

Die aktuell in der Literatur vorherrschenden Modelle zur sekundären Behüllung von Herpesviren beschreiben den Prozess so, dass kleine Vesikel einzelne Viruskapside umschließen und durch Abschnürung der Membran ein einzelnes doppelt behülltes Partikel entsteht. Dieses kann dann exozytiert werden, indem es zur Zytoplasmamembran transportiert wird und die äußere Hülle des Vesikels mit dieser fusioniert. Die vorliegende Arbeit beschäftigt sich insbesondere mit der Koordinierung des Behüllungs- und Exozytoseprozesses von HCMV Partikeln in Zeit und Raum. Ein besonderer Fokus liegt hierbei auf den Mechanismen, mit denen HCMV Partikel aus der Zelle ausgeschleust werden. Experimente mit Mikroskopiertechniken, wie der internen Totalreflexionsfluoreszenzmikroskopie und Lattice-Lichtblattmikroskopie, die speziell für die Untersuchung lebender Zellen geeignet sind, zeigen, dass große Mengen Virus in unregelmäßigen Pulsen durch große Vesikel aus infizierten Zellen freigesetzt werden. Daten aus korrelativer Licht- und Elektronenmikroskopie deuten darauf hin, dass diese großen Vesikel aus multivesikulären Strukturen bestehen, welche behülltes virales Material wie Virionen und *dense bodies* (virale Tegument Partikel ohne Kapsid und Genom) beinhalten. Mit Hilfe von pH-abhängig fluoreszenten Fusionsproteinen konnte nachgewiesen werden, dass diese multiviralen Körper (eng. *multiviral bodies*, kurz: *MViBs*) mit der Zytoplasmamembran fusionieren können, um ihren Inhalt aus der Zelle freizusetzen. Hierdurch entstehen charakteristische extrazelluläre virale Akkumulationen (eng. *extracellular viral accumulations*, kurz: *EVAs*) an der Zelloberfläche. Untersuchungen der Zusammensetzung von Viruspartikeln und *MViBs* zeigen, dass diese Proteine tragen, welche an exosomalen und endosomalen Prozessen beteiligt sind. Beispielsweise sind CD63 auf *MViBs* und Rab5C und Syntaxin-12 auf Viruspartikeln präsent. Die Kombination aus dem charakteristischen Freisetzungsmechanismus mit der Präsenz von endosomalen und exosomalen Faktoren suggeriert Parallelen zwischen den zellulären Prozessen, die multivesikuläre Körper (eng. *multivesicular bodies*, kurz: *MVBs*) erzeugen und dem viralen Prozess der *MViBs* hervorbringt. Jedoch weisen

Experimente mit Wirkstoffen, welche die Produktion von zellulären *MVBs* (U18666A) und exosomale Prozesse (Ketotifen und Tipifarnib) inhibieren darauf hin, dass trotzdem deutliche Unterschiede zwischen den zellulären und dem viralen Prozess existieren. Von den drei Substanzen war lediglich Tipifarnib in der Lage die HCMV Replikation signifikant zu blockieren. Interessanterweise war das Ausmaß, mit dem *MViB*-mediierte Freisetzung von Virus zu *EVAs* führt, unterschiedlich für die verschiedenen HCMV Stämme TB40 und Merlin. Es ist daher möglich, dass der hier beschriebene Freisetzungsmechanismus bei den Unterschieden im Verbreitungsverhalten verschiedener HCMV Stämme in Zellkultur eine Rolle spielt.

2 Abstract

The human cytomegalovirus (HCMV) is an opportunistic pathogen of high clinical importance. This virus can cause severe disease and disabilities, especially in vulnerable patient groups with a weakened or immature immune system. Despite continuous efforts and more than 60 years of HCMV research, no vaccine has been approved to date. Inhibitors of viral replication approved today for clinical use exclusively target nuclear stages of HCMV replication, whereas no approved pharmaceuticals target the later cytoplasmic steps of viral morphogenesis. An HCMV particle acquires its final envelope in a step called secondary envelopment before egressing the cell. This process is critical for the virus since the final envelope must contain all factors necessary to mediate entry into the next host cell. To achieve this, HCMV significantly remodels cell membranes and trafficking processes to form a specialized viral assembly complex (AC).

The models of herpesvirus secondary envelopment currently prevailing in the literature suggest that single capsids are individually enveloped by budding into single vesicles. These double enveloped particles can subsequently be released by fusion with the plasma membrane. This study focused on the spatio-temporal organization of HCMV secondary envelopment and egress, examining the dynamics and mechanics of the release of viral progeny. Experiments utilizing high-end live-cell microscopy such as lattice-light-sheet- and total internal reflection fluorescence (TIRF) microscopy revealed that, in contrast to the models mentioned above, large amounts of HCMV viral material are exocytosed in intermittent pulses from large bodies in infected cells. Correlative light and electron microscopy investigations showed that these bodies are multivesicular structures filled with virus particles and dense bodies (viral tegument particles without capsid and genome). Experiments with pH-sensitive reporter proteins show that these multiviral bodies (MViBs) release their content to the extracellular medium by fusion with the plasma membrane. These release events produce characteristical extracellular viral accumulations (EVAs) at the surface of infected cells. Moreover, an analysis of the composition of virions and MViBs confirms the presence of endosomal and exosomal markers such as CD63 on MViBs as well as e.g. Rab5C and Syntaxin-12 on virions. Together with bulk release phenotype, these data suggest the involvement of endosomal and exosomal pathways in the MViB generation. However, experiments with inhibitors of classical MVB biogenesis (U18666A) and exosome release processes (Ketotifen and Tipifarnib) showed that the viral process that generates MViBs likely differs considerably from the cellular process to produce MVBs. Only Tipifarnib could interfere with viral replication, whereas U18666A and Ketotifen had no significant effect. Interestingly, the prevalence of the release from MViBs into EVAs varied between the HCMV strains TB40 and Merlin, suggesting a role for bulk release in strain-specific spreading behaviour.

3 Introduction

3.1 Human cytomegalovirus

3.1.1 Pathogenesis and clinical relevance

The first evidence of human cytomegalovirus (HCMV) infections was discovered when pathologists noticed enlarged cells with characteristically shaped inclusions in tissue samples of stillborn infants (1). In the following decades, researchers noticed similar structures in the contexts of various illnesses, which could, in hindsight, potentially have resulted from HCMV infection (2–4). However, the virus itself was not discovered until 1953, when scientists found particles reminiscent of viruses in electron microscopy studies of cytomegalic cells (5). With the advent of cell culture techniques, the isolation and *in situ* propagation of HCMV became possible. In fact, HCMV was isolated independently in three laboratories in the 1950s. Margaret Smith, Wallace Rowe and Thomas Weller each isolated HCMV from patient material and cultivated it *in situ* (6–8). The name cytomegalovirus was coined by Thomas Weller, who received, together with John Enders and Frederick Robbins, the Nobel Prize for Medicine in 1957 for their work on the cultivation of the poliomyelitis virus in cell culture (9).

Today, HCMV has a worldwide seroprevalence ranging from 45-100% depending on the country and socioeconomic status (reviewed in (10)). The virus is categorized as a member of the subfamily of *betaherpesvirinae* in the overarching family of *herpesviridae* in the order of *herpesvirales* (11). HCMV can spread in the population vertically from mother to child through congenital transmission and horizontally by contact with almost all bodily fluids (12,13). Like all herpesviruses, HCMV establishes a life-long latent infection in the host (14,15). In an immunocompetent person, a primary infection with HCMV usually causes, if any at all, only unspecific and mild symptoms and, therefore, often passes unnoticed (16–19). In rare cases, a primary HCMV infection can cause mononucleosis similar to the related Epstein-Barr virus (EBV) from the *gammaherpesvirinae* subfamily (16,18,19). After establishing a latent infection, HCMV reactivation can lead to drastically different clinical manifestations depending on the host's immune status. Since a functional immune system can usually control HCMV well, a reactivating infection leads mostly to subclinical viremia without significant symptoms in healthy people (18,19). Still, research has proposed a potential link of HCMV infection to immune senescence, cardiovascular diseases and general morbidity, especially in older age groups (20–26).

On the other hand, HCMV infection poses a severe threat to immunocompromised patients (18,19,27). Two major groups of individuals with an impaired immune system can be distinguished. In one group are unborn and newborn children whose immune system is not yet fully developed. They are at risk of being congenitally infected when the mother has a primary HCMV infection or a reactivation of a latent infection. Mother-to-child transmission can occur intrauterine by trans-placental viral transmission, at birth through blood contact or during breastfeeding (28–31). Congenital HCMV infection *in utero* is associated with several severe complications affecting multiple organs (31,32). Congenitally infected newborn children can show diseases affecting their retina, central nervous system (CNS), liver, gastrointestinal organs, pneumonia, as well as hematologi-

cal conditions (33–35). In some cases, a congenital HCMV infection can cause a lifelong impairment of vision, hearing or cognitive function (35). As a result, congenital HCMV is a significant disease burden by being the leading cause of disabilities in children in industrialized nations (35).

The other major group of concern consists of patients with a suppressed immune system due to underlying conditions. This immunosuppression can either be due to another disease, such as acquired immunodeficiency syndrome (AIDS), or from immunosuppressive drugs used to treat autoimmune and inflammatory diseases, in cancer therapy or to prevent graft rejection after organ transplantation. HCMV is among the most important opportunistic pathogens in these high-risk patients, requiring close monitoring and prophylactic medication (36–39). HCMV seronegative transplant patients receiving solid organ transplantation from an HCMV-positive donor are at the greatest risk of developing disease (40). Likely due to its ability to infect almost all organs in the human body, HCMV can cause a wide range of severe complications (36,37). Besides common unspecific symptoms, such as malaise, fever and pain, HCMV can cause leukopenia, pneumonia, encephalitis, hepatitis and many other serious diseases (19,27). Consequently, although usually benign in healthy individuals, an HCMV infection is a significant risk factor for mortality in these vulnerable patient groups (19,27,41–43).

3.1.2 Structure and cellular replication cycle

The HCMV virion has a diameter of approximately 230 nm and a structure similar to the other members of the herpesvirus family (44–46). The mature virus particle can be separated into four fundamental layers: genome, capsid, tegument and envelope (Figure 1A-B). At the core of the virion is the double-stranded DNA genome, which consists of approximately 230 kbps and is, therefore, the largest genome of all human-infecting herpesviruses (Figure 1A) (44,46,47). Around the DNA is an icosahedral protein shell called the capsid. This capsid consists of approximately 4000 molecules, organized into 150 hexons, 12 pentons (11 regular and 1 specialized portal penton) and 320 triplexes (44,46). The main capsid proteins are the Major Capsid Protein (MCP, pUL86), Triplex Proteins 1 and 2 (TRI-1, pUL85; TRI-2, pUL46), Scaffold protein (AP, pUL80.5), a viral protease (NP1c, pUL80a) and the Small Capsid Protein (SCP, pUL48.5). The actual capsid shell is mainly made up of the MCP (hexons and pentons), TRI-1 and TRI-2 (triplexes) and SCP (on hexons) (44,46,48). Incorporated on each of the icosahedron vertices are, in varying ratios, pp150 and the capsid-vertex-specific components (CVSCs) pUL93, pUL77 and pUL48 (48). Essential for the function of the capsid as the carrier of the genome is the portal complex, through which the viral DNA enters and exits the capsid. The portal is built from a 12-fold symmetric pUL104 dodecamer topped by a portal cap, predicted to consist of pUL93, anchored to the capsid through pUL77 (48–51). Tightly associated with the outer capsid surface is a layer of the tegument protein pp150, which is believed to secure the capsid's integrity against internal pressure caused by the genomic DNA (46,52–54). Encasing the capsid is the tegument, an amorphous protein layer with a thickness of about 50 nm (44). The tegument layer consists of protein and RNA from the virus and the host, including ca. 70 different host protein species (55–57). The function of most of the tegument proteins remains elusive, although they appear to play roles in almost all stages of the viral life-

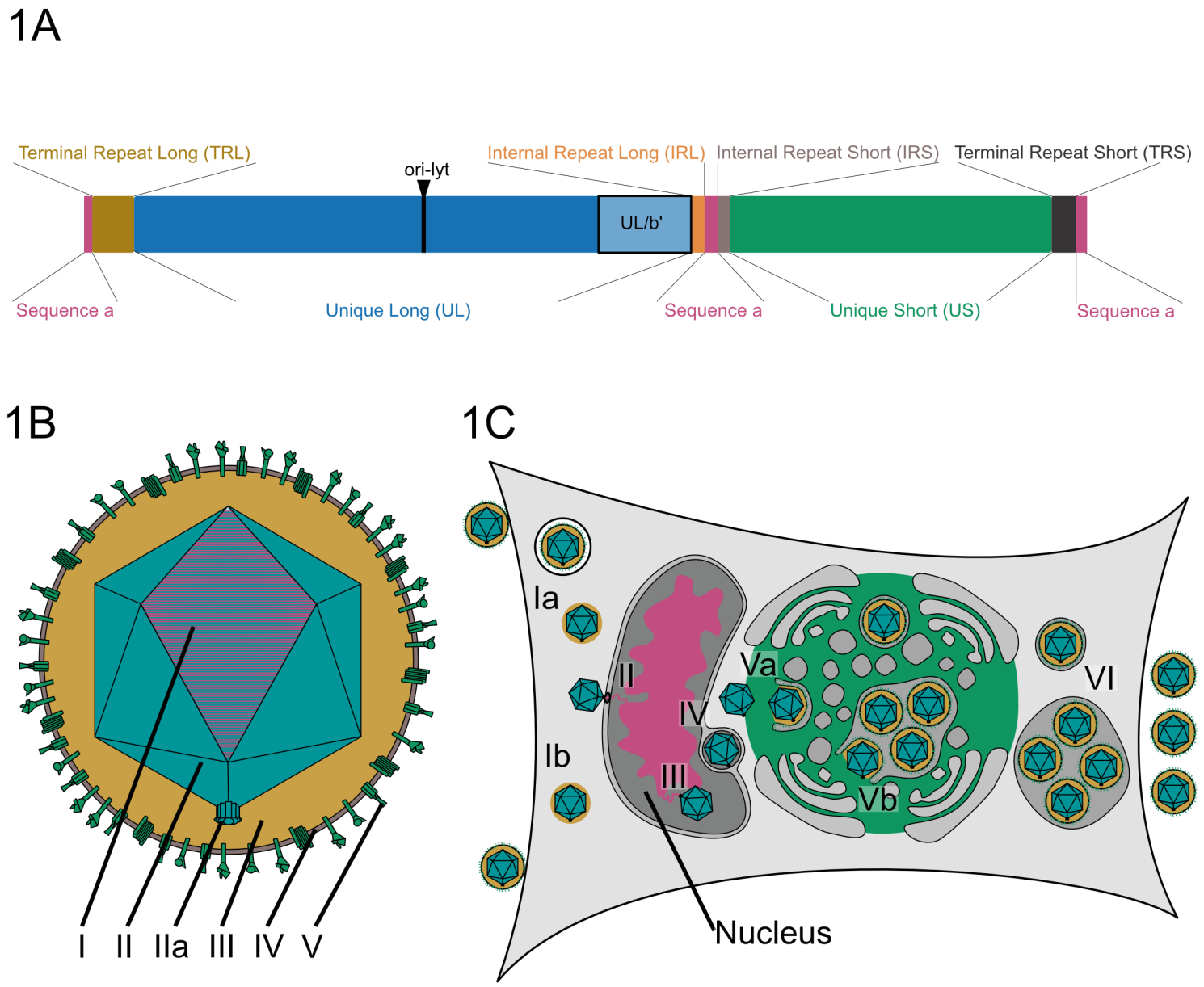

Figure 1. HCMV genome organization, structure and replication cycle.

1A This schematic shows a configuration of the HCMV genome, adapted from (69). Depicted are the different genomic regions and their names. Highlighted are a sub-region from the UL segment, called the UL/b' region, and the lytic origin of replication (ori-lyt).

1B Simplified structure of the HCMV virion: Viral genome (I) encapsulated in its icosahedral capsid shell (II) with the specialized portal vertex (IIa) and surrounded by the amorphous tegument layer (III). The particle is enveloped with a lipid bilayer (IV) decorated with various viral glycoproteins (V).

1C Overview of the HCMV replication cycle. HCMV enters the cell either by endocytosis and escaping from the endosome (Ia) or by fusion with the plasma membrane (Ib). Subsequently, the capsid travels to the nucleus and injects the viral DNA through the nuclear pore (II). Viral DNA is replicated in the replication compartment (pink) and subsequently packaged into newly preformed capsids (III). These particles exit the nucleus through a primary envelopment/-de-envelopment process (IV) and travel to the assembly complex (green). Here, the tegument layer of the capsid is completed before secondary envelopment of the particle by budding into individual small vesicles (Va) or large multivesicular structures (Vb). The mature virions egress from the cell, by fusion of the outer membrane of the transport vesicle with the plasma membrane (VI).

cycle from entry to egress (reviewed in (57)). The final layer of the virion is a lipid bilayer decorated with viral surface proteins, called the viral envelope. Virion surface proteins function primarily as mediators for entry into host cells. Two major variations of the glycoprotein heterodimer of gH and gL called the trimer (complex with gO) and the pentamer (complex with pUL128, pUL130 and pUL131A) are mainly responsible for the recognition of cell-type-specific receptors on host cells, and thereby involved in controlling host cell tropism (discussed in more detail in chapter 3.2.2, also reviewed in (58–60)). The glycoprotein gB and the complex of gM and gN are responsible for unspecific binding to cell surfaces by interaction with heparan sulfate glucosaminoglycans (61–63). Moreover, gB is responsible for fusing the viral envelope with the host endosomal- or plasma membrane (64–66). Finally, thirteen more membrane glycoproteins (pUL116, pRL10, pRL13, pTRL10, pUL1, pUL4, pUL33, pUL73, pUL75, pUL78 pUS27, pUS28 and pUL132) were identified in the HCMV envelope. For some of these proteins, studies showed that they are involved in immune modulation, e.g. as chemokine receptors (pUS28). For others, their functions remain poorly defined (67,68).

This viral envelope mediates the first contact of an HCMV virion with a potential host cell. After adsorption to the cell surface and recognition through one of the gH/gL complexes, it is hypothesized that they trigger the structurally highly conserved herpesviral fusion protein gB (70,71). An initial conformational rearrangement in the activated gB inserts a fusion loop into the target membrane and fuses it to the virion envelope through a second conformational change (72–74). This process happens either directly at the cell surface or at endosomal membranes after the initial endocytosis of the viral particle (Figure 1C) (62,75–77). Upon release from the envelope, the tegument gradually dissociates from the capsid. In this initial phase of infection, some of the tegument proteins are involved in immune evasion (pUL83/pp65), inhibition of apoptosis (pUL36, pUL38) and support the initiation of gene expression and genome replication (pUL82/pp71, ppUL69, pUL26, pUL35) (reviewed in (78)). Meanwhile, the HCMV capsids use the microtubule (MT) network to travel toward the host cell's nucleus (79–82). Upon arrival, a model based on alphaherpesviruses suggests that the capsids dock to the nuclear pores and release their genome through the portal complex (Figure 1C) (57,83,84). Subsequently, the viral DNA is injected through the nuclear pore into the nucleoplasm, where the association with histones chromatinizes the HCMV genome (85–87). To start a lytic replication cycle, HCMV must overcome intrinsic nuclear host restriction mechanisms, such as PML-nuclear body- (PML-NB) and HDAC-dependent repression, to initiate gene expression and genome replication (85–87). Interestingly, HCMV has evolved an intricate relationship with PML-NBs. While an initial interaction of the incoming viral genome appears essential to prime transcription of the viral genome, HCMV disrupts PML-NBs immediately after to avoid inhibitory effects by PML-NB constituents, such as Daxx and Sp100 (78,88–92).

In the following, HCMV launches a transcription cascade, which is divided into three major phases: immediate-early- (IE), early- (E) and late (L) gene expression. Accordingly, viral gene products can be assigned to a kinetic class, corresponding to the phase in which their expression starts. The group of IE proteins contains factors essential for the initiation of viral transcription and replication. The major IE proteins IE1/p72/pUL123 and IE2/p86/pUL122 counteract host repression of the viral genome at this point and

act as important transactivators to the expression of proteins from the E- and L classes (78,87,93). The other IE- and E genes are responsible for the extensive reprogramming of the host cell. Their products are involved in the inhibition of cell death pathways, modulation of innate immune responses, transcriptional control, replication of the viral genome and prime the cell for the production of infectious virus progeny (87,94,95). Moreover, several major tegument proteins (pp150, pp65, pp71, ppUL48), partially involved in HCMV particle assembly, are also expressed at this stage (57,96). Together, the IE protein IE2 and the E proteins pUL84 and pUL112-113 initiate the viral genome replication by activating the lytic origin of replication (oriLyt) promoter (IE2 and pUL84) and recruiting polymerase components (pUL112-113) (97–101).

The six core constituents of the HCMV replisome perform the synthesis of new viral DNA: the viral DNA polymerase, consisting of the catalytical subunit pUL54 and the processivity subunit pUL44, a ssDNA binding protein pUL57 and a helicase-primase heterotrimer complex of pUL105, pUL70 and pUL102 (102,103). Since the viral DNA replication produces concatemers of HCMV genomes, it is likely that the process is mainly performed on a circularized template episome in a rolling circle mode (104). This phase of the infection also marks the beginning of the expression of the L genes. This class contains virion structural components and proteins, which control genome packaging, virion assembly, maturation, and egress (87).

Genome encapsidation occurs in the nucleus, where round procapsids are preformed from the core capsid constituents MCP, TRI1, TRI2 and SCP with a scaffold of pUL80a and pUL80.5 in the core and one specialized portal penton (44,105–107). The packaging of the viral DNA is initiated by the interaction of the terminase complex, made of pUL56, pUL89 and pUL51, with the capsid portal complex and a genome concatemer (108–112). After recognizing the free end of a genome concatemer, the terminase pumps the DNA through the portal channel in an ATP-dependent process, similar to the packaging process of bacteriophages (112,113). During the genome encapsidation, the scaffold inside the procapsid is cleaved by the protease subunit of pUL80a and replaced by the viral DNA, also leading to a shift of the capsid structure to an icosahedral shape (105,114–117). Two signal elements within the DNA sequence called pac-1 and pac-2 communicate to the terminase that an entire genome has been packaged. Upon detecting this signal, the terminase cleaves the concatemer and thereby concludes the packaging (118). Interestingly, three structurally different particle types are present in the nuclei of late infected cells. Historically they were termed A, B and C capsids, and their phenotype is conserved between most herpesviruses (119). Whereas A and B capsids appear to be defective dead-end products, only C capsids have a fully encapsulated genome and can mature into infectious virions (44,120). It has been suggested that the viral CVSC proteins preferably assemble on C capsids to prime them for further maturation and thereby act as a quality control instance (121,122).

For the final morphogenesis steps, the C-type capsids are translocated from the nucleus to the cytoplasm (Figure 1C). This step is accomplished by an envelopment-deenvelopment process at the nuclear membrane, conserved among herpesviruses (123). Mediated by the nuclear egress complex (NEC), consisting in HCMV of pUL50 and pUL53, a capsid can bud at the inner nuclear membrane into an intraluminal vesicle. Subsequently,

this vesicle can fuse with the outer nuclear membrane to release the capsid into the cytoplasm (124–128). In the last maturation step, the HCMV capsid acquires the tegument and is enveloped by budding into host membranes before being transported to the plasma membrane for egress. These last steps of the HCMV morphogenesis are described in detail in chapter 3.2.1 (Figure 1C).

3.1.3 Therapeutic approaches and limitations

Antiviral therapy for HCMV infection is a complex problem, which must balance risk factors from the virus and the available antivirals. Apart from the therapy of active infections, there are two major strategies for preventative HCMV management in high-risk patients: For a prophylaxis strategy, antiviral therapy is given to patients regardless of their infection status. In contrast, in a preemptive therapy scheme, the patient's blood is regularly tested for HCMV DNA, and only upon crossing a defined threshold, antiviral therapy is administered (39). Although HCMV is on a high priority list for vaccine development, no vaccine has been approved (129,130).

Consequently, antiviral drugs constitute the only option for HCMV management. Seven small molecule drugs are currently approved for the prevention and treatment of HCMV infections: Ganciclovir and its prodrug Valganciclovir, Cidofovir, Foscarnet, Letermovir and Maribavir. Generally, immunocompetent individuals are rarely treated for an active HCMV infection since their risk of severe disease from HCMV infection is low, and even the first-line choices of these drugs can cause severe side effects (39,131). Otherwise, Ganciclovir and Valganciclovir (in the following together addressed as GCV) are the substances of choice for prevention and treatment in patients with a high risk of mortality or disability from HCMV infection. Cidofovir and Foscarnet are second-line substances since they suffer from strong nephrotoxic and myelosuppressive side effects. Letermovir has recently been approved for HCMV prophylaxis in stem cell transplant patients due to its high efficacy and a favorable safety profile (39,131–133).

GCV is a nucleotide analogue that inhibits viral DNA synthesis through chain termination (134). For its active function, GCV is phosphorylated by pUL97 before the viral polymerase pUL54 incorporates it into the viral DNA (135,136). Consequently, HCMV can acquire resistance against GCV through mutation of the UL54 or UL97 genes, both of which can be observed in patients (137–140). In this case, Cidofovir, Foscarnet and Letermovir act as second-line drugs (39). Cidofovir and Foscarnet also target DNA synthesis by the viral polymerase. However, they do not require phosphorylation and can be used to treat variants which acquired GCV resistance through mutation of the UL97 gene (136). Letermovir, on the other hand, does not target the viral DNA synthesis but acts instead on the terminase subunit pUL56 (141,142). Although Letermovir is not affected by mutations in UL97 or UL54, resistances by mutation of UL56 have been reported (143). Maribavir acts as an inhibitor of the kinase pUL97. However, the inhibitory effect of Maribavir on HCMV replication seems to be less dependent on inhibition of DNA synthesis but rather due to a blockage of nuclear egress (144–146). Furthermore, hyper-immune globulin formulations against HCMV are approved to prevent viral reactivation in immunosuppression. However, their reported efficacy appears to be low (136,147).

Since antiviral treatment of HCMV is often a long-term recurrent necessity in

high-risk patients, the emergence of drug resistance is a problem of great concern (148–152). Since the recommended substances of choice for first-line therapy act mainly on the viral polymerase, therapeutic options for resistant HCMV are severely limited (151,152). For this reason, novel therapeutics are highly desirable, and last-line drugs like Maribavir have held an orphan drug status in the EU and the US for a long time (153,154). Just very recently, Maribavir has been approved by the FDA for use against pan-resistant HCMV, which illustrates the urgent need for novel antivirals (155–157).

3.2 HCMV final cytoplasmic assembly and egress

3.2.1 HCMV secondary envelopment

After packaged HCMV capsids leave the nucleus, they undergo further maturation before leaving the cell as fully infectious virions (Figure 1C) (158). A cellular phenotypic hallmark of human cytomegalovirus infection is the emergence of a prominent viral assembly complex (AC) during infection, which is a novel cytoplasmic organelle that hosts the last assembly steps ((159), also reviewed in (160)). The AC is a circular membrane-rich cytoplasmic compartment surrounding a microtubule-organizing center (MTOC), in which viral tegument and membrane proteins accumulate (159,161,162). Moreover, electron microscopic studies showed that viral capsids associate with membranes inside the AC (158,163–166), which strongly indicates that the final maturation steps of HCMV occur there. While little is known about the sequence and mechanism of the tegument assembly, HCMV secondary envelopment is more intensively studied. In addition, this process is highly interesting from a medical perspective since it must incorporate all the essential tegument and membrane proteins to generate fully infectious viral progeny (44).

Together, viral proteins and hijacked host processes and factors orchestrate HCMV secondary envelopment. During the process, a tegumented capsid buds into the membrane of a host-derived vesicle, which wraps around the particle and is pinched off upon complete envelopment (166). Several viral proteins were identified to be essential in this process. Early on, it has been described that deletion of the major tegument protein pp150, encoded by the gene UL32, leads to inhibition of viral spread in cell culture. Interestingly, the authors could detect little effects on viral replication, suggesting that pp150 is involved in the final stages of HCMV envelopment and egress (167). Another critical factor is the UL99 encoded phosphorylated tegument protein pp28, which has a myristoylation site to anchor it to membranes (168). Both modifications are necessary for the stability and function of the protein, which seems to play a role in the AC formation and secondary envelopment (168–170). HCMV mutants lacking UL99 or with mutations in critical positions display defects in secondary envelopment and egress (169–171). Still, some cell-to-cell spread of HCMV could be detected independently of pp28/UL99 presence (172). A direct interaction partner of pp28/pUL99 is the viral tegument protein pUL94 (173). The absence of pUL94 has also been shown to be detrimental to viral replication, leading to the accumulation of unenveloped capsids in the AC (171). Both proteins pUL99 and pUL94 are mutually necessary for their correct localization and proper virus replication. Moreover, mutations of the interacting domains phenocopy the aberrant localization for both proteins and the defective replication phenotype, highlighting the importance of the direct protein-protein interaction of the two partners (171). Another intensively studied tegument protein involved in secondary envelopment is pUL71. Stop mutants of pUL71 displayed a significant inhibitory effect on HCMV morphogenesis and a striking structural phenotype. In the absence of pUL71, the infected cells develop large vacuoles at the AC, accumulating capsids and dense bodies (viral tegument particles without capsid and genome) at their margins. Moreover, these viral products appeared to be halfway enveloped at the surface of these bodies, indicating an incomplete secondary envelopment process due to an inability to complete membrane fission (174,175). These vacu-

oles contained the tetraspanin CD63 and small intraluminal vesicles resembling those of MVBs, suggesting that MVBs might be the origin of the aberrant vacuoles and a target for secondary envelopment (166,175). A well-established interaction partner of pUL71 is pUL103, an interaction which is also conserved in their homologs in other herpesviruses (176–178). However, instead of the extensive phenotypical disturbances seen in pUL71 mutants, pUL103 was found to function mainly in post-envelopment steps of virus egress (179). Finally, the role of the envelope glycoprotein gO in secondary envelopment has been discussed in the literature. While initial reports suggested a role for gO in secondary envelopment for HCMV-TB40 (180), contradictory results were reported for the strain TR (181). A later study confirmed that a gO-stop variant of HCMV-TB40 can perform secondary envelopment in contrast to the variant used in the earlier study, which contained a 37-nucleotide deletion in gO (182).

In addition to the virus-encoded proteins, the host cell provides several critical components for HCMV maturation. Primarily, the cell provides lipid membranes in the form of cytoplasmic vesicles, which HCMV uses for secondary envelopment (183). Furthermore, the virus co-opts proteins from host trafficking and membrane remodeling processes to perform envelopment and egress. The source of the membranes used for HCMV envelopment has been debated for a long time. Historically, researchers searched for organelle-specific markers and pathway-specific trafficking motifs inside viral proteins to identify the target membranes. Initially, it has been reported that HCMV utilizes so-called endocytic cisternae for secondary envelopment, based on the presence of internalized horseradish peroxidase (HRP) in endocytic tracing experiments (184). This finding fits well with reports that the essential glycoprotein gB carries an acidic trafficking motif, which allows it to shuttle through the plasma membrane into endocytic compartments (185,186). An important step towards understanding the final assembly and egress steps of HCMV replication was the discovery of a cytoplasmic structure, which was found to contain several virus proteins as well as trans-Golgi network (TGN) markers. Because multiple tegument proteins accumulated specifically in this compartment, the authors suggested that this structure might be a cytoplasmic assembly site for HCMV (159). Later publications refer to this complex as the viral assembly complex/compartment (AC). Following studies aimed to determine the source of membranes for HCMV secondary envelopment by analyzing the AC's protein composition. However, extensive studies with organelle-specific markers found that the AC is a complex structure consisting of membranes from Golgi, TGN, endoplasmic reticulum-Golgi-intermediate compartments (ERGIC), and endocytic membranes (159,161,187). To further complicate the picture, other research strengthened the idea of a role for the endocytic- and recycling pathways for HCMV assembly and egress. While investigating the trafficking of the chemokine receptor-like membrane proteins pUL33, pUS27 and pUS28, one study found intracellular HCMV particles in endosomal structures, such as MVBs, and follow-up work found those structures associated with late endosomal markers such as CD63 (188–190). These findings were accompanied by investigations into whether the endosomal sorting complex required for transport (ESCRT) has a function in HCMV assembly. The ESCRT complex is involved in forming MVBs by mediating the inward budding and scission process at endosomal membranes (reviewed in (192)). The role of the ESCRT machinery in HCMV envel-

opment is a topic of ongoing controversy. Early on, studies published conflicting results, especially for the protein Vps4, which was found to be required for HSV-1 envelopment (193). While one study found no inhibition of HCMV progeny production upon siRNA depletion of several ESCRT factors (Vps4, TSG101 and ALIX), another group reported that dominant-negative variants of Vps4 and CHMP1 do inhibit HCMV replication (190,194).

The beginning of the last decade brought a change of perspective on HCMV secondary envelopment and egress. While evidence amounted that factors from different organelles can be found on virions (195) and that viral proteins essential for assembly are partially trafficked through different pathways (196), the hypothesis that HCMV merges and reorganizes membranes of different origins for assembly gained traction and the following research developed this idea further. Two studies found that Rab27A (197) and the SNARE-protein Syntaxin-3 (198) are involved in HCMV assembly, leading the authors to hypothesize that late endosomes and lysosomes play an important role in HCMV morphogenesis (198). In line with this report were results from a study which investigated the lipid composition of HCMV particles. The lipidomic analysis revealed that the composition of infected fibroblast cells is significantly different from the lipidome of viral particles, which resembles the composition of synaptic vesicles. Therefore, the authors suggested that HCMV acquires its envelope from a separate compartment located in the AC (199). Furthermore, it was found that Snap-23 is involved in the production of infectious progeny, fitting the preceding report on the role of Syntaxin-3 and suggesting a role for the SNARE membrane fusion machinery in viral assembly and egress (198,199). Around a similar time, Das et al. described a significant reorganization of the cell's secretory organelles by comparing the spatial colocalization of organelle-specific proteins between HCMV infected and uninfected cells. The authors offer the hypothesis that remodeling of cellular processes by HCMV infection likely leads to a shift in organelle identity through the relocalization of proteins. This reorganization potentially produces novel specialized compartments with distinct properties that mediate HCMV secondary envelopment and egress (200). This idea was further supported by research investigating the proteome of HCMV-infected cells. A large spatio-temporal proteomics study found major relocalization of organelle resident protein during HCMV infection. Most notably, were lysosome resident factors split into two subpopulations with different protein profiles, one of which clustered with Golgi, ER and structural viral proteins, supporting the idea of a novel, virus-generated compartment (201). Since then, multiple studies have added insight into the contributions of different organelles and pathways on the cytoplasmic stages of HCMV assembly. While one study found that Golgi fragmentation by the protein Grasp65 supports AC formation (202), another study showed that the AC acts as a Golgi-derived microtubule-organizing center (MTOC), controlling morphology and motility of the infected cell (162). Moreover, mislocalization of the Golgi resident SNARE constituent Syntaxin-5 mediated by the small molecule Retro94 resulted in an altered AC and significant inhibition of HCMV replication (203). Other research also found that factors from autophagic processes potentially play roles in HCMV envelopment. Infection experiments with autophagy-deficient cells, small molecule inhibitors and over-expression of autophagy blockers show that autophagic processes are not essential but advantageous for HCMV replication. Moreover, the presence of factors from autophagy

pathways in the AC leads the authors to suggest a contributory role for autophagic membranes in HCMV secondary envelopment (204,205). Furthermore, the effect of inhibition of endocytosis on HCMV infection utilizing small molecules and reanalysis of proteomics data from HCMV infection further highlighted the importance of endocytic, exocytic and recycling pathways on viral morphogenesis (206,207). In recent years, the upcoming field of exosome research opened another perspective on HCMV assembly. Regarding the controversy around the importance of ESCRT factors in HCMV infection, recent research found a different role for ESCRT proteins in HCMV spread (208). Instead of acting directly in secondary envelopment, the ESCRT machinery seems to be involved in producing extracellular vesicles with properties facilitating viral spread to neighboring cells (209). Moreover, it was found that herpesviruses also code for viral ESCRT homologs. For HSV-1, it has been described that HSV-1 pUL51 (homolog of HCMV pUL71) structurally resembles the ESCRT protein CHMP4B, leading to similar behavior, such as the ability to oligomerize to filaments. Moreover, the interaction of HSV-1 pUL7 (homolog of HCMV pUL103) with HSV-1 pUL51 inhibits its oligomerization reminiscent of the way CHMP4B filament formation is regulated in the cell. These data suggest that the HCMV homologs of these HSV-1 proteins could potentially perform ESCRT-like functions during viral assembly and explain the independence of HCMV assembly from cellular ESCRT factors (210). Two more large proteomic studies for HCMV recently added more evidence for the role of exosomal pathways in HCMV morphogenesis. The first study looked into the proteome of virions and other vesicular products exocytosed from HCMV-infected cells. Their analysis showed that factors from exosomal pathways are highly present in viral products, and in turn, viral products are present on exosomes released from infected cells (211). The latter fact is supported further by findings from a previous study, which found HCMV proteins on exosomes during infection (212). Moreover, the researchers could identify another SNARE protein, VAMP3, as an important factor for HCMV maturation (211). The other study from the group of Ileana Cristea investigated the temporal dynamics of protein-protein interactions in HCMV infected cells (213). Here, the authors could identify the proviral activity of the tetraspanin CD63, which regulates the trafficking of cargo from the plasma membrane through endocytic compartments and to exosomes (213–218). CD63 was found to internalize and degrade the HCMV receptor integrin beta-1 and subsequently localize to the AC, where, as the authors hypothesize, CD63 plays a role in HCMV particle maturation and egress (213). However, at this point, it must be noted that even though Hashimoto *et al*. found a reduction of viral titers upon CD63 knock-down, these results are in conflict with the publication mentioned above by Streck *et al.*, who do not find decreased viral titers in the absence of CD63 (209,213). Finally, recent research also suggests that the type of infected cell likely has a significant impact on the property of the membranes used for HCMV envelopment. In fibroblasts, HCMV progeny was found in large bodies, similar to MVBs, decorated with classical MVB markers. However, in human microvascular endothelial cells (HMVEC), phenotypically similar vesicles contained lysosomal (LAMP1) and cis-Golgi (GM130) markers, leading the authors to conclude that HCMV egress co-opts factors from different trafficking pathways for egress depending on the type of infected cell (219).

Closely related to the question about the identity of the membranes involved in

HCMV envelopment is the morphology of the vesicles used for viral egress. For herpesviruses in general, it has been shown that secondary envelopment likely happens by budding of a single particle into a small vesicle, generating a double-enveloped particle (reviewed in (220,221)). These vesicles can subsequently be transported to the plasma membrane to release the virion to the extracellular space (222,223). This model is also often provided as the basis of publications investigating ultrastructural aspects of HCMV secondary envelopment (166,205,224–226). However, many studies also found multivesicular structures as putative targets for HCMV envelopment, although the description, ultrastructure and assigned identity differ between the publications (158,163,175,184,187 ,189,190,219,227,228). To date, it is unclear whether different types of vesicles containing viral products belong to divergent egress routes or are derived from the same pathways and just varied in scale.

3.2.2 Diversity of HCMV virion compositions and cell tropism

It is well established that HCMV variants, which were extensively propagated in fibroblasts, accumulate significant mutations in their genome (229–232). The genetic variation in these strains, such as AD169 and Towne, also leads to a severe change in their behavior in cell culture and their target cell tropism (230,233–237). A significant effect on these phenotypic variations could be mapped to a region in the HCMV genome, called the UL/b' region, which sits on the boundary between the unique long (UL) region and the internal repeat long section (IRL) (229,233) (Figure 1A). This region is not essential for cultivating HCMV in fibroblast cell culture, and laboratory-adapted strains show substantial deletion mutations in this part of their genome (229,238,239). The observed deletions are likely preexisting genetic variants in the initially isolated virus populations and selected for during passage in fibroblasts (230). Genes in this part of the UL sequence are associated with multiple functions, e.g. a viral chemokine (UL146), immune evasion (UL141, UL142, UL144) and latency regulation (UL138) (240–246). Furthermore, the four genes UL128, UL130, UL131A and RL13 could be identified to be highly involved in the striking variability of cell tropism and virus spread seen between laboratory strains and clinical isolates (76,233–235,240,247,248). The three proteins pUL128, pUL130 and pUL131A form a pentameric complex with the viral glycoproteins gH and gL (235). In short, this complex is often referred to as the pentamer, in contrast to its counterpart, the trimer, which is a trimeric complex of gH, gL and gO (181). These two complexes have been identified in multiple studies to be the main drivers of cell tropism for HCMV. The trimer was shown to be generally required for the spread in all cell types, especially by cell-free virus particles (181,249). However, it has also been reported that cell-associated spread of the HCMV strain Merlin with fully repaired UL128 and RL13 loci is possible in the absence of gO (250).

The trimer and its interaction with the receptor PDGFR-α appears to be sufficient for the infection of fibroblasts (182,249,251,252). In contrast, the pentamer is essential for entry into other cell types, such as endothelial-, epithelial- and myeloid cells (181,233–236,248,249). For recognizing target cells, neuropilin-2, the olfactory receptor family member OR14l1 and thrombomodulin have been identified as binding partners for the pentamer (253–256). Since mutations in the UL/b' region are rapidly selected for when HCMV isolates are cultured continuously on fibroblasts, bacterial artificial chromosomes

(BACs) of low-passage or repaired strains such as TB40, TR and Merlin are essential tools in HCMV virology (229,232,237,238,240,257). BACs allow for the production of faithfully replicated, infectious viral DNA, as well as seamless *en-passant* mutagenesis via Red-recombination in specialized *E.coli* (95,240,257–262). With the help of BAC mutagenesis, an HCMV-Merlin strain was generated, which was fully repaired to the genetic status from the time-point of its isolation (240,263). Comparing this strain to other BACs such as TB40, FIX, and TR showed that a single nucleotide substitution in UL128 already resulted in significant changes in spreading behavior and cell tropism between the HCMV variants (264). Moreover, different HCMV strains also vary in the expression levels of gO, which also displays a high sequence variability between strains (248,249,265–267). These variations can affect virion infectivity; however, the complex effects and the mechanisms remain obscure (267,268).

In addition to mutations of the genes coding for the trimer and pentamer proteins, other factors have been described to influence viral replication and cell tropism, partially by altering the abundance of gH/gL glycoprotein complexes on virions. On the viral side, a large deletion in UL148 caused a disruption in the maturation of the trimer and a shift towards tropism for endothelial cells. In contrast, the presence of the intact gene stabilized gO expression and was associated with reduced levels of pentamer on the virion, suggesting a role for pUL148 in managing the glycoprotein composition of virus particles (269,270). This function is potentially performed in cooperation with the gene UL116 (271). Its product pUL116 has been found to interact with pUL148 but also to form a complex with gH (271). The absence of pUL116 caused a reduction in viral infectivity and the level of gH complexes on the virion, suggesting a function in the trafficking of gH to envelopment sites (271,272). Furthermore, the gene US16 was shown to be essential specifically for replication in endothelial- and epithelial cells (273). Later, the same group reported that US16 is involved in incorporating the pentamer into virions without interfering with the expression and assembly of the protein complex itself (274). From the host side, a study found that the tropism of HCMV progeny varies significantly depending on the infected host cell type (275). Whereas fibroblast cells produce cell-free fibroblast-tropic (FB-tropic) and endothelial-cell-tropic (EC-tropic) virus, endothelial cells release almost exclusively FB-tropic virus to the supernatant. However, EC-tropic progeny from endothelial cells is retained and only spreads cell-associated. Moreover, the study showed that the EC-tropic and FB-tropic progeny released from fibroblast cells does not consist of a single homogeneous-, but separate populations with different glycoprotein compositions and cell tropisms (275). Still, the molecular mechanisms of how the different virus populations are generated and differentially released remain elusive.

4 Aims and significance of this study

HCMV secondary envelopment is a critical step in viral morphogenesis since it concludes virion maturation and, if executed properly, yields infectious virus which can egress and infect the next cell. Although a wealth of data exists regarding viral and host proteins involved in the final steps of HCMV virion maturation, little is known about the spatio-temporal dynamics of the process. While experiments with alphaherpesviruses suggest that envelopment and egress are conducted by exocytosis of individually enveloped particles (222,223), the mechanism of HCMV egress is much less defined. Although evidence from other members of the herpesvirus family often serves as a good starting point to explore corresponding processes in HCMV, details between the viruses may vary. HCMV accumulates viral material in phenotypically distinct vesicles, from individually enveloped single particles to large MViBs containing tens to hundreds of virions, dense bodies and other vesicular material (158,163,184,189,219,228). However, the significance of this observation remains largely unclear, and a role for these structures is not established. Moreover is the origin of these MViBs still a mystery. While their phenotype suggests similar biogenesis to classical cellular MVBs, HCMV morphogenesis has been found to involve multiple proteins from different organelles and pathways. HCMV performs this feat by significantly remodeling cellular membranes and trafficking processes, relocalizing and recruiting viral and host protein to its advantage (161,195,196,200,201).

In the light of this complexity, this study aims to decipher the spatio-temporal coordination and cellular mechanisms of HCMV envelopment and egress. HCMV products and their vessels are tracked in infected, living cells to elucidate release mechanisms and dynamics. These data are complemented by correlative two- and three-dimensional electron microscopy data to bridge the gap between live-cell fluorescence- and ultrastructural information. Hereby, this work intends to fill in the knowledge gaps regarding the morphology of HCMV egress vesicles and release mechanisms. Moreover, the work presented here aims to explore the origin and generation of the MViBs to investigate parallels with cellular MVBs by investigating the presence of markers from endosomal and exosome pathways and evaluate the effect of inhibitors of MVB and exosome biogenesis.

The knowledge generated in this work is of particular interest for research into the viral and host factors involved in HCMV morphogenesis and egress. This is especially important in HCMV research since the impact of the diversity of vesicles containing viral products remains to date largely undefined. Here, the combination of ultrastructural and live-cell information provides critical information about the function of virus-containing vesicles and thereby helps to inform future research assessing the location and function of host and viral proteins. Furthermore, this study relates to investigations into the diverging spreading characteristics observed depending on HCMV strains and infected cell type (230,240,275–278). Regarding the observed diversity in spreading modes, the results of this study will aid future investigations into the potential role of distinct egress routes for different modes of HCMV spread. Finally, this study also provides a technical framework to investigate interventions, such as host and viral mutants and small molecule inhibitors of HCMV envelopment and egress.

5 Results

5.1 Technical challenges limit single particle tracking of HCMV envelopment in infected cells by fluorescence microscopy

To investigate the kinetics of HCMV secondary envelopment in living infected cells, a workflow for live-cell single particle tracking was developed. The workflow was based on a cell culture infection model consisting of the dual fluorescent HCMV-TB40-pp150-EGFP-gM-mCherry and HFF cells. The cells were infected at an MOI of 1 and imaged by live-cell fluorescence spinning-disk microscopy at 72-96 hpi. A motorized, computer-controlled spinning-disk microscope allowed for the automatic acquisition of 10-minute videos of predefined, manually selected positions. In the selection process, cells were chosen which showed a well-defined, gM-mCherry positive AC and pp150-EGFP positive spots in the cytoplasm (Figure 2A). The acquisition settings were optimized to minimize the excitation light input and thereby reduce photobleaching of the fluorophores and phototoxicity affecting the imaged cell. The acquisition framerate was set between 8-15 frames/second to allow tracking of fast-moving particles. After the acquisition, the two-channel movies were split, and the pp150-EGFP channel was denoised using the deep-learning algorithm Noise2Void (279). The Noise2Void algorithm was trained on the first three frames of each individual acquisition, and the denoising prediction was subsequently applied to the whole movie, using a custom Jupyter notebook for batch processing (Code 1). With this, the contrast in the pp150-EGFP channel was enhanced (Figure 2B). These enhanced movies were subsequently used for single particle tracking of the pp150-EGFP positive spots using the Fiji plugin Trackmate (280). Hereby, the denoising increased the average length and duration of the tracks, indicating that denoising of the low-contrast raw data improves the tracking by Trackmate (Figure 2C). Afterwards, the tracks were analyzed and segmented according to their movement patterns and the brightness of the tracked spot in the gM-mCherry channel using the custom Matlab script tool TrISS (Code 2). To assess the movement mode of the particle, a mean squared displacement analysis was performed with the MatLab class msdanalyzer, and the alpha value was calculated for segments of the tracks (281). Briefly, the alpha value is called the anomalous diffusion exponent and indicates whether a particle is diffusing freely ($\alpha = 1$), is restricted in its movement ($\alpha < 1$) or experiences superdiffusion/active transport ($\alpha > 1$) (281,282). As a result, 78503 tracks were analyzed and segmented into sections of restricted diffusion, diffusion and active transport, as well as gM-mCherry signal above or below local background levels (Figure 2D-E). With this, it was possible to separate tracks of enveloped particles (actively transported particles with gM signal above local background) from non-enveloped particles (actively transported without elevated gM signal) (Figure 2E). However, this method could detect no particles that transitioned from a non-enveloped to an enveloped state.

However, several aspects of the experimental setup restricted the feasibility of tracking virus particles and identifying envelopment events. The main limitations concerned track length (the time frame in which information about a particle was recorded) and spatial resolution. Since the lengths of the tracks were shorter than the video length, it is likely that movement of the particle in the z-direction, rather than restriction of ac-

quisition time by phototoxicity and photobleaching, was the limiting factor (Figure 3A). Also, a negative correlation between track displacement and mean velocity compared to track duration could be observed. This indicates that faster movement and a larger displacement, two properties experienced by actively transported particles, limit the tracking time (Figure 3A). This can be due to movement of the particle out of the focal plane, crossing of tracks, or loss of the track. Moreover, the spatial resolution of the light microscope affects the ability to track a single particle in dense environments. Since the replication compartment becomes increasingly crowded with virus particles late in infection, tracking of single particles is only possible at earlier time points or the periphery (Figure 3B). This limits the spatio-temporal window in which single particle tracking can be applied for tracking secondary envelopment.

2A

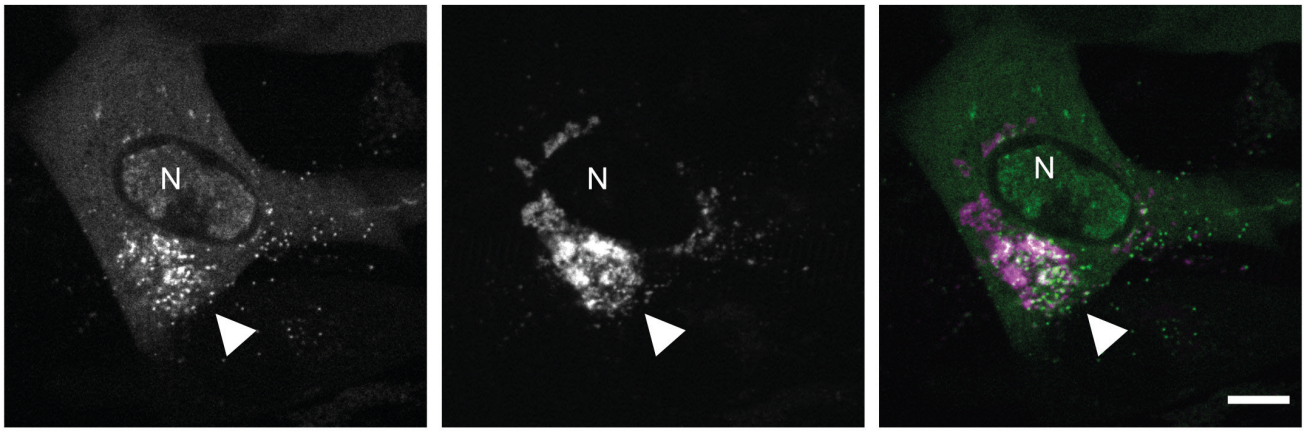

pp150-EGFP gM-mCherry merge

2B

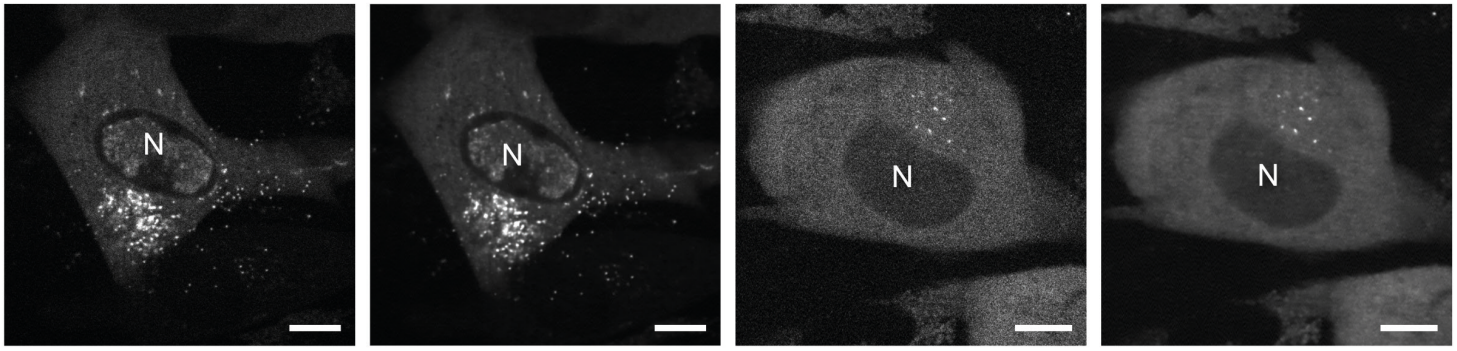

raw denoised raw denoised

2C

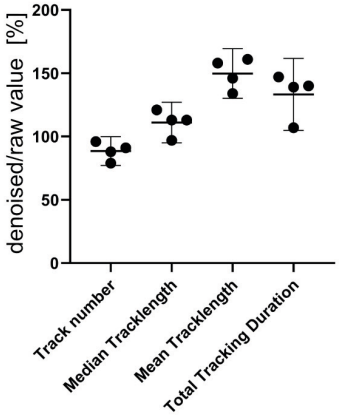

2D

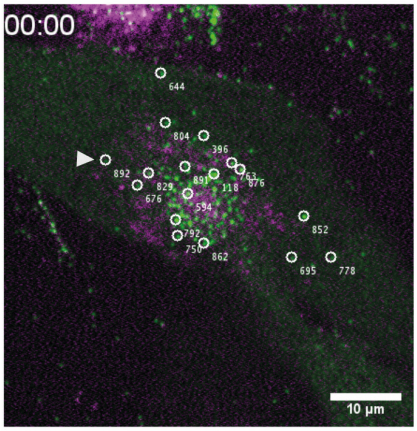

2E

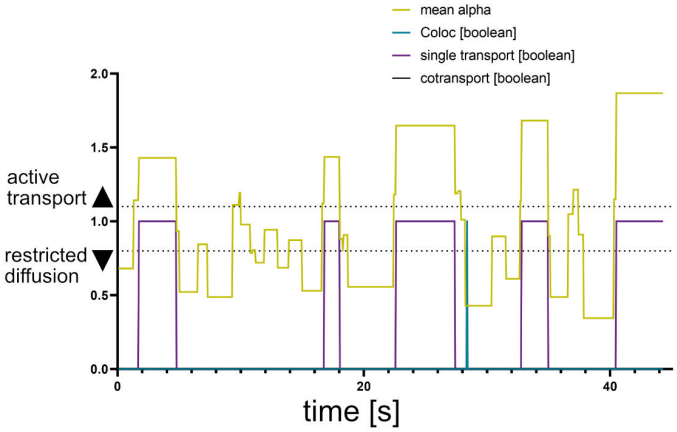

Figure 2. Single particle tracking and automated track segmentation to investigate HCMV secondary envelopment.

2A HFF cells were infected with HCMV-TB40-pp150-EGFP-gM-mCherry at an MOI of 1. The cells were imaged live at 4 dpi by spinning-disk microscopy, and 10-minute videos were acquired per cell at a framerate of 8 fps. The panel shows the first image of the sequence. The white triangle indicates the juxtanuclear viral assembly complex, and the N marks the host cell nucleus. Scale bar represents 10 µm.

2B Two pairs show two images of an HFF cell infected with HCMV-TB40-pp150-EGFP-gM-mCherry. The cells were imaged at 4 dpi with spinning-disk microscopy as described in 2A. All images show only the first image in the sequence from the EGFP channel. As indicated below the panels, the right image of each pair is denoised using the algorithm Noise2Void (279), whereas the left image shows the corresponding raw data. N marks the cells' nuclei, and the scale bar represents 10 µm.

2C HFF cells (HFF-1 and BJ) were infected with HCMV-TB40-pp150-EGFP-gM-mCherry at an MOI of 1 and imaged live for 10 minutes at 4 dpi. After the acquisition, the EGFP channel was denoised using Noise2Void. EGFP-positive dots, indicating viral particles, were tracked using TrackMate (280) in both the denoised and the raw videos. The number of tracks, median and mean track length, as well as the total tracking duration of all tracks combined, were quantified and compared between the two conditions for four representative cells. Plotted is the value of the denoised set versus the raw set in percent. Error bars show the 95% confidence interval of the mean.

2D BJ-cells were infected with HCMV-TB40-pp150-EGFP-gM-mCherry at an MOI of 1. After 4 days, 10-minute live-cell videos were acquired at a framerate of 16.6 fps by spinning-disk microscopy. Subsequently, the EGFP-channel was denoised using Noise2Void, and single particles were tracked with TrackMate. Tracks were further analyzed and segmented using the custom Matlab tool TrISS (Code 2). Shown is the first image of the sequence as a merge of the two channels pp150-EGFP (denoised) and gM-mCherry. Marked with the white circles are all particles which displayed active transport during the acquisition, while the gM-mCherry signal on the particle showed no elevation over the local background (termed here as single transport). The white triangle marks the particle, of which the movement behavior is shown further in figure 2E. Scale bar represents 10 µm.

2E Exemplary breakdown of the movement behavior of the particle indicated with the white triangle in 2D, as analyzed by TrISS. The yellow line indicates the alpha value averaged over a segment. The other lines show the colocalization status with gM (Coloc, cyan) and whether pp150 particles are transported together with gM (cotransport, black) or without (single transport, magenta). The last three values are binary, whereas 1 means true and 0 false. Segments of active transport (average alpha above 1.2), with a Coloc value at 0, generate a true (1) signal for the single transport property.

3A

Cell 1 Displacement

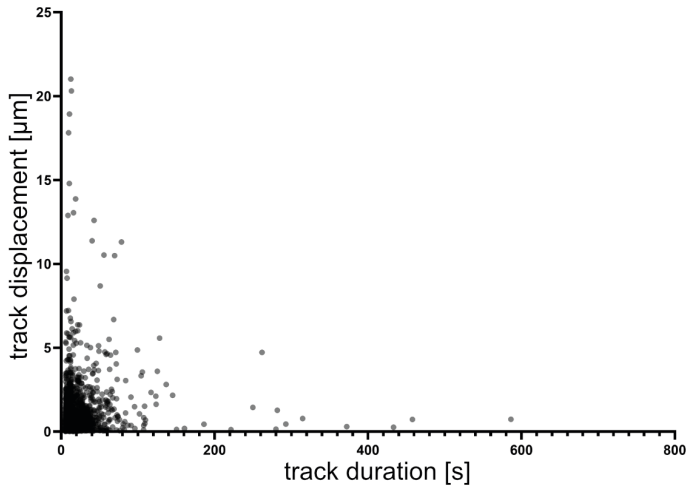

Cell 2 Displacement

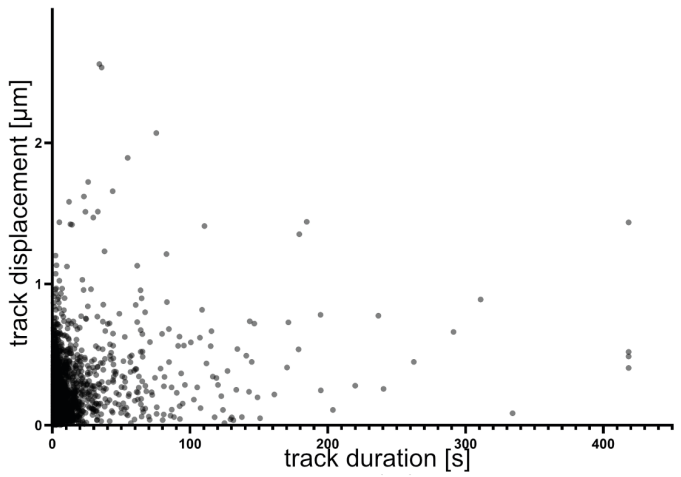

Cell 1 Velocity

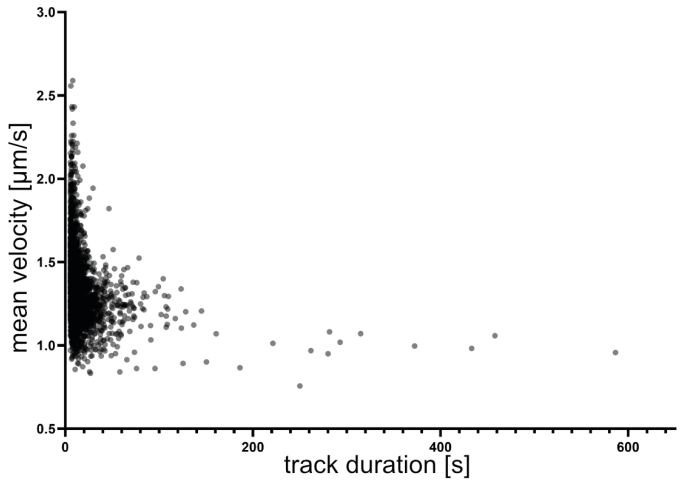

Cell 2 Velocity

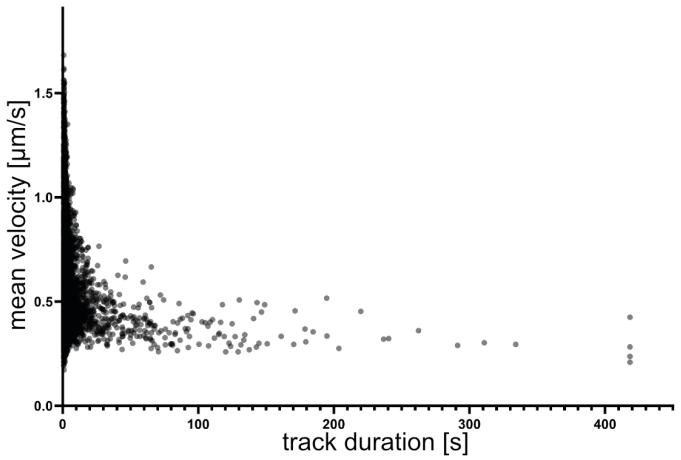

3B

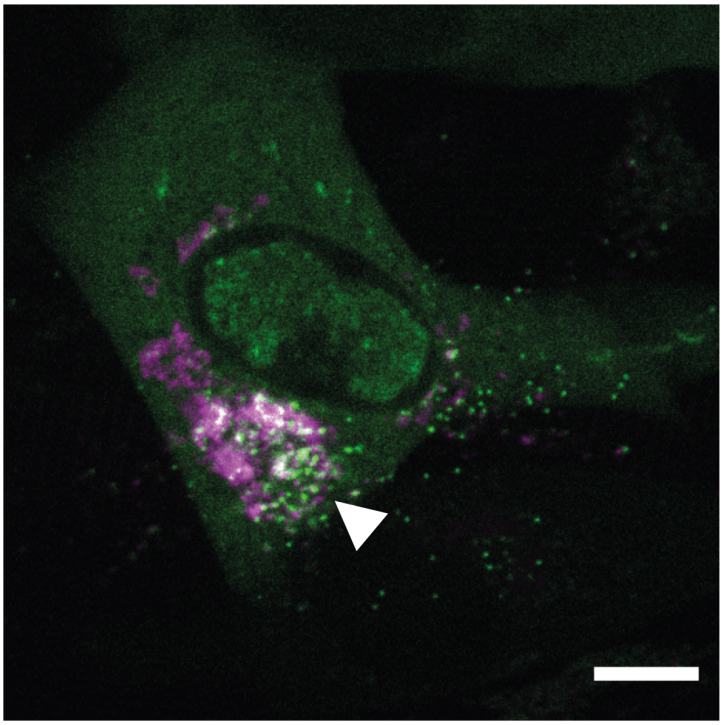

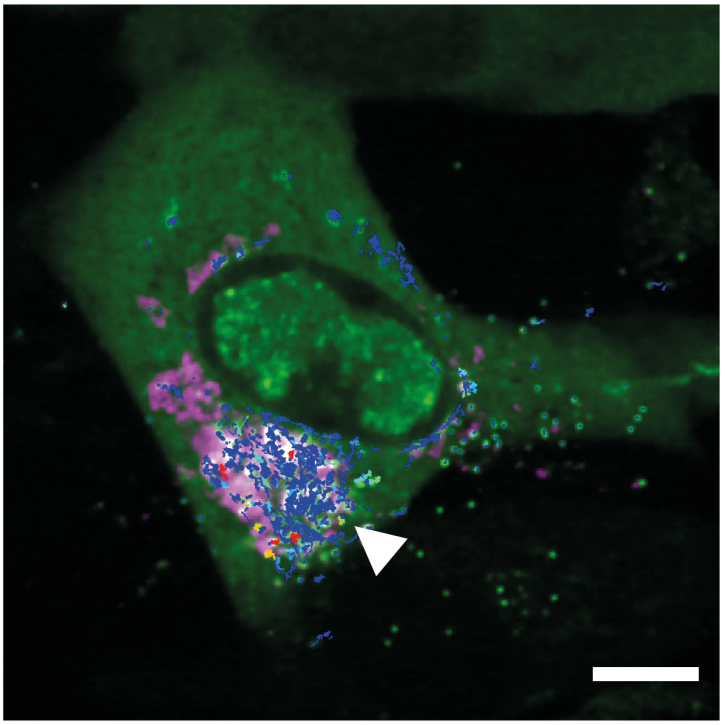

Figure 3. Limitations to single particle tracking of HCMV particles in infected cells.

3A Tracking statistics from the tracks acquired from the cell shown in figure 2A. The graphs show the track displacement and mean velocity for each track plotted against the track's duration.

3B HFF cell infected and imaged as described for figure 2A. Shown in the right panel are all tracks colored on a spectrum from red (long tracks) to blue (short tracks). Indicated with the white triangle is an area dense with pp150 (green) particles in the viral AC, in which recorded track lengths are short. Scale bar represents 10 µm.

5.2 3D CLEM reveals HCMV accumulations in specific extracellular sites and intracellular multivesicular structures

In late infected cells, HCMV particles accumulate in dense regions at the AC and in specific regions at the plasma membrane, which are subsequently referred to as extracellular viral accumulations (EVAs) (Figure 4A-C). Since these regions were too dense to be resolved with fluorescence light microscopy, electron microscopy was used to investigate the accumulations. To this end, a novel CLEM workflow was established, which combined fluorescence spinning-disk microscopy with serial block-face scanning electron microscopy (SBF-SEM). For this experiment, HFF cells seeded on Ibidi plastic bottom microscopy Petri dishes with grids etched in the growth substrate were infected with HCMV-TB40-pp150-EGFP-gM-mCherry at an MOI of 3 and fixed at 4 dpi. The cells were imaged by fluorescence spinning-disk microscopy, and z-stacks of infected cells were acquired (Figure 4A). The accumulations at the plasma membrane were visible as large patches positive for pp150-EGFP and gM-mCherry at the bottom of the cell, whereas the intracellular regions could be seen as large round bodies likewise positive for both markers (Figure 4B-C). The positions of the imaged cells were noted, and the sample was processed for SBF-SEM. In the 3D electron microscopy dataset acquired by SBF-SEM (Figure 4D), the accumulations at the plasma membrane were revealed to be large accumulations of virus particles, dense bodies and other viral material (Figure 5A-C). Also, cases could be seen where invaginations of these accumulations reached into the cell, possibly indicating an event in which these accumulations are generated (Figure 5D).

The dense regions, positive for pp150-EGFP and gM-mCherry, which resided inside the cytoplasm of the infected cells, could be resolved by SBF-SEM (Figure 6A-C). Volume rendering of these structures in the EM data revealed them to be large, closed multivesicular structures filled with virions, dense bodies and other vesicles (Figure 6C). Due to their multivesicular nature, these bodies will be subsequently referred to as multiviral bodies (MViBs). The MViBs were very heterogeneous in size and could harbor from a few up to hundreds of virus particles, dense bodies and other vesicles. To investigate a putative relationship between the MViBs and EVAs, their contents were quantified and analyzed. Random volumes from the SBF-SEM data containing parts of MViBs or EVAs were extracted, and their content was manually classified into virions, dense bodies and other vesicular material. Quantification and statistical comparison of the groups yielded no statistically significant difference between the contents of MViBs and EVAs (Figure 6D).

The EM images showed furthermore that viral capsids and dense structures localize to indentations at the surface of these structures, indicating that *de novo* envelopment occurs at their surfaces (Figure 6E). However, since the EM images are static, careful interpretation of the directionality of processes is essential. This topic is further discussed in 6.3.

The SBF-SEM data also contained examples of virus capsids interacting with single vesicles, as previously described in publications investigating HCMV secondary envelopment (Figure 7A-B; (166)). Moreover, the SBF-SEM technique could show multiple stages of the virus life-cycle, from nuclear stages to fully enveloped and exocytosed particles, showcasing this technique's usefulness in investigating the cellular replication cycle of HCMV in 3D (Figure 7C).

4A

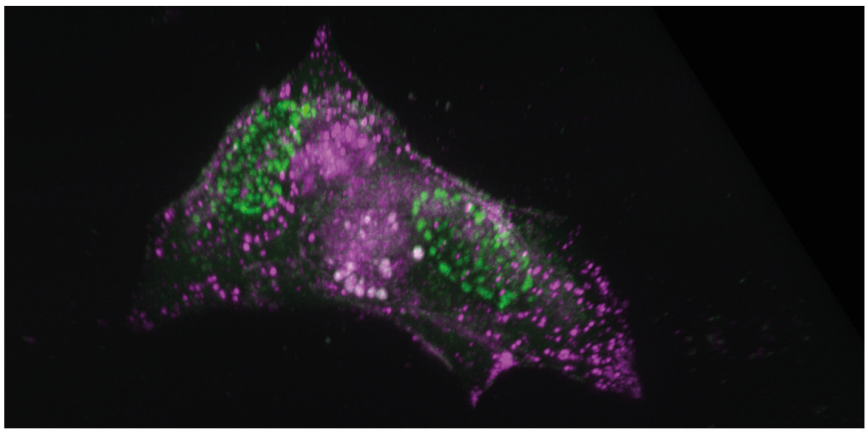

4B

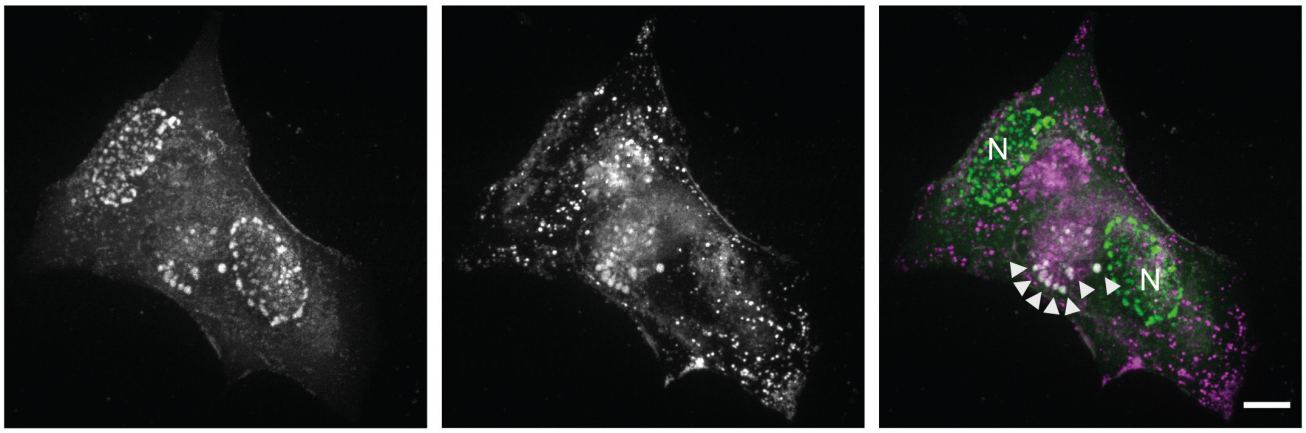

pp150-EGFP gM-mCherry merge

4C

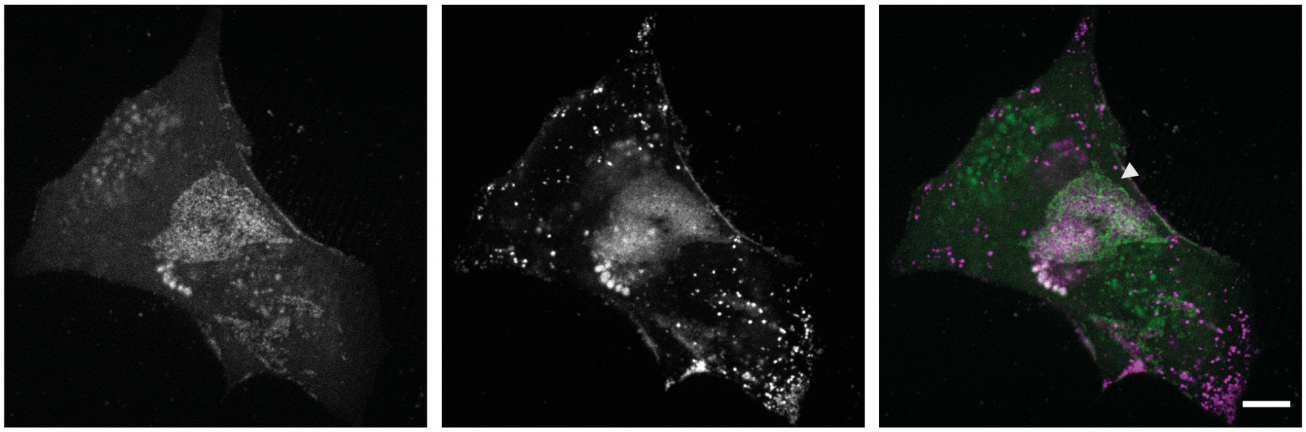

pp150-EGFP gM-mCherry merge

4D

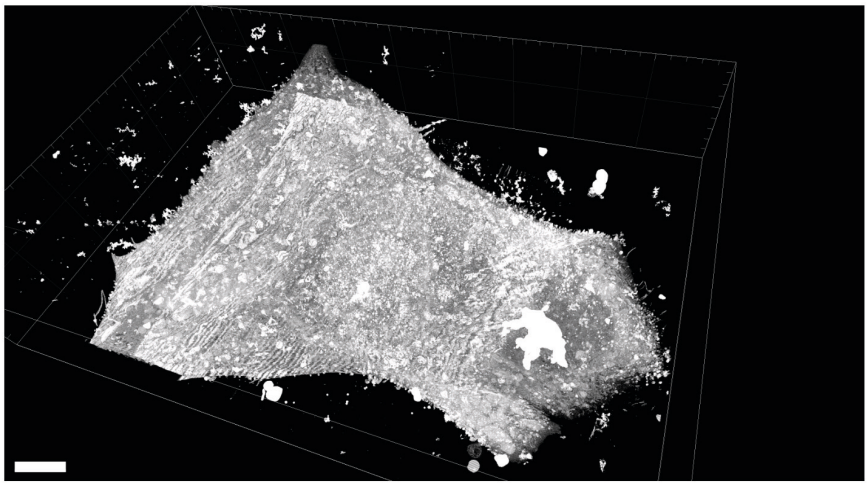

Figure 4. Correlative spinning-disk fluorescence imaging and serial block-face scanning electron microscopy (SBF-SEM) allow 3D CLEM of HCMV infected cells.

4A HFF cells were infected with HCMV-TB40-pp150-EGFP-gM-mCherry (MOI of 3). After fixation at 4 dpi, z-stacks of the cells were acquired by spinning-disk microscopy. The signal of pp150-EGFP is rendered in green and gM-mCherry in magenta.

4B A maximum projection of the data, acquired as described for figure 4A. White triangles indicate examples of large, round and dense objects in the cytoplasm positive for pp150-EGFP (green) and gM-mCherry (magenta). N indicates nuclei, and the scale bar represents 10 µm.

4C A single z-slice from the lower plasma membrane of the cells shown in figure 4A-B. The white triangle indicates a large patch with accumulated pp150-EGFP and gM-mCherry signals. Scale bar represents 10 µm.

4D After the cells' fixation, as described in figure 4A, the sample was further processed for SBF-SEM. EM-stacks were acquired by repeated scanning and ablation of 50 nm sections. Shown is a 3D render of a reconstruction of the sections. Scale bar represents 7 µm. See also supplementary video 3A from (283,284).

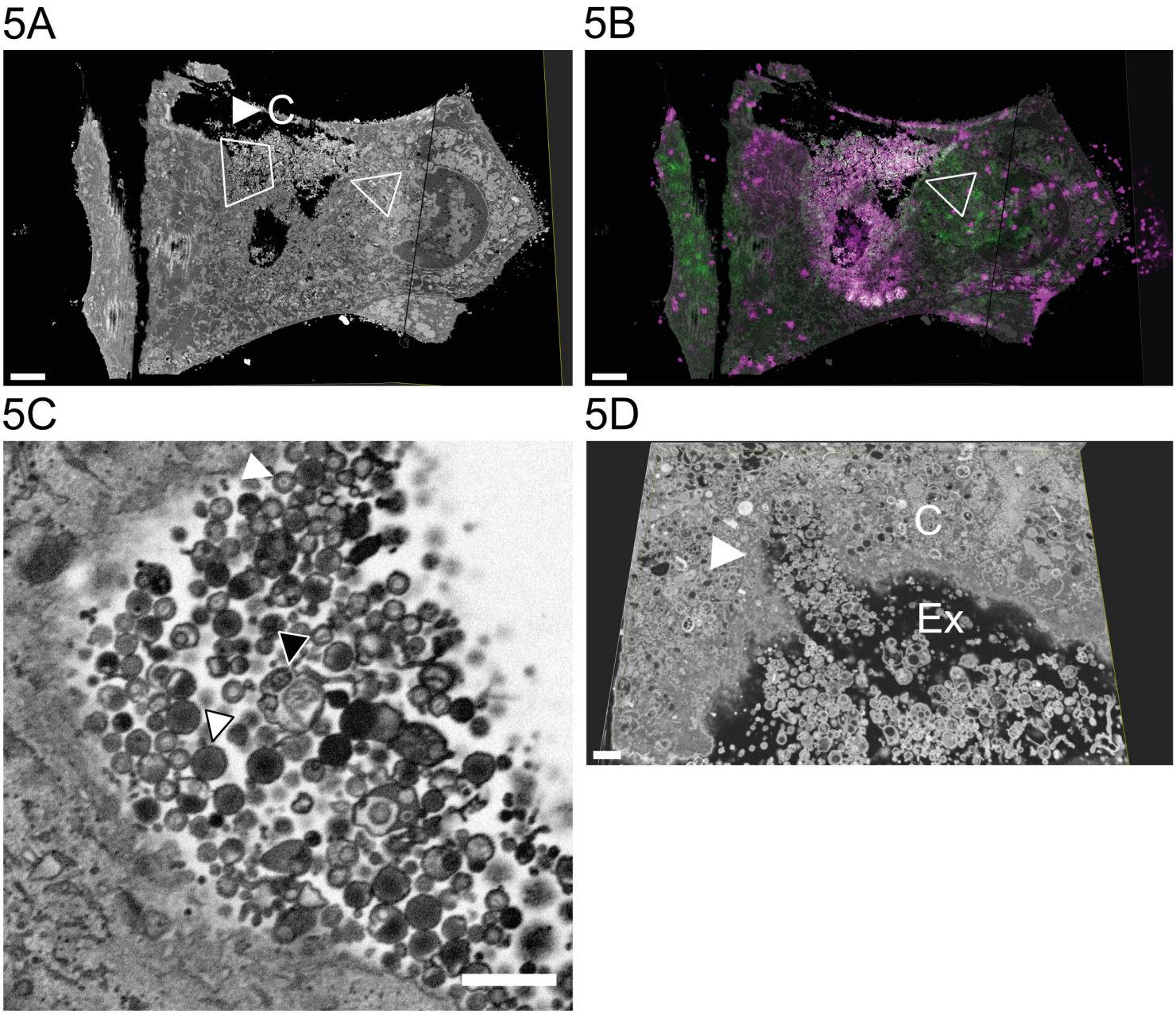

Figure 5. 3D CLEM reveals extracellular viral accumulations (EVAs) at the lower plasma membrane.

5A A resliced SBF-SEM section from the lower plasma membrane of the cells, prepared as described for figure 4D. The white contoured triangle indicates an extracellular accumulation of viral material (the white frame indicates a magnification of that area shown in 5C). Scale bar represents 3 µm.

5B CLEM overlay of the fluorescence signal of the same area with the SBF-SEM data. The white contoured triangle indicates the overlapping fluorescent patch of pp150-EGFP (green) and gM-mCherry (magenta) with the EVA shown in 5A. Scale bar represents 3 µm.

5C A single section of the SBF-SEM data enlarged. The area is part of the EVA shown in 5A and illustrates the diversity of material, such as virions (example marked with a white triangle), dense bodies (black contoured white triangle) and other vesicles (white contoured black triangle) found in EVAs. The signal is inverted to facilitate comparison with classical transmission electron microscopy (TEM) images. Scale bar represents 1 µm.

5D Example section of the SBF-SEM data produced as described before, showing an invagination (white triangle) in the cytoplasm (marked by the white C) next to an EVA in the extracellular space (marked with the white Ex). Scale bar represents 700 nm.

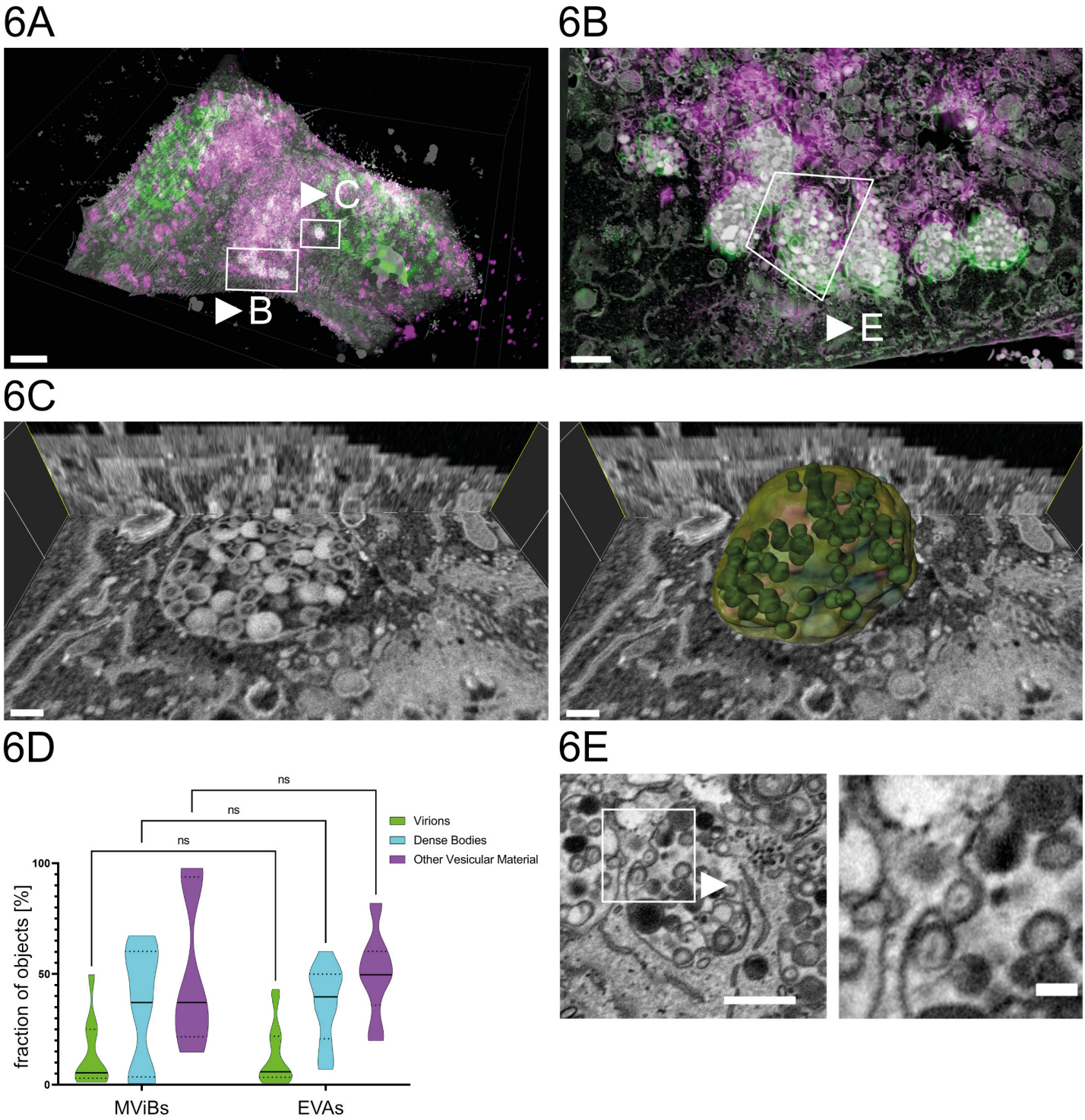

Figure 6. 3D CLEM detects HCMV progeny accumulating in MViBs.

6A Correlative overlay of the data shown in 4A and 4D. White frames indicate the areas which are enlarged in the indicated panels. Scale bar represents 7 µm. See also supplementary video 3B in (283,284).

6B Correlation of fluorescence to a resliced SBF-SEM section from the area indicated in 6A. The white frame indicates the area of the dataset from which figure 6E is enlarged. Scale bar represents 1 µm.

6C 3D render and a surface rendering is shown for a representative MViB from the area indicated in 6A. The colors of the surfaces indicate the rendered structures: MViB limiting membrane: Yellow, Virions: green, dense bodies: blue, other vesicular material: magenta. Scale bar represents 300 nm. A video of the rendered data can be found in (283,284), supplementary video 2.

6D Comparison of quantification of vesicular material in MViBs versus EVAs from four cells. Statistical significance was probed using a 2-way ANOVA and Šídák's multiple comparisons test. No significant difference was detected in the material between the two structures.

6E Sections of the SBF-SEM data enlarged from the area indicated in 6B. SEM signal is inverted. The white frame in the left panel indicates the area further enlarged in the right panel. Scale bars represent 1 µm (left panel) and 200 nm (right panel).

7A

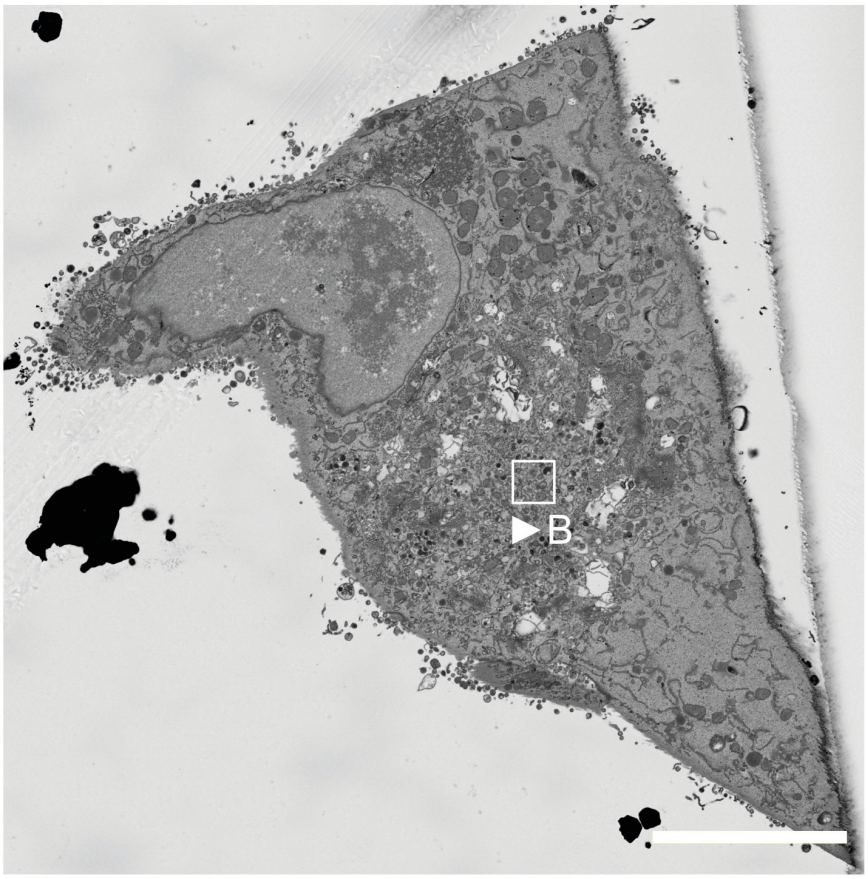

7B

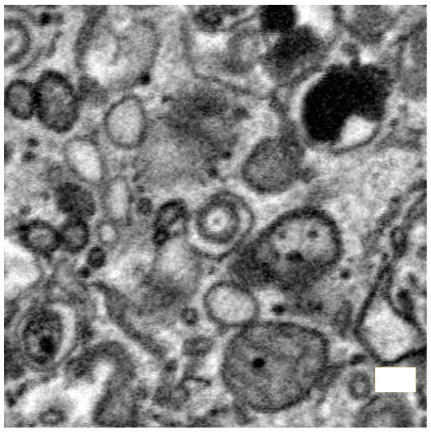

7C

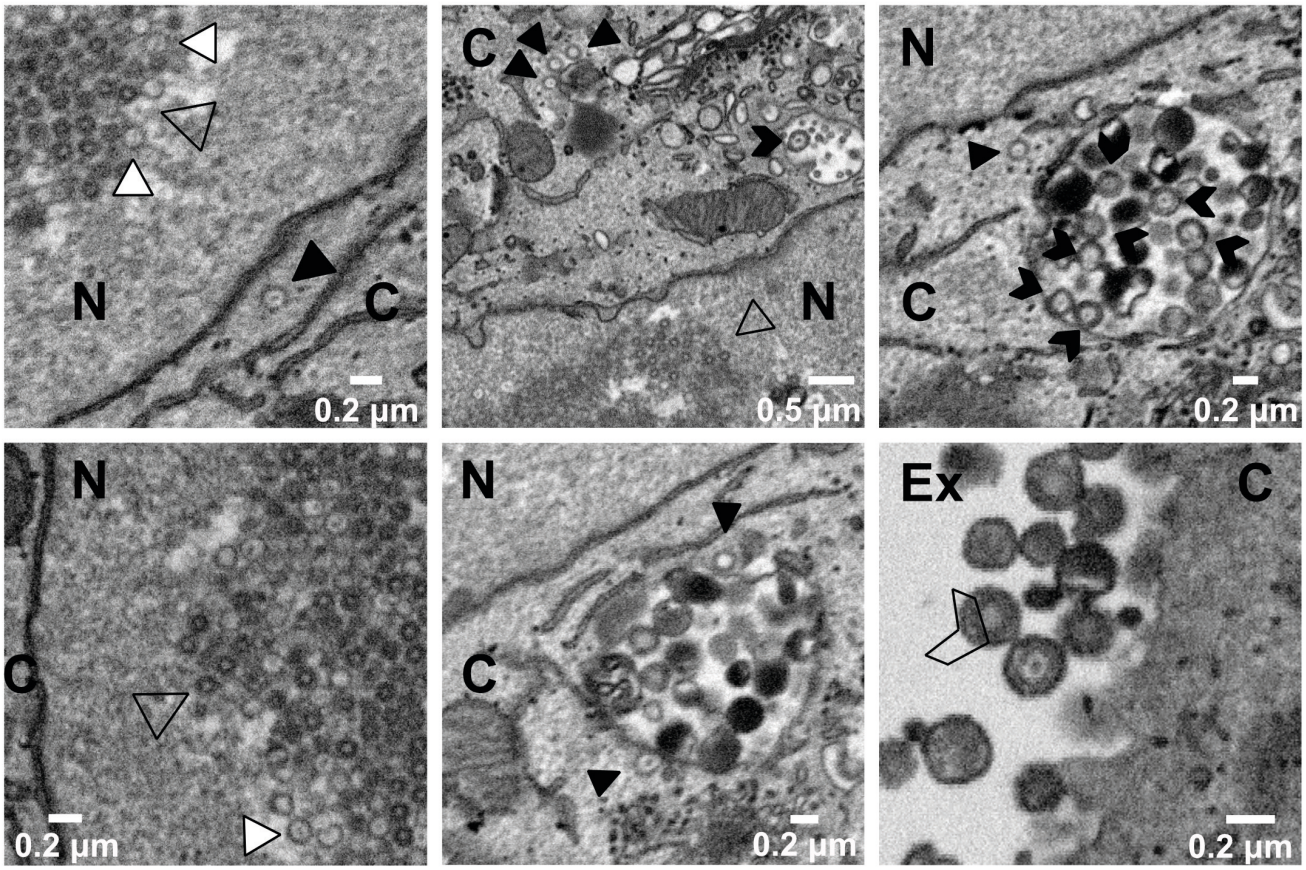

Figure 7A. SBF-SEM allows the investigation of the whole viral morphogenesis process.

7A Single section through a whole cell from the SBF-SEM data described in figure 4D. The white frame indicates the area enlarged in 7B. SEM signal is inverted. Scale bar represents 10 µm.

7B Enlargement of the area indicated in 7A shows a single vesicle enwrapping a single capsid. Signals are inverted. Scale bar represents 200 nm.

7C The panels show enlargement of SBF-SEM data from infected cells as described in figure 3D. N marks nucleoplasm, C marks cytoplasm, and Ex indicates the extracellular space. Highlighted are virus particles in different stages of the viral morphogenesis: nuclear B-capsids (black contoured triangles), nuclear C-capsids (black contoured white triangles), cytoplasmic non-enveloped C-capsids (black triangles), intracellular enveloped virions (black arrowheads) and extracellular enveloped virions (black contoured arrowheads). Signals are inverted, and scale bar lengths are indicated in the panels.

5.3 Quantification indicates EVAs to be a common phenotype in HCMV infection

To further improve the fluorescent properties of the dual-tagged HCMV variant, the fluorescent tags on the viral proteins were changed. TB40-WT maintained as a BAC in *E. coli* (257), was tagged by two rounds of homologous recombineering by *en-passant* BAC mutagenesis (261). The tegument protein pp150 was C-terminally tagged with a SNAP-tag (performed by Timothy Soh in (284)), and the membrane glycoprotein gM was tagged after amino acid V62 with mScarlet-I (284,285). The positions of the tags matched the positions of the tags in the virus published in (286). To control for growth defects of the virus due to the switched fluorescent tags, growth curves were performed for HCMV-TB40-WT and HCMV-TB40-pp150-SNAP-gM-mScarlet-I. The dual-tagged virus grew with slightly slower kinetics than HCMV-WT, but the overall growth properties remained similar (Figure 8A). In order to elucidate if EVAs are a common phenotype or an exception in these experiments, the occurrence of these structures was quantified. Fluorescent protein tags can sometimes interfere with correct protein function. Therefore it was also necessary to confirm that the phenotype investigated in this study was not an artifact of the genetic modification of the viral proteins. To control for this possibility, the following experiment was carried out in HFF cells infected with HCMV-TB40-WT and HCMV-TB40-pp150-SNAP-gM-mScarlet-I. At first, HFF cells were infected at an MOI of 1 and fixed 5 dpi. The HFF cells infected with HCMV-TB40-WT were IF stained for gB and in the HCMV-TB40-pp150SNAP-gM-mScarlet-I infected HFFs, the SNAP-tag was labelled with SNAP-Cell-SiR. Large 3D overviews were acquired on a spinning-disk microscope by automated tiling and z-stack acquisition. Cells in late infection stages and cells with EVAs were counted. Strikingly, for both viruses, 80-90% of late-stage infected cells had EVAs at their lower plasma membrane (Figure 8B).

5.4 Long time-lapse imaging reveals bulk release dynamics for HCMV

To investigate the fate of these MViBs found through SBF-SEM and to determine their role in viral egress, HCMV egress was analyzed in a larger spatio-temporal window. For this experiment, volumetric long time-lapse spinning-disk fluorescence microscopy was used. However, the limited temporal resolution did not allow for direct investigation of secondary envelopment but only allowed for analysis of HCMV cellular egress on a longer timescale. Therefore, HFF cells were infected with this novel HCMV-TB40-pp150-SNAP-gM-mScarlet-I at an MOI of 1 and imaged between 3 dpi and 5 dpi. Right before imaging, pp150-SNAP was labelled with SNAP-Cell-SiR according to the manufacturer's instructions. Z-stacks with 1 µm steps were acquired in 45 min intervals to minimize phototoxicity and photobleaching. The time-lapse data shows that accumulations of virus particles, determined by pp150-SNAP and gM-mScarlet-I positive patches at the plasma membrane, appeared in intermittent pulses beginning at approximately 3 dpi (Figure 9). Preceding the appearance of the accumulations, large bodies, also positive for both markers, emerged in the cytoplasm (Figure 9). These structures had a strong resemblance to the MViBs discussed before and indicated that they are likely the source of the accumulations.

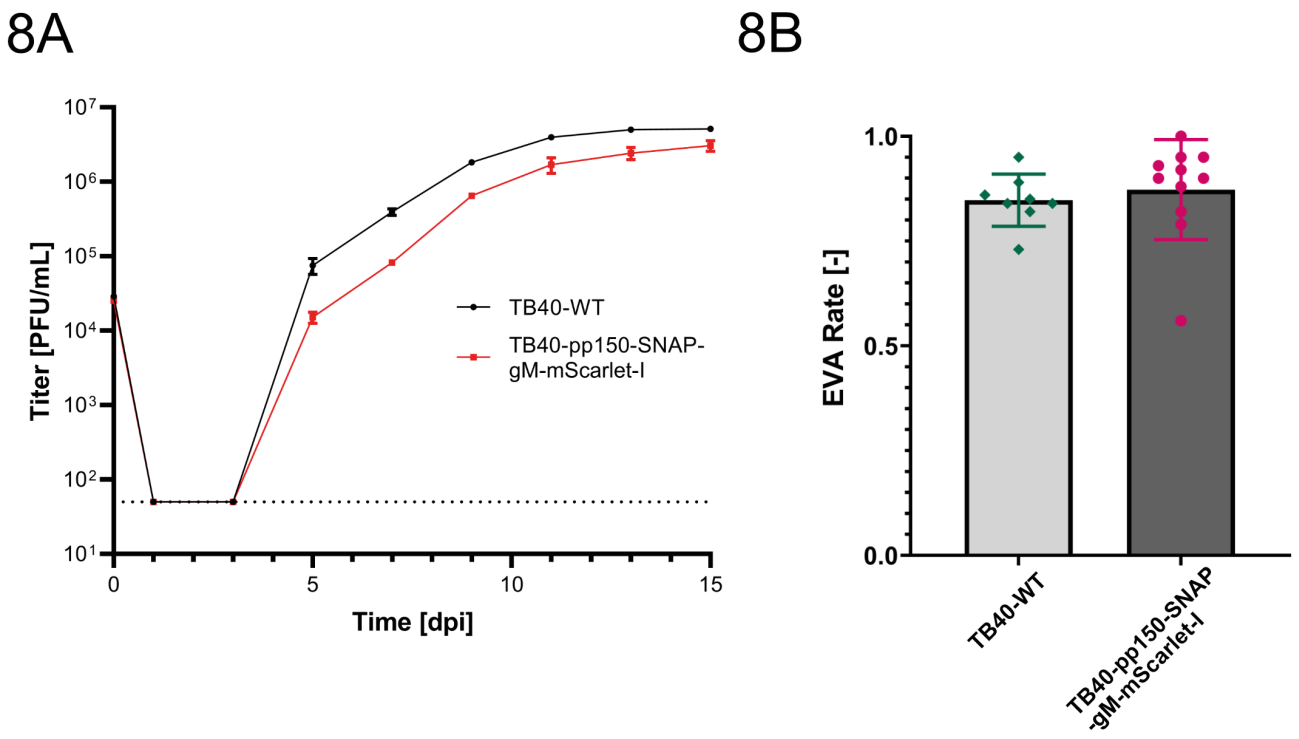

Figure 8. HCMV-TB40-pp150-SNAP-gM-mScarlet-I growth is attenuated, but EVA prevalence is similar to WT.

8A HFF cells were infected with either HCMV-TB40-WT or HCMV-TB40-pp150-SNAP-gM-mScarlet (MOI of 0.05). Growth properties were probed with a growth curve.

8B HFF cells were infected with HCMV-TB40-WT or HCMV-TB40-pp150-SNAP-gM-mScarlet-I (MOI of 1). At 5 dpi, the cells were fixed and stained. The SNAP-tag in TB40-pp150-SNAP-gM-mScarlet-I cells was stained with SNAP-Cell-SiR, and TB40-WT infected cells were immunofluorescence (IF) stained against HCMV gB. Overviews of the infected cells were acquired by spinning-disk microscopy, and EVA prevalence was quantified in late-stage infected cells. Borders show the 95% confidence interval of the mean. 11 replicates were performed for TB40-pp150-SNAP-gM-mScarlet-I (N=269) and 8 replicates for TB40-WT (N=750).

9

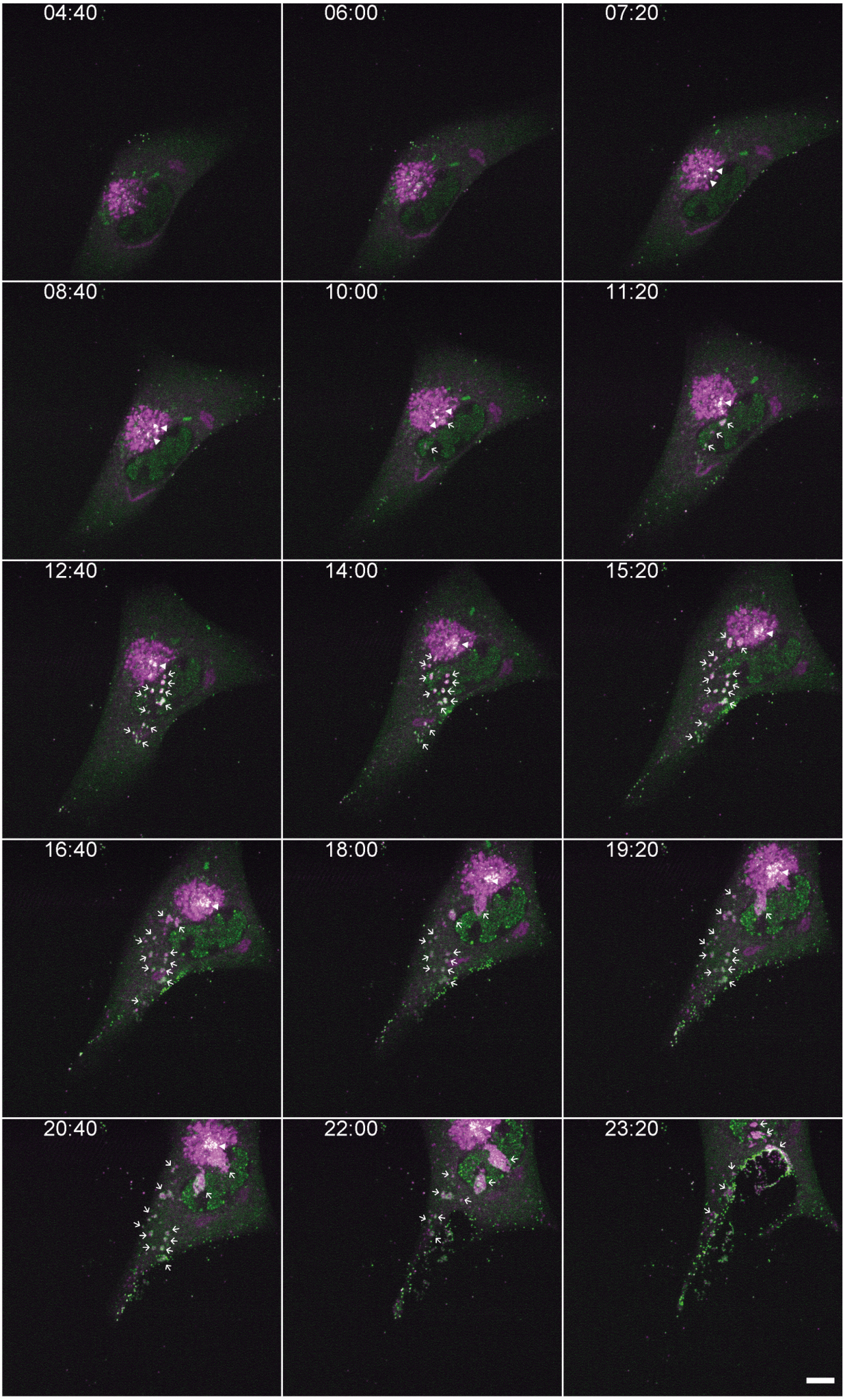
04:40
06:00
07:20
08:40
10:00
11:20
12:40
14:00
15:20
16:40
18:00
19:20
20:40
22:00
23:20

Figure 9. Live-cell microscopy shows EVA generation in intermittent pulses.
HFF-cells were infected with HCMV-TB40-pp150-SNAP-gM-mScarlet-I (MOI of 1). At 3 dpi, the sample was stained with SNAP-Cell-SiR, and the cells were subsequently imaged live by spinning-disk microscopy. Z-stacks were acquired with a height of 8 µm and a 1 µm step size. Volumes were acquired every 40 minutes. Shown is a montage of the z-section at the lower plasma membrane directly at the cover-glass with pp150-SNAP colored in green and gM-mScarlet-I in magenta. White triangles indicate objects with colocalizing pp150 and gM signals prior to EVA generation, and the white arrows point to the areas where EVAs are generated during the acquisition. The time format is hh:mm, and the scale bar represents 10 µm. A video of the data can be found in (283,284) supplementary video 6.

5.5 Live-cell TIRF and lattice-light sheet microscopy confirms HCMV release from MViBs by membrane fusion

To follow the fate of MViBs and confirm that they are the source of EVAs, live-cell lattice-light-sheet microscopy was used. HFF cells were infected with HCMV-TB40-pp150-EGFP-gM-mCherry and imaged live at 96 hpi. Large bodies could be seen moving through the cytoplasm to the plasma membrane. Upon arrival at the plasma membrane, the round bodies transformed into a flattened patch at the growth substrate (Figure 10). The same phenotype could be observed in HFF cells using the fluorophore-switched TB40-pp150-SNAP-gM-mScarlet-I in infected HFF-mNeongreen-Rab5 (Figure 11). With the lattice-light-sheet microscope, it was also possible to observe that HCMV-filled MViBs did not just fuse with the lower plasma membrane but also travelled to the upper membrane and released virus particles to the cell surface (Figure 11).

To verify that the putative MViB-to-EVA transition events were bulk releases of virus particles by fusion of a large vesicle with the plasma membrane, a pH-sensitive biosensor based on the tetraspanin CD63 was used (287). CD63 is a classical marker for late endosomes, MVBs and exosomes. Therefore, it seemed likely that it is also present in the MViBs. The CD63pHluorin construct was cloned from the original plasmid into the lentiviral vector pLenti-CMV-puro-dest by two steps of single-fragment gateway cloning (ThermoFisher). Lentivirus particles were reconstituted in HEK293XT cells and used to transduce HFF cells. Afterwards, the mixed population was sorted by FACS for the 10% brightest fluorescent cells and expanded. The correct function of the CD63-pHluorin construct was assessed by spinning-disk fluorescence microscopy. The cells were imaged live and fixed to analyze the fluorescent properties of the pHluorin. As expected, in the live cells, where the intracellular CD63-pHluorin is exposed to an acidic pH in the lumen of endosomal compartments, the fluorescence was detected almost exclusively at the plasma membrane (Figure 12A). However, small and large intracellular vesicles positive for CD63-pHluorin became visible when the cells were imaged in the fixed state, where intracellular pH gradients equilibrated to neutral pH due to the loss of function of intracellular proton pumps (Figure 12B). Furthermore, the colocalization of the CD63-pHluorin construct with viral proteins was analyzed. For this, the transduced cells were infected with HCMV-TB40-pp150-SNAP-gM-mScarlet-I and either labelled with SNAP-Cell-SiR for pp150 or IF stained for gB. Colocalization of CD63-pHluorin with gM, gB and pp150 could be observed (Figure 12B-D).

Then the HFF-CD63-pHluorin were infected with HCMV-TB40-pp150-SNAP-gM-mScarlet-I at an MOI of 0.6 and between 72 and 100 hpi imaged by total internal reflection fluorescence (TIRF) microscopy. Time-lapse videos were acquired for up to 1 h at the lower plasma membrane at the cover glass at an average frame rate of 0.57 frames per second (fps). EVA formation events during the acquisition time were collected and analyzed (example in Figure 13A). For the quantification, signal intensities of pp150-SNAP, gM-mScarlet-I and CD63pHluorin were measured at the release sites. The intensities at the release time points (t_0 = 175 s) +/- 100 frames were normalized and plotted (Figure 13B). The intensity of pp150-SNAP and gM-mScarlet-I rose as the MViBs approached the plasma membrane and peaked about 8 seconds before t_0. Then it started to decline for 7 seconds until it stayed constantly elevated when EVA formation was complete. In con-

trast, the intensity of CD63pHluorin rose only slightly until t = t_0-8 s, when it started to rise significantly until it peaked at t_0. Afterwards, the signal intensity fell for 8-9 seconds until it stayed only slightly elevated. Due to the heterogeneity of the release events, the intensity curves have large variability in some parts of the plot, which is in line with the afore-described data that MViBs and EVAs are heterogeneous in size and content.

Fusion events of large bodies positive for CD63-pHluorin, pp150-SNAP and gM-mScarlet-I with the plasma membrane could also be visualized with lattice-light-sheet microscopy. Large bodies positive for pp150-SNAP and gM-mScarlet could be seen to approach the plasma membrane (Figure 14A). After the arrival of the MViBs at the plasma membrane, a sudden increase in CD63-pHluorin intensity indicated a fast change of the pH inside these bodies, suggesting a fusion with the plasma membrane (Figure 14A-B). Subsequently, the intensity decreases for all channels, and the time-lapse video shows that an EVA had formed (Figure 14A-B).

10

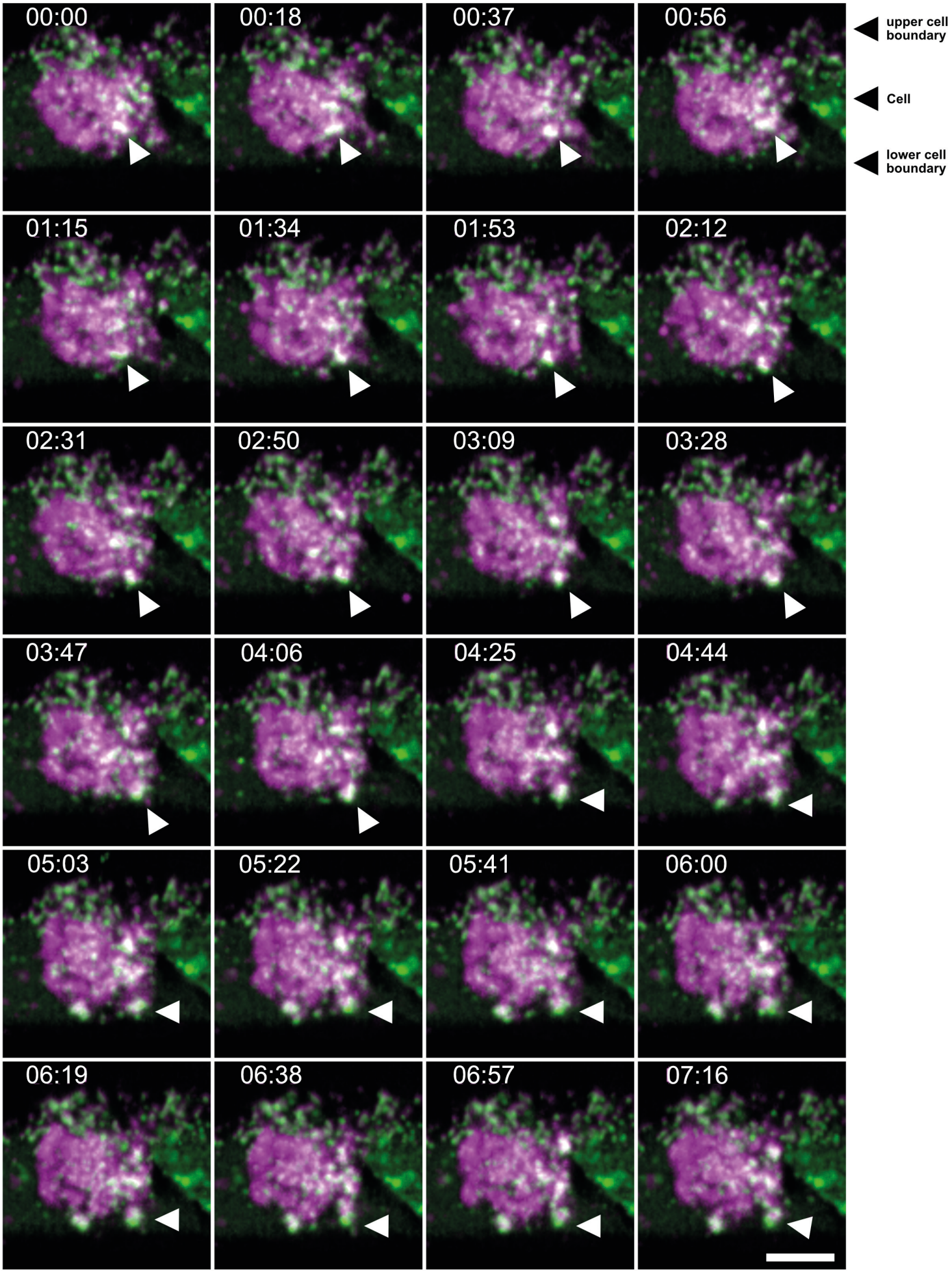
00:00
00:18
00:37
00:56
01:15
01:34
01:53
02:12
02:31
02:50
03:09
03:28
03:47
04:06
04:25
04:44
05:03
05:22
05:41
06:00
06:19
06:38
06:57
07:16
upper cell boundary
Cell
lower cell boundary

Figure 10. Lattice-light-sheet shows the release of viral material from MViBs.
HFF cells were infected with HCMV-TB40-pp150-EG-FP-gM-mCherry (MOI of 1). The cells were imaged at 4 dpi by lattice-light-sheet microscopy. Volumes of the whole cell were acquired every 2.11 seconds. Due to the optical setup of the microscope, the single planes of the volume are acquired at a 30° angle to the growth substrate. Shown in the panels are maximum projections of 20 sections (2 µm) illustrating the movement of a pp150 (green) and gM (magenta) positive MViB (white triangle) to the lower plasma membrane, where it forms an EVA. Since the 4-dimensional data is difficult to convey in a 2D montage, a rendering of the data, including reslicing and side-views, can be found in (283,284), supplementary video 5. The time format is mm:ss, and the scale bar represents 5 µm.

11

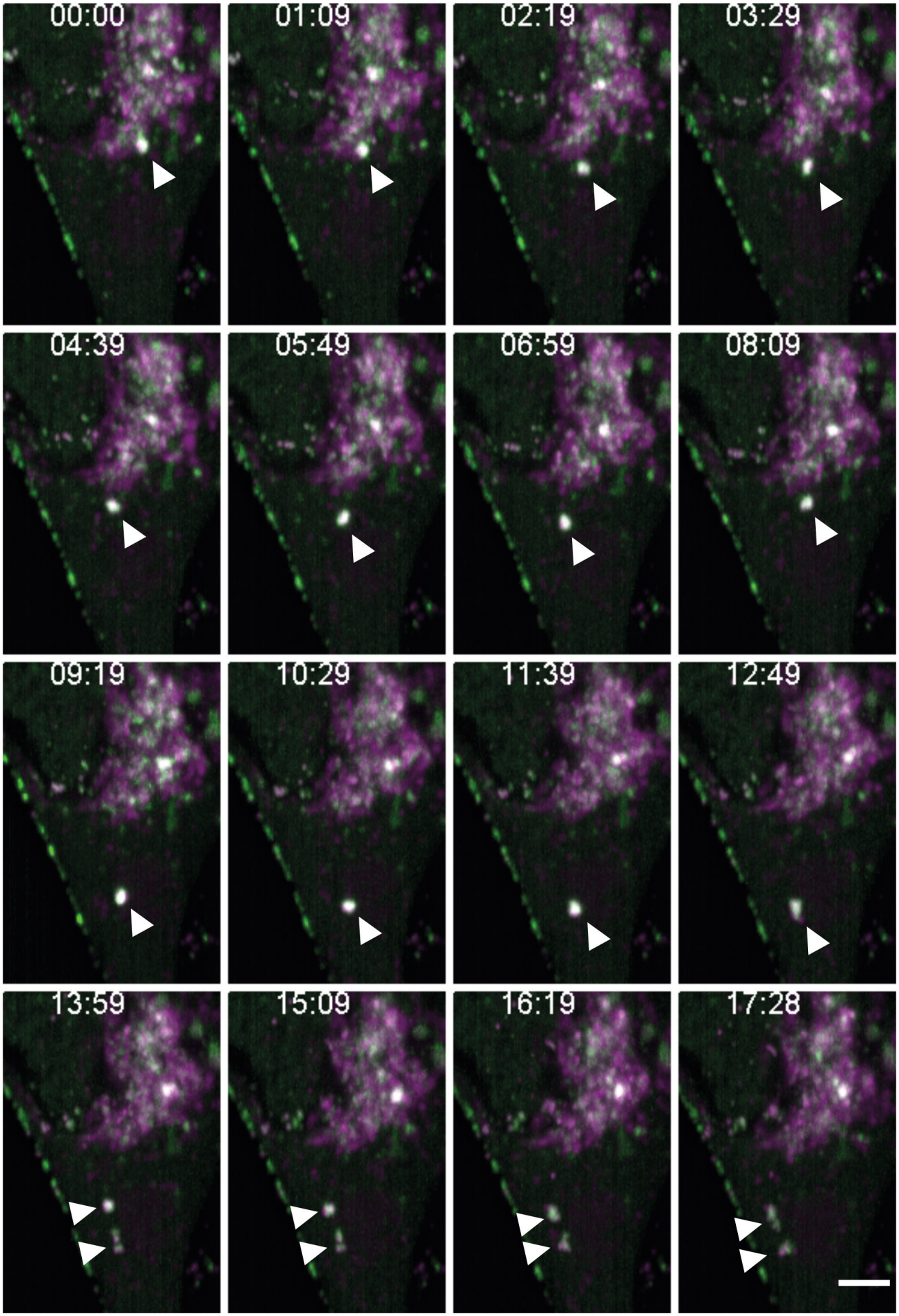
00:00
01:09
02:19
03:29
04:39
05:49
06:59
08:09
09:19
10:29
11:39
12:49
13:59
15:09
16:19
17:28

Figure 11. MViBs release viral content also to the upper plasma membrane.
HFF-mNeongreen-Rab5 were infected with HCMV-TB40-pp150-SNAP-gM-mScarlet-I (MOI of 1). After 4 dpi, the cells pp150-SNAP was stained with SNAP-Cell-SiR, and the cells were imaged with lattice-light-sheet microscopy. Volumes were acquired every 10 seconds. The data was transformed and resliced to facilitate comparison with classical inverted fluorescence microscopy. A maximum projection of 14 sections (2 µm) was generated to present the fate of objects moving in 3D in a 2D figure. The white triangles indicate an MViB, positive for pp150 (green) and gM (magenta), traversing the cytoplasm and releasing its content in two pulses at the plasma membrane (starting around 11:39-12:49). The mNeongreen-Rab5 fluorescence is not shown in this montage. The time format is mm:ss, and the scale bar represents 5 µm.

12A

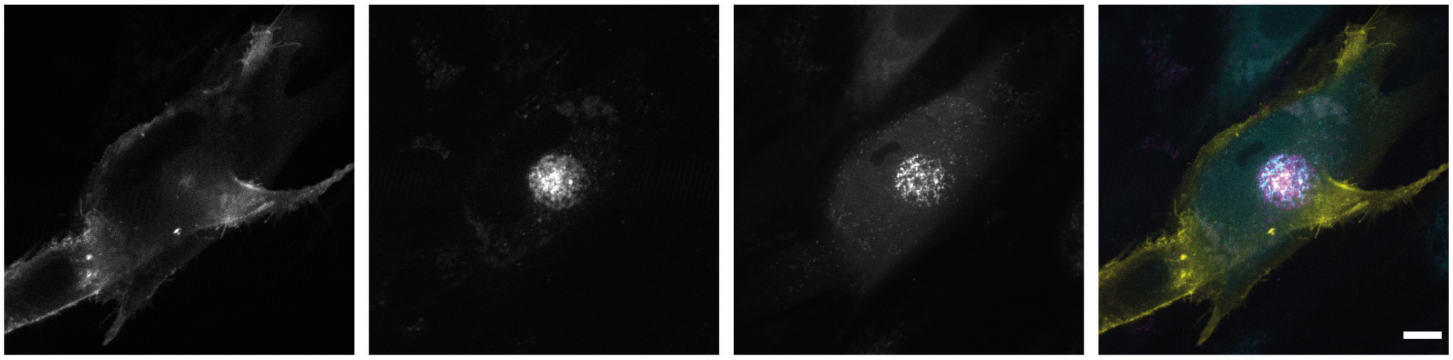

CD63-pHluorin gM-mScarlet-I pp150-SNAP merge

12B

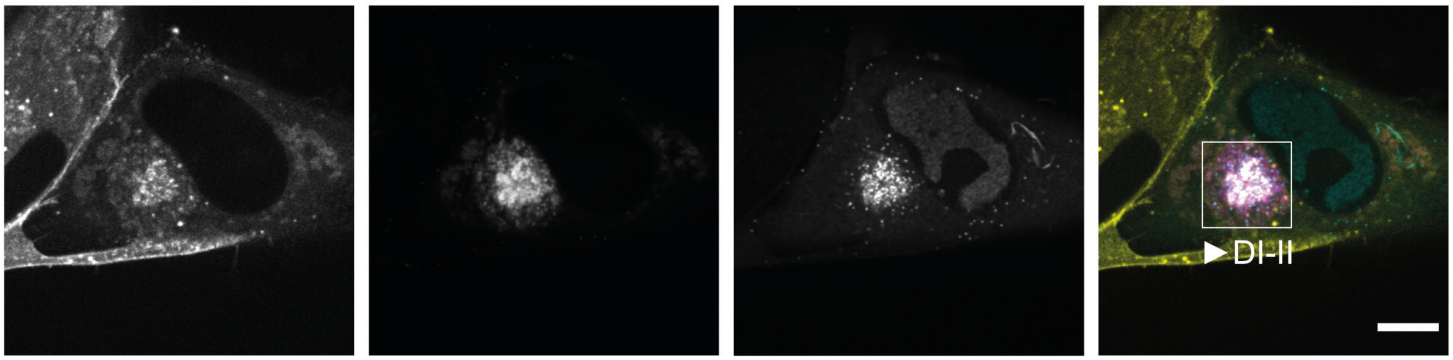

CD63-pHluorin gM-mScarlet-I pp150-SNAP merge

12C

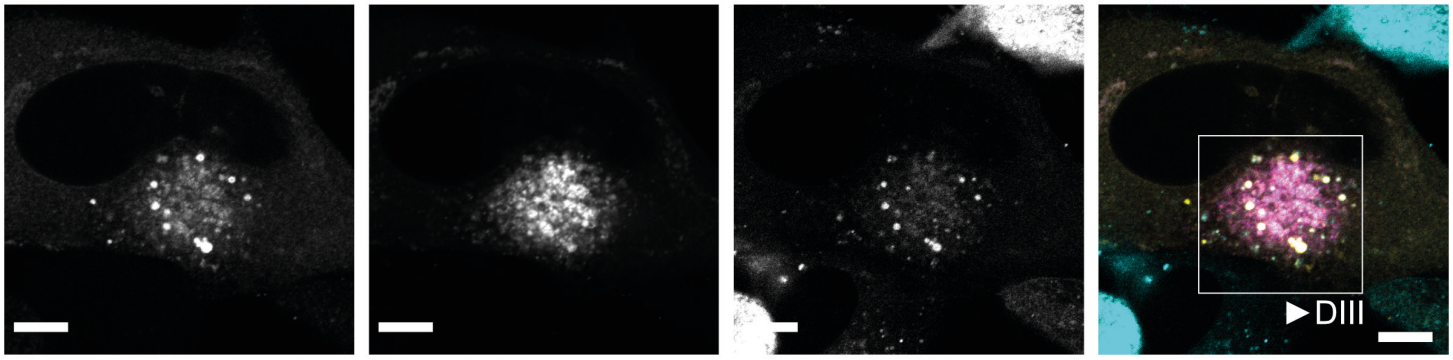

CD63-pHluorin gM-mScarlet-I α-gB merge

12D

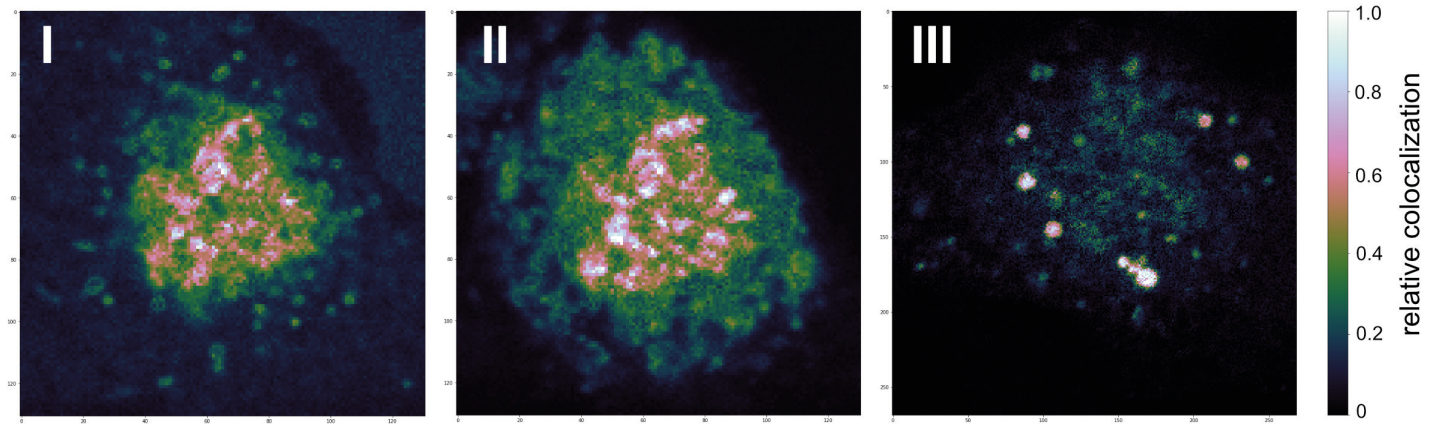

CD63-pHluorin vs. pp150-SNAP CD63-pHluorin vs. gM-mScarlet-I CD63-pHluorin vs. α-gB

Figure 12. A pH-sensitive CD63-pHluorin colocalizes with HCMV pp150, gM and gB.

12A HFF-CD63-pHluorin were infected with HCMV-TB40-pp150-SNAP-gM-mScarlet-I (MOI of 1). After 4 dpi, the cells were labelled with SNAP-Cell-SiR and imaged live by spinning-disk microscopy. Scale bar represents 10 µm.

12B HFF-CD63-pHluorin were prepared as described for 12A. However, after 4 dpi, the cells were fixed before imaging by spinning-disk microscopy. The white frame indicates the area used for spatial colocalization analysis. Scale bar represents 10 µm.

12C HFF-CD63-pHluorin were prepared as described for figure 12B, with the difference that no SNAP labelling was performed. After fixation, the cells were instead IF stained against gB and subsequently imaged by scanning-confocal microscopy. The white frame indicates the area used for spatial colocalization analysis, and the scale bar represents 10 µm.

12D Spatial colocalization heatmaps for the indicated areas in figures 12D-C. Colocalization between the markers could be observed in specific areas at the viral AC.

13A

before

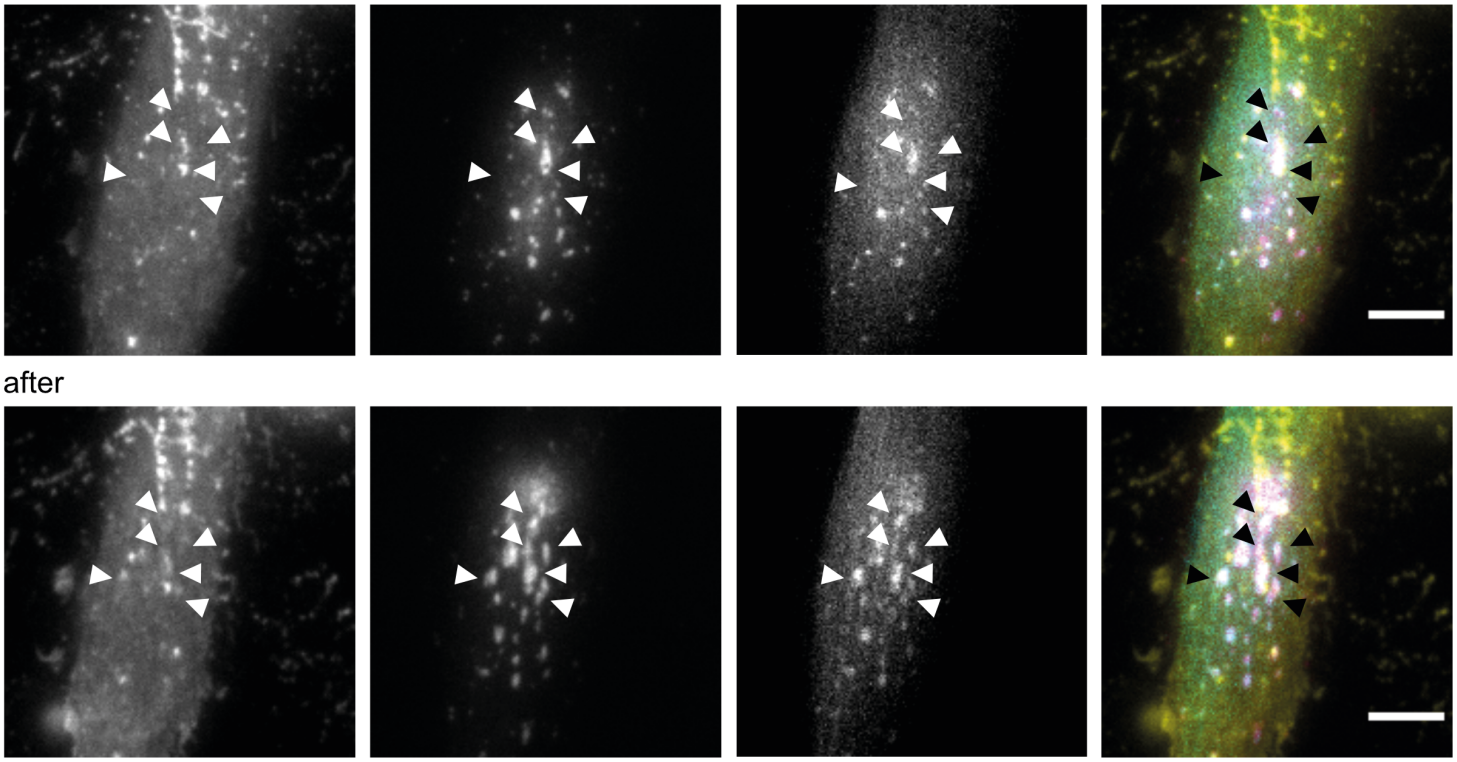

CD63-pHluorin gM-mScarlet-I pp150-SNAP merge

13B

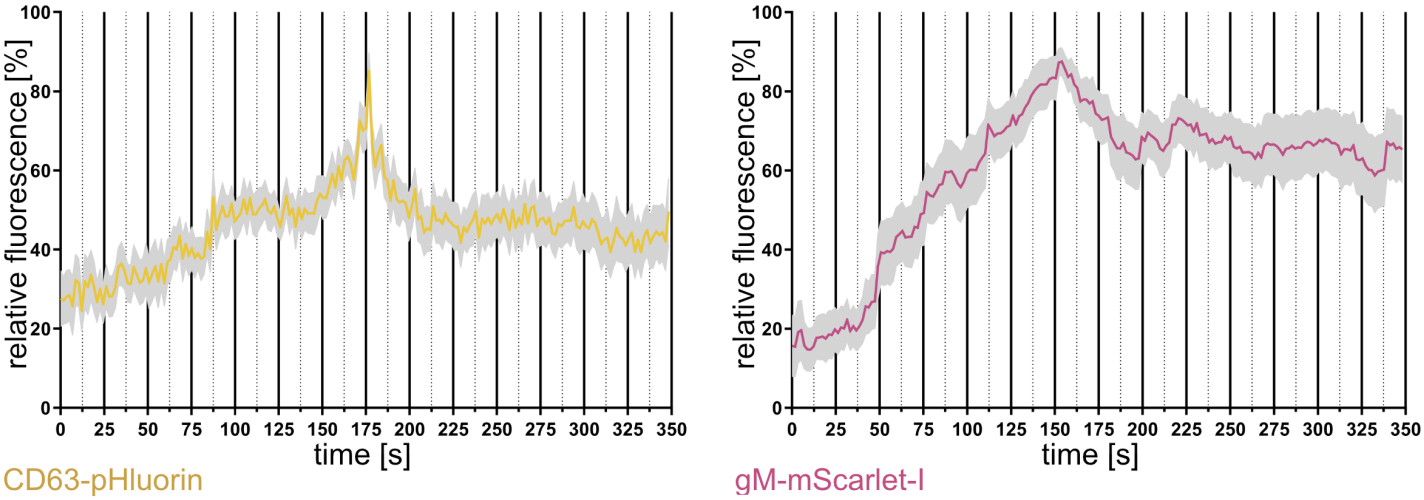

CD63-pHluorin gM-mScarlet-I

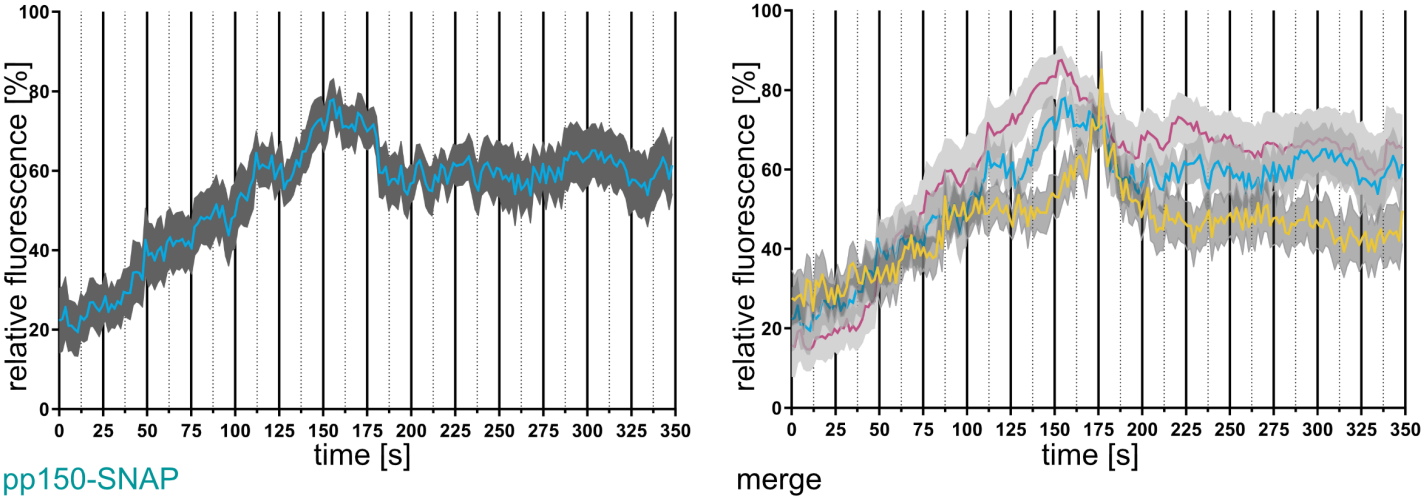

pp150-SNAP merge

Figure 13. TIRF microscopy shows membrane fusion at MViB release into EVAs.

13A HFF-CD63-pHluorin were infected with HCMV-TB40-pp150-SNAP-gM-mScarlet-I (MOI of 0.6) and imaged between 72 and 100 hpi by TIRF microscopy after labelling with SNAP-Cell-SiR. The lower plasma membranes of the infected cells were individually imaged consecutively for 1 h at an average framerate of 0.57 fps. The panels show an infected cell at the beginning and the end of the acquisition (before and after EVA formation events). The triangles (both black and white) highlight the positions at which EVAs were generated during the acquisition. Scale bar represents 10 µm.

13B Fluorescence signals at EVA generation events were quantified for 5 cells from 4 replicates of the experiment described in 13A. The signals were aligned and averaged for the different events. The CD63-pHluorin intensity spikes directly after the arrival of an MViB at the imaging plane, indicated by the increase of gM-mScarlet-I and pp150-SNAP signals. Gray areas indicate the standard error of the mean.

14A

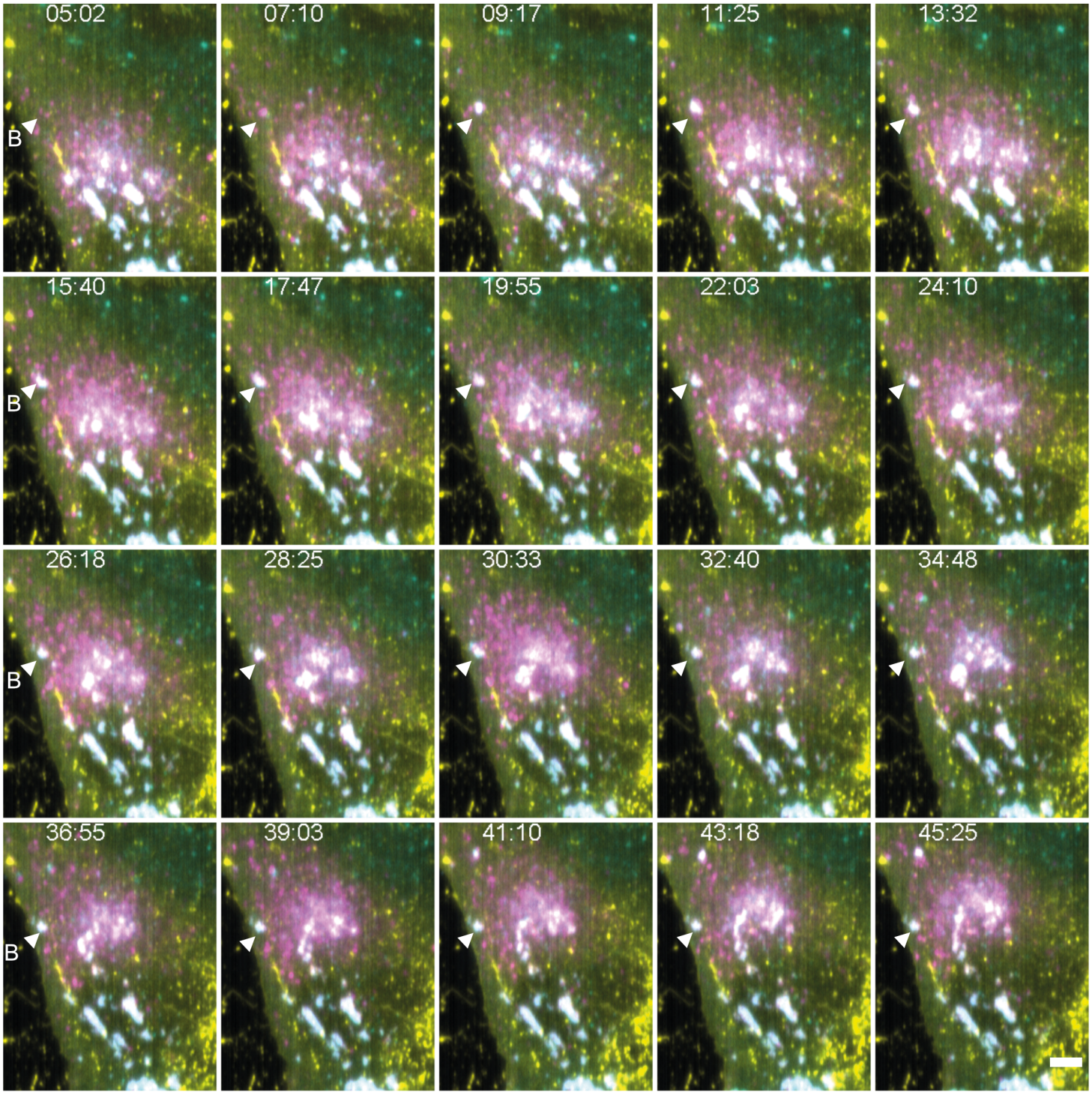
05:02
07:10
09:17
11:25
13:32
15:40
17:47
19:55
22:03
24:10
26:18
28:25
30:33
32:40
34:48
36:55
39:03
41:10
43:18
45:25
B

14B

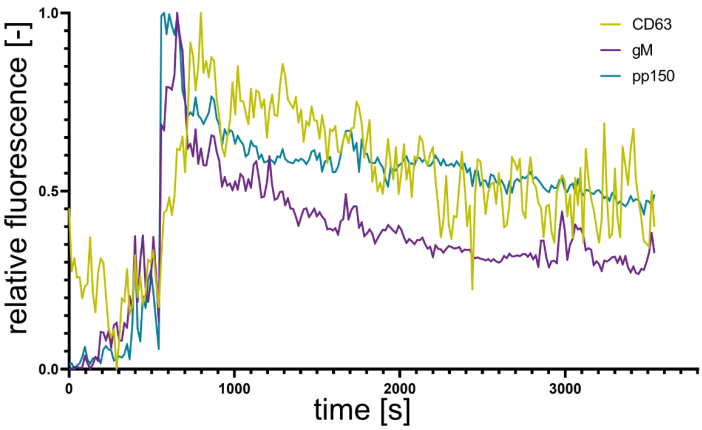
CD63
gM
pp150
relative fluorescence [-]
1.0
0.5
0.0
0
1000
2000
3000
time [s]

Figure 14. Lattice-light-sheet microscopy confirms membrane fusion at MViB release events.

14A HFF-CD63-pHluorin were infected with HCMV-TB40-pp150-SNAP-gM-mScarlet-I (MOI of 1). The cells were SNAP-Cell-SiR labelled at 4 dpi and subsequently imaged with lattice-light-sheet microscopy. Volumes were acquired every 16 seconds for 1h. The data was transformed to facilitate comparison to data from classical inverted microscopes. The montage shows the sum intensity of 7 slices (1 µm) of the lower plasma membrane of an infected cell with CD63-pHluorin in yellow, gM-mScarlet-I in magenta and pp150-SNAP in cyan. Indicated with the white triangle is the position where an MViB, arriving at the lower plasma membrane, releases its content into an EVA (around 11:25). A video of this data can be found in (283,284), supplementary video 9. The time format is mm:ss, and the scale bar represents 5 µm.

14B Quantification of fluorescence at the position indicated in 14A. After the arrival of the MViB (ca. 600 seconds or 10 minutes), a spike in CD63-pHluorin fluorescence can be seen around 700-800 seconds (ca 11:30 to 13 minutes).

5.6 MViBs contain markers of endosomes and exosomes

The release of vesicles in bulk from large MVBs is a hallmark of exosomal pathways. Therefore, it is likely that the bulk release mechanism used by HCMV might exploit some of the factors involved in exosome generation. Exosomes released from MVBs carry markers of the endocytic pathway such as the tetraspanins CD9, CD81 and CD63 and the Rab GTPases Rab5 and Rab7 (192). Since the MViB fusion assay already suggested that CD63 is present at the fusion events, the presence of other factors from endocytic-/exosome pathways in EVAs and MViBs was investigated. At first, the presence of the tetraspanins CD9, CD81 and CD63 at the assembly complex and EVAs was probed by immunofluorescence (Figures 15-17). CD63 localizes in the assembly complex to large bodies positive for pp150-SNAP and gM-mScarlet-I, supporting the results from the previous experiments that CD63 is present at MViBs (Figures 15A-B). At EVAs, however, only weak colocalization of CD63 with pp150 and gM could be detected, indicating that CD63 is less present on virions compared to the limiting membrane of the virion containing MViBs (Figure 15A-B).

CD9, on the other hand, although localizing to the assembly complex, colocalizes not as strongly with pp150-SNAP and gM-mScarlet (Figure 16A-B). Overall, the colocalization of CD9 and gM is stronger than the colocalization with pp150, suggesting that CD9 does not localize to MViBs (Figure 16A-B).

A similar picture was observed with CD81. Besides a strong surface localization, CD81 signal can also be detected at the assembly complex. The colocalization to pp150-SNAP and gM-mScarlet-I, though, was poor (Figure 16A-B).

Since CD9 and CD81 localized to the plasma membrane, colocalization of CD81 or CD9 with gM-mScarlet and pp150-SNAP could be observed at the plasma membrane occasionally (Figure 17A-B). This included weak colocalization with the viral proteins in EVAs (Figure 17B). However, the plasma membrane was almost entirely positive for CD9 and CD81 (Figures 16A, 17A), thus questioning the significance of this colocalization.

To confirm the localization of CD63 on MViBs, immunolabelling for electron microscopy was performed in HCMV-TB40-WT infected HFF cells. Fixation, cryo-sectioning and immunolabelling with nanogold conjugated antibodies were performed according to the Tokuyasu technique (288). Even though the content of cytoplasmic multivesicular structures was poorly preserved, large bodies containing viral products, which were also positive for CD63, were present in the sample (Figure 18).

Finally, in connection to this study, Timothy Soh and Hannah Britt (coauthors in (284)) performed a proteomic analysis of gradient purified HCMV-TB40-WT virions. The results showed that HCMV-TB40-WT virions contained factors for Golgi-to-endosome trafficking (Syntaxin-12, Rab14, VAMP3), markers for early endosomes (Rab5C, Syntaxin-7) and exosomes (HSP70, HSP90, 14-3-3 and PKM2 (289)), suggesting a role for these compartments in HCMV envelopment and egress (284).

15A

cell middle

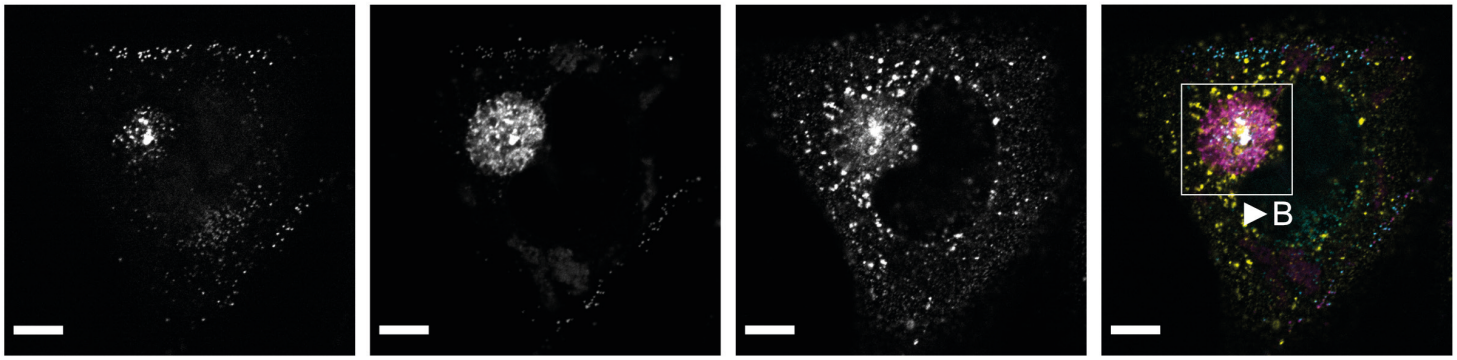

pp150-SNAP gM-mScarlet-I α-CD63 merge

lower plasma membrane

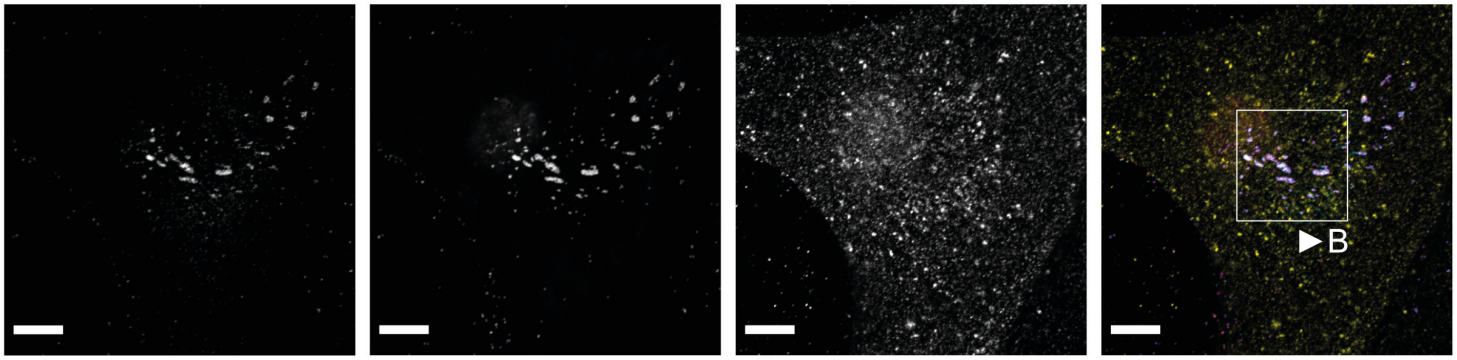

pp150-SNAP gM-mScarlet-I α-CD63 merge

15B

cell middle

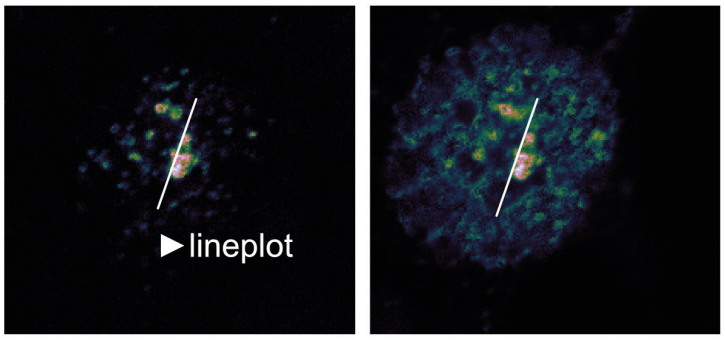

CD63 vs. pp150 CD63 vs. gM

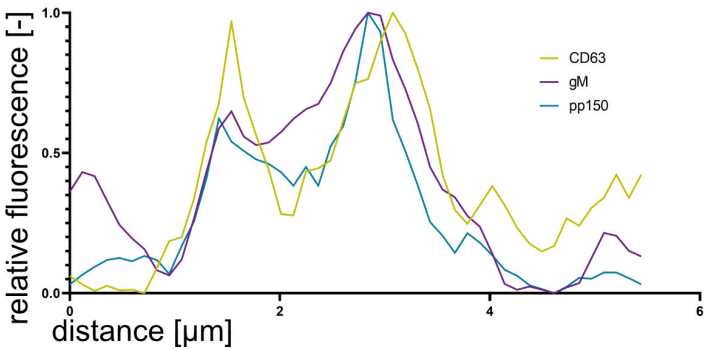

lower plasma membrane

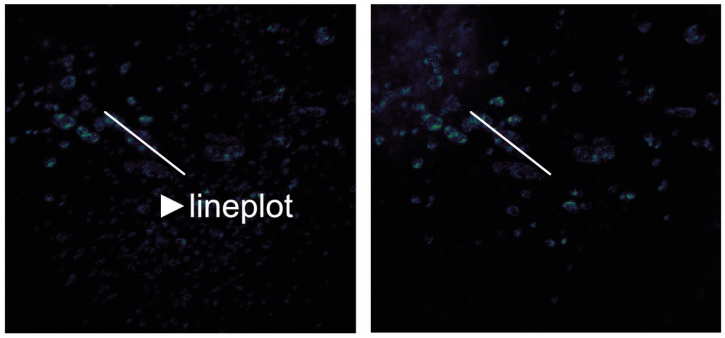

CD63 vs. pp150 CD63 vs. gM

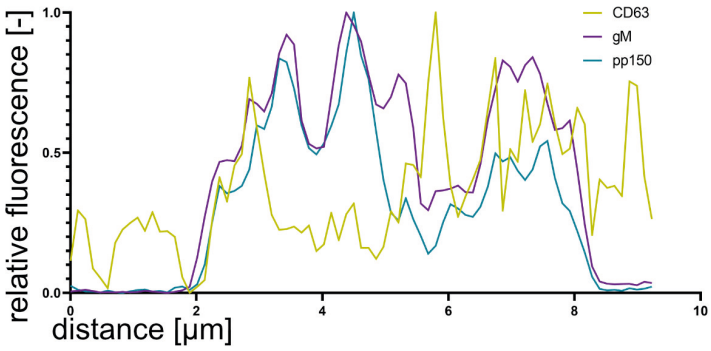

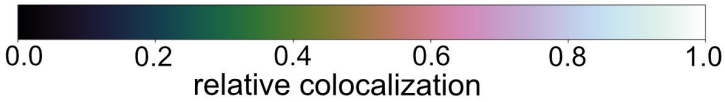

Figure 15. Immunofluorescence shows colocalization of CD63 with gM and pp150 in the cytoplasm but not at EVAs.

15A HFF cells were infected with HCMV-TB40-pp150-SNAP-gM-mScarlet-I (MOI of 1), and at 4 dpi, SNAP-Cell-SiR labelled and fixed. The cells were IF stained against CD63, and images were acquired using scanning-confocal fluorescence microscopy. The white frame indicates the areas investigated with spatial colocalization analysis. Scale bar represents 10 µm.

15B Colocalization of CD63 with the viral proteins pp150 and gM was analyzed by spatial colocalization analysis for the areas indicated in 15A. Moreover, line profiles were plotted on the right for the indicated lines in the heat maps on the left.

16A

α-CD9

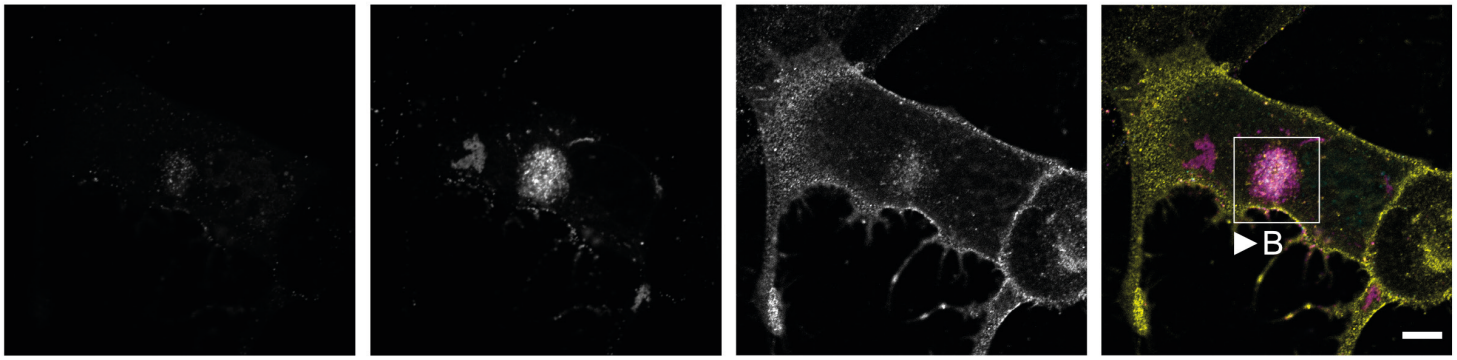

pp150-SNAP | gM-mScarlet-I | α-CD9 | merge

α-CD81

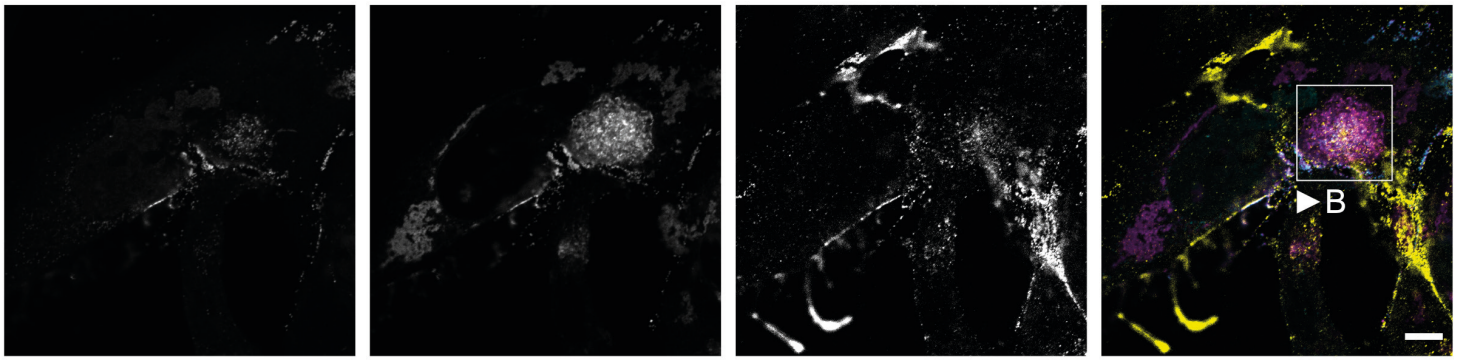

pp150-SNAP | gM-mScarlet-I | α-CD81 | merge

16B

CD9

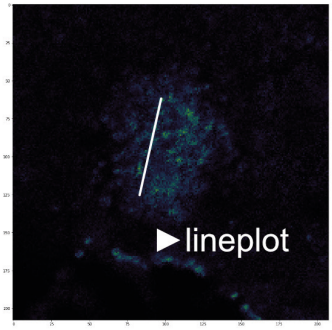

CD9 vs. pp150

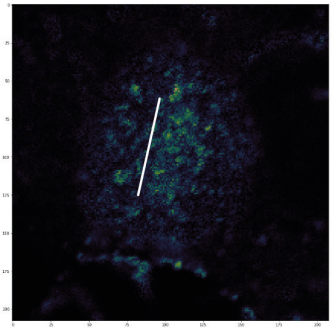

CD9 vs. gM

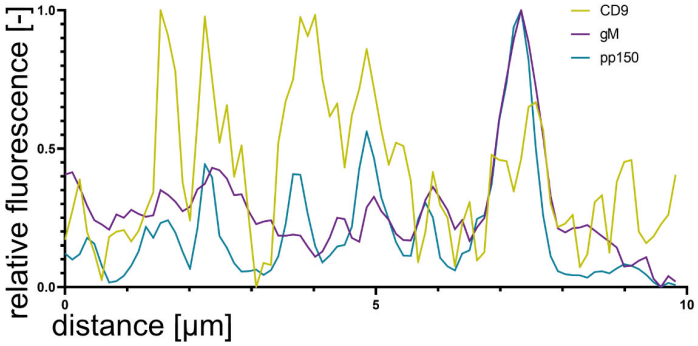

CD81

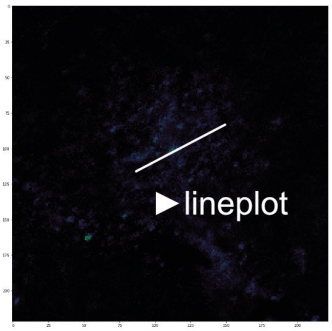

CD81 vs. pp150

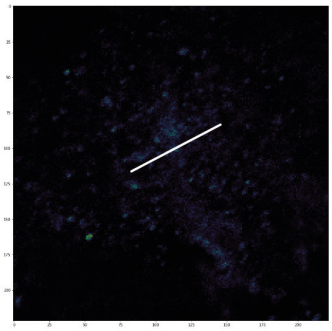

CD81 vs. gM

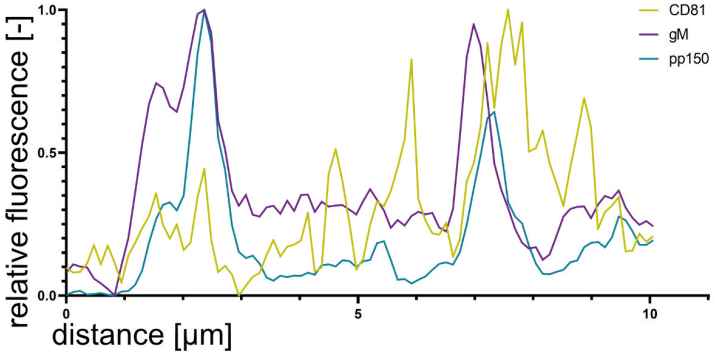

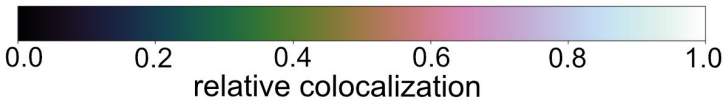

Figure 16. Tetraspanins CD9 and CD81 localize to the AC, but colocalization with pp150 and gM is low.

16A HFF cells were infected, labelled and fixed as described in figure 15A. Afterwards, the cells were IF stained with antibodies against CD9 or CD81. Images were acquired using scanning-confocal fluorescence microscopy. The white frames indicate the areas for spatial colocalization analysis in 16B. Scale bar represents 10 µm.

16B Colocalization heat maps for the areas indicated in figure 16A on the left. The white lines indicate the locations plotted as line profiles on the right.

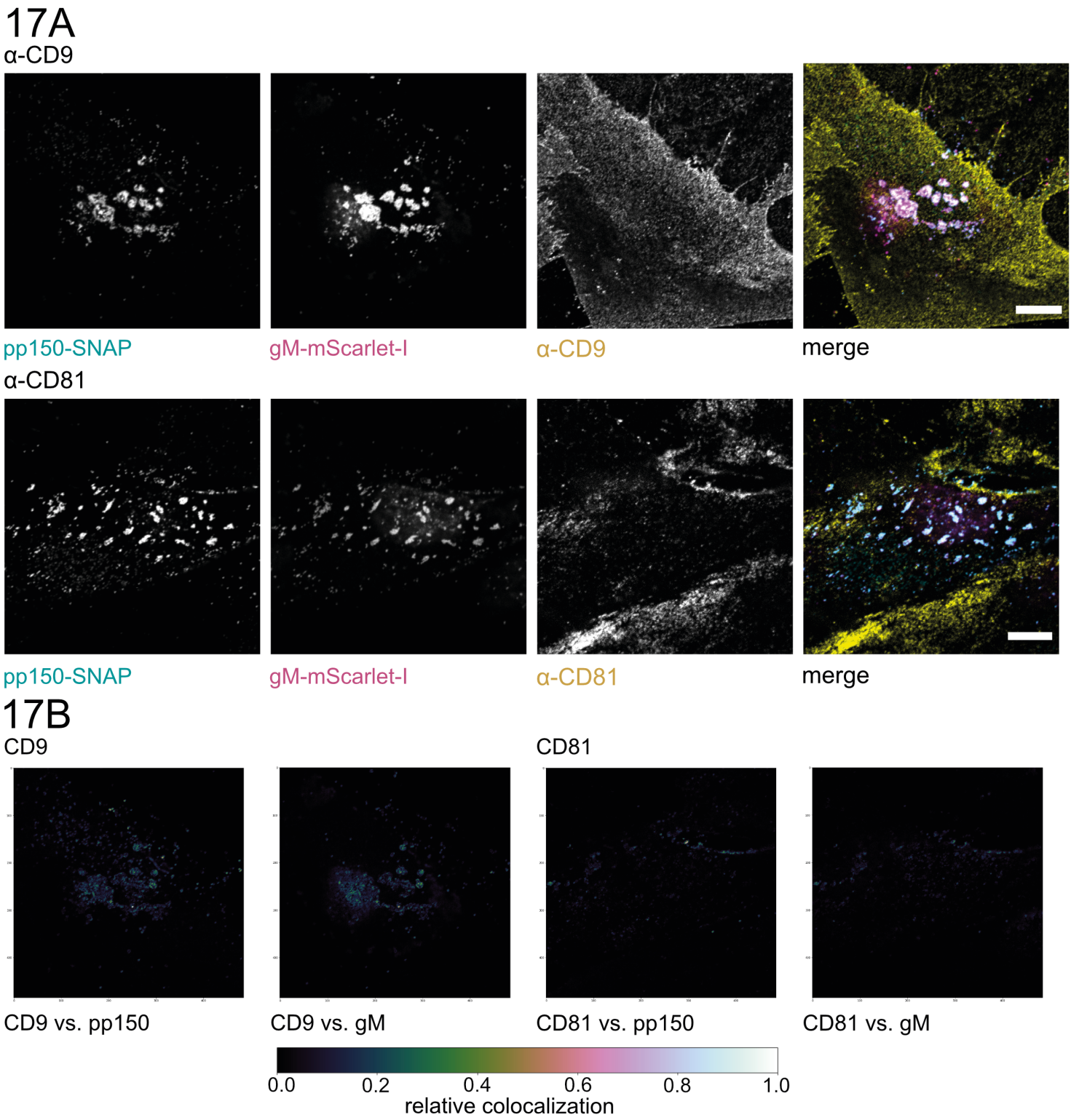

Figure 17. Tetraspanins CD9 and CD81 do not specifically localize to EVAs.

17A HFF cells were treated and imaged as described in figure 16A. The panels show sections from the lower plasma membrane with EVAs visible as patches of pp150-SNAP and gM-mScarlet-I signals. Scale bars indicate 10 µm.

17B Heat maps of a spatial colocalization analysis of the whole areas, shown in 17A.

18

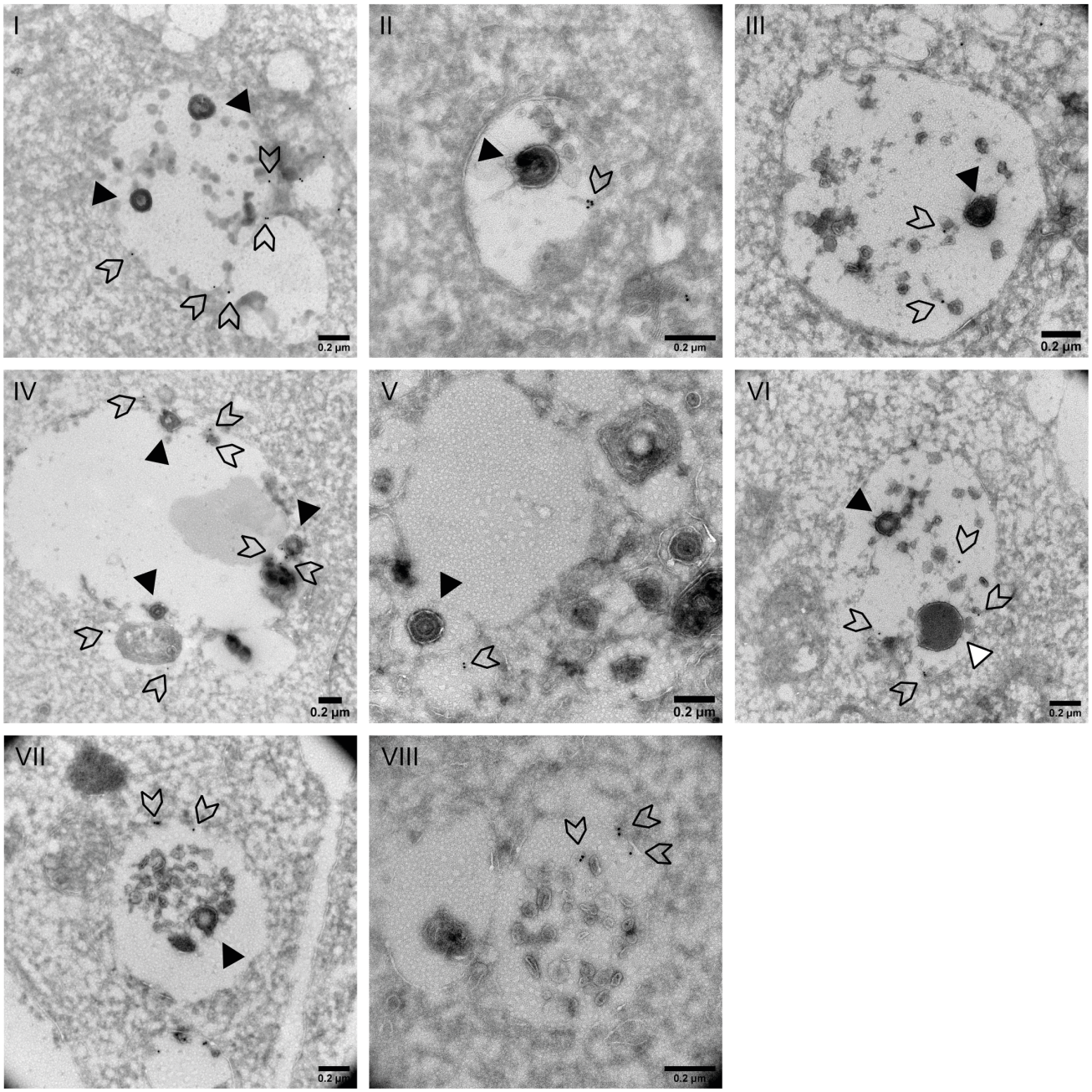

Figure 18. Electron microscopy with immunogold labelled CD63 confirms localization to MViBs.
HFF cells were infected with HCMV-TB40-WT (MOI of 0.5) after 4 dpi, fixed and labelled by immunogold staining against CD63. Black triangles indicate enveloped virus particles, black contoured white triangles show enveloped dense bodies and black contoured arrowheads point at 10 nm gold particles indicating the presence of CD63 molecules. Panels I-VII show large vesicles containing viral products and CD63 molecules, although the fixation poorly preserved their contents. Panel VIII shows a classical MVB containing CD63. Scale bars represent 200 nm.

5.7 HCMV-Replication is sensitive to farnesyl-transferase inhibition

Together, the release mechanism, the proteomic analysis and the localization studies of late-endosome-/exosome-associated marker proteins strengthened the hypothesis that cellular pathways related to multivesicular body and exosome biogenesis might be involved in the envelopment and release of HCMV progeny. Therefore, three inhibitors of MVB generation (U18666A; (290,291)) or exosome generation and release (Tipifarnib, Ketotifen; (292,293)) were analyzed regarding their ability to interfere with HCMV replication. At first, an effect on viral growth was probed by infecting HFF-WT cells with HCMV-TB40-pp150-SNAP-gM-mScarlet-I and treatment with each inhibitor until 4 dpi. Only the farnesyl-transferase inhibitor Tipifarnib was able to reduce viral titers significantly, whereas Ketotifen and U18666A had no significant effect (Figure 19A). Further characterization showed that Tipifarnib had no significant cytotoxic effect on the HFF cells (Figure 19B). Furthermore, quantification of EVAs in HCMV-TB40-pp150-SNAP-gM-mScarlet-I infected HFF-WT cells fixed at 5 dpi showed that Tipifarnib treatment could significantly reduce the amount of EVAs in a dose-dependent manner (Figure 20A-B). To test the influence of Tipifarnib on viral gene expression, viral gene products from the three major kinetic classes of viral genes (IE, E and L genes) were analyzed by western blotting. HFF cells were infected with HCMV-WT and harvested at different time points from 0 dpi (input) to 4 dpi during Tipifarnib or DMSO (vehicle control) treatment. A western blot assay to detect the proteins IE1/2 (IE class), pUL44 (E class) and pp150 (L class) showed that while the IE1/2 and pUL44 expression was not altered by Tipifarnib, a reduction of pp150 protein levels at 3 and 4 dpi was detectable (Figure 20C).

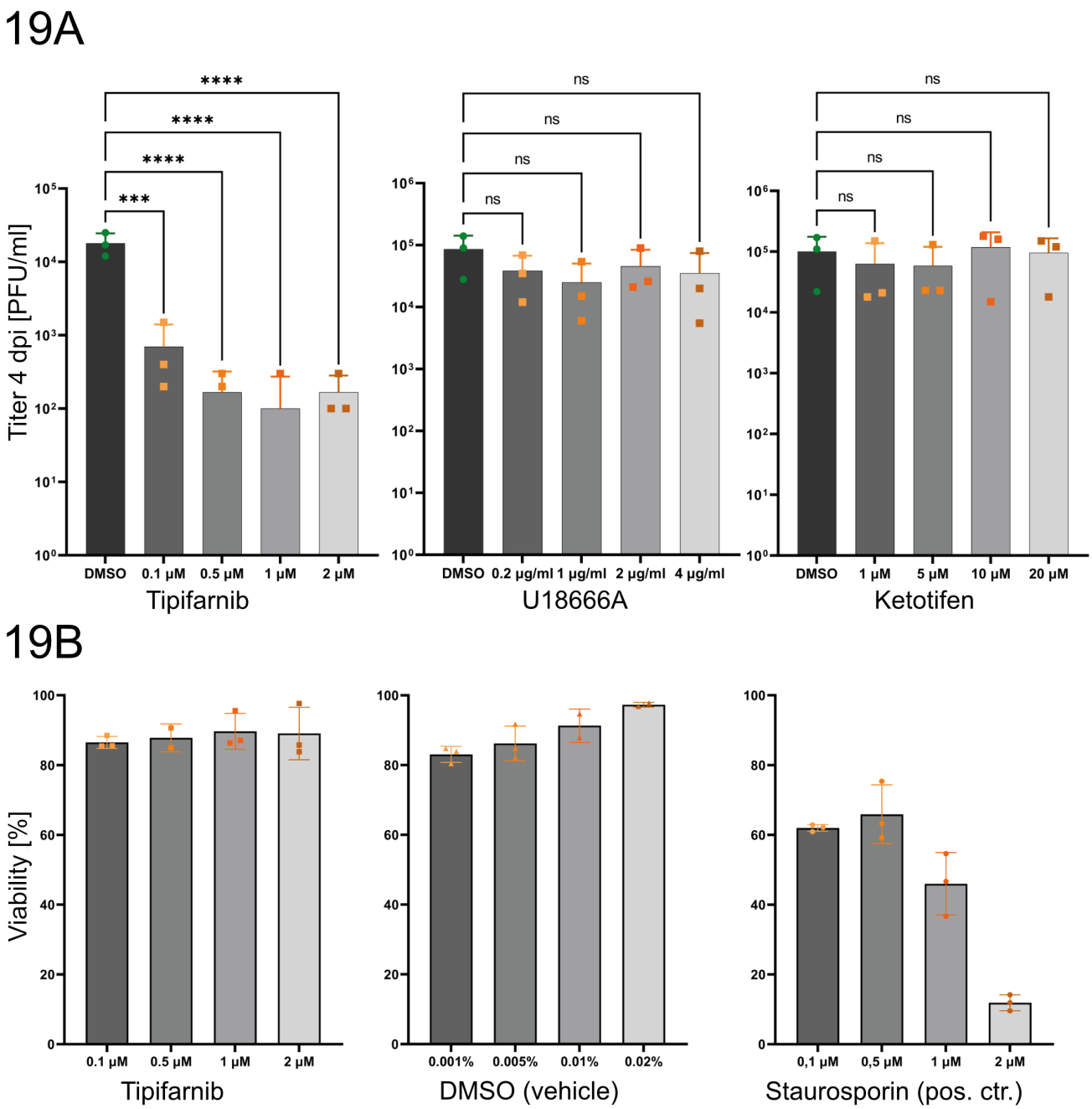

Figure 19. Tipifarnib reduces viral titers while exerting no detectable cytotoxicity.

19A HFF cells were infected with HCMV-TB40-pp150-SNAP-gM-mScarlet-I (MOI of 2). The cells were treated with the indicated substance until 4 dpi. The medium with the drug was refreshed every 24 hours. At 4 dpi, the supernatant was harvested, and the viral titer was determined by plaque assay. The bars show the mean and the error bars the standard deviation. The data were analyzed by a one-way ANOVA (p-values: Tipifarnib: <0.0001, U18666A: 0.4154, Ketotifen: 0.8364) and Dunnet's multiple comparisons tests (results shown on the graph).

19B HFF cells were treated for 24 h with the indicated substance. Afterwards, cell viability was probed with an ATP assay, where Staurosporin served as a positive control. The bars show the mean and the error bars the standard deviation. Statistical analysis with a 2-way ANOVA confirms statistically significant differences between the three groups ($p < 0.0001$). However, the cell viability of Tipifarnib treated cells did not differ statistically significantly from the vehicle control (DMSO), as determined by Tukey's multiple comparisons test. The same test found the differences for both DMSO and Tipifarnib compared to Staurosporin to be statistically significant (max. p-value = 0.0005)

20A

Lower plasma membrane

DMSO 1:5000

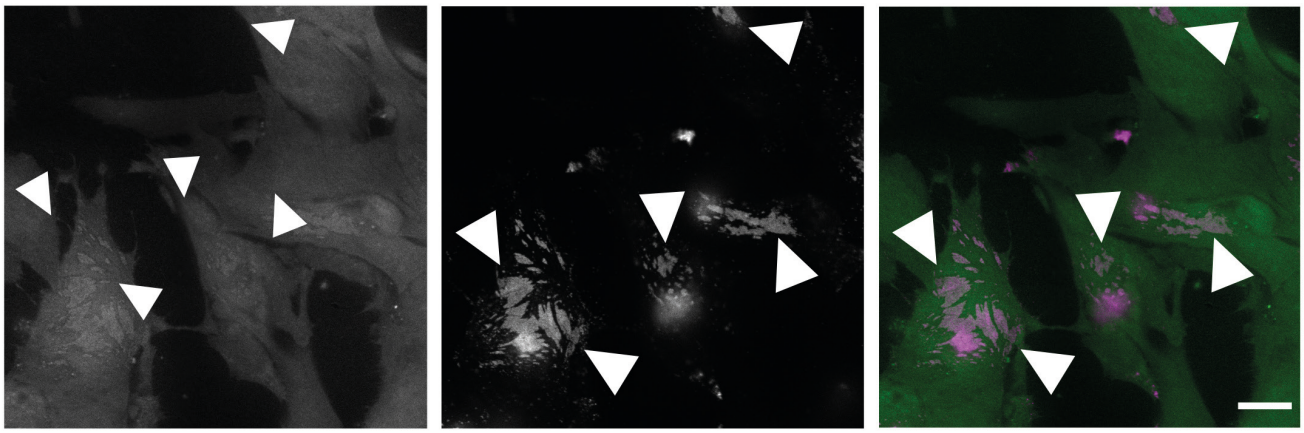

Tipifarnib (1 µM)

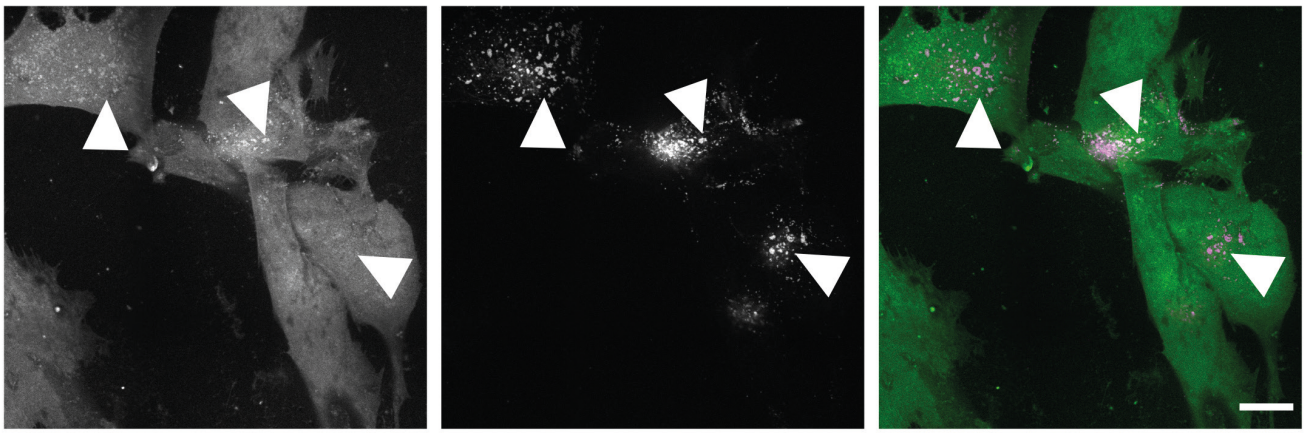

pp150-SNAP gM-mScarlet-I merge

20B

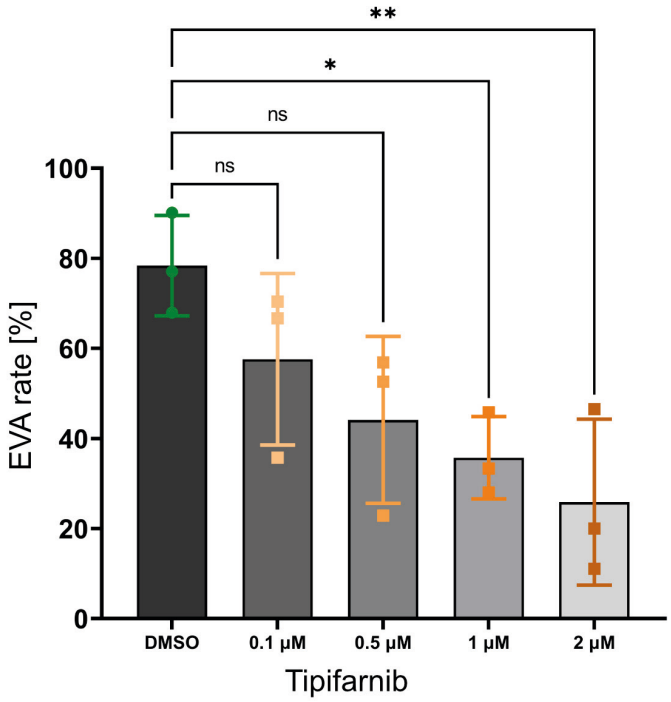

20C

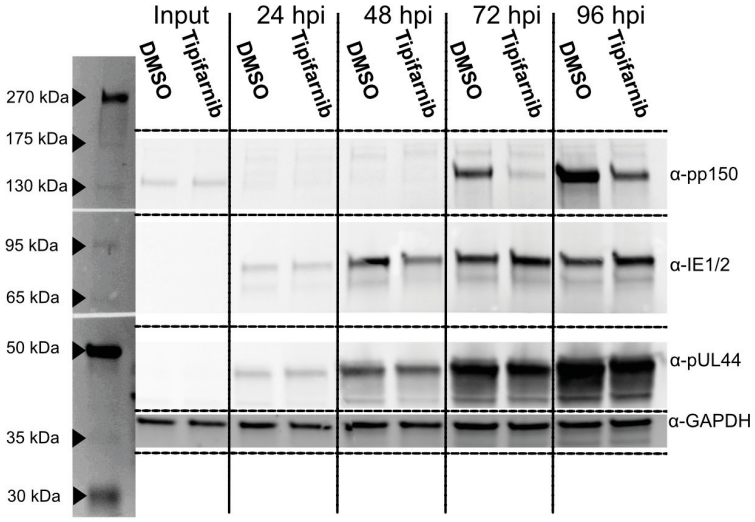

Figure 20. Tipifarnib reduces EVA prevalence and affects late gene expression.

20A HFF cells were infected and treated as described for figure 19A. At 5 dpi, the cells were SNAP-Cell-SiR labelled and subsequently fixed. Large overviews were acquired by spinning-disk microscopy. Shown are representative images from the lower plasma membrane after treatment with the indicated substance. Highlighted with the white triangles are EVAs at the lower plasma membrane. Although EVAs are present in the Tipifarnib treated cells, their overall area appears smaller. The scale bar indicates 10 µm.

20B HFF cells were treated and imaged as described in figure 20A. The prevalence of EVAs was quantified for the indicated conditions. The bars show the mean prevalence, and the error bars indicate the standard deviation. Statistical analysis was performed using a one-way ANOVA ($p = 0.0179$ from 697 late infected cells from triplicates included in the analysis). The treatment conditions were compared to the DMSO control using Dunnet's multiple comparisons test (shown on the graph).

20C HFF cells were infected with HCMV-TB40-WT (MOI of 3) and treated with 1 µM Tipifarnib for 4 days as described for 19A. At each indicated time point, cells were harvested and processed for SDS-PAGE. Shown is a western blot against pp150 (viral late protein), IE1/2 (viral immediate early proteins), pUL44 (viral early protein) and GAPDH (host loading control).

5.8 A repaired HCMV Merlin produces MViBs and EVAs

To investigate if the bulk release of HCMV viral products is a phenotype specific to HCMV-TB40, MViB and EVA production was probed in an HCMV-Merlin variant. For these experiments, a version of HCMV-Merlin was used, in which the genomic loci UL128 and RL13 were repaired to clinical status. Moreover, this specific version carries tet-operator elements in the promoter regions of both genes. Since the expression of UL128 and RL13 suppresses the production of infectious cell-free virus particles, propagated virus derived from supernatant accumulate mutations in these genes (237,240). By inserting the tet operator into the promotor regions, phenotypically mutant (RL13/UL128 -/-) fibroblast-tropic infectious supernatant virus can be generated in modified, tet-repressor-expressing cell lines without risking the selection of variants with mutations in these genes. Upon infection of normal HFF-cells, the phenotype is restored to wild-type (240,278,294). At first, the ability to generate EVAs was probed for two versions of this virus: the untagged wild-type and a pp150-EGFP-gM-mCherry tagged mutant (294). Both viruses could produce EVAs late in infection, albeit with a lower prevalence than HCMV-TB40 (Figure 21A-B, Figure 8B). Since the fluorescence images from both viruses suggested that large vesicles positive for pp150, gB, and gM are common in HCMV-Merlin-pAL1502 infected HFF cells (Figure 21C-D), the ultrastructure of these objects was explored with electron microscopy. CLEM data from HCMV-Merlin-pAL1502-pp150-EGFP-gM-mCherry infected HFF-cells confirmed that these large vesicles are MViBs with a phenotype similar to the MViBs in HCMV-TB40 infected cells (Figure 22A-B). Interestingly, colocalization of pp150 and gM was not only observed with CD63, as described above for HCMV-TB40, but also with CD9 in large vesicles resembling MViBs (Figure 23A-B). However, it is possible that MViBs in HCMV-TB40 are more transient because of the higher EVA prevalence observed in infection. This may lessen the likelihood of observing large MViBs positive for CD9 in TB40 infection and thereby biasing the results reported here. Therefore, it remains unclear whether the MViBs in HCMV-Merlin have a different composition or if they are less likely to release and, therefore, more readily observed.

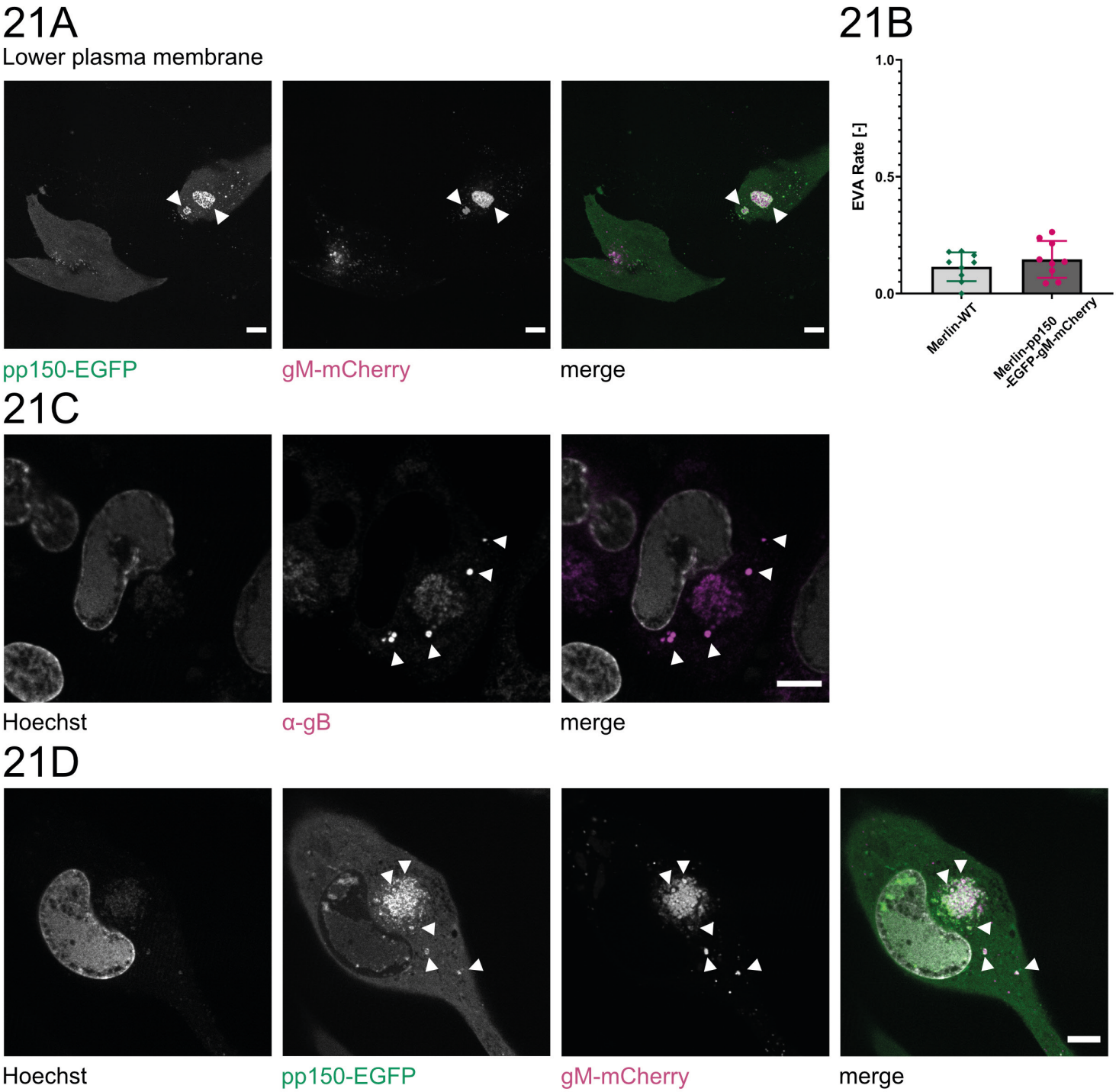

Figure 21 HCMV-Merlin produces EVAs and MViBs.
21A HFF cells were infected with HCMV-Merlin-pAL1502-pp150-EGFP-gM-mCherry (MOI of 1). At 5 dpi, the cells were fixed, and large overviews were acquired by spinning-disk microscopy. Shown are the lower plasma membranes from infected cells. The white triangles indicate EVAs found in HCMV-Merlin infected cells. Scale bar represents 10 µm.
21B HFF cells were treated and imaged as described in 21A. Additionally, HFF cells were infected with HCMV-Merlin-pAL1502-WT at an MOI of 1 and fixed at 5 dpi. The HCMV-Merlin-WT infected cells were subsequently IF stained against gB and imaged by spinning-disk microscopy. Late infected cells with EVAs at their lower plasma membrane were quantified. The bars indicate the mean EVA rate, and the error bars show the 95% confidence interval of the mean. Both viruses were quantified in 9 replicates with 327 cells counted for HCMV-Merlin-WT and 333 cells counted for Merlin-pp150-EGFP-gM-mCherry.
21C HFF cells were infected with HCMV-Merlin-pAL1502-WT as described for figure 21B. The shown images are excerpts from the dataset quantified in 21B. Large cytoplasmic vesicles, positive for gB, are indicated with the white arrows. Scale bar represents 10 µm.
21D HFF cells were treated and imaged as described in 21A. The images are part of the dataset acquired in 21B. Also here, large cytoplasmic vesicles, positive for pp150 and gM, resembling the MViBs in TB40 infection (Figure 4, 6), are indicated with the white triangles. Scale bar represents 10 µm.

22A

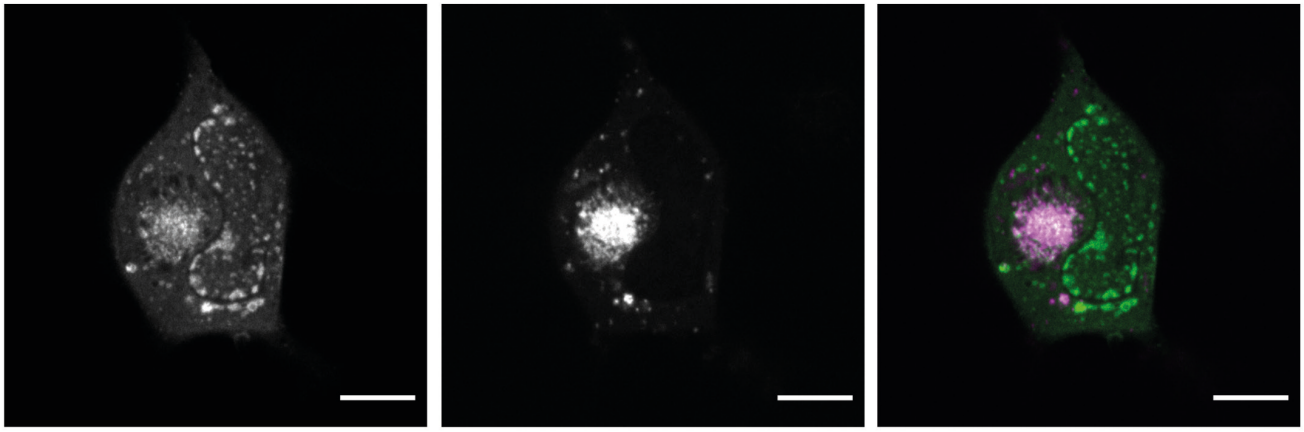

pp150-EGFP gM-mCherry merge

22B

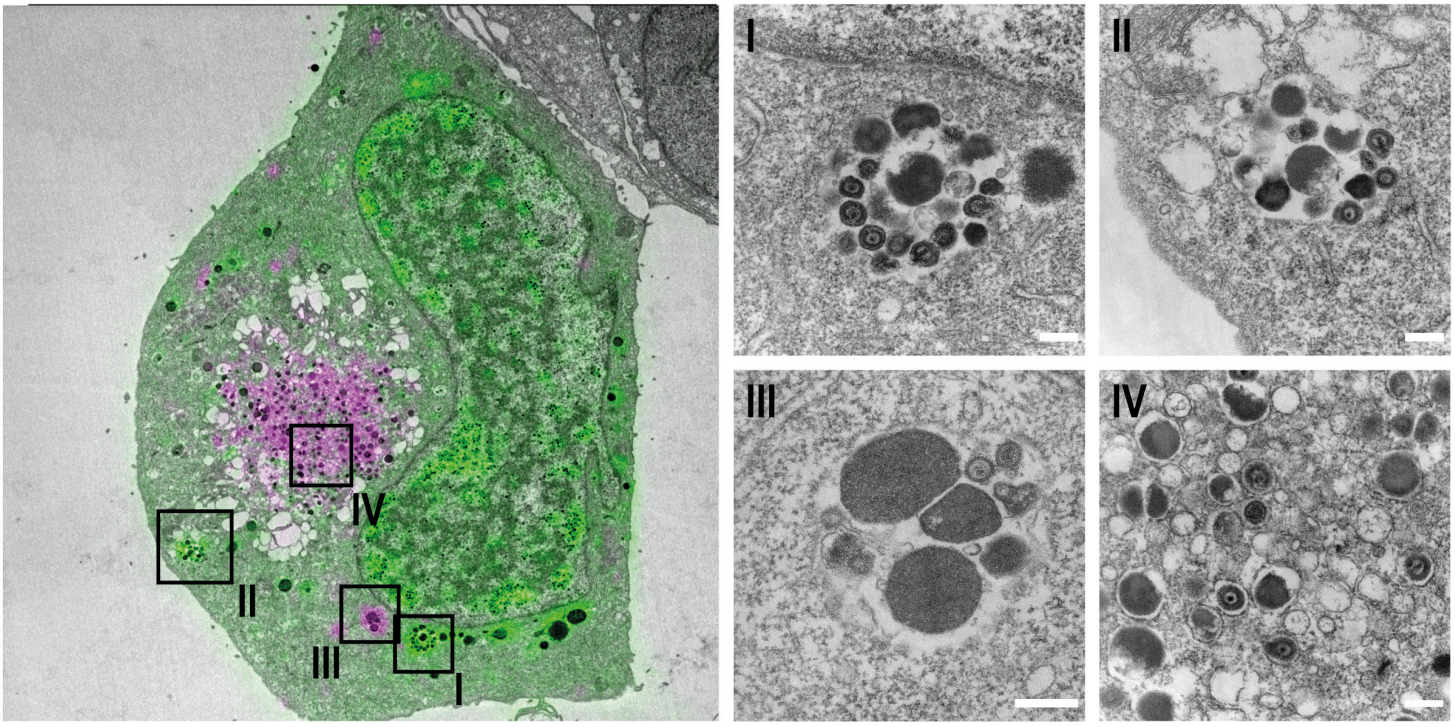

Figure 22. CLEM confirms MViB presence in HCMV-Merlin infected Cells.

22A HFF cells were infected with HCMV-Merlin-pAL1502-pp150-EGFP-gM-mCherry (MOI of 1). After 4 dpi, the cells were fixed and imaged with spinning-disk microscopy. Scale bar represents 10 µm.

22B The cells prepared in 22A were further processed for TEM. The images show CLEM data of the cell shown in 22A. The overview in the left panel shows an overlay of the fluorescence data with the EM images. The black frames and roman numbering indicate the areas of which corresponding high-magnification EM images are shown in the right panels. Panels I-III show large vesicles, reminiscent of the MViBs in HCMV-TB40 infected cells (Figure 6), whereas panel IV shows apparently single enveloped particles in the AC. Scale bars in panels I-IV represent 250 nm.

23A

α-CD63

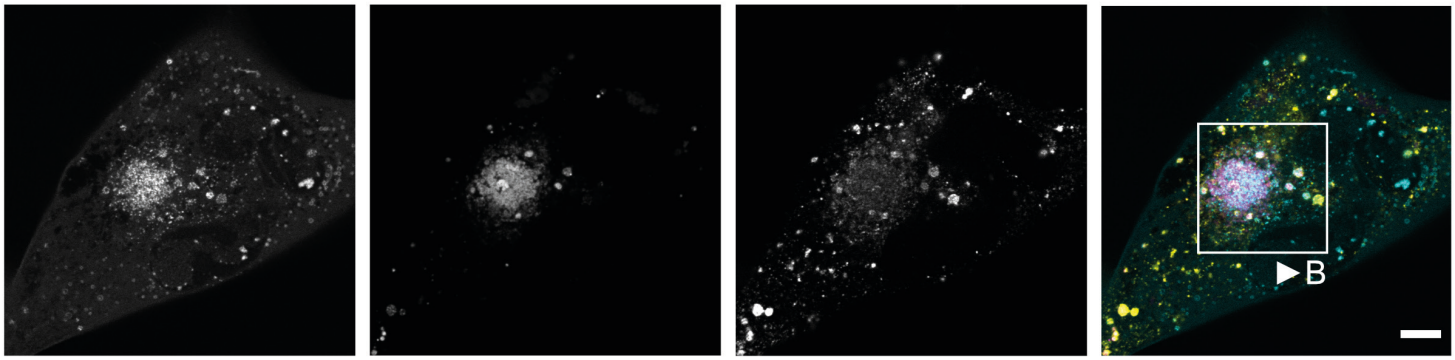

pp150-EGFP gM-mCherry α-CD63 merge

α-CD9

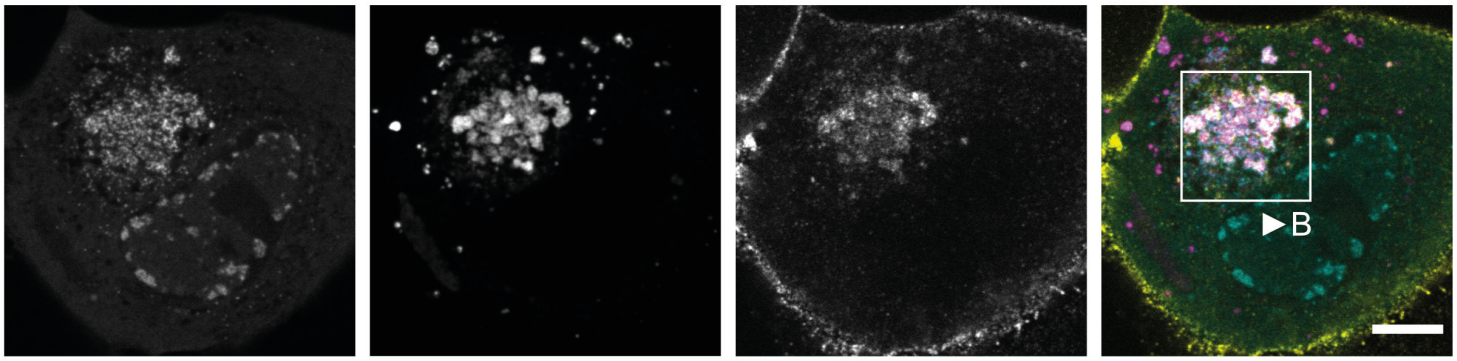

pp150-EGFP gM-mCherry α-CD9 merge

23B

CD63

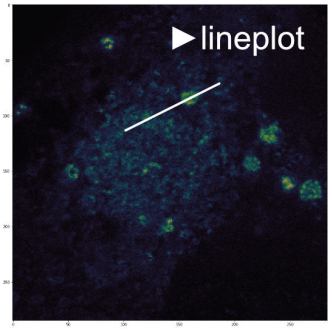

CD63 vs. pp150

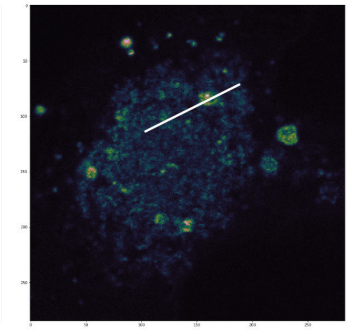

CD63 vs. gM

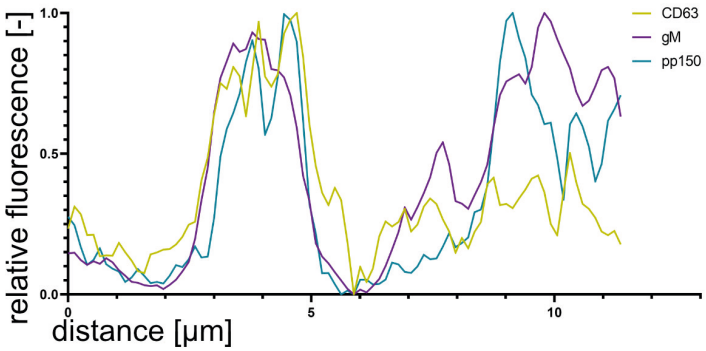

CD9

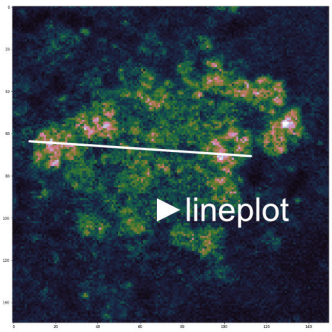

CD9 vs. pp150

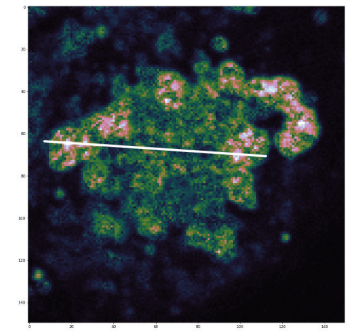

CD9 vs. gM

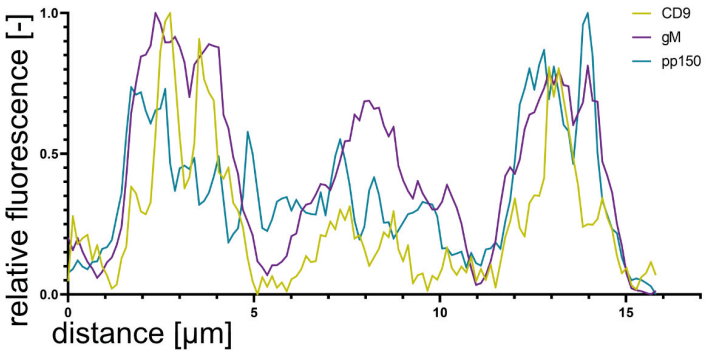

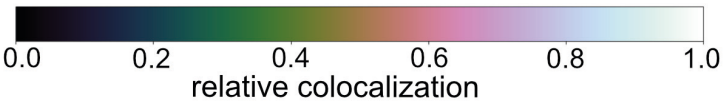

Figure 23. Tetraspanins CD63 and CD9 localize to MViBs in HCMV-Merlin infected cells.

23A HFF cells were infected with HCMV-Merlin-pAL1502-pp150-EGFP-gM-mCherry (MOI of 1). At 4 dpi, the cells were fixed, IF stained against CD63 or CD9, and images were acquired using spinning-disk microscopy. The white frames indicate the areas investigated with colocalization analysis, and the scale bar represents 10 µm.

23B Colocalization analysis for the areas indicated in 23A. The heat maps on the left show colocalization of CD63 and CD9 with viral proteins in large vesicles resembling the phenotype of MViBs. The white lines indicate the area plotted as a line profile on the right.

6 Discussion

6.1 Evidence for differential release mechanisms of herpesviruses

Our understanding of the HCMV virion structure and replication processes has benefitted significantly from knowledge acquired about related viruses from the *alphaherpesvirinae* subfamily. Processes like e.g. nuclear egress have been extensively studied in alphaherpesviruses such as HSV-1, and due to the conserved nature of key players in these processes give valuable insight into the corresponding process in HCMV (123–128). Still, important differences exist between the human-infecting herpesviruses, and the transfer of models between the viruses without experimental verification can lead to erroneous conclusions. Also, for secondary envelopment, the mechanistic models in the literature are quite similar between alphaherpesviruses and HCMV (166,220,225,295). This model is based on the hypothesis that individual viral capsids bud into small vesicles, forming single, double enveloped particles (295). These particles are then continuously transported for release to the plasma membrane. However, while there is convincing evidence for the alphaherpesvirus PRV, showing the release of single virions by live-cell microscopy, data like this is lacking for HCMV (222,223). Instead, the investigation into the mechanics of HCMV envelopment and egress presented in this work showed a distinct, intermittently timed pulse release of large amounts of viral material in bulk from infected cells, mostly between 4 and 5 dpi (Figures 9-11 and 13-14, (284)). These events lead to localized accumulations of viral material at the cell surface, which were termed extracellular viral accumulations (EVAs, Figures 4-5, (284)). Similar structures were also found for the alphaherpesvirus HSV-1. However, the authors of that study suggest that locally confined release hotspots are responsible for this phenomenon (296). Correlation of live-cell fluorescence microscopy data to 2D and 3D CLEM datasets strongly suggests that the bulk release events are caused by the fusion of large MViBs with the plasma membrane (Figures 4-6, 9-11 and 13-14, (284)). Evidence for the presence of structures like the MViBs shown in this work has been present in the literature for a long time. Their significance, though, has remained poorly understood (158,163,175,184,187,189,190,219, 227,228). Similar structures have moreover been described for other herpesviruses, such as the closely related HHV-6 and MCMV (297,298), and hypothesized to be involved in viral egress, albeit without dynamic information about the process (298). Even though the data presented in this work do not support the idea of a release pathway for HCMV involving individual double enveloped particles, such a pathway might still exist. Further analysis involving efficient blocking of MViB-based release mechanisms is needed to explore this possibility.

6.2 The specialized HCMV enveloping membrane impedes juxtaposition with host processes

While the evidence is accumulating for a specialized compartment designed for HCMV envelopment and egress, little is known about its ultrastructure and working mechanisms (161,195,196,201). However, several host proteins, such as Rab27a, Syntaxin-3, Syntaxin-5, Snap-23, VAMP3 and CD63 were identified to be important for viral egress processes (197–199,203,211,213). Together with the proposed role of ESCRT proteins and

viral ESCRT homologs in virion maturation, this set of proteins strongly suggests that hijacked components of endocytic-, recycling- and exosome pathways are important for HCMV (190,194,206,207,209–211). The MViBs presented in this work carry CD63 (in the strains TB40 and Merlin) and CD9 (in the strain Merlin) and are responsible for the release of viral material to the cell surface with a mechanism reminiscent of the release of exosomes through MVBs (Figures 9-18 and 23, (192,211,284,287)). Moreover, ultrastructural analysis shows HCMV capsids in indentations on the surface of these MViBs resembling budding processes and suggesting that MViBs have the potential to constitute the specialized compartment generated by HCMV to mediate maturation and egress (Figure 6E, (284)). Future experiments evaluating the full proteome of MViBs are needed to ascertain the validity of this hypothesis.

Furthermore, the generation of these MViBs remains obscure. If they are generated through the remodelling of host processes by HCMV, it is likely that redirection of protein trafficking, fusion and mixing of membranes, as well as remodelling of existing organelles, creates specialized MViB progenitor membranes (161,196,200–202). Subsequently, these novel structures would interact with viral capsids and tegument proteins to execute secondary envelopment. Supportive for this hypothesis are also findings that viral proteins are trafficked through different pathways to assembly sites (185,186,195,196,299). Whether MViBs are generated by consecutive budding of capsids into a growing body or by fusion of individually enveloped particles into a larger structure is at this point unclear. The EM data presented in this study, though, suggests that envelopment takes place at the MViB surface, rather than double pre-enveloped particles being assimilated into MViBs (Figure 6E, (284)).

These data show that HCMV egress is reminiscent of endocytic-recycling/exosomal processes in the host cell, both in a phenotypic way and from the host proteins involved (Figures 5-6, 9-15 and 21-23, (211,284)). These similarities include endocytic trafficking of viral proteins, such as gB, towards viral assembly sites, a budding process into multivesicular structures, as well as bulk release of vesicles by fusion with the plasma membrane (186,192,212,214)(Figures 5-6, 9-11 and 13-14, (284)). Moreover, some of these phenomena, such as endocytic gB trafficking and viral exploitation of endocytic membranes and exosome biogenesis, have also been reported for HSV-1 (300–302). Consequently, studies have shown that inhibition of endocytic processes has the potential to inhibit HCMV replication. As described earlier, several host proteins from these pathways were found to be essential for HCMV replication, but, especially for the ESCRT machinery, key proteins have also been described as dispensable (190,198,199,211,213). However, especially for CD63 and the ESCRT machinery, conflicting results were published as outlined in 3.2.1. (190,208,209,213). Furthermore, successful pharmacological inhibition of viral production was achieved using endocytosis inhibitors, e.g. dynasore and pitstop 2. However, an effect on secondary envelopment could not be dissected (206). A curious effect was described for the treatment of HCMV-infected cells with the exosome inhibitor GW4869. While the substance did not affect the production of infectious virus, the spread of the infection *in vitro* was found to be less efficient (209). The data presented here show an HCMV-inhibiting potential for the farnesyl-transferase blocker Tipifarnib, whereas the cholesterol-trafficking inhibitor U18666A and the anti-histamine drug Keto-

tifen show no effect on viral replication (Figures 19-20, (284)). Tipifarnib has been shown in a drug-repurposing study to be a highly active blocker of ESCRT-dependent and independent exosome biogenesis and is extensively tested as an anti-cancer agent (292,303). A definitive effect of Tipifarnib on HCMV replication, however, could not be determined. While the production of viral progeny was reduced, and the EVA rate strongly decreased (Figures 19A and 20A-B), a reduction in the levels of the late protein pp150 was also detected (Figure 20C). Therefore, it is possible that Tipifarnib acts on viral gene regulation and blocks viral replication upstream of the late cytoplasmic assembly steps (284). A potential explanation for this effect lies in the ability of Tipifarnib to inhibit Ras signalling pathways, which was previously described to have a proviral effect on HCMV, HSV-1 and other herpesviruses (304–306). Moreover, farnesyl-transferases, inhibited by Tipifarnib, might be involved directly in the post-translational modification of viral proteins. A blocking of farnesylation of viral or host proteins, as described for EBV (307), might have antiviral effects. Further experimentation is needed to explore this connection. The modest overall efficacy of drugs targeting host endosomal- and exosomal pathways in inhibiting HCMV replication might stem from the extensive viral remodelling of host organelles and processes as described above. Moreover, since herpesviruses likely also code for viral mimics and substitutes for e.g. ESCRT proteins (210), it is plausible that drugs that inhibit host processes might fail to block the viral counterparts.

6.3 The importance and problems of dynamic data for designing HCMV egress models

To elucidate the mechanisms of viral assembly processes, prior publications, as well as the data shown here, heavily rely on the ultrastructural investigation of the involved macromolecular complexes by electron microscopy (158,163,166)(Figures 4-6, 18 and 22, (284)). This is largely due to the fact that light microscopy is severely limited in its ability to generate contrast and resolution sufficient to investigate biological samples at the required magnification (308). On the other hand, electron microscopy requires several conditions incompatible with living cells, such as observation in vacuum (all modes), heavy-metal staining (classical TEM, SEM) or sample thinning (classical and cryo TEM). Consequently, the samples need to be fixed and embedded or, in the case of cryo-TEM, immobilized by rapid freezing. Therefore, to date, subcellular EM data is exclusively static images, in which the temporal context is obscured. This creates an important caveat when investigating assumed linear processes such as viral maturation from a naked capsid to an exocytosed, complete virion. Just based on EM images without temporal or molecular information, it is impossible to determine whether a capsid in an indentation is budding into or escaping from a vesicle or whether an invagination at the plasma membrane is exocytosis or endocytosis (Figures 5D and 6E, (158,163,166)). One way to overcome this limitation is the usage of inhibitors or mutant organisms, in which specific pathways or processes are blocked. In the best-case scenario, this disruption causes the process under investigation to freeze in a specific state and allows the researcher to make reasonable assumptions about the directionality in which the process has been stalled (175,309). Still, interferences of these kinds are always disruptions from the natural state of the investigated system and can have unintended consequences. Therefore, side effects must be

expected and considered when designing and evaluating such experiments. For this work, another approach was chosen, in which the EM data is correlated to fluorescence light microscopy (CLEM). In this technique, the correlation between fluorescence microscopy and EM data serves as the bridge between ultrastructural- and temporal information (Figure 4-6 and 22, (284)). Another advantage of this approach is, that the specific labelling by fluorescent proteins can probe the presence of molecules in the structures resolved by EM when other techniques like Tokuyasu immunolabeling are not applicable. The dynamic data obtained by light microscopy allowed the investigation of the fate of the MViBs and showed that they release their content to the cell surface generating EVAs (Figures 9-11 and 13-14, (284)). This is of special significance since it shows that MViBs are not targeted for degradation or dead-end vacuoles accumulating endocytosed material. Nevertheless, capturing MViB release events posed a major challenge since cells released viral material into EVAs in a limited time period, usually starting sometime between 4 and 5 days (Figures 9-11 and 13-14, (284)). This required long time-lapse imaging, and it was, therefore, difficult to get temporally and spatially highly resolved 3D videos without major disruption of the imaged cells. Luckily, the acquisition of high-speed multi-channel 3D live-cell data has significantly improved with the recent development of the lattice-light-sheet microscope (310). A light-sheet microscope reduces phototoxicity and photobleaching by confining the excitation laser beam to the focal plane of the detection objective, avoiding unnecessary illumination of the sample outside of the detected area (310). The lattice-light-sheet further improved this technique by taking advantage of the special optical properties of a focused lattice beam to achieve a resolution useful for subcellular imaging (310,311). With this microscope, it was possible to investigate HCMV-infected cells for at least one hour with up to three channels in 3D and a temporal resolution sufficient to follow the fate of MViBs and capture their release at the plasma membrane (Figures 11 and 14, (284)). However, while the acquisition settings might allow for the tracking of large objects, such as MViBs, the tracking of single virus particles is unfortunately not possible. The reasons for this are a combination of the high density of particles inside the infected cell, a low resolution compared to e.g. confocal microscopes and a time delay of several seconds between two time points. Therefore, although the data clearly shows the bulk release of virus particles, a release of individually exocytosed virions cannot be excluded. Taken together, the correlation of such dynamic live-cell information obtained from light microscopy to ultrastructural investigations by SBF-SEM and TEM is a powerful tool to elucidate viral replication mechanics. Nevertheless, the temporal dimension is lost during EM, and correlation can still bear errors. Hence appropriate critical evaluation of the data is still indicated.

6.4 HCMV phenotypical diversity and the argument for multiple spatio-temporally separated egress pathways

While HCMV displays a broad cell tropism *in vivo*, this property is rapidly lost through continuous culture in fibroblasts *in vitro* (229,230,277). This loss of genetic information is often accompanied by a change in spreading behavior. Whereas low-passage clinical isolates usually spread cell-associated with a limited release of infectious virus into the supernatant, cell culture adapted viruses produce large amounts of this cell-free

infectivity (230,240,276). The restriction to a direct cell-to-cell spread mode for clinical HCMV has been proposed to be a mechanism to evade antibody-mediated immunity in an *in vivo* infection setting (278,294,312). The exact mechanism of how cell-associated spread is achieved remains unknown, but in addition to the already outlined herpesviral egress mechanisms, transmission via cell-cell fusions and syncytia formation has been reported (234,313–315). Regardless of the actual mechanism by which cell-to-cell spread is mediated, it is a hallmark of clinical viral isolates, which have retained an intact genome, and observations from MCMV and HCMV transmission through blood transfusions predict it to be the primary mode of HCMV spread *in vivo* (278,316–319). Although a release of viral material in bulk through MViBs seems counter-intuitive for a cell-to-cell spread mechanism, MViBs and EVAs were observed both in infection with a BAC-derived TB40 from a low-passage endotheliotropic TB40 variant (TB40/E (257)) and a fully repaired Merlin (Figures 5-8 and 21-22, (284)). However, the infection with TB40, a strain which produces high levels of supernatant virus, yielded significantly higher amounts of EVAs than Merlin, suggesting that bulk release is indeed rather responsible for cell-free than cell-associated transmission (Figures 8B and 21B, (284)). Nevertheless, MViBs with a very similar phenotype to those in TB40 could readily be identified in HCMV-Merlin infected cells, suggesting that Merlin has the potential for bulk release (Figures 21-23, (284)). This apparent inconsistency might be owed to the fact that HCMV also produces cell-free virus *in vivo* for secretion into the urine, saliva and breast milk (320–323). Although the importance of infectious virus in infected and shed cells compared to the cell-free secreted virus has, to the author's knowledge, not been studied in detail, a role specifically for cell-free infectious HCMV populations has been reported for the transmission through breast milk (323). These observations suggest that both spread modes are important *in vivo* and that clinical isolates likely also possess the ability to produce cell-free virus, potentially through a bulk release mechanism.

However, an important question remains, whether the bulk release of cell-free virus is just a variation in the scale of cell-to-cell spread mechanisms or if the two are separate egress pathways. The literature about HCMV morphogenesis contains descriptions of mature virions in a wide variety of ultrastructurally different vesicles as already described in 3.2.2. Moreover, HCMV populations with different properties dependent on the combination of virus strain and infected cell type have been reported, with one publication even describing two distinct populations released from a single combination of strain and cell type (see 3.2.2. and (275)). In the results presented here, both individual double-enveloped particles and MViBs were observed in the cytoplasm of infected cells (Figures 5-7 and 22, (284)). Furthermore, intermediate stages were observed, which could constitute budding, with the aforementioned caveat that the temporal information is lost in static EM images (see 6.3. Figures 6E, (284)). One hypothesis to explain this variety could be spatio-temporally distinct envelopment pathways, one analogous to the single particle release observed in alphaherpesviruses (222,223) and the bulk release described here. Such a separation of morphogenesis routes for different viral particles could also mediate differential spread modes and the production of viral populations with distinct envelope glycoprotein compositions and thereon-based properties. However, differential proteomic analysis of the viral populations released in different conditions, as well as

live-cell data for the release of individually enveloped particles, are needed to explore this concept. Finally, the reduction of the complex behavior of the virus *in vivo* to a convoluted mix of phenotypes *in vitro* highlights the importance of more complex cell culture models for investigations in the laboratory. The advances in cell culture techniques, e.g. organoids, have enormous potential for HCMV, which is highly species-specific and limited to human cells. Thus, research of HCMV in animal models is severely limited, and simple human cell cultures lack the complexity the virus encounters *in vivo* (324). New model systems would allow researchers to define cell types and interfaces where HCMV transmission occurs, to differentiate between secretion on epithelial cells, spread between endothelium and leukocytes, or dissemination within a specific organ. With this, researchers would gain a clearer picture of which proteins are involved in which stage of infection *in vivo*, and this understanding would be beneficial to the development of effective antivirals.

7 Material

7.1 Organisms

Name	*Description/Usage Note*	*Reference/Vendor*
HFF-1	Primary human foreskin fibroblasts referred to here as “HFF cells”	ATCC SCRC-1041
BJ-5ta	hTERT immortalized human foreskin fibroblasts referred to here as “BJ cells”	ATCC CRL-4001
HCMV-TB40-pp150-EGFP-gM-mCherry	Dual labeled HCMV-TB40 variant	Gift from Christian Sinzger/(286)
E. coli HCMV-TB40-BAC4-WT	*E. coli* strain GS1783 maintaining the HCMV genome as a BAC	Gift from Wolfram Brune
E. coli HCMV-TB40-BAC4-pp150-SNAP	*E. coli* strain GS1783 maintaining the HCMV genome as a BAC	(284)
E. coli HCMV-TB40-BAC4-pp150-SNAP-gM-mScarlet-I	*E. coli* strain GS1783 maintaining the HCMV genome as a BAC	This study
NEB 5-alpha Competent *E. coli* (High Efficiency)	Chemically competent *E. coli* strain 5-alpha	NEB
NEB Stable Competent *E. coli* (High Efficiency)	Chemically competent *E. coli* for maintenance of lentiviral vectors	NEB
E. coli pENTR-1-5r-mNeongreen	*E. coli* NEB 5-alpha maintaining the plasmid pENTR-1-5r-mNeongreen	This study
E. coli pENTR-5-2-Rab5B	*E. coli* NEB 5-alpha maintaining the plasmid pENTR-5-2-Rab5B	This study
E. coli pENTR-1-2-CD63-pHluorin	*E. coli* NEB 5-alpha maintaining the plasmid pENTR-1-2-CD63-pHluorin	This study
E. coli pLenti CMV Puro mNeongreen-Rab5B	*E. coli* NEB Stable maintaining the plasmid pLenti CMV Puro mNeongreen-Rab5B	This study
E. coli pLenti CMV Puro CD63-pHluorin	*E. coli* NEB Stable maintaining the plasmid pLenti CMV Puro CD63-pHluorin	This study
Lenti-X™ 293T Cell Line	HEK293T cell line for lentivirus production	Takara
HFF-mNeongreen-Rab5	HFF-1 cells stably expressing transgenic the mNeongreen-Rab5 fusion protein	This study
HFF-CD63-pHluorin	HFF-1 cells stably expressing transgenic the CD63-pHluorin fusion protein	This study
HCMV-Merlin-pAL1502-WT	HCMV strain Merlin with repaired RL13 and UL128 gene locus, both under tet-operator control	Gift from Christian Sinzger
HCMV-Merlin-pAL1502-pp150-EGFP-gM-mCherry	Dual labeled HCMV-Merlin-pAL1502 variant	Gift from Christian Sinzger

7.2 Reagents

Name	*Description/Usage Note*	*Reference/Vendor*
10 nm gold coupled donkey-anti-mouse antibody	Used dilutions: Tokuyasu: 1:20	Aurion
20% Paraformaldehyde (Formaldehyde) Aqueous Solution, EM Grade		Science-Services
2-mercaptoethanol		Sigma-Aldrich
2-propanol		Carl-Roth
Agar-Agar, Kobe I	For agar plates for bacteria culture	Carl-Roth
Agarose NEEO ultra-quality	Agarose used for DNA gel electrophoresis	Carl-Roth
Alexa 488 goat anti-mouse	Used dilutions: IF: 1:1000	ThermoFisher
Alexa 647 goat anti-mouse	Used dilutions: IF: 1:1000	ThermoFisher
Ampicillin		Sigma-Aldrich
Anti-CMV ICP36 monoclonal antibody 10D8	Anti HCMV-pUL44 antibody. Used dilutions: WB: 1:1000	Virusys
Anti-Cytomegalovirus Glycoprotein B antibody [2F12]	Used dilutions: IF: 1:200,	Abcam
Anti-GAPDH hFAB Rhodamine Antibody	Used dilutions: WB: 1:5000	BioRad
Anti-HCMV pp150 mouse antibody	Used dilutions: WB: 1:2000	Gift by Eva-Maria Borst and Stipan Jonjic
Anti-IE1/2 mouse Hybridoma Supernatant	Used dilutions: WB: 1:3, IF: undiluted	Gift by Wolfram Brune/ (325)
Aqua ad injectabilia 10ml Mini-Plasco	Pharmaceutical grade distilled water for injection	Braun
Aurion donkey serum	For Tokuyasu immuno-EM	Aurion
Bovine serum albumin		Sigma-Aldrich
Bromophenol blue		Sigma-Aldrich
Calcium Chloride		Sigma-Aldrich
Chloramphenicol		Sigma-Aldrich
CircuitWorks Conductive Silver Epoxy	Conductive expoxy glue for SBF-SEM sample mounting	Chemtronics
CutSmart Buffer	Buffer for restriction enzyme digestion reactions	NEB
DDSA ((2-Dodecen-1-yl)succinic anhydride)	EM grade	Carl-Roth
Deoxynucleotide (dNTP) Solution Mix	For PCR	NEB
Dimethylsulfoxide (DMSO)		Sigma-Aldrich
DMEM, high glucose, GlutaMAX™ Supplement	Basal medium for mammalian cell culture	ThermoFisher

Name	*Description/Usage Note*	*Reference/Vendor*
DMP-30 (2,4,6-Tris(dimethylaminomethyl)-phenol)	Glycidether Accelerator, EM grade	Carl-Roth
Dulbecco's Phosphate Buffered Saline	Modified, without calcium chloride and magnesium chloride, liquid, sterile-filtered, suitable for cell culture	Sigma-Aldrich
Ethanol Rotipuran ≥99,8 %		Carl-Roth
FBS Superior	Former biochrome, product discontinued	Merck
Fibronectin bovine plasma	Coating reagent for glass coverslips	Sigma-Aldrich
Gallic acid		Sigma-Aldrich
Gateway BP Clonase II Enzyme mix	Gateway reaction enzyme mix for BP cloning	ThermoFisher
Gateway LR Clonase II Enzyme mix	Gateway reaction enzyme mix for single-fragment LR cloning	ThermoFisher
Gateway LR Clonase II plus Enzyme mix	Gateway reaction enzyme mix for multi-fragment LR cloning	ThermoFisher
Gel Loading Dye, Purple (6X)	For DNA agarose gel electrophoresis	NEB
Gelatine	Food grade gelatin used in Tokuyasu immuno-EM	Dr. Oetker
Glutaraldehyde EM Grade, 25% Aqueous Solution		Science-Services
Glycerol ROTIPURAN ≥99,5 %		Roth
Glycid ether 100	Epon 812, EM grade	Carl-Roth
Glycine		Sigma-Aldrich
Goat Anti-Mouse IgG StarBright Blue 700	Used dilutions: WB: 1:5000	BioRad
Hoechst 33342	Nuclear counterstain for fluorescence microscopy	ThermoFisher
Hygromycin B Gold	Antibiotic for selection of mammalian cells	Invivogen
Kanamycin		Sigma-Aldrich
Ketjen Black	Conductive filler for epon resins for SBF-SEM	TAAB
Ketotifen fumarate		Sigma-Aldrich
L-Arabinose		Sigma-Aldrich
L-Aspartatic acid		Carl-Roth
Lead nitrate		Carl-Roth
Medium 199 (Earles Salts)	Medium supplement	ThermoFisher
Methylcellulose 4000cp		Sigma-Aldrich
Milk Powder	For western blot	Roth

Name	*Description/Usage Note*	*Reference/Vendor*
MNA (1-Methyl-5-norbornene-2,3-dicarboxylic acid anhydride)	EM grade	Carl-Roth
Optimem	Reduced serum medium for transfection	ThermoFisher
Osmium tetroxide		Roth, Science-Services
Osmium tetroxide, 4% Aqueous Solution		Science-Services
Penicillin-Streptomycin (10.000 U/ml)		ThermoFisher
Polyethyleneimine, Branched, Mw 2000 (bPEI 2000)	For transfection	Polysciences
Potassium ferricyanide		Sigma-Aldrich
Potassium hydroxide		Merck
Broad Multi Color Pre-Stained Protein Standard	Protein ladder for protein gel electrophoresis	GenScript
Proteinase K		ThermoFisher
Purified anti-human CD81 (TAPA-1) 5A6	Used dilutions: IF: 1:100	Biolegend
Purified anti-human CD9 HI9a	Used dilutions: IF: 1:200	Biolegend
Puromycin	Antibiotic for selection of mammalian cells	Invivogen
Quick-Load 1 kb Plus DNA Ladder	For DNA gel electrophoresis	NEB
Recombinant Human FGF-basic (154 a.a.)	Medium supplement for HFF cells	PeproTech
ROTIPHORESE 50x TAE Buffer	Diluted to 1x in water before use	Roth
Silver Flakes	Conductive filler for epon resins for SBF-SEM	Sigma-Aldrich
SNAP-Cell-SiR	Live-cell dye for covalent labeling of SNAP-tags	NEB
Sodium dodecyl sulfate (SDS)		Sigma-Aldrich
Sodium pyruvate (100mM)	Medium supplement	ThermoFisher
Staurosporine		Merck
Sucrose		Sigma-Aldrich
SYBR Safe DNA Gel Stain	For DNA agarose gels	ThermoFisher
TE-Buffer	Tris-EDTA buffer.	ThermoFisher
Terrific-Broth-Medium	Liquid medium was prepared according to the manufacturers instructions.	Carl-Roth
Thiocarbohydrazide		Sigma-Aldrich
Tipifarnib		Sigma-Aldrich
TRIS		MP Biomedicals
Triton X-100		Sigma-Aldrich

Name	*Description/Usage Note*	*Reference/Vendor*
TrypLE™ Express Enzyme (1X), phenol red	Cell dissociation reagent, replacement for trypsine	ThermoFisher
Tween 20		Sigma-Aldric
U18666A		Merck
UHU Plus Endfest 300	2-component epoxy glue	UHU
Ultra-LEAF Purified anti-human CD63 H5C6	Used dilutions: IF: 1:200, Tokuyasu: 1:5	Biolegend
Uranyl Acetate		Merck
Xho-I	Restriction enzyme	NEB

7.3 Plasmids/BACs

Name	*Description/Usage Note*	*Selection Marker*	*Reference/Vendor*
HCMV-TB40-BAC4-WT	Prepared from *E. coli* GS1783	Chloramphenicol	(257)
HCMV-TB40-BAC4-pp150-SNAP	Prepared from *E. coli* GS1783	Chloramphenicol	(284)
pexA257 mScarlet-I KanR BAC cassette	Universal shuttle vector for Red-recombination mediated insertion of mScarlet-I	Ampicillin	This study
HCMV-TB40-BAC4-pp150-SNAP-gM-mScarlet-I	Prepared from *E. coli* GS1783	Chloramphenicol	This study
pDONR 221	Gateway DONR Vektor	Kanamycin	ThermoFisher
pDONR 221 P1-P5r	MultiSite Gateway DONR Vektor	Kanamycin	ThermoFisher
pDONR 221 P5-P2	MultiSite Gateway DONR Vektor	Kanamycin	ThermoFisher
pLenti CMV Puro DEST (w118-1)	3rd generation lentiviral destination vektor for Gateway cloning	Ampicillin, Chloramphenicol	(326)
/Addgene #17452			
pCMV-Sport6-CD63-pHluorin	Mammalian expression vektor for a CD63-pHluorin fusion protein	Ampicillin	(287) /Addgene #130901
GFP-Rab5B	Mammalian expression vektor for a GFP-Rab5B fusion protein	Kanamycin	(327) /Addgene #61802
pENTR-1-5r-mNeongreen	Gateway ENTR vector for C-terminal fusion	Kanamycin	This study
pENTR-5-2-Rab5B	Gaterway ENTR vetor for N-terminal fusion	Kanamycin	This study
pENTR-1-2-CD63-pHluorin	Gateway ENTR vector	Kanamycin	This study

Name	*Description/Usage Note*	*Selection Marker*	*Reference/Vendor*
pLenti CMV Puro mNeongreen-Rab5B	Lentiviral vektor containing mNeongreen-Rab5B	Ampicillin	This study
pLenti CMV Puro CD63-pHluorin	Lentiviral vektor containing CD63-pHluorin	Ampicillin	This study
pRSV-Rev	3rd generation lentiviral helper plasmid	Ampicillin	(328)/ Addgene #12253
pMD2.G	Mammalian expression vector for VSV-G envelope for lentivirus production	Ampicillin	Gift from Didier Trono/ Addgene #12259
pMDLg/pRRE	3rd generation lentiviral helper plasmid	Ampicillin	(328)/ Addgene #12251
pp71 expression plasmid	Mammalian expression vector for the HCMV pp71 protein (pCGN71)		(329)/ Gift from Wolfram Brune

7.4 Primer

Name	*Description/Usage Note*	*Sequence*	*Reference/Vendor*
UL100-mScarlet-I For	Primer for BAC mutagenesis mediated tagging of gM with mScarlet-I	ACT ATC ACG TCG TGG ACT TTG AAA GGC TCA ACA TGT CGG CCT ACA ACG TAG TG AGC AAG GGC GAG GC	This Study/Eurofins
UL100-mScarlet-I Rev	Primer for BAC mutagenesis mediated tagging of gM with mScarlet-I	CAC ACC AGC TGC ACC GAG TCT AAG AAA AGC ATA GGC GTG TGC AGG TGC ATC TTG TAC AGC TCG TCC ATG CC	This Study/Eurofins
UL100 ctr For	Primer for amplification of the region of interest for gM tagging	CCA TCG TAG TAT TTA ACG ACC CG	This Study/Eurofins
UL100 ctr Rev	Primer for amplification of the region of interest for gM tagging	GCT AAA AAG ACG AGC TGC ATG A	This Study/Eurofins
ATTB1-mNeongreen For	Dissolved and diluted for PCR in Aqua ad injectabilia	GGG GAC AAG TTT GTA CAA AAA AGC AGG CTT AAT GGT GAG CAA GGG CGA G	This Study/Eurofins
ATTB5r-mNeongreen Rev	Dissolved and diluted for PCR in Aqua ad injectabilia	GGG GAC AAC TTT TGT ATA CAA AGT TGT CTT GTA CAG CTC GTC CAT GCC	This Study/Eurofins
ATTB5-Rab5B For	Dissolved and diluted for PCR in Aqua ad injectabilia	GGG GAC AAC TTT GTA TAC AAA AGT TGT AAT GAC TAG CAG AAG CAC AGC T	This Study/Eurofins

Name	*Description/Usage Note*	*Sequence*	*Reference/Vendor*
ATTB2-Rab5B Rev	Dissolved and diluted for PCR in Aqua ad injectabilia	GGG GAC CAC TTT GTA CAA GAA AGC TGG GTT TCA GTT GCT ACA ACA CTG GCT CT	This Study/Eurofins

Kits

Name	*Description/Usage Note*	*Reference/Vendor*
Cell Titer-Glo Luminescent Cell Viability Assay kit	Kit for assessing intracellular ATP levels	Promega
NucleoBond Xtra Midi	Plasmid/BAC DNA extraction kit from bacterial culture	Macherey-Nagel
Phusion Polymerase	Kit including enzyme, dNTPs and reaction buffer	NEB
QIAprep Spin Miniprep Kit	Plasmid DNA extraction kit from bacterial culture	Qiagen
QIAquick PCR Purification Kit	Quick DNA purification kit	Qiagen
Taq Polymerase	Kit including enzyme, dNTPs and reaction buffer	NEB

7.5 Software

Name	*Description/Usage Note*	*Reference/Vendor*
Adobe Photoshop	Graphic program	Adobe
Affinity Photo	Graphic program	Serif
Anaconda 3	Python distribution	Anaconda
Digital Micrograph	Software for viewing and processing electron microscopy data	Gatan
FIJI/ImageJ	Standard image analysis tool for scientific images	(330)
GraphPad Prism 9	Software for statistical analysis and graphical data presentation	Dotmatics
Imaris 8	Software for 3D presentation and rendering of imaging data	Bitplane
Matlab 2019	Skripting editor and environment	MathWorks
msdanalyzer	Matlab class for analyzing the msd of single particle tracks	(281)
NIS-Elements	Software for control and image acquisition for Nikon microscopes	Nikon
Noise2Void	Jupyter notebook customized for batch-denoising (see Code 1)	(279)
SnapGene	Software for viewing genomic information, simulate and plan cloning experiments	Dotmatics

Name	*Description/Usage Note*	*Reference/Vendor*
Trackmate	Fiji-plugin for single particle tracking	(280)
TrISS	Tracking information segmenting and search tool (see Code 2)	This study
Zen Blue	Software for control and image acquisition for Zeiss microscopes	Zeiss

7.6 Special Equipment

Name	*Description/Usage Note*	*Reference/Vendor*
µ-Dish 35 mm, high Glass Bottom	Glass coverslip bottom microscopy petri dish	Ibidi
µ-Slide 8 Well high Glass Bottom	Glass coverslip bottom microscopy 8-well chamber slide	Ibidi
4–15% Mini-PROTEAN® TGX™ Precast Protein Gels, 15-well, 15 µl	Precast polyacrylamide gels for protein gel electrophoresis	BioRad
Amersham Protran 0.45 NC	Nitrocellulose membranes for western blotting	Cytiva
Diatome cryo immuno	Diamond knife for thin-sectioning of gelatin embedded biological specimens under cryo conditions	Diatome
Diatome cryo trim 45°	Diamond trimming knife for use with a cryo microtome	Diatome
Diatome ultra 35°	Diamond knife for ultra thin-sectioning of resin embedded biological specimens	Diatome
Diatome ultra trim 45°	Diamond trimming knife for use with a microtome	Diatome
Formvar coated Nickel grids	TEM grids for Tokuyasu immunolabeling	Prepared by Rudolph Reimer
Gatan 3View sample pin stubs	Sample stubs for SBF-SEM using a 3view stage	Micro to Nano
Ibidi µ-Dish 35 mm, high Grid-500	Polymer coverslip bottom microscopy petri dish	Ibidi
Perfect Loop	Loop for transfer of cryosections to grids	Diatome
TEM Grids, 200 Mesh, hexagonal, Cu	Copper grids for TEM	Science-Services

8 Methods

8.1 Mammalian cell culture methods and virus work

General

All cell culture and infection experiments were carried out under biosafety level 2 conditions in biosafety laminar-air-flow cabinets. All liquid handling and cell culture was performed with scientific grade single use, sterile equipment and culture vessels as well as scientific grade pipetting devices, micropipettes and accessory equipment. Cell culture consumables, such as Petri dishes, serological pipettes, reaction tubes, vials, and pipette tips, were bought from Sarstedt unless otherwise indicated.

Mammalian cell culture

HFF-1 cells were cultivated in Dulbeccos Modified Eagles Medium Glutamax (DMEM-Glutamax; ThermoFisher), supplemented with 5% (v/v) fetal bovine serum (FBS; Merck) and 5 µl of 10^5 units/ml recombinant human FGF (PeproTech). BJ cells were cultivated in special formulated BJ media consisting of DMEM-Glutamax containing 20% (v/v) Medium 199 (Earles Salts) (ThemoFisher), 10% (v/v) FBS (Merck), 0.8 mM sodium pyruvate and 0.01 mg/ml hygromycin B (ThermoFisher), according to the vendor's instructions (ATCC). HEK293XT were cultured in DMEM-Glutamax, supplemented with 10% (v/v) FBS (Merck). These media compositions are referred to in the following as the "growth medium" for the respective cell lines. To avoid overgrowth, the cell cultures were subcultured regularly by dissociating the cells using appropriate amounts of TrypLe Express cell dissociation reagent (Thermofisher), followed by reseeding appropriate amounts of cells. The subculturing process is referred to as "splitting" in the following. Cells were cultured at 37°C, 5% CO_2 and >90% relative humidity.

Cryopreservation and thawing of mammalian cells

Cell thawing was performed by removing a vial containing a frozen cell suspension from liquid nitrogen gas-phase storage and letting it warm up at room temperature. As soon as the cell suspension was completely thawed, 1 ml of the suspension was diluted to 10 ml with the growth medium appropriate for the cell line. Afterwards, the cells were pelleted by centrifugation at 800 g for 5 minutes, and the supernatant was discarded. The pellet was resuspended in 10 ml of the appropriate growth medium and seeded in the desired culture vessel.

Cell freezing media for all cell lines consisted of 80% (v/v) of their respective growth medium, 10% (v/v) additional FBS (Merck) and 10% (v/v) DMSO (Sigma-Aldrich). Cells were grown in Petri dishes of 10 cm or 15 cm diameter to 80-90% confluence in their normal growth medium. Then, the cells were dissociated with TrypLE Express (ThermoFisher) and pelleted by centrifugation at 800 g for 5 minutes. The cell pellet was afterwards resuspended in 1 ml of cell freezing medium per 10 cm dish and 3 ml of cell freezing medium per 15 cm dish. Subsequently, the cell suspension was aliquoted at 1 ml into 1.5 ml cryo-vials. These vials were placed in a styrofoam box at -80°C to allow slow freezing of the suspension for 2 days. Afterwards, the vials were moved to liquid-nitrogen gas-

phase storage containers for long-term storage.

Plaque assay

Overlay medium was produced by adding 3.75 g of methylcellulose 4000cp (Sigma-Aldrich) to 125 ml ddH_2O and autoclaving. Afterwards, the mixture was stirred at 4°C until the methylcellulose had dissolved completely. Afterwards, 500 ml DMEM and 10 ml FBS were added to the solution, mixed and stored at 4°C.

Plaque assays were performed to determine the titer of virus stocks and virus-containing supernatant of infected cells. For this, HFF-WT cells were seeded in 24-well dishes to reach 90% confluency on the next day. The examined virus-containing solution was serially diluted in tenfold steps in HFF growth medium in ranges from 10^{-0} to 10^{-5}, depending on the expected amount of virus. The medium from the HFF cells in the 24-well dishes was removed and replaced with a 100 µl inoculum of the virus dilutions. In the following 1 hour after adding the inoculum, the plate was agitated every 15 minutes to distribute the inoculum evenly on the cell layer. Subsequently, 0.5 ml of overlay medium was added per well to the infected cells, and the cells were incubated for 14 days under cell culture conditions.

Afterwards, the cells were fixed, and plaques were counted manually on a cell culture microscope. When fluorescent virus variants were investigated, the fluorescent plaques were counted. For non-fluorescent viruses, the cells were IF-stained against IE1/2, and fluorescent plaques were counted afterwards. The viral titer was quantified in plaque-forming units per ml (PFU/ml) by the following formula.

$$Titer[\frac{PFU}{ml}] = \frac{plaque\ count[PFU]}{inoculum[ml] * dilution[\frac{ml}{ml}]}$$

Formula 1: Calculation of virus titer in virus-containing solutions following plaque assay.

Virus reconstitution

Virus reconstitution from BAC DNA was performed by electroporation of the viral DNA into HFF-WT cells. For this, two 15 cm dishes of HFF cells were grown to 90% confluency and harvested by dissociation with TrypLE. The cells were pelleted by centrifugation at 180 g for 8 minutes, washed with 10 ml Optimem and pelleted again. Subsequently, the cells were resuspended in 250 µl Optimem and transferred to a sterile 4 mm gap width electroporation cuvette on ice. 3 µg of BAC DNA and 1.5 µg of pp71 expression plasmid were added to the cells. Afterwards, the cells were electroporated using a BioRad Gene Pulser XCell (BioRad) and the following settings.

Mode: Exponential
Voltage: 220 V
Capacitance: 950 µF
Resistance: ∞ Ω
Gap width: 4 mm

In the following, the cells were recovered in HFF growth medium from the cuvette, seeded on a 10 cm Petri dish, and incubated under cell culture conditions. The cells were subcultured every 7 days and expanded until the first plaques appeared. Then the cells were incubated without further subculturing until >90% of cells displayed cytopathic effects (CPE). The cells were collected together with the supernatant by scraping, aliquoted at 1 ml, and frozen at -80°C. The titer of the stock was determined by plaque assay.

Infection experiments

Cell infections were carried out by adding the appropriate amount of virus stock to the cells in their respective growth medium. The amount of virus added is specified by the multiplicity of infection (MOI). This metric describes how many plaque-forming units of virus (PFU) were added per cell in the infected culture. The amount of virus stock for infection was determined by the following formulas.

$$PFU_{added}[PFU] = MOI_{target}[PFU] * cellcount$$

Formula 2: Determination of the total PFU to be added to the cell culture (PFU_{added}) determined by the target MOI (MOI_{target}) and the number of cells on the dish (cellcount).

$$stock[ml] = \frac{PFU_{added}[PFU]}{Titer[\frac{PFU}{ml}]}$$

Formula 3: Calculation of the amount of virus stock used for infection determined on the PFU to be added to the cell layer (PFU_{added}) (see formula 2) and the stock titer (see formula 1).

Virus stock production

HCMV stocks were produced by growing a 15 cm cell culture dish with HFF cells to 70-80% confluence. The cells were afterwards infected with virus stock at an MOI of 0.01. The infection was allowed to proceed for 7 days before the culture was split onto two 15 cm dishes and cultured for another 7 days or until >90% of the cells showed CPE. Afterwards, the cells were scraped, collected together with the supernatant and frozen at -80°C for 24 hours. Afterwards, the suspension was thawed, and cell debris was pelleted by centrifugation at 5000 g and 4°C for 10 minutes. The supernatant was aliquoted at 1 ml and frozen at -80°C for storage. The stock titer was afterwards determined by plaque assay.

Growth curve

Growth curves were performed to determine the growth kinetics of HCMV variants. To this end, HFF-WT cells were seeded in 24-well dishes to reach 80-90% confluency on the next day. Afterwards, the cells were infected at an MOI of 0.05, and the virus was grown for 15 days. The medium was collected and renewed after 2 hours to determine the inoculum titer (t = 0), after one day and subsequently every two days until 15 dpi and frozen at -80°C. After collecting all time points, the supernatants were thawed and titrated by a plaque assay. The viral production for each interval was calculated (see formula 1), and the titer was summed up to each time-point to determine the total production (see formula 4). The growth curve was plotted from the summed titers using GraphPad prism.

$$SumTiter_t[\frac{PFU}{ml}] = \sum_{i=1}^{t} Titer_i$$

Formula 4: Calculation of sum titers for plotting of growth curves.

Lentivirus production

Lentiviruses for transduction of cells were produced in HEK293XT (Takara). For this, 106 cells were seeded in 6-well culture dishes in their growth medium. On the following day, the cells were transfected with the desired lentivirus vector plasmid and the three helper plasmids pRSV-Rev, pMD2.G and pMDLg. For the transfection, 600 ng lentiviral vector, 300 ng pRSV-Rev, 200 ng pMD2.G and 300 ng pMDLg plasmids were added to 200 µl Optimem and mixed. At last, 8 µl polyethyleneimine (PEI) was added, and the mixture was incubated for 15 minutes at RT. The growth medium from the HEK293XT in the 6-well dishes was reduced to 1 ml, and the PEI/DNA mix was pipetted dropwise to the cells. Subsequently, the dish was agitated gently to distribute the transfection solution evenly. The medium was changed 24 hours after the transfection to 1 ml of complete growth medium. The lentivirus-containing supernatant was collected every day until 4 days after the transfection and stored at 4°C. Afterwards, the supernatants were pooled and filtered through syringe filters with a 0.45 µm pore size. The filtered lentivirus stock was either directly used for transduction or stored at -80°C.

Lentivirus transduction

Lentivirus supernatants were used as delivery systems to create cell lines stably expressing transgenes. To create such a cell line, cells from the parent cell line were seeded in 3 wells in a 6-well culture dish to reach 70-80% confluency the next day. Then, the cells were infected with the lentivirus stock at 1:1, 1:10 and 1:100 dilution in a total volume of 1 ml growth medium. The cells were afterwards incubated under cell culture conditions over the weekend. In the following, one of the transduced wells was chosen for further cultivation, which showed the best transduction rate while displaying no CPE at the same time. Those cells were expanded for two weeks under selection by adding an appropriate antibiotic to the complete growth medium. Stocks of the transduced cells were cryopreserved as described above.

Inhibitor treatments

Tipifarnib, Ketotifen-fumarate and U18666A were acquired from Merck/Sigma-Aldrich. 5 mg of Tipifarnib were dissolved in 2.04 ml DMSO to achieve a 5 mM stock solution, which was sterile filtered using 200 nm pore size syringe filter before aliquoting at 200 µl and storing at -80°C. 20 mg of Ketotifen-fumarate were dissolved in 2.35 ml DMSO to generate a 20 mM stock solution, which was also sterile filtered, aliquoted and stored at -80°C. 10 mg of U18666A was dissolved in 2.51 ml DMSO to yield a 9.4 mM stock solution, which was sterile filtered, aliquoted and stored at -80°C.

Inhibitor treatments were performed by adding an appropriate amount of stock solution, as indicated in the experimental conditions, to the complete growth medium.

The medium containing the inhibitors was refreshed every 24 hours unless otherwise indicated.

Cell viability assay

To assess the cytotoxicity of small molecule inhibitors, HFF cells were seeded on black 96-well dishes to reach >90% confluency the next day. The cells were then incubated in complete growth medium with the indicated substance added at the described concentration for 24 hours under cell culture conditions. Cell viability was assessed using the CellTiter-Glo ATP assay kit (Promega) in combination with a FLUOStar Omega plate reader (BGM Labtech), both according to the instructions from their manufacturers. Non-treated cells served as the 100% viability control.

8.2 Light microscopy methods

General

For microscopic investigations, experiments were carried out in special cell culture dishes with either glass or polymer coverslip bottoms. For experiments including adherent cells, glass bottom dishes were fibronectin coated prior to cell seeding. Fibronectin coating was performed by covering the cover glass bottom of the dish with a 1:100 dilution of a fibronectin solution (Sigma-Aldrich) in sterile Dulbecco's phosphate buffered saline (D-PBS; Sigma-Aldrich). Following a 30 min incubation at 37°C, the fibronectin dilution was removed, and the dish was washed with D-PBS once. The coated dish was left open in the biosafety cabinet to dry. The coated dishes were afterwards either directly used or stored at 4°C.

Immunofluorescence

Immunofluorescence (IF) was performed to label proteins with specific primary antibodies against the protein and secondary antibodies against the primary antibodies, marked with a fluorophore. Prior to the staining, the cells were fixed for 10 min at 37°C with 4% (m/v) paraformaldehyde (PFA; Science Services) in D-PBS. In the following, the IF staining was performed at room temperature, and between each of the following steps, the samples were washed 3 times with D-PBS. The fixed cells were permeabilized with a 0.1% (v/v) solution of Triton X-100 (Sigma-Aldrich) in D-PBS for 20 min and blocked with a 3% (m/v) solution of bovine serum albumin (BSA; Sigma Aldrich) in D-PBS for 1 h to prevent unspecific antibody binding. Afterwards, the sample was incubated with an appropriate dilution of the primary antibody (see Materials for specifications) for 1 h and subsequently with a secondary antibody (here, either Alexa 488 or Alexa 647 labelled goat anti-mouse antibodies (ThermoFisher)) dilution in D-PBS (see Materials for specifications). After final washes, the sample was imaged using the indicated imaging modality.

Hoechst 33342 labelling

Nuclear counterstaining for fluorescence microscopy was performed with Hoechst 33342 (ThermoFisher). The dye was dissolved in DMSO to 10 mg/ml according to the manufacturer's instruction. Staining of fixed cells in D-PBS was performed for 10 minutes at 2 µg/

ml according to the manufacturer's instructions. Afterwards, the cells were washed three times in D-PBS before imaging.

SNAP-Cell-SiR labelling

SNAP-Cell-SiR (NEB) labelling was performed according to the manufacturer's instructions. In brief, the live cells were incubated with a 1:200 dilution of the dye solution in appropriate growth medium for 30 minutes, washed 3 times, and incubated in fresh medium for 30 minutes before a final replacement with fresh medium. All incubations were carried out under cell culture conditions.

Spinning-disk fluorescence microscopy

Spinning-disk fluorescence microscopy was performed on a Nikon TI2 (Nikon) microscope equipped with a Yokogawa W2 spinning-disk unit (Yokogawa), an Andor iXON888 electron-multiplying charge-coupled device (EMCCD) camera (Andor Technology) and a 1.49 numerical aperture (NA) Apo- TIRF objective (Nikon). The pixel size resulting from the setup was 130 nm. The setup also included laser lines with 405 nm, 488 nm, 561 nm and 640 nm wavelengths and appropriate filter sets. Microscope control and image acquisition were done using NIS-Elements (Nikon). Imaging conditions were optimized for each sample. For live-cell experiments, environmental control (37°C, 5% CO_2) was achieved with a heated, humidified incubation chamber and a gas mixer (Okolab).

Confocal-laser-scanning fluorescence microscopy

Confocal-laser-scanning fluorescence microscopy was done with a Nikon TI2 microscope, equipped with a 1.4 NA 60x Plan Apo objective and an A1 confocal-laser-scanning unit (Nikon), including photomultiplier tube (PMT) and gallium-arsenide-phosphide (GaAsP) detectors and 404 nm, 489 nm, 561 nm and 637 nm laser lines and filters. Imaging conditions were optimized for each sample with the microscope control and acquisition software NIS-Elements, including the pixel size, which was adapted to fulfill the Nyquist-criterion for sampling (331).

Lattice-light-sheet fluorescence microscopy

Lattice-light-sheet fluorescence microscopy was performed on a Zeiss lattice-light-sheet 7 (Zeiss), controlled by the software Zen Blue (Zeiss). The microscope was equipped with a pco.edge scientific complementary metal-oxide-semiconductor (sCMOS) camera (PCO), 488 nm, 561 nm and 640 nm laser lines, filters and an environmentally controlled (37°C, 5% CO_2, humidified) incubation chamber for live-cell imaging. The optical setup resulted in a final pixel size of 145 nm. The acquired 4D datasets were deconvolved (constrained-iterative mode) and transformed as indicated for the experiments, using the algorithms provided by Zen Blue.

Total-internal-reflection-fluorescence microscopy

Live-cell TIRF microscopy was performed using a Nikon TI microscope equipped for TIRF microscopy, including 488 nm, 561nm and 640 nm laser lines, corresponding filter sets, an Andor iXon Ultra 897 EMCCD camera and an environmentally controlled (37°C) incu-

bation chamber. Microscope control and image acquisition were performed with NIS-Elements.

8.3 Electron microscopy methods

General

For electron microscopic investigations of adherent cells, except for Tokuyasu immunolabeling, cells were grown in Ibidi microscopy polymer bottom dishes, with a grid on the coverslip (Ibidi). The water used in all protocols here was always distilled, CO_2-free H_2O unless otherwise indicated.

Preparation of lead aspartate solution according to Walton (332)

1N KOH was prepared by dissolving 5.6 g solid KOH (Merck) in 100 ml H_2O. The L-aspartic acid stock was prepared by dissolving 0-998 g L-Aspartate (Roth) in 250 ml H_2O and raising the pH to 3.8 by adding 1N KOH solution. The L-aspartate stock solution was stored at 4°C. Waltons lead aspartate solution was always freshly prepared by adding 0.066 g $Pb(NO_3)_2$ (Roth) to 10 ml of L-aspartate stock solution and raising the pH to 5.5 by adding 1N KOH. The solution was incubated at 60°C for 1 h and only used if no precipitate had formed.

Preparation of Epon embedding medium according to Luft (333)

Epon embedding medium was prepared by mixing two separate monomer mixtures and a polymerization accelerator. The first monomer mixture, Epon I, was prepared by mixing of 44% (m/m) glycid ether 100 (Roth) and 56% (m/m) DDSA (Roth), and for the second, Epon II, 53.6 % (m/m) glycid ether 100 was mixed with 46.4 % (m/m) of MNA (Roth). The final Epon embedding medium was prepared by mixing 27.4% (m/m) Epon I, 71.3% (m/m) Epon II and 1.3% (m/m) DMP-30 accelerator.

Preparation of saturated solutions of uranyl acetate (UA)

Saturated UA solutions were produced by adding UA (Merck) in excess to the indicated solvent, followed by sonification for 15 minutes, with thorough vortexing every 5 minutes in-between. Residual solid UA was pelleted by centrifugation at 13,000g for 15 minutes, and the clear supernatant was transferred to a fresh 1.5 ml safe-lock reaction tube.

SBF-SEM staining and sample processing

A special contrasting protocol was employed to stain samples for SBF-SEM. The cells were fixed with a mix of 2% (m/v) PFA and 2.5% (m/v) glutaraldehyde (GA; Science Services) in D-PBS for 5 minutes at RT and 55 minutes on ice. For CLEM samples, fluorescence microscopy was performed as indicated after this initial fixation. After washing the samples 5x with ice-cold D-PBS, the cells were post-fixed by 1:1 mixing of ice-cold 4% (m/v) OsO_4 (Science Services)/D-PBS and 5% (m/v) GA/D-PBS solutions directly on the dish by careful agitation. Afterwards, the samples were stained at RT (unless otherwise indicated) with the steps outlined in the following, and after each step, the cells were washed 10x with H_2O. The sample was stained with 2% (m/v) OsO4/1.5% (m/v) $K_4Fe[CN]_6$

(Sigma-Aldrich)/ 2 mM $CaCl_2$ (Sigma-Aldrich) in H_2O for 1 h, with 0.5% (m/v) thiocarbohydrazide (Sigma-Aldrich) in H_2O for 30 min, followed by 2% (m/v) OsO_4 in H_2O for 20 min, 1% (m/v) gallic acid (Sigma-Aldrich) in H_2O for 10 min and 2% (m/v) uranyl acetate (Merck) in H_2O at 4°C overnight. On the next day, the sample was stained with Waltons lead aspartate (see above) solution for 30 minutes at 60°C.

After the staining, the sample was dehydrated using a progressive lowering of temperature dehydration process (PLT). For this, the sample was incubated in a series of ethanol-water mixtures with increasing ethanol content while lowering the temperature at each step. The process started by cooling the sample to 0°C in 30% (v/v) ethanol (Roth), holding the temperature for 30 min, followed by 50% (v/v) ethanol at -20°C for 30 min, 70% (v/v) ethanol at -35°C for 30 min and 2 rounds of 100% ethanol at -35°C for 20 minutes each. Afterwards, the sample was allowed to warm to room temperature and incubated with a mixture of 70% (v/v) freshly prepared Epon embedding medium (see above) in ethanol for 1 h at RT, followed by incubation in 100% Epon overnight. Lastly, the sample was incubated for 6 h in a conductive embedding medium consisting of 3% (m/m) Ketjen Black (TAAB) and 3% (m/m) silver flakes in Epon at RT before transferring the sample to 60°C for polymerization for 3 days.

The region of interest (ROI) was cut out of the dish with cutting pliers and mounted coverslip facing upwards on a solid Epoxy block using 2 component glue (UHU Plus Endfest 300, UHU). The sample was manually roughly trimmed to a 1.5 mm x 1.5 mm flat-top pyramid using a razor blade. Subsequently, the polymer coverslip was trimmed off using a diamond trimming knife (Diatome) and a Leica Ultracut microtome (Leica) until approximately 175 of 180 µm were removed. Then the pyramid was trimmed to its final block face size of 0.5 mm x 0.5 mm and removed from the mounting block with a total height of ca. 3 mm using a razor blade. Finally, the sample block was mounted on a Gatan 3view sample stub (Micro to Nano) using a conductive silver epoxy glue (Chemtronics) and sputter coated with a 10 nm gold layer.

TEM staining and sample processing

To prepare samples for TEM, cells were initially fixed with 4% (m/v) PFA/D-PBS at cell culture conditions for 10 minutes. In CLEM experiments, fluorescence microscopy was performed after this step in D-PBS. Afterwards, the cells were fixed again with 2.5% (m/v) GA/D-PBS overnight at 4°C. On the next day, the samples were washed with cold D-PBS, and the following staining protocol was executed on ice. Unless otherwise indicated, the cells were washed 2 times with H_2O after each of the following steps. First the cells were incubated in 1% (m/v) OsO_4/D-PBS for 30 min and subsequently in 2% (m/v) UA/H_2O for 30 min.

Afterwards, the cells were dehydrated on ice by incubation in a series of increasing ethanol concentrations in water (30% (v/v), 50% (v/v), 70% (v/v) and 3x 100% Ethanol) each for 10 minutes. Subsequently, the sample was infiltrated with embedding Medium at RT, first by incubation in a 50% (v/v) dilution of Epon in Ethanol for 30 min, followed by 70% (v/v) Epon/Ethanol for 1 h 30 min and finally 100%Epon overnight on a shaker. Over the next 2 days, the sample was incubated shaking while replacing the Epon in the morning and evening with fresh Epon, prepared each day. At the end of the second day,

the sample was put at 60°C for two days for polymerization.

The region of interest was removed from the dish with cutting pliers and mounted coverslip facing upwards on an empty Epoxy block as described for the SBF-SEM protocol. Trimming of the ROI was performed as described above for SBF-SEM. After removal of the coverslip and final trimming, however, ultra-thin sectioning was performed with a diamond knife and a Leica Ultracut microtome to generate 50 nm sections. These sections were transferred to 200 mesh copper grids (Science-Services). Afterwards, the sections were post-stained by placing the grids face-down on droplets of a saturated solution of UA in 70% (v/v) Ethanol/H_2O for 7 minutes at RT, followed by thorough washing in a running stream of H_2O and drying on a filter paper (Whatman).

Tokuyasu immunolabelling

For immunogold labelling for TEM, a protocol was used derived from the methods developed by Tokuyasu (288). For this experiment, a 10 cm dish of HFF cells was grown to 80-90% confluency before infection with HCMV-TB40-WT at an MOI of 0.5. The cells were fixed 4 dpi with 2% (m/v) PFA and 0.5% (m/v) GA in D-PBS for 10 minutes at cell culture conditions. After a wash with D-PBS, the cells were scraped in a 1% (m/v) solution of food grade Gelatin (Dr. Oetker) and pelleted by centrifugation at 800 g for 10 min. Subsequently, the pellet was resuspended in a 40°C 10% (m/v) gelatin solution and pelleted at the same conditions at RT, letting the gelatin solidify in the process. The gelatin containing the cell pellet was removed from its container and cut into 3 mm pieces using a scalpel. The pieces were immersed in a 2.3 M sucrose in D-PBS solution and incubated overnight at 4°C. Afterwards, the pieces were mounted on sample holders and flash-frozen by immersion in liquid nitrogen. Subsequently, the samples were trimmed and cut into 70 nm thin sections using a Leica EM FC7 cryo microtome (Leica), equipped with diamond knives (Diatome). The sections were transferred with a Perfect Loop (Diatome) and a droplet of 2.3 M sucrose to Formvar and carbon-coated Nickel TEM grids at RT (gift from Rudolph Reimer).

The following protocol for immunolabeling was carried out at RT unless otherwise specified. Incubations were performed by placing the grids, sections facing downwards, on droplets of the respective solution for the indicated time. Firstly, the embedding gelatin was removed by incubation with 40°C D-PBS for 2x 20 minutes. Then, three washes were performed in D-PBS, followed by 3x incubation with 0.1% (m/v) Glycin in D-PBS for 2 min each, blocking with donkey serum (Aurion) for 3 min, incubating with the indicated primary antibody diluted in donkey serum (See Material for specifications) for 30 min. After 5 washes in D-PBS, the sample was incubated with a secondary 10 nm gold coupled donkey-anti-mouse antibody (Aurion) diluted 1:20 in donkey serum for 1 h. After 5 more washes in D-PBS, a final fixation with 1% (m/v) GA in D-PBS was carried out for 5 minutes. 5 final washes in H_2O were performed before the samples were contrasted with a saturated solution of UA in H_2O for 5 min on ice. Final contrasting and embedding were performed by 10 minutes of incubation on a 1:1 mixture of saturated UA in H_2O and 2% (m/v) methylcellulose in H_2O on ice, followed by removal of the grids from the droplet using a wire loop, blotting off excess liquid using Whatman filter paper and letting the grids air-dry for at least 10 min.

Serial-block-face scanning electron microscopy (SBF-SEM)

Serial-block-face scanning electron microscopy was performed using a Jeol JSM-7100F scanning electron microscope (Jeol) equipped with a Gatan 3view stage (Gatan). Imaging was performed with a beam acceleration voltage of 3 kV, the probe current set to 1 and a 500 V positive charge applied to the sample holder. ROIs were defined manually, and the pixel size was set to 3 nm. To generate 3D datasets, repeated ablation of 50 nm sections was performed using the built-in diamond knife microtome of the 3view stage while acquiring an image after each cut. The microscope, stage and acquisition were controlled using the Digital Micrograph software from Gatan, which was also used for the initial 2 x 2 binning and alignment of the acquired stacks.

Transmission electron microscopy (TEM)

Transmission electron microscopy was performed on an FEI Tecnai G20 (FEI/ThermoFisher) transmission electron microscope, equipped with an Olympus Veleta side-mounted camera (Olympus). The microscope was operated at 80 kV.

8.4 Microbiological and biochemical methods

General

All liquid handling and other work were performed with scientific grade equipment and culture vessels as well as scientific grade pipetting devices, micropipettes and accessory equipment. Consumables, such as plates, reaction tubes, vials and pipette tips, were bought from Sarstedt unless otherwise indicated. All water used was filtered and demineralized H_2O unless otherwise indicated.

Polymerase chain reaction (PCR)

PCR was performed using either Taq-polymerase or Phusion-polymerase kits, with the enzymes, dNTPs and reaction buffers acquired from NEB. The water used in this process was pharmaceutical grade aqua ad injectabilia (Braun). The reaction mixtures were prepared according to the manufacturer's instructions for the respective polymerase, and the reaction was performed in a thermocycler (VWR) accordingly. The reaction products were purified using a QIAquick PCR purification kit (Qiagen) according to the manufacturer's instructions, followed by separation by agarose gel electrophoresis to assess the reaction product and confirm the successful amplification of the desired DNA fragment.

Agarose gel electrophoresis

For agarose gel electrophoresis, 1% (m/v) agarose gels in TAE buffer were prepared by dissolving appropriate amounts of agarose (Roth) in 1x TAE buffer, prepared by dilution of 50x Rotiphorese TAE buffer (Roth) with H_2O. The mixture was microwaved using a standard microwave at 600 W until the agarose had fully dissolved. SYBR Safe DNA gel stain (ThermoFisher) was added to the hot solution in appropriate amounts according to the manufacturer's instructions. The solution was subsequently poured into a gel chamber (VRW) with an appropriate comb and let to cool and solidify. The gel was placed into an electrophoresis chamber (VWR) and submerged in 1x TAE buffer. Appropriate amounts

of 6x DNA gel loading dye (NEB) were added to the sample before 5-10 µl were pipetted into the sample pockets in the gel. 5 µl NEB 1kb plus quick loading DNA ladder (NEB) were added to the sample pocket in the first lane. Gel electrophoresis was executed at 130 V for 45 min. After separation, the DNA bands on the gel were observed using a blue light transilluminator (analytik Jena).

Bacterial culture

Escherichia coli variants were grown on agar plates prepared from Agar-Agar (Roth) and terrific broth medium (TB; Roth) or in liquid TB, according to the manufacturer's instructions, complemented, when necessary, with an appropriate antibiotic for selection. For long-term storage, 5 ml overnight cultures were grown from single *E.coli* colonies in an incubation shaker at 37°C (30°C for *E. coli* strain GS1783). 1 ml of the culture was mixed with a 1:1 mixture of glycerol (Roth) and TB and frozen at -80°C.

Preparation of plasmid DNA (miniprep)

Plasmid DNA was amplified by inoculation of 5 ml of TB supplemented with appropriate selection antibiotics with a single colony of *E. coli*, maintaining the desired plasmid and overnight growth at 37°C in an incubation shaker. Plasmid DNA was extracted with a QIAprep Spin miniprep kit (Qiagen) following the manufacturer's instructions. The concentrations of the extracted DNA were measured using a NanoDrop spectrophotometer (ThermoFisher).

Preparation of BAC DNA

BAC DNA was prepared by inoculating 100 ml TB with a single colony of *E. coli* maintaining the desired BAC and overnight growth at 30°C in an incubation shaker. BAC DNA was extracted using a NucleoBond Xtra Midi kit (Macherey-Nagel) according to the manufacturer's instructions, with the exception that all vortexing steps were replaced with mixing by carefully inverting the tube to avoid shearing of the BAC DNA. After Ethanol precipitation, the BAC DNA was dissolved in aqua ad injectabilia, and DNA concentrations were measured with a NanoDrop spectrophotometer.

Preparation of electro- and Red recombination competent *E. coli*

Electro- and Red-recombination competent *E. coli* strain GS1783 maintaining HCMV BACs were prepared for *en-passant* Red recombination (261) according to the following protocol. 5 ml overnight cultures were grown in an incubation shaker at 30°C in TB from single picked colonies and used to inoculate 200 ml of LB medium. Subsequently, the large volume culture was grown at 30°C while constantly shaking until an OD600 of 0.5 to 0.6 was reached. Then the culture was incubated at 42°C for 15 minutes in a shaking water bath to induce the expression of the Red-recombination enzymes. Subsequently, the culture was cooled by submersion of the culture vessel in ice for 20 minutes. The bacteria were subsequently pelleted by centrifugation at 5000 g and 4°C and washed two times by resuspension in 100 ml sterile ice-cold H_2O, followed by pelleting the bacteria after each wash. Finally, the bacteria were washed by resuspension in ice-cold 10% (v/v) glycerol/water, pelleted again and resuspended in 1 ml of ice-cold 10% (v/v) glycerol/

water. 100 µl aliquots were made of the suspension, flash-frozen in liquid nitrogen and subsequently stored at -80°C.

BAC cloning by Red recombination

BAC-mutagenesis of HCMV genomes by *en-passant* Red-recombination was performed as previously described (261). A linear PCR product with homologous overhangs to the target region, containing mScarlet-I (285), interrupted by an I-SceI-aphAI-cassette, a kanamycin resistance and an internal homology site was amplified by PCR with the Phusion polymerase and the UL100-mScarlet-I forward (For) and reverse (Rev) primers (see Materials) from the shuttle plasmid pexA257 mScarlet-I KanR BAC cassette (see Materials). The PCR product was electroporated with a Gene Pulser XCell (BioRad) into electro- and red-recombination competent *E. coli*, maintaining the target HCMV genome as a BAC, prepared as described above. Electroporation settings were set as follows: 2500 V, 25 µF and 100 Ω. The bacteria were recovered in 0.5 ml of 30°C TB and incubated shaking for 1 h at 30°C. Subsequently, the bacteria were plated on TB agar containing chloramphenicol and kanamycin to select for successful insertion of the mScarlet-I cassette. Bacteria were grown for 2 days at 30°C. Successful insertion was tested by PCR with the Taq polymerase, UL100 control (ctr) (see Materials) primers and using a minimal amount of bacteria from each colony as the template (colony PCR). Two positive colonies were selected, and overnight cultures were grown in 2 ml TB with chloramphenicol at 30°C. 2% (m/v) arabinose TB medium was prepared through dilution of an appropriate amount of sterile-filtered 25% (m/v) L-arabinose/H_2O stock solution in TB. 2 ml of 2% (m/v) arabinose TB medium with chloramphenicol were added to the culture for a total L-arabinose concentration of 1% (m/v). The culture was subsequently incubated shaking at 30°C for 1h. Afterwards, the bacteria were incubated at 42°C in a shaking water bath for 30 min, followed by incubation shaking at 30°C until the culture reached an OD600 of ca 1.0. Then, 100 µl of the culture was plated on TB-agar containing chloramphenicol and incubated for 2 days at 30°C. Colonies were tested for successful recombination by patching colonies on TB-agar with kanamycin for 2 days at 30°C and performing colony PCR of kanamycin-sensitive colonies. Two successfully recombined clones were selected for the preparation of BAC-DNA, and glycerol stocks were prepared as described above.

After the preparation of BAC DNA, the mutated region of the genome was amplified using the Phusion polymerase and the UL100 control primers (see Materials), and the PCR product was analyzed by sequencing (Eurofins). Furthermore, the integrity of the BAC was probed by digestion of the mutated and the parental BAC with Xho-I (NEB) according to the manufacturer's instructions, followed by gel electrophoresis of both products and comparison of the bands.

Gateway cloning

Gateway cloning was performed using Gateway BP II, LR II and LR II plus clonases according to the manufacturer's instructions. Genes of interest were amplified with appropriate overhangs in the primers (see Material) by PCR with the Phusion polymerase prior to use for Gateway cloning. Products of the cloning reactions were transformed into NEB 5-alpha (pENTR plasmids) or NEB stable (pLenti plasmids) chemically competent E. coli by heat shock according to the manufacturer's instructions (NEB). Plasmids were isolated by miniprep and analyzed for successful cloning by sequencing. Glycerol stocks of *E. coli* maintaining the new plasmids were prepared and stored at -80°C

Western blotting (WB)

Cell lysates for western blot were prepared by scraping in D-PBS and pelleting the cells of a 6-well dish at 800g for 10 minutes. After removal of the supernatant, the pellet was resuspended in 25 µl D-PBS. For lysis, 5 µl of SDS 6x loading dye (300 mM Tris (pH 6.8), 4.2% (v/v) 2-mercaptoethanol, 12% (m/v) SDS, 60% (v/v) glycerol and 0.02% (m/v) bromophenol blue in H_2O) were added to the cell suspension and the mixture was heated to 95°C for 10 minutes. Subsequently, 10 µl of the lysate, as well as a protein ladder as a reference, were separated on a 4–15% Mini-PROTEAN® TGX™ Precast protein gel (BioRad) in a Mini-PROTEAN Tetra cell gel electrophoresis chamber (BioRad). Electrophoresis was performed ad 130 V for 1 h in SDS running buffer (25 mM Tris (pH 8.3), 192 mM glycine, 3.45 mM SDS in H_2O). Afterwards, the protein was blotted on Amersham Protran 0.45 µm nitrocellulose membranes (Cytiva) for 1 h at 100 V in ice-cold transfer buffer (25 mM Tris (pH 8.3), 192 mM Glycine, 20% (v/v) Ethanol in H_2O). The membrane with the proteins was subsequently blocked for 1h in 5% (m/v) milk powder in PBS-T (0.1% (v/v) Tween 20 in D-PBS) before cutting the membrane with a scalpel into sections, in which the different proteins of interest are expected to band according to their size. Subsequently, the membrane sections were stained against the respective protein of interest using a primary antibody for 3 days at 4°C in an appropriate dilution in PBS-T (see Materials), followed by 4 washes for 5 minutes in PBS-T and a secondary StarBright 700 anti-mouse antibody (see Materials) staining for 1 h. The secondary antibody step was omitted if the primary antibody was directly conjugated to a fluorophore. After 4 final washes in PBS-T for 5 minutes, the membranes were imaged using a ChemiDoc MP imager (BioRad).

8.5 Computational methods

Image processing and analysis

Image analysis, cropping, format conversion, montages, fluorescence multi-channel merges, fluorescence measurements for line profiles and measurements over time, as well as cell counting, were performed in Fiji/ImageJ (330). Transformation and deconvolution of 4-dimensional Lattice-Light-Sheet data were performed in Zen-Blue (Zeiss). The alignment and binning of 3-dimensional SBF-SEM data were performed in Digital Micrograph (Gatan).

Denoising

Denoising of videos was performed using a customized Jupyter notebook for batch denoising of stacks (Code 1) adapted from the original Jupyter notebook for 2D denoising using Noise2Void (279).

Single particle tracking

Single particle tracking was performed in Fiji with the plugin Trackmate (280). Tracking settings were optimized for each batch of data.

Track segmentation

Track segmentation was performed using the custom tool TrISS (Code 2). Briefly, TrISS uses the tracking data from Trackmate and initially performs segmentation of the track according to two properties. At first, the movement mode of the particle is analyzed by performing a mean squared displacement (MSD) analysis, using the msdanalyzer class (281) in a rolling window manner along the whole track with a customizable window size. The track is then separated into segments of active transport, free diffusion and restricted diffusion according to the alpha value from the MSD analysis. An alpha value below 0.8 was classified as restricted diffusion, between 0.8 and 1.2, particles were assumed to diffuse freely, and above 1.2 the program detected active transport. Secondly, the fluorescence signal in the channel, which is not used for tracking, is measured at each time point and compared against the local background. The program segments the tracks into subsections where the fluorescence is above the local background or on/below the local background. The measurement radius for the local background as well as the threshold is customizable. All these segments are stored in an SQLite event database. In the next step, the user can define correlative events where two of the aforementioned segment types coincide. For example, a “co-transport” property can be defined in which a particle is actively transported, and at the same time, the fluorescence in the second channel is above the background. TrISS then searches the event database for tracks which fulfill the defined criterion at any time during the track and saves the correlative event for that track in the same database with start- and end time-point. Minimum lengths for the correlative events can be customized. Later, the database can be filtered to find all tracks with a single or a combination of properties of interest. Tracks which fulfill the desired criteria can be plotted in a tiff file using the TrackVisualizer.m script, which can be overlaid with the original video for visualization. Tabular “roadmaps” are saved for all tracks of a video,

which fulfill the criteria the user searched for and allow the investigation of all events and segmentation properties saved for that track.

Spatial colocalization analysis

Spatial colocalization heatmaps were generated using the custom spatial colocalization analysis Jupyter notebook (Code 3), using the Anaconda 3 python distribution. For this, the fluorescence images of two channels were normalized, and each pixel is represented by a position vector (see formula 5) pointing to the position of each pixel if they were placed in a scatter plot with the x-axis being the intensity in channel 1 and the y- axis being the intensity in channel two. Subsequently, the length of the vector was multiplied by 1-|sin(α)-cos(α)| where α is the angle between the pixel vector and the x-axis. By this multiplication, pixels are emphasized that have similar relative intensities in both channels, while values for pixels with strong relative intensities in only one of the channels are reduced. The resulting value is then plotted back to its position in the original image, and a heatmap is generated using the cubehelix colormap from the matplotlib python library.

$$\overrightarrow{pixel} = \frac{Int_{Ch1}}{Int_{Ch2}}$$

Formula 5: Position vector describing each pixel in a two-channel image with normalized intensities.

Statistical analysis and graphing

Statistical analysis and graphing of data were performed in GraphPad Prism 9 (Dotmatics).

CLEM image processing

CLEM overlays from fluorescence and EM images were created in Adobe Photoshop (Adobe) or Affinity Photo (Serif).

9 References

1. Jesionek A, Kiolemenoglou. B. Ueber einen Befund von protozoenartigen Gebilden in den Organen eines hereditar-luetischen Foetus. Munch Med Wochenschr. 1904;51(51):1905–7.

2. Vonglahn WC, Pappenheimer AM. Intranuclear Inclusions in Visceral Disease. Am J Pathology. 1925;1(5):445-466.3.

3. Farber S, Wolbach SB. Intranuclear and Cytoplasmic Inclusions ("Protozoan-Like Bodies") in the Salivary Glands and Other Organs of Infants. Am J Pathology. 1932;8(2):123-136.3.

4. Wyatt JP, Saxton J, Lee RS, Pinkerton H. Generalized cytomegalic inclusion disease. J Pediatrics. 1950;36(3):271–94.

5. MINDER WH. Die Ätiologie der Cytomegalia infantium. Schweiz Med Wschr. 1953;83(49):1180–2.

6. Smith MG. Propagation in Tissue Cultures of a Cytopathogenic Virus from Human Salivary Gland Virus (SGV) Disease. P Soc Exp Biol Med. 1956;92(2):424–30.

7. Rowe WP, Hartley JW, Waterman S, Turner HC, Huebner RJ. Cytopathogenic Agent Resembling Human Salivary Gland Virus Recovered from Tissue Cultures of Human Adenoids. P Soc Exp Biol Med. 1956;92(2):418–24.

8. Weller TH, MacAuley JC, Craig JM, Wirth P. Isolation of Intranuclear Inclusion Producing Agents from Infants with Illnesses Resembling Cytomegalic Inclusion Disease.†. P Soc Exp Biol Med. 1957;94(1):4–12.

9. Weller TH, Hanshaw JB, Scott DE. Serologic differentiation of viruses responsible for cytomegalic inclusion disease. Virology. 1960;12(1):130–2.

10. Cannon MJ, Schmid DS, Hyde TB. Review of cytomegalovirus seroprevalence and demographic characteristics associated with infection. Rev Med Virol. 2010;20(4):202–13.

11. Davison AJ. Herpesvirus systematics. Vet Microbiol. 2010;143(1–2):52–69.

12. Cannon MJ, Hyde TB, Schmid DS. Review of cytomegalovirus shedding in bodily fluids and relevance to congenital cytomegalovirus infection. Rev Med Virol. 2011;21(4):240–55.

13. Hyde TB, Schmid DS, Cannon MJ. Cytomegalovirus seroconversion rates and risk factors: implications for congenital CMV: CMV seroconversion. Rev Med Virol. 2010;20(5):311–26.

14. Jarvis MA, Nelson JA. Human Herpesviruses. 2007;765–79.

15. Reeves M, Sinclair J. Aspects of human cytomegalovirus latency and reactivation. Curr Top Microbiol. 2008;325:297–313.

16. Klemola E, Essen R von, Henle G, Henle W. Infectious-mononucleosis-like Disease with Negative Heterophil Agglutination Test. Clinical Features in Relation to Epstein-Barr Virus and Cytomegalovirus Antibodies. J Infect Dis. 1970;121(6):608–14.

17. Eddleston M, Peacock S, Juniper M, Warrell DA. Severe Cytomegalovirus Infection in Immunocompetent Patients. Clin Infect Dis. 1997;24(1):52–6.

18. Sissons JGP, Carmichael AJ. Clinical Aspects and Management of Cytomegalovirus Infection. J Infection. 2002;44(2):78–83.

19. Gandhi MK, Wills MR, Sissons JGP, Carmichael AJ. Human cytomegalovirus-specific immunity following haemopoietic stem cell transplantation. Blood Rev. 2003;17(4):259–64.

20. Lunardi C, Dolcino M, Peterlana D, Bason C, Navone R, Tamassia N, et al. Antibodies against Human Cytomegalovirus in the Pathogenesis of Systemic Sclerosis: A Gene Array Approach. Plos Med. 2006;3(1):e2.

21. Potena L, Valantine HA. Cytomegalovirus-associated allograft rejection in heart transplant patients. Curr Opin Infect Dis. 2007;20(4):425–31.

22. Simanek AM, Dowd JB, Pawelec G, Melzer D, Dutta A, Aiello AE. Seropositivity to Cytomegalovirus, Inflammation, All-Cause and Cardiovascular Disease-Related Mortality in the United States. Plos One. 2011;6(2):e16103.

23. Rosenfeld ME, Campbell LA. Pathogens and atherosclerosis: Update on the potential contribution of multiple infectious organisms to the pathogenesis of atherosclerosis. Thromb Haemostasis. 2011;106(05):858–67.

24. Pawelec G, Derhovanessian E, Larbi A, Strindhall J, Wikby A. Cytomegalovirus and human immunosenescence. Rev Med Virol. 2009;19(1):47–56.

25. Wang GC, Kao WHL, Murakami P, Xue QL, Chiou RB, Detrick B, et al. Cytomegalovirus Infection and the Risk of Mortality and Frailty in Older Women: A Prospective Observational Cohort Study. Am J Epidemiol. 2010;171(10):1144–52.

26. Roberts ET, Haan MN, Dowd JB, Aiello AE. Cytomegalovirus Antibody Levels, Inflammation, and Mortality Among Elderly Latinos Over 9 Years of Follow-up. Am J Epidemiol. 2010;172(4):363–71.

27. Gandhi MK, Khanna R. Human cytomegalovirus: clinical aspects, immune regulation, and emerging treatments. Lancet Infect Dis. 2004;4(12):725–38.

28. Reynolds DW, Stagno S, Hosty TS, Tiller M, Alford CA. Maternal Cytomegalovirus Excretion and Perinatal Infection. New Engl J Medicine. 1973;289(1):1–5.

29. Pereira L, Maidji E. Cytomegalovirus infection in the human placenta: maternal immunity and developmentally regulated receptors on trophoblasts converge. Curr Top Microbiol. 2008;325:383–95.

30. Hamprecht K, Maschmann J, Jahn G, Poets CF, Goelz R. Cytomegalovirus transmission to preterm infants during lactation. J Clin Virol. 2008;41(3):198–205.

31. Pass RF, Anderson B. Mother-to-Child Transmission of Cytomegalovirus and Prevention of Congenital Infection. J Pediatric Infect Dis Soc. 2014;3(suppl_1):S2–6.

32. Liesnard C, Donner C, Brancart F, Gosselin F, Delforge ML, Rodesch F. Prenatal diagnosis of congenital cytomegalovirus infection: prospective study of 237 pregnancies at risk. Obstet Gynecol. 2000;95(6 Pt 1):881–8.

33. Boppana SB, Pass RF, Britt WJ, Stagno S, Alford CA. Symptomatic congenital cytomegalovirus infection: neonatal morbidity and mortality. Pediatric Infect Dis J. 1992;11(2):93–8.

34. Whitley RJ. Congenital cytomegalovirus infection: epidemiology and treatment. Adv Exp Med Biol. 2004;549:155–60.

35. Dollard SC, Grosse SD, Ross DS. New estimates of the prevalence of neurological and sensory sequelae and mortality associated with congenital cytomegalovirus infection. Rev Med Virol. 2007;17(5):355–63.

36. Griffiths P, Baraniak I, Reeves M. The pathogenesis of human cytomegalovirus. J Pathology. 2015;235(2):288–97.

37. Griffiths P, Reeves M. Pathogenesis of human cytomegalovirus in the immunocompromised host. Nat Rev Microbiol. 2021;19(12):759–73.

38. Kotton CN, Kumar D, Caliendo AM, Asberg A, Chou S, Danziger-Isakov L, et al. Updated International Consensus Guidelines on the Management of Cytomegalovirus in Solid-Organ Transplantation. Transplant J. 2013;96(4):333–60.

39. Kotton CN, Kumar D, Caliendo AM, Huprikar S, Chou S, Danziger-Isakov L, et al. The Third International Consensus Guidelines on the Management of Cytomegalovirus in Solid-organ Transplantation. Transplantation. 2018;102(6):900–31.

40. Humar A, Snydman D, Practice the AIDC of. Cytomegalovirus in Solid Organ Transplant Recipients. Am J Transplant. 2009;9:S78–86.

41. Jabs DA, Martin BK, Forman MS, Group CR and VRR. Mortality Associated with Resistant Cytomegalovirus among Patients with Cytomegalovirus Retinitis and AIDS. Ophthalmology. 2010;117(1):128-132.e2.

42. Ljungman P, Hakki M, Boeckh M. Cytomegalovirus in Hematopoietic Stem Cell Transplant Recipients. Hematology Oncol Clin North Am. 2011;25(1):151–69.

43. Ljungman P, Schmitt M, Marty FM, Maertens J, Chemaly RF, Kartsonis NA, et al. A Mortality Analysis of Letermovir Prophylaxis for Cytomegalovirus (CMV) in CMV-seropositive Recipients of Allogeneic Hematopoietic Cell Transplantation. Clin Infect Dis Official Publ Infect Dis Soc Am. 2020;70(8):1525–33.

44. Gibson W. Structure and formation of the cytomegalovirus virion. Curr Top Microbiol. 2008;325:187–204.

45. Grünewald K, Desai P, Winkler DC, Heymann JB, Belnap DM, Baumeister W, et al. Three-Dimensional Structure of Herpes Simplex Virus from Cryo-Electron Tomography. Science. 2003;302(5649):1396–8.

46. Yu X, Jih J, Jiang J, Zhou HZ. Atomic structure of the human cytomegalovirus capsid with its securing tegument layer of pp150. Science. 2017;356(6345):eaam6892.

47. Liu F, Zhou ZH. Human Herpesviruses. 2007;27–43.

48. Li Z, Pang J, Dong L, Yu X. Structural basis for genome packaging, retention, and ejection in human cytomegalovirus. Nat Commun. 2021;12(1):4538.

49. Heming JD, Conway JF, Homa FL. Cell Biology of Herpes Viruses. 2017;119–42.

50. Borst E, Bauerfeind R, Binz A, Stephan T, Neuber S, Wagner K, et al. The Essential Human Cytomegalovirus Proteins pUL77 and pUL93 Are Structural Components Necessary for Viral Genome Encapsidation. J Virol. 2016;90(13):5860–75.

51. Liu YT, Jih J, Dai X, Bi GQ, Zhou ZH. Cryo-EM structures of herpes simplex virus type 1 portal vertex and packaged genome. Nature. 2019;570(7760):257–61.

52. Dai X, Yu X, Gong H, Jiang X, Abenes G, Liu H, et al. The Smallest Capsid Protein Mediates Binding of the Essential Tegument Protein pp150 to Stabilize DNA-Containing Capsids in Human Cytomegalovirus. Plos Pathog. 2013;9(8):e1003525.

53. Bhella D, Rixon FJ, Dargan DJ. Cryomicroscopy of human cytomegalovirus virions reveals more densely packed genomic DNA than in herpes simplex virus type 1. J Mol Biol. 2000;295(2):155–61.

54. Bauer DW, Huffman JB, Homa FL, Evilevitch A. Herpes virus genome, the pressure is on. J Am Chem Soc. 2013;135(30):11216–21.

55. Varnum SM, Streblow DN, Monroe ME, Smith P, Auberry KJ, Paša-Tolić L, et al. Identification of Proteins in Human Cytomegalovirus (HCMV) Particles: the HCMV Proteome. J Virol. 2004;78(20):10960–6.

56. Terhune SS, Schröer J, Shenk T. RNAs are packaged into human cytomegalovirus virions in proportion to their intracellular concentration. J Virol. 2004;78(19):10390–8.

57. Kalejta RF. Tegument proteins of human cytomegalovirus. Microbiol Mol Biology Rev Mmbr. 2008;72(2):249–65

58. Heldwein EE. gH/gL supercomplexes at early stages of herpesvirus entry. Curr Opin Virol. 2016;18:1–8.

59. Nguyen CC, Kamil JP. Pathogen at the Gates: Human Cytomegalovirus Entry and Cell Tropism. Viruses. 2018;10(12):704.

60. Pino GLGD, Heldwein EE. Well Put Together—A Guide to Accessorizing with the Herpesvirus gH/gL Complexes. Viruses. 2022;14(2):296.

61. Kari B, Gehrz R. Structure, composition and heparin binding properties of a human cytomegalovirus glycoprotein complex designated gC-II. J Gen Virol. 1993;74(2):255–64.

62. Compton T, Nepomuceno RR, Nowlin DM. Human cytomegalovirus penetrates host cells by PH-independent fusion at the cell surface. Virology. 1992;191(1):387–95.

63. Mach M, Kropff B, Monte PD, Britt W. Complex formation by human cytomegalovirus glycoproteins M (gpUL100) and N (gpUL73). J Virol. 2000;74(24):11881–92.

64. Navarro D, Paz P, Tugizov S, Topp K, Vail JL, Pereira L. Glycoprotein B of Human Cytomegalovirus Promotes Virion Penetration into Cells, Transmission of Infection from Cell to Cell, and Fusion of Infected Cells. Virology. 1993;197(1):143–58.

65. Bold S, Ohlin M, Garten W, Radsak K. Structural Domains Involved in Human Cytomegalovirus Glycoprotein B-Mediated Cell-cell Fusion. J Gen Virol. 1996;77(9):2297–302.

66. Isaacson MK, Compton T. Human Cytomegalovirus Glycoprotein B Is Required for Virus Entry and Cell-to-Cell Spread but Not for Virion Attachment, Assembly, or Egress. J Virol. 2009;83(8):3891–903.

67. Gao JL, Murphy PM. Human cytomegalovirus open reading frame US28 encodes a functional beta chemokine receptor. J Biol Chem. 1994;269(46):28539–42.

68. Foglierini M, Marcandalli J, Perez L. HCMV Envelope Glycoprotein Diversity Demystified. Front Microbiol. 2019;10:1005.

69. Martí-Carreras J, Maes P. Human cytomegalovirus genomics and transcriptomics through the lens of next-generation sequencing: revision and future challenges. Virus Genes. 2019;55(2):138–64.

70. Vanarsdall AL, Ryckman BJ, Chase MC, Johnson DC. Human cytomegalovirus glycoproteins gB and gH/gL mediate epithelial cell-cell fusion when expressed either in cis or in trans. J Virol. 2008;82(23):11837–50.

71. Vanarsdall AL, Howard PW, Wisner TW, Johnson DC. Human Cytomegalovirus gH/gL Forms a Stable Complex with the Fusion Protein gB in Virions. Plos Pathog. 2016;12(4):e1005564.

72. Vollmer B, Pražák V, Vasishtan D, Jefferys EE, Hernandez-Duran A, Vallbracht M, et al. The prefusion structure of herpes simplex virus glycoprotein B. Sci Adv. 2020;6(39):eabc1726.

73. Liu Y, Heim KP, Che Y, Chi X, Qiu X, Han S, et al. Prefusion structure of human cytomegalovirus glycoprotein B and structural basis for membrane fusion. Sci Adv. 2021;7(10):eabf3178.

74. Si Z, Zhang J, Shivakoti S, Atanasov I, Tao CL, Hui WH, et al. Different functional states of fusion protein gB revealed on human cytomegalovirus by cryo electron tomography with Volta phase plate. Plos Pathog. 2018;14(12):e1007452.

75. Bodaghi B, Drunen MES van, Topilko A, Perret E, Vossen RC, Dam-Mieras MC van, et al. Entry of human cytomegalovirus into retinal pigment epithelial and endothelial cells by endocytosis. Invest Ophth Vis Sci. 1999;40(11):2598–607.

76. Ryckman BJ, Jarvis MA, Drummond DD, Nelson JA, Johnson DC. Human Cytomegalovirus Entry into Epithelial and Endothelial Cells Depends on Genes UL128 to UL150 and Occurs by Endocytosis and Low-pH Fusion. J Virol. 2006;80(2):710–22.

77. Isaacson MK, Juckem LK, Compton T. Human Cytomegalovirus. 2008;85–100.

78. Kalejta RF. Functions of human cytomegalovirus tegument proteins prior to immediate early gene expression. Curr Top Microbiol. 2008;325:101–15.

79. Ogawa-Goto K, Tanaka K, Gibson W, Moriishi E, Miura Y, Kurata T, et al. Microtubule network facilitates nuclear targeting of human cytomegalovirus capsid. J Virol. 2003;77(15):8541–7.

80. Mocarski ES. Human Herpesviruses. 2007;204–30.

81. Cohen T, Schwarz TM, Vigant F, Gardner TJ, Hernandez RE, Lee B, et al. The Microtubule Inhibitor Podofilox Inhibits an Early Entry Step of Human Cytomegalovirus. Viruses. 2016;8(10):295.

82. Döhner K, Cornelius A, Serrero MC, Sodeik B. The journey of herpesvirus capsids and genomes to the host cell nucleus. Curr Opin Virol. 2021;50:147–58.

83. Ojala PM, Sodeik B, Ebersold MW, Kutay U, Helenius A. Herpes Simplex Virus Type 1 Entry into Host Cells: Reconstitution of Capsid Binding and Uncoating at the Nuclear Pore Complex In Vitro. Mol Cell Biol. 2000;20(13):4922–31.

84. Newcomb WW, Booy FP, Brown JC. Uncoating the Herpes Simplex Virus Genome. J Mol Biol. 2007;370(4):633–42.

85. Murphy JC, Fischle W, Verdin E, Sinclair JH. Control of cytomegalovirus lytic gene expression by histone acetylation. Embo J. 2002;21(5):1112–20.

86. Groves IJ, Reeves MB, Sinclair JH. Lytic infection of permissive cells with human cytomegalovirus is regulated by an intrinsic 'pre-immediate-early' repression of viral gene expression mediated by histone post-translational modification. J Gen Virol. 2009;90(10):2364–74.

87. Reeves MB. Chromatin-mediated regulation of cytomegalovirus gene expression. Virus Res. 2011;157(2):134–43.

88. Ahn JH, Jang WJ, Hayward GS. The Human Cytomegalovirus IE2 and UL112-113 Proteins Accumulate in Viral DNA Replication Compartments That Initiate from the Periphery of Promyelocytic Leukemia Protein-Associated Nuclear Bodies (PODs or ND10). J Virol. 1999;73(12):10458–71.

89. Ahn JH, Hayward GS. Disruption of PML-Associated Nuclear Bodies by IE1 Correlates with Efficient Early Stages of Viral Gene Expression and DNA Replication in Human Cytomegalovirus Infection. Virology. 2000;274(1):39–55.

90. Maul GG. Initiation of cytomegalovirus infection at ND10. Curr Top Microbiol. 2008;325:117–32.

91. Schilling EM, Scherer M, Reuter N, Schweininger J, Muller YA, Stamminger T. The Human Cytomegalovirus IE1 Protein Antagonizes PML Nuclear Body-Mediated Intrinsic Immunity via the Inhibition of PML De Novo SUMOylation. J Virol. 2017;91(4).

92. Adler M, Tavalai N, Müller R, Stamminger T. Human cytomegalovirus immediate-early gene expression is restricted by the nuclear domain 10 component Sp100. J Gen Virol. 2011;92(7):1532–8.

93. Spector DH. Activation and Regulation of Human Cytomegalovirus Early Genes. Intervirology. 1996;39(5–6):361–77.

94. Dunn W, Chou C, Li H, Hai R, Patterson D, Stolc V, et al. Functional profiling of a human cytomegalovirus genome. Proc National Acad Sci. 2003;100(24):14223–8.

95. Yu D, Silva MC, Shenk T. Functional map of human cytomegalovirus AD169 defined by global mutational analysis. Proc National Acad Sci. 2003;100(21):12396–401.

96. Tomtishen JP. Human cytomegalovirus tegument proteins (pp65, pp71, pp150, pp28). Virol J. 2012;9(1):22.

97. Xu Y, Cei SA, Huete AR, Colletti KS, Pari GS. Human cytomegalovirus DNA replication requires transcriptional activation via an IE2- and UL84-responsive bidirectional promoter element within oriLyt. J Virol. 2004;78(21):11664–77.

98. Xu Y, Cei SA, Huete AR, Pari GS. Human cytomegalovirus UL84 insertion mutant defective for viral DNA synthesis and growth. J Virol. 2004;78(19):10360–9.

99. Colletti KS, Xu Y, Cei SA, Tarrant M, Pari GS. Human cytomegalovirus UL84 oligomerization and heterodimerization domains act as transdominant inhibitors of oriLyt-dependent DNA replication: evidence that IE2-UL84 and UL84-UL84 interactions are required for lytic DNA replication. J Virol. 2004;78(17):9203–14.

100. Colletti KS, Smallenburg KE, Xu Y, Pari GS. Human cytomegalovirus UL84 interacts with an RNA stem-loop sequence found within the RNA/DNA hybrid region of oriLyt. J Virol. 2007;81(13):7077–85.

101. Pari GS. Nuts and bolts of human cytomegalovirus lytic DNA replication. Curr Top Microbiol. 2008;325:153–66.

102. Pari GS, Anders DG. Eleven loci encoding trans-acting factors are required for transient complementation of human cytomegalovirus oriLyt-dependent DNA replication. J Virol. 1993;67(12):6979–88.

103. Sarisky RT, Hayward GS. Evidence that the UL84 gene product of human cytomegalovirus is essential for promoting oriLyt-dependent DNA replication and formation of replication compartments in cotransfection assays. J Virol. 1996;70(11):7398–413.

104. McVoy MA, Adler SP. Human cytomegalovirus DNA replicates after early circularization by concatemer formation, and inversion occurs within the concatemer. J Virol. 1994;68(2):1040–51.

105. Wood LJ, Baxter MK, Plafker SM, Gibson W. Human cytomegalovirus capsid assembly protein precursor (pUL80.5) interacts with itself and with the major capsid protein (pUL86) through two different domains. J Virol. 1997;71(1):179–90.

106. Brown JC, Newcomb WW. Herpesvirus capsid assembly: insights from structural analysis. Curr Opin Virol. 2011;1(2):142–9.

107. Cardone G, Heymann JB, Cheng N, Trus BL, Steven AC. Procapsid assembly, maturation, nuclear exit: dynamic steps in the production of infectious herpesvirions. Adv Exp Med Biol. 2012;726:423–39.

108. Bogner E, Radsak K, Stinski MF. The gene product of human cytomegalovirus open reading frame UL56 binds the pac motif and has specific nuclease activity. J Virol. 1998;72(3):2259–64.

109. Krosky PM, Underwood MR, Turk SR, Feng KWH, Jain RK, Ptak RG, et al. Resistance of Human Cytomegalovirus to Benzimidazole Ribonucleosides Maps to Two Open Reading Frames: UL89 and UL56. J Virol. 1998;72(6):4721–8.

110. Thoma C, Borst E, Messerle M, Rieger M, Hwang JS, Bogner E. Identification of the Interaction Domain of the Small Terminase Subunit pUL89 with the Large Subunit pUL56 of Human Cytomegalovirus †. Biochemistry-us. 2006;45(29):8855–63.

111. Thoma C, Bogner E. Short hairpin RNAs specific to human cytomegalovirus terminase subunit pUL89 prevent viral maturation. Antivir Ther. 2009;15(3):391–400.

112. Borst EM, Kleine-Albers J, Gabaev I, Babic M, Wagner K, Binz A, et al. The human cytomegalovirus UL51 protein is essential for viral genome cleavage-packaging and interacts with the terminase subunits pUL56 and pUL89. J Virol. 2012;87(3):1720–32.

113. Casjens SR. The DNA-packaging nanomotor of tailed bacteriophages. Nat Rev Microbiol. 2011;9(9):647–57.

114. Welch AR, Woods AS, McNally LM, Cotter RJ, Gibson W. A herpesvirus maturational proteinase, assemblin: identification of its gene, putative active site domain, and cleavage site. Proc National Acad Sci. 1991;88(23):10792–6.

115. Jones TR, Sun L, Bebernitz GA, Muzithras VP, Kim HJ, Johnston SH, et al. Proteolytic activity of human cytomegalovirus UL80 protease cleavage site mutants. J Virol. 1994;68(6):3742–52.

116. Chan CK, Brignole EJ, Gibson W. Cytomegalovirus Assemblin (pUL80a): Cleavage at Internal Site Not Essential for Virus Growth; Proteinase Absent from Virions. J Virol. 2002;76(17):8667–74.

117. Loveland AN, Nguyen NL, Brignole EJ, Gibson W. The Amino-Conserved Domain of Human Cytomegalovirus UL80a Proteins Is Required for Key Interactions during Early Stages of Capsid Formation and Virus Production. J Virol. 2007;81(2):620–8.

118. Wang JB, McVoy MA. A 128-Base-Pair Sequence Containing the pac1 and a Presumed Cryptic pac2 Sequence Includes cis Elements Sufficient To Mediate Efficient Genome Maturation of Human Cytomegalovirus. Journal of Virology. 2011;85(9):4432–9.

119. Gibson W, Roizman B. Proteins Specified by Herpes Simplex Virus VIII. Characterization and Composition of Multiple Capsid Forms of Subtypes 1 and 2. J Virol. 1972;10(5):1044–52.

120. Gibson W. Structural and nonstructural proteins of strain Colburn cytomegalovi. Virology. 1981;111(2):516–37.

121. DeRussy BM, Boland MT, Tandon R. Human Cytomegalovirus pUL93 Links Nucleocapsid Maturation and Nuclear Egress. J Virol. 2016;90(16):7109–17.

122. Yang K, Baines JD. Selection of HSV capsids for envelopment involves interaction between capsid surface components pUL31, pUL17, and pUL25. Proc National Acad Sci. 2011;108(34):14276–81.

123. Roller RJ, Baines JD. Herpesvirus Nuclear Egress. Adv Anat Embryology Cell Biology. 2017;223:143–69.

124. Hagen C, Dent KC, Zeev-Ben-Mordehai T, Grange M, Bosse JB, Whittle C, et al. Structural Basis of Vesicle Formation at the Inner Nuclear Membrane. Cell. 2015;163(7):1692–701.

125. Zeev-Ben-Mordehai T, Weberruß M, Lorenz M, Cheleski J, Hellberg T, Whittle C, et al. Crystal Structure of the Herpesvirus Nuclear Egress Complex Provides Insights into Inner Nuclear Membrane Remodeling. Cell Reports. 2015;13(12):2645–52.

126. Walzer SA, Egerer-Sieber C, Sticht H, Sevvana M, Hohl K, Milbradt J, et al. Crystal Structure of the Human Cytomegalovirus pUL50-pUL53 Core Nuclear Egress Complex Provides Insight into a Unique Assembly Scaffold for Virus-Host Protein Interactions* ♦. J Biol Chem. 2015;290(46):27452–8.

127. Marschall M, Häge S, Conrad M, Alkhashrom S, Kicuntod J, Schweininger J, et al. Nuclear Egress Complexes of HCMV and Other Herpesviruses: Solving the Puzzle of Sequence Coevolution, Conserved Structures and Subfamily-Spanning Binding Properties. Viruses. 2020;12(6):683.

128. Muller YA, Häge S, Alkhashrom S, Höllriegl T, Weigert S, Dolles S, et al. High-resolution crystal structures of two prototypical β- and γ-herpesviral nuclear egress complexes unravel the determinants of subfamily specificity. J Biol Chem. 2020;295(10):3189–201.

129. Lawrence RS, Durch JS, Stratton KR. Vaccines for the 21st Century: A Tool for Decisionmaking. Washington, DC: The National Academies Press. 2001;472 p.

130. Schleiss MR. Cytomegalovirus vaccine development. Curr Top Microbiol. 2008;325:361–82.

131. Helou GE, Razonable RR. Letermovir for the prevention of cytomegalovirus infection and disease in transplant recipients: an evidence-based review. Infect Drug Resist. 2019;12:1481–91.

132. Marty FM, Ljungman P, Chemaly RF, Maertens J, Dadwal SS, Duarte RF, et al. Letermovir Prophylaxis for Cytomegalovirus in Hematopoietic-Cell Transplantation. New Engl J Medicine. 2017;377(25):2433–44.

133. Styczyński J, Tridello G, Xhaard A, Medinger M, Mielke S, Taskinen M, et al. Use of letermovir in off-label indications: Infectious Diseases Working Party of European Society of Blood and Marrow Transplantation retrospective study. Bone Marrow Transpl. 2021;56(5):1171–9.

134. Chen H, Beardsley GP, Coen DM. Mechanism of ganciclovir-induced chain termination revealed by resistant viral polymerase mutants with reduced exonuclease activity. Proc National Acad Sci. 2014;111(49):17462–7.

135. Littler E, Stuart AD, Chee MS. Human cytomegalovirus UL97 open reading frame encodes a protein that phosphorylates the antiviral nucleoside analogue ganciclovir. Nature. 1992;358(6382):160–2.

136. Perera MR, Wills MR, Sinclair JH. HCMV Antivirals and Strategies to Target the Latent Reservoir. Viruses. 2021;13(5):817.

137. Chou S, Waldemer RH, Senters AE, Michels KS, Kemble GW, Miner RC, et al. Cytomegalovirus UL97 Phosphotransferase Mutations That Affect Susceptibility to Ganciclovir. J Infect Dis. 2002;185(2):162–9.

138. Chou S. Recombinant phenotyping of cytomegalovirus UL97 kinase sequence variants for ganciclovir resistance. Antimicrob Agents Ch. 2010;54(6):2371–8.

139. Hantz S, Garnier-Geoffroy F, Mazeron MC, Garrigue I, Merville P, Mengelle C, et al. Drug-resistant cytomegalovirus in transplant recipients: a French cohort study. J Antimicrob Chemoth. 2010;65(12):2628–40.

140. Fischer L, Imrich E, Sampaio KL, Hofmann J, Jahn G, Hamprecht K, et al. Identification of resistance-associated HCMV UL97- and UL54-mutations and a UL97-polymporphism with impact on phenotypic drug-resistance. Antivir Res. 2016;131:1–8.

141. Lischka P, Hewlett G, Wunberg T, Baumeister J, Paulsen D, Goldner T, et al. In vitro and in vivo activities of the novel anticytomegalovirus compound AIC246. Antimicrob Agents Ch. 2010;54(3):1290–7.

142. Goldner T, Hewlett G, Ettischer N, Ruebsamen-Schaeff H, Zimmermann H, Lischka P. The Novel Anticytomegalovirus Compound AIC246 (Letermovir) Inhibits Human Cytomegalovirus Replication through a Specific Antiviral Mechanism That Involves the Viral Terminase. J Virol. 2011;85(20):10884–93.

143. Razonable RR. Role of letermovir for prevention of cytomegalovirus infection after allogeneic haematopoietic stem cell transplantation. Curr Opin Infect Dis. 2018;31(4):286–91.

144. Drew WL, Miner RC, Marousek GI, Chou S. Maribavir sensitivity of cytomegalovirus isolates resistant to ganciclovir, cidofovir or foscarnet. J Clin Virol. 2006;37(2):124–7.

145. Biron KK, Harvey RJ, Chamberlain SC, Good SS, Smith AA, Davis MG, et al. Potent and Selective Inhibition of Human Cytomegalovirus Replication by 1263W94, a Benzimidazole l -Riboside with a Unique Mode of Action. Antimicrob Agents Ch. 2002;46(8):2365–72.

146. Krosky PM, Baek MC, Coen DM. The human cytomegalovirus UL97 protein kinase, an antiviral drug target, is required at the stage of nuclear egress. J Virol. 2003;77(2):905–14.

147. Ishida JH, Patel A, Mehta AK, Gatault P, McBride JM, Burgess T, et al. Phase 2 Randomized, Double-Blind, Placebo-Controlled Trial of RG7667, a Combination Monoclonal Antibody, for Prevention of Cytomegalovirus Infection in High-Risk Kidney Transplant Recipients. Antimicrob Agents Ch. 2017;61(2).

148. Lurain NS, Chou S. Antiviral Drug Resistance of Human Cytomegalovirus. Clin Microbiol Rev. 2010;23(4):689–712.

149. Chou S. Approach to drug-resistant cytomegalovirus in transplant recipients. Curr Opin Infect Dis. 2015;28(4):293–9.

150. Chou S. Rapid In Vitro Evolution of Human Cytomegalovirus UL56 Mutations That Confer Letermovir Resistance. Antimicrob Agents Ch. 2015;59(10):6588–93.

151. Britt WJ, Prichard MN. New therapies for human cytomegalovirus infections. Antivir Res. 2018;159:153–74.

152. Piret J, Boivin G. Clinical development of letermovir and maribavir: Overview of human cytomegalovirus drug resistance. Antivir Res. 2019;163:91–105.

153. Trofe J, Pote L, Wade E, Blumberg E, Bloom RD. Maribavir: A Novel Antiviral Agent with Activity Against Cytomegalovirus. Ann Pharmacother. 2008;42(10):1447–57.

154. European Medicines Agency. EU/3/07/519: Orphan designation for the prevention of cytomegalovirus disease in patients with impaired cell-mediated immunity [Internet]. Available from: https://www.ema.europa.eu/en/medicines/human/orphan-designations/eu307519

155. US Food and Drug Administration. FDA Approves First Treatment for Common Type of Post-Transplant Infection that is Resistant to Other Drugs [Internet]. Available from: https://www.fda.gov/news-events/press-announcements/fda-approves-first-treatment-common-type-post-transplant-infection-resistant-other-drugs

156. Mullard A. FDA approves decades-old maribavir for CMV infection. Nat Rev Drug Discov. 2022;21(1):9–9.

157. Kang C. Maribavir: First Approval. Drugs. 2022;82(3):335–40.

158. Severi B, Landini MP, Govoni E. Human Cytomegalovirus morphogenesis: an ultrastructural study of the late cytoplasmic phases. Arch Virol. 1988;98(1–2):51–64.

159. Sanchez V, Greis KD, Sztul E, Britt WJ. Accumulation of Virion Tegument and Envelope Proteins in a Stable Cytoplasmic Compartment during Human Cytomegalovirus Replication: Characterization of a Potential Site of Virus Assembly. J Virol. 2000;74(2):975–86.

160. Alwine JC. The Human Cytomegalovirus Assembly Compartment: A Masterpiece of Viral Manipulation of Cellular Processes That Facilitates Assembly and Egress. Plos Pathog. 2012;8(9):e1002878.

161. Das S, Vasanji A, Pellett PE. Three-Dimensional Structure of the Human Cytomegalovirus Cytoplasmic Virion Assembly Complex Includes a Reoriented Secretory Apparatus †. J Virol. 2007;81(21):11861–9.

162. Procter DJ, Banerjee A, Nukui M, Kruse K, Gaponenko V, Murphy EA, et al. The HCMV Assembly Compartment Is a Dynamic Golgi-Derived MTOC that Controls Nuclear Rotation and Virus Spread. Dev Cell. 2018;45(1):83-100.e7.

163. Iwasaki Y, Furukawa T, Plotkin S, Koprowski H. Ultrastructural study on the sequence of human cytomegalovirus infection in human diploid cells. Archiv Für Die Gesamte Virusforschung. 1973;40(3–4):311–24.

164. Smith JD, Harven E de. Herpes Simplex Virus and Human Cytomegalovirus Replication in WI-38 Cells I. Sequence of Viral Replication. J Virol. 1973;12(4):919–30.

165. Nassiri MR, Gilloteaux J, Taichman RS, Drach JC. Ultrastructural aspects of cytomegalovirus-infected fibroblastic stromal cells of human bone marrow. Tissue Cell. 1998;30(4):398–406.

166. Schauflinger M, Villinger C, Mertens T, Walther P, Einem J. Analysis of human cytomegalovirus secondary envelopment by advanced electron microscopy. Cell Microbiol. 2013;15(2):305–14.

167. AuCoin DP, Smith GB, Meiering CD, Mocarski ES. Betaherpesvirus-Conserved Cytomegalovirus Tegument Protein ppUL32 (pp150) Controls Cytoplasmic Events during Virion Maturation. J Virol. 2006;80(16):8199–210.

168. Sanchez V, Sztul E, Britt WJ. Human Cytomegalovirus pp28 (UL99) Localizes to a Cytoplasmic Compartment Which Overlaps the Endoplasmic Reticulum-Golgi-Intermediate Compartment. J Virol. 2000;74(8):3842–51.

169. Silva MC, Yu QC, Enquist L, Shenk T. Human Cytomegalovirus UL99-Encoded pp28 Is Required for the Cytoplasmic Envelopment of Tegument-Associated Capsids. J Virol. 2003;77(19):10594–605.

170. Seo JY, Britt WJ. Cytoplasmic Envelopment of Human Cytomegalovirus Requires the Postlocalization Function of Tegument Protein pp28 within the Assembly Compartment. J Virol. 2007;81(12):6536–47.

171. Phillips SL, Cygnar D, Thomas A, Bresnahan WA. Interaction between the Human Cytomegalovirus Tegument Proteins UL94 and UL99 Is Essential for Virus Replication. J Virol. 2012;86(18):9995–10005.

172. Silva MC, Schröer J, Shenk T. Human cytomegalovirus cell-to-cell spread in the absence of an essential assembly protein. P Natl Acad Sci Usa. 2005;102(6):2081–6.

173. Liu Y, Cui Z, Zhang Z, Wei H, Zhou Y, Wang M, et al. The tegument protein UL94 of human cytomegalovirus as a binding partner for tegument protein pp28 identified by intracellular imaging. Virology. 2009;388(1):68–77.

174. Womack A, Shenk T. Human Cytomegalovirus Tegument Protein pUL71 Is Required for Efficient Virion Egress. Mbio. 2010;1(5):e00282-10.

175. Schauflinger M, Fischer D, Schreiber A, Chevillotte M, Walther P, Mertens T, et al. The Tegument Protein UL71 of Human Cytomegalovirus Is Involved in Late Envelopment and Affects Multivesicular Bodies. J Virol. 2011;85(8):3821–32.

176. To A, Bai Y, Shen A, Gong H, Umamoto S, Lu S, et al. Yeast Two Hybrid Analyses Reveal Novel Binary Interactions between Human Cytomegalovirus-Encoded Virion Proteins. Plos One. 2011;6(4):e17796.

177. Ortiz DA, Glassbrook JE, Pellett PE. Protein-Protein Interactions Suggest Novel Activities of Human Cytomegalovirus Tegument Protein pUL103. J Virol. 2016;90(17):7798–810.

178. Roller RJ, Fetters R. The Herpes Simplex Virus 1 UL51 Protein Interacts with the UL7 Protein and Plays a Role in Its Recruitment into the Virion. J Virol. 2015;89(6):3112–22.

179. Ahlqvist J, Mocarski E. Cytomegalovirus UL103 Controls Virion and Dense Body Egress. J Virol. 2011;85(10):5125–35.

180. Jiang X, Adler B, Sampaio K, Digel M, Jahn G, Ettischer N, et al. UL74 of Human Cytomegalovirus Contributes to Virus Release by Promoting Secondary Envelopment of Virions. J Virol. 2008;82(6):2802–12.

181. Wille PT, Knoche AJ, Nelson JA, Jarvis MA, Johnson DC. A human cytomegalovirus gO-null mutant fails to incorporate gH/gL into the virion envelope and is unable to enter fibroblasts and epithelial and endothelial cells. J Virol. 2009;84(5):2585–96.

182. Stegmann C, Hochdorfer D, Lieber D, Subramanian N, Stöhr D, Sampaio KL, et al. A derivative of platelet-derived growth factor receptor alpha binds to the trimer of human cytomegalovirus and inhibits entry into fibroblasts and endothelial cells. Plos Pathog. 2017;13(4):e1006273.

183. Munger J, Bennett BD, Parikh A, Feng XJ, McArdle J, Rabitz HA, et al. Systems-level metabolic flux profiling identifies fatty acid synthesis as a target for antiviral therapy. Nat Biotechnol. 2008;26(10):1179–86.

184. Tooze J, Hollinshead M, Reis B, Radsak K, Kern H. Progeny vaccinia and human cytomegalovirus particles utilize early endosomal cisternae for their envelopes. Eur J Cell Biol. 1993;60(1):163–78.

185. Tugizov S, Maidji E, Xiao J, Pereira L. An Acidic Cluster in the Cytosolic Domain of Human Cytomegalovirus Glycoprotein B Is a Signal for Endocytosis from the Plasma Membrane. J Virol. 1999;73(10):8677–88.

186. Radsak K, Eickmann M, Mockenhaupt T, Bogner E, Kern H, Eis-Hübinger A, et al. Retrieval of human cytomegalovirus glycoprotein B from the infected cell surface for virus envelopment. Arch Virol. 1996;141(3–4):557–72.

187. Homman-Loudiyi M, Hultenby K, Britt W, Söderberg-Nauclér C. Envelopment of Human Cytomegalovirus Occurs by Budding into Golgi-Derived Vacuole Compartments Positive for gB, Rab 3, Trans-Golgi Network 46, and Mannosidase II. J Virol. 2003;77(5):3191–203.

188. Fraile-Ramos A, Kledal TN, Pelchen-Matthews A, Bowers K, Schwartz TW, Marsh M. The Human Cytomegalovirus US28 Protein Is Located in Endocytic Vesicles and Undergoes Constitutive Endocytosis and Recycling. Mol Biol Cell. 2001;12(6):1737–49.

189. Fraile-Ramos A, Pelchen-Matthews A, Kledal TN, Browne H, Schwartz TW, Marsh M. Localization of HCMV UL33 and US27 in Endocytic Compartments and Viral Membranes. Traffic. 2002;3(3):218–32.

190. Fraile-Ramos A, Pelchen-Matthews A, Risco C, Rejas MT, Emery VC, Hassan-Walker AF, et al. The ESCRT machinery is not required for human cytomegalovirus envelopment. Cell Microbiol. 2007;9(12):2955–67.

191. Babst M. A Protein's Final ESCRT. Traffic. 2005;6(1):2–9.

192. Colombo M, Raposo G, Théry C. Biogenesis, Secretion, and Intercellular Interactions of Exosomes and Other Extracellular Vesicles. Annu Rev Cell Dev Bi. 2014;30(1):1–35.

193. Crump CM, Yates C, Minson T. Herpes Simplex Virus Type 1 Cytoplasmic Envelopment Requires Functional Vps4. J Virol. 2007;81(14):7380–7.

194. Tandon R, AuCoin DP, Mocarski ES. Human Cytomegalovirus Exploits ESCRT Machinery in the Process of Virion Maturation. J Virol. 2009;83(20):10797–807.

195. Cepeda V, Esteban M, Fraile-Ramos A. Human cytomegalovirus final envelopment on membranes containing both trans-Golgi network and endosomal markers. Cell Microbiol. 2010;12(3):386–404.

196. Moorman NJ, Sharon-Friling R, Shenk T, Cristea IM. A Targeted Spatial-Temporal Proteomics Approach Implicates Multiple Cellular Trafficking Pathways in Human Cytomegalovirus Virion Maturation. Mol Cell Proteomics. 2010;9(5):851–60.

197. Fraile-Ramos A, Cepeda V, Elstak E, Sluijs P van der. Rab27a Is Required for Human Cytomegalovirus Assembly. Plos One. 2010;5(12):e15318.

198. Cepeda V, Fraile-Ramos A. A role for the SNARE protein syntaxin 3 in human cytomegalovirus morphogenesis. Cell Microbiol. 2011;13(6):846–58.

199. Liu STH, Sharon-Friling R, Ivanova P, Milne SB, Myers DS, Rabinowitz JD, et al. Synaptic vesicle-like lipidome of human cytomegalovirus virions reveals a role for SNARE machinery in virion egress. Proc National Acad Sci. 2011;108(31):12869–74.

200. Das S, Pellett PE. Spatial Relationships between Markers for Secretory and Endosomal Machinery in Human Cytomegalovirus-Infected Cells versus Those in Uninfected Cells. J Virol. 2011;85(12):5864–79.

201. Jean Beltran PM, Mathias RA, Cristea IM. A Portrait of the Human Organelle Proteome In Space and Time during Cytomegalovirus Infection. Cell Syst. 2016;3(4):361-373.e6.

202. Rebmann GM, Grabski R, Sanchez V, Britt WJ. Phosphorylation of Golgi Peripheral Membrane Protein Grasp65 Is an Integral Step in the Formation of the Human Cytomegalovirus Cytoplasmic Assembly Compartment. Mbio. 2016;7(5):e01554-16.

203. Cruz L, Streck NT, Ferguson K, Desai T, Desai DH, Amin SG, et al. Potent Inhibition of Human Cytomegalovirus by Modulation of Cellular SNARE Syntaxin 5. J Virol. 2017;91(1):e01637-16.

204. Mouna L, Hernandez E, Bonte D, Brost R, Amazit L, Delgui LR, et al. Analysis of the role of autophagy inhibition by two complementary human cytomegalovirus BECN1/Beclin 1-binding proteins. Autophagy. 2015;12(2):327–42.

205. Taisne C, Lussignol M, Hernandez E, Moris A, Mouna L, Esclatine A. Human cytomegalovirus hijacks the autophagic machinery and LC3 homologs in order to optimize cytoplasmic envelopment of mature infectious particles. Sci Rep-uk. 2019;9(1):4560.

206. Archer MA, Brechtel TM, Davis LE, Parmar RC, Hasan MH, Tandon R. Inhibition of endocytic pathways impacts cytomegalovirus maturation. Sci Rep-uk. 2017;7(1):46069.

207. Close WL, Glassbrook JE, Gurczynski SJ, Pellett PE. Infection-Induced Changes Within the Endocytic Recycling Compartment Suggest a Roadmap of Human Cytomegalovirus Egress. Front Microbiol. 2018;9:1888.

208. Streck NT, Carmichael J, Buchkovich NJ. Nonenvelopment Role for the ESCRT-III Complex during Human Cytomegalovirus Infection. J Virol. 2018;92(12):e02096-17.

209. Streck NT, Zhao Y, Sundstrom JM, Buchkovich NJ. Human Cytomegalovirus Utilizes Extracellular Vesicles to Enhance Virus Spread. J Virol. 2020;

210. Butt BG, Owen DJ, Jeffries CM, Ivanova L, Hill CH, Houghton JW, et al. Insights into herpesvirus assembly from the structure of the pUL7:pUL51 complex. Elife. 2020;9:e53789.

211. Turner DL, Korneev DV, Purdy JG, Marco A de, Mathias RA. The host exosome pathway underpins biogenesis of the human cytomegalovirus virion. Elife. 2020;9:e58288.

212. Zicari S, Arakelyan A, Palomino RAÑ, Fitzgerald W, Vanpouille C, Lebedeva A, et al. Human cytomegalovirus-infected cells release extracellular vesicles that carry viral surface proteins. Virology. 2018;524:97–105.

213. Hashimoto Y, Sheng X, Murray-Nerger LA, Cristea IM. Temporal dynamics of protein complex formation and dissociation during human cytomegalovirus infection. Nat Commun. 2020;11(1):806.

214. Théry C, Zitvogel L, Amigorena S. Exosomes: composition, biogenesis and function. Nat Rev Immunol. 2002;2(8):569–79.

215. Yáñez-Mó M, Barreiro O, Gordon-Alonso M, Sala-Valdés M, Sánchez-Madrid F. Tetraspanin-enriched microdomains: a functional unit in cell plasma membranes. Trends Cell Biol. 2009;19(9):434–46.

216. Takino T, Miyamori H, Kawaguchi N, Uekita T, Seiki M, Sato H. Tetraspanin CD63 promotes targeting and lysosomal proteolysis of membrane-type 1 matrix metalloproteinase. Biochem Bioph Res Co. 2003;304(1):160–6.

217. van Niel G, Charrin S, Simoes S, Romao M, Rochin L, Saftig P, et al. The Tetraspanin CD63 Regulates ESCRT-Independent and -Dependent Endosomal Sorting during Melanogenesis. Dev Cell. 2011;21(4):708–21.

218. Perez-Hernandez D, Gutiérrez-Vázquez C, Jorge I, López-Martín S, Ursa A, Sánchez-Madrid F, et al. The Intracellular Interactome of Tetraspanin-enriched Microdomains Reveals Their Function as Sorting Machineries toward Exosomes. J Biol Chem. 2013;288(17):11649–61.

219. Momtaz S, Molina B, Mlera L, Goodrum F, Wilson JM. Cell type-specific biogenesis of novel vesicles containing viral products in human cytomegalovirus infection. J Virol. 2021;

220. Owen DJ, Crump CM, Graham SC. Tegument Assembly and Secondary Envelopment of Alphaherpesviruses. Viruses. 2015;7(9):5084–114.

221. Johnson DC, Baines JD. Herpesviruses remodel host membranes for virus egress. Nat Rev Microbiol. 2011;9(5):382–94.

222. Hogue IB, Bosse JB, Hu JR, Thiberge SY, Enquist LW. Cellular Mechanisms of Alpha Herpesvirus Egress: Live Cell Fluorescence Microscopy of Pseudorabies Virus Exocytosis. Plos Pathog. 2014;10(12):e1004535.

223. Hogue IB, Scherer J, Enquist LW. Exocytosis of Alphaherpesvirus Virions, Light Particles, and Glycoproteins Uses Constitutive Secretory Mechanisms. Mbio. 2016;7(3):e00820-16.

224. Read C, Schauflinger M, Nikolaenko D, Walther P, Einem J von. Regulation of Human Cytomegalovirus Secondary Envelopment by a C-Terminal Tetralysine Motif in pUL71. J Virol. 2019;93(13).

225. Devan KS, Walther P, Einem J von, Ropinski T, Kestler H, Read C. Improved automatic detection of herpesvirus secondary envelopment stages in electron microscopy by augmenting training data with synthetic labelled images generated by a generative adversarial network. Cell Microbiol. 2021;23(2):e13280.

226. Devan KS, Walther P, Einem J von, Ropinski T, Kestler HA, Read C. Detection of herpesvirus capsids in transmission electron microscopy images using transfer learning. Histochem Cell Biol. 2019;151(2):101–14.

227. Bughio F, Elliott DA, Goodrum F. An Endothelial Cell-Specific Requirement for the UL133-UL138 Locus of Human Cytomegalovirus for Efficient Virus Maturation. J Virol. 2013;87(6):3062–75.

228. Bughio F, Umashankar M, Wilson J, Goodrum F. Human Cytomegalovirus UL135 and UL136 Genes Are Required for Postentry Tropism in Endothelial Cells. J Virol. 2015;89(13):6536–50.

229. Cha TA, Tom E, Kemble GW, Duke GM, Mocarski ES, Spaete RR. Human cytomegalovirus clinical isolates carry at least 19 genes not found in laboratory strains. J Virol. 1996;70(1):78–83.

230. Sinzger C, Schmidt K, Knapp J, Kahl M, Beck R, Waldman J, et al. Modification of human cytomegalovirus tropism through propagation in vitro is associated with changes in the viral genome. J Gen Virol. 1999;80(11):2867–77.

231. Dolan A, Cunningham C, Hector RD, Hassan-Walker AF, Lee L, Addison C, et al. Genetic content of wild-type human cytomegalovirus. J Gen Virol. 2004;85(5):1301–12.

232. Dargan DJ, Douglas E, Cunningham C, Jamieson F, Stanton RJ, Baluchova K, et al. Sequential mutations associated with adaptation of human cytomegalovirus to growth in cell culture. J Gen Virology. 2010;91(Pt 6):1535–46.

233. Hahn G, Revello MG, Patrone M, Percivalle E, Campanini G, Sarasini A, et al. Human Cytomegalovirus UL131-128 Genes Are Indispensable for Virus Growth in Endothelial Cells and Virus Transfer to Leukocytes. J Virol. 2004;78(18):10023–33.

234. Wang D, Shenk T. Human cytomegalovirus UL131 open reading frame is required for epithelial cell tropism. J Virol. 2005;79(16):10330–8.

235. Wang D, Shenk T. Human cytomegalovirus virion protein complex required for epithelial and endothelial cell tropism. P Natl Acad Sci Usa. 2005;102(50):18153–8.

236. Ryckman BJ, Chase MC, Johnson DC. HCMV gH/gL/UL128–131 interferes with virus entry into epithelial cells: Evidence for cell type-specific receptors. Proc National Acad Sci. 2008;105(37):14118–23.

237. Murrell I, Wilkie GS, Davison AJ, Statkute E, Fielding CA, Tomasec P, et al. Genetic Stability of Bacterial Artificial Chromosome-Derived Human Cytomegalovirus during Culture In Vitro. J Virol. 2016;90(8):3929–43.

238. Prichard MN, Penfold MET, Duke GM, Spaete RR, Kemble GW. A review of genetic differences between limited and extensively passaged human cytomegalovirus strains. Rev Med Virol. 2001;11(3):191–200.

239. Bradley AJ, Lurain NS, Ghazal P, Trivedi U, Cunningham C, Baluchova K, et al. High-throughput sequence analysis of variants of human cytomegalovirus strains Towne and AD169. J Gen Virology. 2009;90(Pt 10):2375–80.

240. Stanton RJ, Baluchova K, Dargan DJ, Cunningham C, Sheehy O, Seirafian S, et al. Reconstruction of the complete human cytomegalovirus genome in a BAC reveals RL13 to be a potent inhibitor of replication. J Clin Investigation. 2010;120(9):3191–208.

241. Penfold MET, Dairaghi DJ, Duke GM, Saederup N, Mocarski ES, Kemble GW, et al. Cytomegalovirus encodes a potent α chemokine. Proc National Acad Sci. 1999;96(17):9839–44.

242. Benedict CA, Butrovich KD, Lurain NS, Corbeil J, Rooney I, Schneider P, et al. Cutting edge: a novel viral TNF receptor superfamily member in virulent strains of human cytomegalovirus. J Immunol Baltim Md 1950. 1999;162(12):6967–70.

243. Wills MR, Ashiru O, Reeves MB, Okecha G, Trowsdale J, Tomasec P, et al. Human Cytomegalovirus Encodes an MHC Class I-Like Molecule (UL142) That Functions to Inhibit NK Cell Lysis. J Immunol. 2005;175(11):7457–65.

244. Tomasec P, Wang ECY, Davison AJ, Vojtesek B, Armstrong M, Griffin C, et al. Downregulation of natural killer cell–activating ligand CD155 by human cytomegalovirus UL141. Nat Immunol. 2005;6(2):181–8.

245. Goodrum F, Reeves M, Sinclair J, High K, Shenk T. Human cytomegalovirus sequences expressed in latently infected individuals promote a latent infection in vitro. Blood. 2007;110(3):937–45.

246. Petrucelli A, Umashankar M, Zagallo P, Rak M, Goodrum F. Interactions between Proteins Encoded within the Human Cytomegalovirus UL133-UL138 Locus. J Virol. 2012;86(16):8653–62.

247. Adler B, Scrivano L, Ruzcics Z, Rupp B, Sinzger C, Koszinowski U. Role of human cytomegalovirus UL131A in cell type-specific virus entry and release. J Gen Virol. 2006;87(9):2451–60.

248. Zhou M, Yu Q, Wechsler A, Ryckman BJ. Comparative analysis of gO isoforms reveals that strains of human cytomegalovirus differ in the ratio of gH/gL/gO and gH/gL/UL128-131 in the virion envelope. J Virol. 2013;87(17):9680–90.

249. Zhou M, Lanchy JM, Ryckman BJ. Human Cytomegalovirus gH/gL/gO Promotes the Fusion Step of Entry into All Cell Types, whereas gH/gL/UL128-131 Broadens Virus Tropism through a Distinct Mechanism. J Virol. 2015;89(17):8999–9009.

250. Sampaio KL, Stegmann C, Brizic I, Adler B, Stanton RJ, Sinzger C. The contribution of pUL74 to growth of human cytomegalovirus is masked in the presence of RL13 and UL128 expression. J Gen Virol. 2016;97(8):1917–27.

251. Kabanova A, Marcandalli J, Zhou T, Bianchi S, Baxa U, Tsybovsky Y, et al. Platelet-derived growth factor-α receptor is the cellular receptor for human cytomegalovirus gHgLgO trimer. Nat Microbiol. 2016;1(8):16082.

252. Wu Y, Prager A, Boos S, Resch M, Brizic I, Mach M, et al. Human cytomegalovirus glycoprotein complex gH/gL/gO uses PDGFR-α as a key for entry. Plos Pathog. 2017;13(4):e1006281.

253. Martinez-Martin N, Marcandalli J, Huang CS, Arthur CP, Perotti M, Foglierini M, et al. An Unbiased Screen for Human Cytomegalovirus Identifies Neuropilin-2 as a Central Viral Receptor. Cell. 2018;174.

254. E X, Meraner P, Lu P, Perreira JM, Aker AM, McDougall WM, et al. OR14I1 is a receptor for the human cytomegalovirus pentameric complex and defines viral epithelial cell tropism. Proc National Acad Sci. 2019;116(14):7043–52.

255. Wrapp D, Ye X, Ku Z, Su H, Jones HG, Wang N, et al. Structural basis for HCMV Pentamer recognition by neuropilin 2 and neutralizing antibodies. Sci Adv. 2022;8(10):eabm2546.

256. Kschonsak M, Johnson MC, Schelling R, Green EM, Rougé L, Ho H, et al. Structural basis for HCMV Pentamer receptor recognition and antibody neutralization. Sci Adv. 2022;8(10):eabm2536.

257. Sinzger C, Hahn G, Digel M, Katona R, Sampaio KL, Messerle M, et al. Cloning and sequencing of a highly productive, endotheliotropic virus strain derived from human cytomegalovirus TB40/E. J Gen Virol. 2008;89(2):359–68.

258. Messerle M, Crnkovic I, Hammerschmidt W, Ziegler H, Koszinowski UH. Cloning and mutagenesis of a herpesvirus genome as an infectious bacterial artificial chromosome. Proc National Acad Sci. 1997;94(26):14759–63.

259. Borst EM, Hahn G, Koszinowski UH, Messerle M. Cloning of the Human Cytomegalovirus (HCMV) Genome as an Infectious Bacterial Artificial Chromosome in Escherichia coli : a New Approach for Construction of HCMV Mutants. J Virol. 1999;73(10):8320–9.

260. Brune W, Messerle M, Koszinowski UH, Brune W, Messerle M, Koszinowski UH. Forward with BACs new tools for herpesvirus genomics. Trends Genet. 2000;16(6):254–9.

261. Tischer BK, Einem J von, Kaufer B, Osterrieder N. Two-step Red-mediated recombination for versatile high-efficiency markerless DNA manipulation in Escherichia coli. Biotechniques. 2006;40(2):191–7.

262. Tischer BK, Smith GA, Osterrieder N. In Vitro Mutagenesis Protocols, Third Edition. 2010;421–30.

263. Wilkinson GWG, Davison AJ, Tomasec P, Fielding CA, Aicheler R, Murrell I, et al. Human cytomegalovirus: taking the strain. Med Microbiol Immun. 2015;204(3):273–84.

264. Murrell I, Tomasec P, Wilkie GS, Dargan DJ, Davison AJ, Stanton RJ. Impact of Sequence Variation in the UL128 Locus on Production of Human Cytomegalovirus in Fibroblast and Epithelial Cells. J Virol. 2013;87(19):10489–500.

265. Paterson DA, Dyer AP, Milne RSB, Sevilla-Reyes E, Gompels UA. A Role for Human Cytomegalovirus Glycoprotein O (gO) in Cell Fusion and a New Hypervariable Locus. Virology. 2002;293(2):281–94.

266. Mattick C, Dewin D, Polley S, Sevilla-Reyes E, Pignatelli S, Rawlinson W, et al. Linkage of human cytomegalovirus glycoprotein gO variant groups identified from worldwide clinical isolates with gN genotypes, implications for disease associations and evidence for N-terminal sites of positive selection. Virology. 2004;318(2):582–97.

267. Zhang L, Zhou M, Stanton R, Kamil J, Ryckman BJ. Expression Levels of Glycoprotein O (gO) Vary between Strains of Human Cytomegalovirus, Influencing the Assembly of gH/gL Complexes and Virion Infectivity. J Virol. 2018;92(15).

268. Day LZ, Stegmann C, Schultz EP, Lanchy JM, Yu Q, Ryckman BJ. Polymorphisms in Human Cytomegalovirus gO Exert Epistatic Influences on Cell-Free and Cell-To-Cell Spread, and Antibody Neutralization on gH Epitopes. J Virol. 2020;94(8).

269. Li G, Nguyen CC, Ryckman BJ, Britt WJ, Kamil JP. A viral regulator of glycoprotein complexes contributes to human cytomegalovirus cell tropism. Proc National Acad Sci. 2015;112(14):4471–6.

270. Nguyen CC, Siddiquey MNA, Zhang H, Li G, Kamil JP. Human Cytomegalovirus Tropism Modulator UL148 Interacts with SEL1L, a Cellular Factor That Governs Endoplasmic Reticulum-Associated Degradation of the Viral Envelope Glycoprotein gO. J Virol. 2018;92(18):e00688-18.

271. Vezzani G, Amendola D, Yu D, Chandramouli S, Frigimelica E, Maione D, et al. The Human Cytomegalovirus UL116 Glycoprotein Is a Chaperone to Control gH-Based Complexes Levels on Virions. Front Microbiol. 2021;12:630121.

272. Caló S, Cortese M, Ciferri C, Bruno L, Gerrein R, Benucci B, et al. The Human Cytomegalovirus UL116 Gene Encodes an Envelope Glycoprotein Forming a Complex with gH Independently from gL. J Virol. 2016;90(10):4926–38.

273. Bronzini M, Luganini A, Dell'Oste V, Andrea MD, Landolfo S, Gribaudo G. The US16 Gene of Human Cytomegalovirus Is Required for Efficient Viral Infection of Endothelial and Epithelial Cells. J Virol. 2012;86(12):6875–88.

274. Luganini A, Cavaletto N, Raimondo S, Geuna S, Gribaudo G. Loss of the Human Cytomegalovirus US16 Protein Abrogates Virus Entry into Endothelial and Epithelial Cells by Reducing the Virion Content of the Pentamer. J Virol. 2017;91(11):e00205-17.

275. Scrivano L, Sinzger C, Nitschko H, Koszinowski UH, Adler B. HCMV Spread and Cell Tropism are Determined by Distinct Virus Populations. Plos Pathog. 2011;7(1):e1001256.

276. Yamane Y, Furukawa T, Plotkin SA. Supernatant virus release as a differentiating marker between low passage and vaccine strains of human cytomegalovirus. Vaccine. 1983;1(1):23–5.

277. Sinzger C, Jahn G. Human Cytomegalovirus Cell Tropism and Pathogenesis. Intervirology. 1996;39(5–6):302–19.

278. Murrell I, Bedford C, Ladell K, Miners KL, Price DA, Tomasec P, et al. The pentameric complex drives immunologically covert cell–cell transmission of wild-type human cytomegalovirus. Proc National Acad Sci. 2017;114(23):6104–9.

279. Krull A, Buchholz TO, Jug F. Noise2Void - Learning Denoising from Single Noisy Images. 2018;

280. Tinevez JY, Perry N, Schindelin J, Hoopes GM, Reynolds GD, Laplantine E, et al. TrackMate: An open and extensible platform for single-particle tracking. Methods San Diego Calif. 2017;115.

281. Tarantino N, Tinevez JY, Crowell E, Boisson B, Henriques R, Mhlanga M, et al. TNF and IL-1 exhibit distinct ubiquitin requirements for inducing NEMO–IKK supramolecular structures. J Cell Biology. 2014;204(2):231–45.

282. Tejedor V, Bénichou O, Voituriez R, Jungmann R, Simmel F, Selhuber-Unkel C, et al. Quantitative Analysis of Single Particle Trajectories: Mean Maximal Excursion Method. Biophys J. 2010;98(7):1364–72.

283. Flomm FJ, Soh TK, Schneider C, Wedemann L, Britt HM, Thalassinos K, Pfitzner S, Reimer R, Grünewald K, Bosse JB. „Intermittent Bulk Release of Human Cytomegalovirus" Associated Data; 2022 [cited 2022 July 26]. Database: Dryad [Internet]. Available from: https://doi.org/10.5061/dryad.gtht76hpt

284. Flomm FJ, Soh TK, Schneider C, Wedemann L, Britt HM, Thalassinos K, Pfitzner S, Reimer R, Grünewald K, Bosse JB Intermittent Bulk Release of Human Cytomegalovirus. Plos Pathog. 2022;in production

285. Bindels DS, Haarbosch L, Weeren L van, Postma M, Wiese KE, Mastop M, et al. mScarlet: a bright monomeric red fluorescent protein for cellular imaging. Nat Methods. 2016;14(1):nmeth.4074.

286. Sampaio K, Jahn G, Sinzger C. Virus-Host Interactions, Methods and Protocols. Methods Mol Biology Clifton N J. 2013;1064:201–9.

287. Verweij FJ, Bebelman MP, Jimenez CR, Garcia-Vallejo JJ, Janssen H, Neefjes J, et al. Quantifying exosome secretion from single cells reveals a modulatory role for GPCR signaling. J Cell Biol. 2018;217(3):jcb.201703206.

288. Tokuyasu KT. A TECHNIQUE FOR ULTRACRYOTOMY OF CELL SUSPENSIONS AND TISSUES. J Cell Biology. 1973;57(2):551–65.

289. Dang VD, Jella KK, Ragheb RRT, Denslow ND, Alli AA. Lipidomic and proteomic analysis of exosomes from mouse cortical collecting duct cells. Faseb J. 2017;31(12):5399–408.

290. Jiang B, Himmelsbach K, Ren H, Boller K, Hildt E. Subviral Hepatitis B Virus Filaments, like Infectious Viral Particles, Are Released via Multivesicular Bodies. J Virol. 2016;90(7):3330–41.

291. Lu F, Liang Q, Abi-Mosleh L, Das A, Brabander JKD, Goldstein JL, et al. Identification of NPC1 as the target of U18666A, an inhibitor of lysosomal cholesterol export and Ebola infection. Elife. 2015;4:e12177.

292. Datta A, Kim H, McGee L, Johnson AE, Talwar S, Marugan J, et al. High-throughput screening identified selective inhibitors of exosome biogenesis and secretion: A drug repurposing strategy for advanced cancer. Sci Rep-uk. 2018;8(1):8161.

293. Khan FM, Saleh E, Alawadhi H, Harati R, Zimmermann WH, El-Awady R. Inhibition of exosome release by ketotifen enhances sensitivity of cancer cells to doxorubicin. Cancer Biol Ther. 2017;19(1):1–9.

294. Falk JJ, Winkelmann M, Sampaio KL, Paal C, Schrezenmeier H, Alt M, et al. Large-Scale Screening of HCMV-Seropositive Blood Donors Indicates that HCMV Effectively Escapes from Antibodies by Cell-Associated Spread. Viruses. 2018;10(9):500.

295. Mettenleiter TC. Intriguing interplay between viral proteins during herpesvirus assembly or: The herpesvirus assembly puzzle. Vet Microbiol. 2006;113(3–4):163–9.

296. Mingo RM, Han J, Newcomb WW, Brown JC. Replication of Herpes Simplex Virus: Egress of Progeny Virus at Specialized Cell Membrane Sites. J Virol. 2012;86(13):7084–97.

297. Maninger S, Bosse JB, Lemnitzer F, Pogoda M, Mohr CA, Einem J von, et al. M94 Is Essential for the Secondary Envelopment of Murine Cytomegalovirus ‡. J Virol. 2011;85(18):9254–67.

298. Mori Y, Koike M, Moriishi E, Kawabata A, Tang H, Oyaizu H, et al. Human Herpesvirus-6 Induces MVB Formation, and Virus Egress Occurs by an Exosomal Release Pathway. Traffic. 2008;9(10):1728–42.

299. Krzyzaniak M, Mach M, Britt WJ. The Cytoplasmic Tail of Glycoprotein M (gpUL100) Expresses Trafficking Signals Required for Human Cytomegalovirus Assembly and Replication. J Virol. 2007;81(19):10316–28.

300. Calistri A, Sette P, Salata C, Cancellotti E, Forghieri C, Comin A, et al. Intracellular Trafficking and Maturation of Herpes Simplex Virus Type 1 gB and Virus Egress Require Functional Biogenesis of Multivesicular Bodies. J Virol. 2007;81(20):11468–78.

301. Hollinshead M, Johns HL, Sayers CL, Gonzalez-Lopez C, Smith GL, Elliott G. Endocytic tubules regulated by Rab GTPases 5 and 11 are used for envelopment of herpes simplex virus. Embo J. 2012;31(21):4204–20.

302. Dogrammatzis C, Deschamps T, Kalamvoki M. Biogenesis of extracellular vesicles during herpes simplex virus type 1 infection: The role of the CD63 tetraspanin. J Virol. 2018;93(2):JVI.01850-18.

303. Mesa RA. Tipifarnib: farnesyl transferase inhibition at a crossroads. Expert Rev Anticanc. 2014;6(3):313–9.

304. Filippakis H, Spandidos DA, Sourvinos G. Herpesviruses: Hijacking the Ras signaling pathway. Biochimica Et Biophysica Acta Bba - Mol Cell Res. 2010;1803(7):777–85.

305. Filippakis H, Dimitropoulou P, Eliopoulos AG, Spandidos DA, Sourvinos G. The enhanced host-cell permissiveness of human cytomegalovirus is mediated by the Ras signaling pathway. Biochimica Et Biophysica Acta Bba - Mol Cell Res. 2011;1813(10):1872–82.

306. Farassati F, Yang AD, Lee PWK. Oncogenes in Ras signalling pathway dictate host-cell permissiveness to herpes simplex virus 1. Nat Cell Biol. 2001;3(8):745–50.

307. Kobayashi E, Aga M, Kondo S, Whitehurst C, Yoshizaki T, Pagano JS, et al. C-Terminal Farnesylation of UCH-L1 Plays a Role in Transport of Epstein-Barr Virus Primary Oncoprotein LMP1 to Exosomes. Msphere. 2018;3(1):e00030-18.

308. Heintzmann R, Ficz G. Breaking the resolution limit in light microscopy. Brief Funct Genomics. 2006;5(4):289–301.

309. Wisner TW, Wright CC, Kato A, Kawaguchi Y, Mou F, Baines JD, et al. Herpesvirus gB-Induced Fusion between the Virion Envelope and Outer Nuclear Membrane during Virus Egress Is Regulated by the Viral US3 Kinase. J Virol. 2009;83(7):3115–26.

310. Chen BC, Legant WR, Wang K, Shao L, Milkie DE, Davidson MW, et al. Lattice light-sheet microscopy: Imaging molecules to embryos at high spatiotemporal resolution. Science. 2014;346(6208):1257998.

311. Gao L, Tang WC, Tsai YC, Chen BC. Lattice light sheet microscopy using tiling lattice light sheets. Opt Express. 2019;27(2):1497–506.

312. Sinzger C, Mangin M, Weinstock C, Topp MS, Hebart H, Einsele H, et al. Effect of serum and CTL on focal growth of human cytomegalovirus. J Clin Virol. 2007;38(2):112–9.

313. Gerna G, Percivalle E, Baldanti F, Sozzani S, Lanzarini P, Genini E, et al. Human Cytomegalovirus Replicates Abortively in Polymorphonuclear Leukocytes after Transfer from Infected Endothelial Cells via Transient Microfusion Events. J Virol. 2000;74(12):5629–38.

314. Digel M, Sampaio KL, Jahn G, Sinzger C. Evidence for direct transfer of cytoplasmic material from infected to uninfected cells during cell-associated spread of human cytomegalovirus. J Clin Virol. 2006;37(1):10–20.

315. Kinzler ER, Compton T. Characterization of Human Cytomegalovirus Glycoprotein-Induced Cell-Cell Fusion. J Virol. 2005;79(12):7827–37.

316. Bowden R, Slichter S, Sayers M, Weisdorf D, Cays M, Schoch G, et al. A comparison of filtered leukocyte-reduced and cytomegalovirus (CMV) seronegative blood products for the prevention of transfusion-associated CMV infection after marrow transplant [see comments]. Blood. 1995;86(9):3598–603.

317. Podlech J, Reddehase MJ, Adler B, Lemmermann NAW. Principles for studying in vivo attenuation of virus mutants: defining the role of the cytomegalovirus gH/gL/gO complex as a paradigm. Med Microbiol Immun. 2015;204(3):295–305.

318. Lemmermann NAW, Krmpotic A, Podlech J, Brizic I, Prager A, Adler H, et al. Non-redundant and Redundant Roles of Cytomegalovirus gH/gL Complexes in Host Organ Entry and Intra-tissue Spread. Plos Pathog. 2015;11(2):e1004640.

319. Ziemann M, Hennig H. Prevention of Transfusion-Transmitted Cytomegalovirus Infections: Which is the Optimal Strategy? Transfus Med Hemoth. 2014;41(1):40–4.

320. Lee FK, Nahmias AJ, Stagno S. Rapid Diagnosis of Cytomegalovirus Infection in Infants by Electron Microscopy. New Engl J Medicine. 1978;299(23):1266–70.

321. Henry C, Hartsock RJ, Kirk Z, Behrer R. Detection of Viruria in Cytomegalovirus-infected Infants by Electron Microscopy. Am J Clin Pathol. 1978;69(4):435–9.

322. Tamura T, Chiba S, Chiba Y, Nakao T. Virus excretion and neutralizing antibody response in saliva in human cytomegalovirus infection. Infect Immun. 1980;29(3):842–5.

323. Hamprecht K, Witzel S, Maschmann J, Dietz K, Baumeister A, Mikeler E, et al. Rapid detection and quantification of cell free cytomegalovirus by a high-speed centrifugation-based microculture assay: comparison to longitudinally analyzed viral DNA load and pp67 late transcript during lactation. J Clin Virol. 2003;28(3):303–16.

324. Brune W. Molecular Basis of Cytomegalovirus Host Species Specificity. In: Cytomegaloviruses: from molecular pathogenesis to intervention. 2013. p. 322–9.

325. Zhu H, Shen Y, Shenk T. Human cytomegalovirus IE1 and IE2 proteins block apoptosis. J Virol. 1995;69(12):7960–70.

326. Campeau E, Ruhl VE, Rodier F, Smith CL, Rahmberg BL, Fuss JO, et al. A Versatile Viral System for Expression and Depletion of Proteins in Mammalian Cells. Plos One. 2009;4(8):e6529.

327. Rowland AA, Chitwood PJ, Phillips MJ, Voeltz GK. ER Contact Sites Define the Position and Timing of Endosome Fission. Cell. 2014;159(5):1027–41.

328. Dull T, Zufferey R, Kelly M, Mandel RJ, Nguyen M, Trono D, et al. A Third-Generation Lentivirus Vector with a Conditional Packaging System. J Virol. 1998;72(11):8463–71.

329. Baldick CJ, Marchini A, Patterson CE, Shenk T. Human cytomegalovirus tegument protein pp71 (ppUL82) enhances the infectivity of viral DNA and accelerates the infectious cycle. J Virol. 1997;71(6):4400–8.

330. Schindelin J, Arganda-Carreras I, Frise E, Kaynig V, Longair M, Pietzsch T, et al. Fiji: an open-source platform for biological-image analysis. Nat Methods. 2012;9(7):676–82.

331. Scriven DRL, Lynch RM, Moore EDW. Image acquisition for colocalization using optical microscopy. Am J Physiol-cell Ph. 2008;294(5):C1119–22.

332. Walton J. Lead asparate, an en bloc contrast stain particularly useful for ultrastructural enzymology. J Histochem Cytochem Official J Histochem Soc. 1979;27(10):1337–42.

333. Luft JH. IMPROVEMENTS IN EPOXY RESIN EMBEDDING METHODS. J Biophysical Biochem Cytol. 1961;9(2):409–14.

10 Appendix

10.1 Hazardous substances

List of Hazardous Substances (GHS Classification)

Product Name	*CAS number*	*H Statements*	*P Statements*	*Hazard Pictogram*
2,4,6-Tris(dimethylaminomethyl) phenol	90-72-2	302, 314	280, 301+312, 302+352, 305+351+338	GHS05, GHS07
2-Mercapto-ethanol	60-24-2	301+331, 310, 315, 317, 318, 361D, 373, 410	273, 280, 301+310, 302+352+310, 304+340+311, 305+351+338	GHS05, GHS06, GHS08, GHS09
2-Propanol	67-63-0	225, 319, 336	210, 233, 305+351+338	GHS02, GHS07
Ampicillin Sodium Salt	69-52-3	317, 334	261, 280, 342+311	GHS08
Buffer N3 (Qiagen)	-	315, 319	280	GHS07
Buffer P2 (Qiagen)	-	290, 314	280, 305+351+338+310	GHS05
Buffer PB (Qiagen)				
	-	225,315, 319, 336	210, 280, 403	GHS02, GHS07
Calcium chloride	10043-52-4	319	305+351+338	GHS07
CellTiter-Glo® Buffer	-	319, 412	264, 273, 280, 305+351+338, 337+313, 501	GHS07
Chloramphenicol	56-75-7	318, 351, 361FD	202, 280, 305+351+338, 308+313, 405, 501	GHS05, GHS08
CIRCUITWORKS® CONDUCTIVE EPOXY - Part A and Part B (Combined)	-	317	280, 261, 272, 362+364, 302+352, 332+313,	GHS07
Epoxy Embedding Medium, Hardener DDSA	26544-38-7	317, 319, 413	261, 264, 273, 280, 302+352, 305+351+338	GHS07
Ethanol ROTIPURAN® ≥ 99,8%, p.a.	64-17-5	255, 319	210, 233, 305+351+338	GHS02, GHS07
Gallic acid	149-91-7	315, 319, 335	302+352, 305+351+338	GHS07
Gel Loading Dye, Purple (6X)	-	412	273,501	-
Glutaraldehyde 25% Solution, EM Grade Distillation Purified	-	330, 334, 314, 318, 302, 317, 335, 400, 411	303+361+353, 305+351+338, 310, 320, 362+364, 405, 501	GHS05, GHS06, GHS07, GHS08, GHS09
Glycidether 100	90529-77-4	302, 315, 319, 341, 361F	280, 301+312, 305+351+338, 333+313, 337+313	GHS07, GHS08

Product Name	*CAS number*	*H Statements*	*P Statements*	*Hazard Pictogram*
Glycidether Hardener MNA	25134-21-8	302, 315, 317, 318, 331, 334	280, 301+312, 302+352, 305+351+338, 310, 333+313	GHS05, GHS06, GHS08
Hygromycin B Gold (solution)	31282-04-9	301+311, 318, 330, 334	264, 280, 301+310, 302+352, 304+340, 305+351+338, 342+311	GHS05, GHS05, GHS08
Kanamycin sulfate, from Streptomyces				
kanamyceticus	25389-94-0	360D	201, 308+313	GHS08
Ketotifen fumarate salt	34580-14-8	302, 319	264, 270, 280, 301+312, 305+351+338, 337+313	GHS07
Lead(II) nitrate ≥99 %, p.a., ACS	10099-74-8	302+332, 360DF, 372, 410	273, 280, 301+312, 304+340, 308+313, 405	GHS07, GHS08, GHS09
NucleoBond Xtra Midi (50) 0.6-100 mg RNase A (lyo)	-	334	261sh, 342+311	GHS08
NucleoBond Xtra Midi (50) 300 ml ELU	-	226, 319	210, 280sh	GHS02, GHS07
NucleoBond Xtra Midi (50) 500 ml LYS	-	315, 319	280sh	GHS07
NucleoBond Xtra Midi (50) 500 ml WASH	-	226	210	GHS02
Osmium tetraoxide ≥99,95 %, p.a., for electron microscopy	20816-12-0	300+310+330, 314	280, 301+330+331, 305+352, 304+340, 305+351+338, 309+311	GHS05, GHS06
Osmium Tetroxide 4% Aqueous Solution	-	200, 301, 310+330, 315, 318	301+310, 330, 305+351+338, 320, 361+364, 373, 380, 401, 405, 501	GHS01, GHS05, GHS06
Paraformaldehyde 20% Solution, EM Grade	-	334, 315, 319, 335, 227, 303	261, 280, 284, 305+351+338, 405, 501	GHS07, GHS08
Penicillin-Streptomycin (10.000 U/ml)	-	361	201, 202, 280, 308+313, 501	GHS08
Polyethyleneimine, Branched, Mw 2000 (bPEI 2000)				
	9002-98-6	302, 317, 318, 401, 411	261, 264, 270, 272, 280, 301+312, 302+352	GHS05, GHS07, GHS09
Potassium hexacyanoferrate (II) trihydrate	14459-95-1	412	273, 501	-
Potassium Hydroxide Pellets for Analysis EMSURE®	1310-58-3	290, 302, 314	280, 301+330+331, 305+351+338, 308+310	GHS05, GHS07

Product Name	*CAS number*	*H Statements*	*P Statements*	*Hazard Pictogram*
Proteinase K	39450-01-6	315, 319, 334	261, 285, 342+311, 305+351+338, 337+313, 280	GHS07, GHS08
Puromycin	58-58-2	302	264, 270, 301+312, 330, 501	GHS07
RNase A (Qiagen)	-	334, 317	261, 280, 304+340, 342+311	GHS08
Sodium dodecyl sulfate	151-21-3	228, 302+332, 315, 318, 335, 412	210, 273, 280, 301+312, 304+340+312, 305+351+338	GHS02, GHS05, GHS07
Staurosporine, Streptomyces sp.	62996-74-1	361D, 413	201, 202, 273, 280, 308+313, 405	GHS08
Thiocarbohydazide	2231-57-4	300+330, 311	260, 264, 270, 280, 302+352+312, 304+340+310	GHS06
Tipifarnib	192185-72-1	315, 319, 335	261, 264, 271, 280, 302+352, 305+351+338	GHS07
Triton™ X-100	9036-19-5	302, 315, 318, 410	264, 273, 280, 301+312, 302+352, 305+351+338	GHS05, GHS07, GHS09
UHU Plus endfest 33g	-	315, 319, 317, 411	101, 102, 261, 280, 302+352, 305+351+338, 501	GHS07, GHS09
Uranyl Acetate Reagent ACS	6159-44-0	300+330, 373, 411	260, 301+310, 330, 320, 405, 501	GHS06, GHS08, GHS09

Hazard Pictograms and Names (GHS)

GHS 01:
Exploding Bomb

GHS 02:
Flame

GHS 03:
Flame over circle

GHS 04:
Gas cylinder

GHS 05:
Corrosion

GHS 06:
Skull and cross-bones

GHS 07:
Exclamation mark

GHS 08:
Health hazard

GHS 01:
Environment

10.2 Code

Code 1:
Jupyter notebook for batch-denoising of time-lapse imaging data in tiff files.

Noise2Void batch denoising for time-lapse microscopy data

This notebook is adapted from Noise2Void Notebooks from the Jug Lab. https://github.com/juglab/n2v (https://github.com/juglab/n2v) Please follow the instructions from their Github page regarding installation of dependencies.

In [ ]:
```
import sys
from csbdeep.models import Config, CARE
import numpy as np
from csbdeep.utils import plot_some, plot_history
from csbdeep.utils.n2v_utils import manipulate_val_data

from matplotlib import pyplot as plt
import tifffile as tff


import urllib
import os

import zipfile
```

In [ ]:
```
# We need to normalize the data before we feed it into our network, and denormalize i
t afterwards.
def normalize(img, mean, std):
    zero_mean = img - mean
    return zero_mean/std

def denormalize(x, mean, std):
    return x*std + mean
```

In [ ]:
```
if not 'workbookDir' in globals():
    workbookDir = os.getcwd()
os.chdir(workbookDir)
inputpath = workbookDir+'/Input/'
print(os.listdir(inputpath))
```

In [ ]:
```
for file in os.listdir(inputpath):
    config = Config('SYXC', n_channel_in=1, n_channel_out=1, unet_kern_size = 3, trai
n_steps_per_epoch=1000, train_loss='mse',
                batch_norm = True, train_scheme = 'Noise2Void', train_batch_size = 12
8, n2v_num_pix = 64,
                n2v_patch_shape = (64, 64), n2v_manipulator = 'uniform_withCP', n2v_n
eighborhood_radius='5')

    vars(config)
    model = CARE(config, 'n2v_2D', basedir='batchmodels/')
    outputpath = workbookDir+'/Results/'+file+'/'
    if not os.path.exists(outputpath):
        os.mkdir(outputpath)
    img = tff.imread(inputpath+file)
    stacked_img = np.stack((img,)*1, axis=-1)
    img = []
    X = X = np.array(stacked_img)[0:2,...]
    mean, std = np.mean(X), np.std(X)
    X = normalize(X, mean, std)
    # We concatenate an extra channel filled with zeros. It will be internally used f
or the masking.
    Y = np.concatenate((X, np.zeros(X.shape)), axis=3)
    # Load the remaining data as validation data
    X_val = np.array(stacked_img)[3:4,...]
    X_val = normalize(X_val, mean, std)

    # 1. Option
    Y_val = np.concatenate((X_val.copy(), np.zeros(X_val.shape)), axis=3)
    manipulate_val_data(X_val, Y_val,num_pix=256*256/64 , shape=(256, 256))

    # 2. Option
    #Y_val = np.concatenate((X_val.copy(), np.ones(X_val.shape)), axis=3)

    history = model.train(X,Y, validation_data=(X_val,Y_val))
    test_lowSNR = np.array(stacked_img)
    stacked_img = []
    # normalize data with mean and std of the training data
    test_lowSNR = normalize(test_lowSNR, mean, std)
    predictions = []
    # Denoise all images
    for i in range(test_lowSNR.shape[0]):
        predictions.append(denormalize(model.predict(test_lowSNR[i], axes='YXC',norma
lizer=None ), mean, std))
    predictions = np.array(predictions, dtype='uint16')
    outfile=outputpath+'prediction.tif'
    tff.imsave(outfile, predictions, photometric='minisblack')
    predictions=[]
    os.remove(inputpath+file)
```

Code 2:
Tracking information segmenting and search tool – TrISS

Table of Contents

Import Fiji and TrackMate classes

```
import java.util.HashMap
import ij.*
import fiji.plugin.trackmate.*
import fiji.plugin.trackmate.detection.*
import fiji.plugin.trackmate.features.*
import fiji.plugin.trackmate.features.track.*
import fiji.plugin.trackmate.tracking.*
import fiji.plugin.trackmate.visualization.hyperstack.*
```

Set Global settings

```
scaleT=0; %if "1" frame numbers are converted to seconds
```

Get Folder of Files

```
folder=uigetdir("Select masterfolder of the tracking result files");
subdirs = dir(folder);
```

```
Error using dir
Name must be a string scalar or character vector.

Error in TrissV0_5tif (line 20)
subdirs = dir(folder);
```

Load or create Event Database

```
evdbpath=uigetdir('E:\\USERDATA\' ,'Select database directory');
input = inputdlg('enter name of the database here. If it does not
 exist it will be created in the current folder','Enter database
 name');
evdb = char(evdbpath+"\"+input{1,1}+".sqlite");
```

Choose between expanding a database and creating one

```
mksqlite('open', evdb);
if questdlg('Is the database new or do you want to expand an old
 database?','Choose','Create NEW','Expand OLD','Expand OLD')=='Create
 NEW'
    % Set Settings for Trackseparation
    dimnanswer = questdlg('is the data 3D?','Define
 dimensionality','2D','3D','2D');
    switch dimnanswer
        case '2D'
            clipZ=1; %1 in 2D case, 3D data =0
            dimension=2;
        case '3D'
            clipZ=0;
            dimension=3;
    end
    Tracksepprompt = {'Enter minimum tracklength', 'Enter window size
 for track analysis','Enter size for spotmask in micron '...
        , 'Enter size for background mask as multiplicator for the
 spotsize ', 'Enter comparator type for comparison of signals. Enter
 either mean, median or stdev for standard deviation '...
        , 'Enter tolerance in percent for calculation if spotsignal is
 greater than background (When stdev is used enter multiplicator for
 the standard deviation) '...
        , 'Enter channel to be measured (The channel that was not used
 for tracking) '...
        , 'Enter pixel x-correction', 'Enter pixel y-correction'};
    Trackseptitle = 'Setup for Trackseparation';
    Tracksepinput = inputdlg(Tracksepprompt, Trackseptitle);
    minimumtracklength = str2double(Tracksepinput{1,1});
    incrementor = str2double(Tracksepinput{2,1});
    spotsize = str2double(Tracksepinput{3,1});
    bgmasksize = str2double(Tracksepinput{4,1});
    comparator = Tracksepinput{5,1};
    tolerance = str2double(Tracksepinput{6,1});
    channel = str2double(Tracksepinput{7,1});
    xcor = str2double(Tracksepinput{8,1});
    ycor = str2double(Tracksepinput{9,1});
    mksqlite('create table Events (ID number, Image varchar, Path
 varchar, Subcell number, TrackID number, Segment number, Startframe
 number, Endframe number, D_Value number, Description varchar)');
    mksqlite('create table Properties (Dimension number,
 Minimumtracklength number, Windowsize number, Spotsize number,
 Backgroundsize number, Tolerance number, Comparator varchar,
 MeasuredChannel number, Xcor number, Ycor number)');
    mksqlite('insert into Properties (Dimension, Minimumtracklength,
 Windowsize, Spotsize, Backgroundsize, Tolerance, Comparator,
 MeasuredChannel, Xcor, Ycor) values (?,?,?,?,?,?,?,?,?,?)',...
    dimension, minimumtracklength, incrementor, spotsize, bgmasksize,
 tolerance, comparator, channel, xcor, ycor);
```

```
else
    properties = struct2cell(mksqlite('SELECT * from Properties'));
    properties = properties';
    dimension = properties{1,1};
    minimumtracklength = properties{1,2};
    incrementor = properties{1,3};
    spotsize = properties{1,4};
    bgmasksize = properties{1,5};
    tolerance = properties{1,6};
    comparator = properties{1,7};
    channel = properties{1,8};
    xcor = properties{1,9};
    ycor = properties{1,10};
end

NewEventNumber = mksqlite('SELECT Count(*) FROM Events');
NewEventNumber= NewEventNumber.Count___+1;
```

Select analysis modes

```
sellist = {'MSD-based segmentation','Over-local-background-intensity-
based segmentation',...
    'Intensity switch events','Event correlation analysis'};
[indx,tf] = listdlg('ListString', sellist);
```

Set Settings for Correlation

```
if ismember(4,indx)
    CRLprompt = {'Enter amount of correlation events to look for'};
    CRLtitle = 'Setup for Eventcorrelation';
    CRLinput = inputdlg(CRLprompt,CRLtitle);
    crlnb = str2double(CRLinput{1,1});
    qrytbl=cell(crlnb,3);
    for z=1:crlnb
        CRL1prompt = {'Enter amount of Events to look for
 coincidence', 'Name of the State where all events coincide', 'Enter
 frame threshold'};
        CRL1title = 'Setup for Eventcorrelation';
        CRL1input = inputdlg(CRL1prompt,CRL1title);
        CRLdescription = CRL1input{2,1};
        CRLthreshold = str2double(CRL1input{3,1});
        qrydata = cell(str2double(CRL1input{1,1}),1);
        allevents = cell(str2double(CRL1input{1,1}),1);
        for i=1:length(qrydata)
            CRL2prompt = {'enter here the descriptor to search the
 database','Enter minimum descriptive value'};
                CRL2title = 'Set search parameters';
                CRL2input = inputdlg(CRL2prompt,CRL2title);
            qrydata{i,1} = CRL2input{1,1};
            qrydata{i,2} = CRL2input{2,1};
        end
        qrytbl{z,2}=CRLdescription;
        qrytbl{z,3}=CRLthreshold;
```

```
        qrytbl{z,1}=qrydata;
    end
end
```

read in xml files and extract tracks for MSD analyzer and separator

```
%the following loops assume the following directory organization
%Main Folder-->Folders for analyzed Pictures/Videos-->Folders for
 tracks in different Cells
%in the picture-->XML File with the naming >>name_of_Picture/
Video<<_Tracks.xml
if ismember(1,indx)||ismember(2,indx)||ismember(3,indx)
for i=1:length(subdirs)
    if isempty(strfind(subdirs(i).name,'.'))%throw out the obligatory
 "."/".." directorys at the beginning and image files
        subcells=dir([folder '\' subdirs(i).name]);
        picturepath=[folder '\' subdirs(i).name];
        picture=subdirs(i).name;
        cellcount=1;
        for k=1:length(subcells)
            if isempty(strfind(subcells(k).name,'.'))%again throwing
 out "." dirs and files.
                foldernames{i}=subdirs(i).name;
                currentfolder=[folder '\' subdirs(i).name '\'
 subcells(k).name '\'];
                cellnb=subcells(k).name;
                trackingfile=[currentfolder picture '_Tracks.xml'];
                [tracks, metadata]=importTrackMateTracks(trackingfile,
 clipZ, scaleT);
                for t=1:length(tracks) %add identifiers to the tracks.
 Without this the tracks will not be retraceable in the original xml
 after filtering.
                    tracks{t,2}=t;
                end

 [filteredtracks]=trackslengthfilterv2(tracks,minimumtracklength);%Filter
 V2 returns also the original identifier to make retracing in the
 original xml possible.
                % Divide the filtered tracklist into a seperate ID and
                % Tracklist. Otherwise the MSD-analyzer complains.
                IDlist=filteredtracks(:,2);
                filteredtracks=filteredtracks(:,1);
                %-
                %Send the tracklist to the track segmentor one cell at
 a
                %time.
                segtracks={};
                if ismember(1,indx)
                 segtracks{end
+1,1}=msdsep(filteredtracks,incrementor,metadata,dimension,IDlist);
                end
```

```
                if ismember(2,indx)
                 segtracks{end
+1,1}=intensitysep2(filteredtracks,metadata,IDlist,spotsize,bgmasksize,tolerance,c
                end
                %write the returned data into the file reorganize the
 data
                %for storage in the database
                for e=1:length(segtracks)
                 for q=1:length(segtracks{e,1})
                     for w=1:length(segtracks{e,1}{q,1})
                        mksqlite('insert into Events (ID, Image,
 Path, Subcell, TrackID, Segment, Startframe, Endframe, D_Value,
 Description) values (?,?,?,?,?,?,?,?,?,?)',...
                            NewEventNumber, picture, picturepath,
 cellcount, segtracks{e,1}{q,2}, segtracks{e,1}{q,1}{w,1}{1,1},
 segtracks{e,1}{q,1}{w,1}{1,2}, segtracks{e,1}{q,1}{w,1}{1,3},
 segtracks{e,1}{q,1}{w,1}{1,4}, segtracks{e,1}{q,1}{w,1}{1,5});
                        NewEventNumber=NewEventNumber+1;
                    end
                 end
                end
                cellcount=cellcount+1;
            end
        end
    end
end
end
```

Call the Correlator with the query data and write the resulting data back into the database

```
if ismember(4,indx)
    for z=1:crlnb
        CRLdes=qrytbl{z,2};
        CRLthresh=qrytbl{z,3};
        qrydata=qrytbl{z,1};
        correlist = correlator(qrydata, CRLthresh, evdb, CRLdes);
        mksqlite('open', evdb);
        NewEventNumber = mksqlite('SELECT Count(*) FROM Events');
        NewEventNumber= NewEventNumber.Count___+1;
        for w=1:length(correlist)
            mksqlite('insert into Events (ID, Image, Path, Subcell,
 TrackID, Segment, Startframe, Endframe, D_Value, Description) values
 (?,?,?,?,?,?,?,?,?,?)',...
            NewEventNumber, correlist{w,1}{1,1}, correlist{w,1}
{1,2}, correlist{w,1}{1,3},correlist{w,1}{1,4}, correlist{w,1}{1,5},
 correlist{w,1}{1,6}, correlist{w,1}{1,7}, correlist{w,1}{1,8},
 correlist{w,1}{1,9});
            NewEventNumber=NewEventNumber+1;
        end
    end
end
```

Close The Database

```
mksqlite('close');
```

Published with MATLAB® R2019b

```
function
 AboveBackground=AboveBackground(signal,background,comparator,tolerance)
%%This function compares a list of signals from a signal roi to a
%%background roi by a either mean or median or standad deviation
 (comparator) with the specified
%%tolerance (tolerance in percent). If the signal roi comparator
 exceeds the
%%background roi comparator plus tolerance the function returns 1/
true.
if strcmp(comparator,'median')
    bg=median(background);
    sg=median(signal);
elseif strcmp(comparator,'mean')
    bg=mean(background);
    sg=mean(signal);
elseif strcmp(comparator,'stdev')
    bg=std(background);
    sg=mean(signal);
end
if ~strcmp(comparator,'stdev')
    bgcorrected = bg*(1+tolerance/100);
else
    bgcorrected = tolerance*bg+mean(background);
end
if sg>bgcorrected
    AboveBackground=1;
else
    AboveBackground=0;
end
end
```

```
Not enough input arguments.

Error in AboveBackground (line 6)
if strcmp(comparator,'median')
```

Published with MATLAB® R2019b

```
function correlist = correlator(qrydata, threshold, evdb,
 CRLdescription)
%This function correlates the events from the eventlist and returns a
 list
%of events where all the selected events cooccur. The threshold is for
%filtering out correlations that occur over the duration of less
 frames
%than the threshold indicates.
mksqlite('open', evdb);
selectracks = mksqlite('select * from Events where Description = ? and
 d_value >= ?', qrydata{1,1}, qrydata{1,2});
eventlist = qrysort(selectracks);
evnmb = length(qrydata);
correlist = {};
for i=1:size(eventlist,1)
    for k=1:size(eventlist(i,2),1)
        for y=1:size(eventlist{i,2}{k,2},1)
            loseventos = cell(evnmb,1);
            framenumber=[];
            for x=1:size(loseventos,1)
                loseventos{x,1} = struct2cell(mksqlite('select *
 from Events where Image = ? and Subcell = ? and TrackID = ? and
 Description = ? and d_value >= ?',...
                    eventlist{i,1}, eventlist{i,2}{k,1},
 eventlist{i,2}{k,2}{y,1}, qrydata{x,1}, qrydata{x,2}))';
                if max([loseventos{x,1}{:,8}])
                    framenumber(end+1,1)=max([loseventos{x,1}{:,8}]);
                end
            end
            maxframe = max(framenumber);
            %make the calculation matrix
            calcmat = zeros(maxframe+1,evnmb+1);%maxframe+1 because
 frames start at zero so entry 1= frame 0
            for n=1:size(loseventos,1)
                for m=1:size(loseventos{n,1},1)
                    for frame=loseventos{n,1}{m,7}:loseventos{n,1}
{m,8}
                        calcmat(frame+1,n)=1;
                    end
                end
            end
            calcmat(:,evnmb+1)=sum(calcmat,2);
            count=0;
            for g=1:size(calcmat,1)
                if calcmat(g,evnmb+1)==evnmb
                    count=count+1;
                elseif count>=threshold
                    correlist{end+1,1}={loseventos{1,1}{1,2}
 loseventos{1,1}{1,3} loseventos{1,1}{1,4} loseventos{1,1}{1,5} 0 g-2-
count g-2 count CRLdescription};
                    count=0;
                else
```

```
                    count=0;
                end
            end
        end
    end
end
```

```
Not enough input arguments.

Error in correlator (line 6)
mksqlite('open', evdb);
```

Published with MATLAB® R2019b

```
function
 intensitytrackseg=intensitysep2(tracklist,metadata,IDlist,spotsize,bgmasksize,tol
img = bfopen([picturepath '.tif']);
omeMeta = img{1, 4};
%seriesCount = size(img, 1);
%series1 = img{1, 1};
%series1_colorMaps = img{1, 3};
%series1_planeCount = size(series1, 1);
%series1_plane1 = series1{1, 1};
%imshow(series1_plane1, []);

% read general properties from header
stackSizeX = omeMeta.getPixelsSizeX(0).getValue; % image width, pixels
stackSizeY = omeMeta.getPixelsSizeY(0).getValue; % image height,
 pixels
stackSizeZ = omeMeta.getPixelsSizeZ(0).getValue; % number of Z slices
stackSizeC = omeMeta.getPixelsSizeC(0).getValue; % number of channels
stackSizeT = omeMeta.getPixelsSizeT(0).getValue; % number of T slices
voxelSizeX = double(omeMeta.getPixelsPhysicalSizeX(0).value()); % in
 #m
voxelSizeY = double(omeMeta.getPixelsPhysicalSizeY(0).value()); % in
 #m
if omeMeta.getPixelsPhysicalSizeZ(0)
    voxelSizeZ = double(omeMeta.getPixelsPhysicalSizeZ(0).value()); %
 in #m
end
dimension=2;
if omeMeta.getPixelsPhysicalSizeZ(0)
    dimension=3;
end
pixelspotsize=ceil(spotsize/((voxelSizeX+voxelSizeY)/2));%always
 rounds up the spotsize that it is rather bigger than smaller

%totalpicnumber=stackSizeC*stackSizeT*stackSizeZ;
%framedata=zeros(totalpicnumber,4);
%for i=1:totalpicnumber
%    framedata(i,1)=double(omeMeta.getPlaneDeltaT(0,i).value());
%    framedata(i,2)=omeMeta.getPlaneTheC(0,i).getValue();
%    framedata(i,3)=omeMeta.getPlaneTheT(0,i).getValue();
%    framedata(i,4)=omeMeta.getPlaneTheZ(0,i).getValue();
%end

signaltbl = cell(length(tracklist),1);%preallocate a cell array with
 the length of the tracklist
for i=1:length(signaltbl)
    signaltbl{i,1}=zeros(length(tracklist{i,1}),1);%preallocate a
 table with the length of the track in that position
    for k=1:length(tracklist{i,1})
        frame=stackSizeC*(tracklist{i,1}(k,1)+1)-(stackSizeC-channel);
        foi=img{1,1}{frame,1};
        foi=imrotate(foi,270);
        foi=flip(foi,2);
```

```
        rois=ROIandDonut(round(tracklist{i,1}(k,2)/voxelSizeX),
 round(tracklist{i,1}(k,3)/voxelSizeY), pixelspotsize,
 bgmasksize,stackSizeX,stackSizeY);
        imgvalues=cell(1,2);
        imgvalues{1,1}=zeros(length(rois{1,1}),1);
        imgvalues{1,2}=zeros(length(rois{1,2}),1);
        for g=1:length(rois{1,1})
                imgvalues{1,1}(g,1)=foi(rois{1,1}(g,1)+xcor,rois{1,1}
(g,2)+ycor);
        end
        for g=1:length(rois{1,2})
                imgvalues{1,2}(g,1)=foi(rois{1,2}(g,1)+xcor,rois{1,2}
(g,2)+ycor);
        end
        %figure(k) plotting the background roi into the tracking
 channel
        %imshow(img{1,1}{frame+1,1},'DisplayRange',[0 10000]);
        %hold on
        %scatter(rois{1,2}(:,1),rois{1,2}(:,2));
        %hold off

        signaltbl{i,1}
(k,1)=AboveBackground(imgvalues{1,1},imgvalues{1,2},comparator,tolerance);
    end
end
%define a cell array for the separated tracks
intensitytrackseg={};
%c is a seperate counter of the Track IDs since too short tracks will
 have
%an empty alphatable and therefore be ignored in the loop.
c=1;
for i=1:length(signaltbl)
    if ~isempty(signaltbl{i,1})
        %send the alphatable to the segmentor function one track at a
 time
        intensitytrackseg{end+1,1}=intsegmentor(signaltbl{i,1},1,1,
{},0);
        intensitytrackseg{c,2}=IDlist{i,1};
        for k=1:length(intensitytrackseg{c,1}) %rewrite start and
 endframe to the real frames
            intensitytrackseg{i,1}{k,1}{1,2}=tracklist{i,1}
(intensitytrackseg{i,1}{k,1}{1,2},1);
            intensitytrackseg{i,1}{k,1}{1,3}=tracklist{i,1}
(intensitytrackseg{i,1}{k,1}{1,3},1);
        end
        c=c+1;
    end

end

end
%segmentor
%Uses a recursive loop to check if the value before fits to the same
```

```
%category as the current value. If not it counts up the segment number
 and
%adds a line to the segtable containing #, start and end of the
 segment
%the envelopment status in the segment and a descriptor string.
function segtable =
 intsegmentor(signallist,x,segment,pretable,prestatus)
if signallist(x,1)>0 %1 means signal is higher than background -->
 possibly enveloped particle
    status=1;
else
    status=0;
end
if x==1 %At x==1 we are in the beginning of the track which means no
 comparison can be made
    prestatus=status;
end
if status==prestatus&&x<length(signallist) %In this case the category
 does not change and we are in the middle of the track.
    prestatus=status;
    segtable=pretable;
    x=x+1;
    segtable=intsegmentor(signallist,x,segment,segtable,prestatus);
elseif status~=prestatus&&x<length(signallist) %In this case the
 category changes in the middle of the track
    if segment==1 %If it is the first segment the startframe will be 1
        startx=1;
    else %If not the startframe has to be calculated from the frame
 number at the end of the previous segment in the pretable
        startx=pretable{segment-1,1}{1,3}+1;
    end
    %decide in which category the segment belongs to
    if prestatus>0
        descriptor = 'abovebg';
    else
        descriptor = 'belowbg';
    end
    %make the new row for the segtable
    newrow={segment startx x prestatus descriptor}; %calculate start
 and endframe of the segment with the window size.
    %The table to be returned takes over the values from the previous
    %iteration
    segtable=pretable;
    %append the new row to the table
    segtable{end+1,1}=newrow;
    %count up the segment number
    segment=segment+1;
    %prestatus is the new status
    prestatus=status;
    %move one further on the track intensities and continue with the
 next loop
    x=x+1;
    segtable=intsegmentor(signallist,x,segment,segtable,prestatus);
```

```
else % if there is only one envelopment status in the whole track
 return one row with the appropriate description.
    if segment==1
        startx=1;
    else
        startx=pretable{segment-1,1}{1,3}+1;
    end
    if status>0
        descriptor = 'abovebg';
    else
        descriptor = 'belowbg';
    end
    newrow={segment startx x status descriptor};
    segtable=pretable;
    segtable{end+1,1}=newrow;

end
end
```

```
Not enough input arguments.

Error in intensitysep2 (line 2)
img = bfopen([picturepath '.tif']);
```

Published with MATLAB® R2019b

```
function alphatrackseg =
 msdsep(tracklist,incrementor,metadata,dimension,IDlist)
%This function is an MSD-Based Track Separator
%Plot all Tracks of the Cell
ma = msdanalyzer(dimension, metadata.spaceUnits, metadata.timeUnits);
ma = ma.addAll(tracklist);
ma.plotTracks;
ma.labelPlotTracks;
%run a sliding window over the tracks and generate a list of time
 resolved
%alphas
alphatable=cell(length(tracklist),1);
counter=1;
errorcounter=0;
for i=1:length(tracklist)
    %determine how many windows have to be analyzed in the track
 dataset.
    windows=length(tracklist{i,1})-incrementor;
    %make list of all alpha values for the windows of each track in
 the
    %cell.
    alphalist=zeros(windows,1);
    for k=1:windows
        counter=counter+1;
        % initiate MSD analyzer file
        ma = msdanalyzer(dimension, metadata.spaceUnits,
 metadata.timeUnits);
        %generate tracklist out of the track positions inside the
 current window.
        currenttracks={};
        currenttracks{1,1}=tracklist{i,1}(k:k+incrementor-1,:);
        %send the tracks inside the window to the msd analyzer
        ma = ma.addAll(currenttracks);
        ma = ma.computeMSD;
        ma = ma.fitLogLogMSD(0.5);
        ma.loglogfit;
        mean(ma.loglogfit.alpha);
        r2fits = ma.loglogfit.r2fit;
        %only take good fits into account.
        if r2fits>=0.8
            alphalist(k,1) = ma.loglogfit.alpha;
        else
            %This definitely needs to be revised! If the fit r2 fit is
 not
            %good enough the alpha value of the calculation before
 will be
            %taken assuming the movement mode did not change.
            errorcounter=errorcounter+1;
            if k-1>=1
                alphalist(k,1) = alphalist(k-1,1);
            else
```

```
                %If we are in the beginning of the track we assume
 free
                %diffusion if the fit is not good enough
                alphalist(k,1) = 1;
            end
        end
    end
    %store the alphas for the tracks in a separate cell for each track
 in
    %the alphatable
    alphatable{i,1}=alphalist;
end
errorrate=(errorcounter/counter)*100;
string=['Errorrate in fitting the curve was ' num2str(errorrate) '%']
%define a cell array for the separated tracks
alphatrackseg={};
%c is a seperate counter of the Track IDs since too short tracks will
 have
%an empty alphatable and therefore be ignored in the loop.
c=1;
for i=1:length(alphatable)
    if ~isempty(alphatable{i,1})
        %send the alphatable to the segmentor function one track at a
 time
        alphatrackseg{end
+1,1}=alphasegmentor(alphatable{i,1},1,incrementor,1,{},0);
        alphatrackseg{c,2}=IDlist{i,1};
        for k=1:length(alphatrackseg{c,1}) %rewrite startframe and
 endframe to actual frames in the picture
            alphatrackseg{c,1}{k,1}{1,2}=tracklist{i,1}
(alphatrackseg{c,1}{k,1}{1,2},1);
            alphatrackseg{c,1}{k,1}{1,3}=tracklist{i,1}
(alphatrackseg{c,1}{k,1}{1,3},1);
        end
        c=c+1;
    end

end
end
%segmentor
%Uses a recursive loop to check if the value before fits to the same
%category as the current value. If not it counts up the segment number
 and
%adds a line to the segtable containing #, start and end of the
 segment
%the mean alpha value in the segment and the description of the
 movement
%mode.
function segtable =
 alphasegmentor(trackalphas,x,window,segment,pretable,prefall)
if trackalphas(x,1)<=0.8 %alphas up to 0.8 are considered as
 restricted diffusion
    fall=1;
```

```
elseif trackalphas(x,1)>0.8&&trackalphas(x,1)<1.2 %alphas above 0.8 up
 to 1.2 are considered free diffusion
    fall=2;
elseif trackalphas(x,1)>1.2 %alphas above 1.2 are considered active
 transport
    fall=3;
end
if x==1 %At x==1 we are in the beginning of the track which means no
 comparison can be made
    prefall=fall;
end
if fall==prefall&&x<length(trackalphas) %In this case the category
 does not change and we are in the middle of the track.
    prefall=fall;
    segtable=pretable;
    x=x+1;

 segtable=alphasegmentor(trackalphas,x,window,segment,segtable,prefall);
elseif fall~=prefall&&x<length(trackalphas) %In this case the category
 changes in the middle of the track
    prefall=fall;
    if segment==1 %If it is the first segment the startframe will be 1
        startx=1;
    else %If not the starting alpha has to be calculated from the
 frame number at the end of the previous segment in the pretable and
 the window size
        startx=pretable{segment-1,1}{1,3}+1-window/2;
    end
    %calculate the mean alphavalue in the segment
    segmean=mean(trackalphas(startx:x,1));
    %decide in which category the mean alpha fits
    if segmean<0.8
        descriptor = 'restricted diffusion';
    elseif segmean>=0.8&&segmean<1.1
        descriptor = 'diffusion';
    elseif segmean>=1.1
        descriptor = 'active transport';
    end
    %make the new row for the segtable
    newrow={segment startx+window/2 x+window/2 segmean
 descriptor}; %calculate start and endframe of the segment with the
 window size. Endframe is defined by the middle of the window in which
 the alpha changes the category.
    %The table to be returned takes over the values from the previous
    %iteration
    segtable=pretable;
    %append the new row to the table
    segtable{end+1,1}=newrow;
    %count up the segment number
    segment=segment+1;
    %move one further on the track alphas and continue with the next
 loop
    x=x+1;
```

```
 segtable=alphasegmentor(trackalphas,x,window,segment,segtable,prefall);
else % if there is only one movement mode in the whole track calculate
 the mean alpha and return the row with the appropriate description.
    if segment==1
        startx=1;
    else
        startx=pretable{segment-1,1}{1,3}+1-window/2;
    end
    segmean=mean(trackalphas(startx:x,1));
    if segmean<0.8
        descriptor = 'restricted diffusion';
    elseif segmean>=0.8&&segmean<1.1
        descriptor = 'diffusion';
    elseif segmean>=1.1
        descriptor = 'active transport';
    end
    newrow={segment startx+window/2 x+window/2 segmean descriptor};
    segtable=pretable;
    segtable{end+1,1}=newrow;

end
end
```

```
Not enough input arguments.

Error in msdsep (line 4)
ma = msdanalyzer(dimension, metadata.spaceUnits, metadata.timeUnits);
```

Published with MATLAB® R2019b

Table of Contents

Import Fiji and TrackMate classes

```
import java.util.HashMap
import ij.*
import fiji.plugin.trackmate.*
import fiji.plugin.trackmate.detection.*
import fiji.plugin.trackmate.features.*
import fiji.plugin.trackmate.features.track.*
import fiji.plugin.trackmate.tracking.*
import fiji.plugin.trackmate.visualization.hyperstack.*
%addpath 'D:\fiji-win64\Fiji.app\scripts'
```

Information about the tracked data for trackmate

```
%Later store this info in database?
scaleT=0;
```

Access Database

```
evdbpath=uigetdir('E:\\USERDATA\' ,'Select database directory');
input = inputdlg('enter name of the database here','Enter database
 name');
%evdb = input{1};
evdb = char(evdbpath+"\"+input{1,1}+".sqlite");
mksqlite('open', evdb);
spotsize=struct2cell(mksqlite('SELECT Spotsize from Properties'));
spotsize=spotsize{1,1};
```

```
Index in position 1 exceeds array bounds.

Error in EventVizualizerV8 (line 18)
evdb = char(evdbpath+"\"+input{1,1}+".sqlite");
```

Prompt for Visualization options

```
charanswer = questdlg('Options','Options','Vizualization of
 Events','Database Properties','Vizualization of Events');
```

```
switch charanswer
    case 'Vizualization of Events'
```

Query the Database

```
    charanswer = questdlg('For how many events are you looking in the
tracks?','/??_?\?','1','2','3','1');
    switch charanswer
        case '1'
            prompt = {'enter here the descriptor to search the
database','Enter minimum descriptive value'};
            title = '/??_?\?';
            input = inputdlg(prompt,title);
            selectracks = mksqlite('select * from Events where
Description = ? and d_value >= ?', input{1,1}, input{2,1});
            evnb = 1;
        case '2'
            prompt = {'enter here the descriptor to search the
database','Enter minimum descriptive value',...
                'enter here the descriptor to search the database
2','Enter minimum descriptive value 2'};
            title = '/??_?\?/??_?\?';
            input = inputdlg(prompt,title);
            selectracks = mksqlite('select * from Events where
Description = ? and d_value >= ? or Description = ? and d_value
>= ?',...
                input{1,1}, input{2,1}, input{3,1}, input{4,1});
            evnb = 2;
        case '3'
            prompt = {'enter here the descriptor to search the
database','Enter minimum descriptive value',...
                'enter here the descriptor to search the database
2','Enter minimum descriptive value 2',...
                'enter here the descriptor to search the database
3','Enter minimum descriptive value 3'};
            title = '/??_?\?/??_?\?/??_?\?';
            input = inputdlg(prompt,title);
            selectracks = mksqlite('select * from Events where
Description = ? and d_value >= ? or Description = ? and d_value >= ?
or Description = ? and d_value >= ?',...
                input{1,1}, input{2,1}, input{3,1}, input{4,1},
input{5,1}, input{6,1});
            evnb = 3;
    end
    properties = mksqlite('select * from Properties');
    properties = struct2cell(properties);
    if properties{1,1}==2
        clipZ=1;
        dimensions=2;
    elseif properties{1,1}==3
        clipZ=0;
        dimensions=3;
    else
```

```
        fprintf('No dimensionality info saved in database');
    end
```

Sort Eventlist by Image,Cell and Track

```
    if length(selectracks)>1
        events = qrysort(selectracks);
        trackcount=0;
        tracklist={};
        for i=1:size(events,1)
            for k=1:size(events{i,2},1)
                for j=1:size(events{i,2}{k,2},1)
                    if length(unique(events{i,2}{k,2}{j,2}
(:,2)))==evnb
                        tracklist{end+1,1} = {events{i,1},
 events{i,3}, events{i,2}{k,1},events{i,2}{k,2}{j,1}};
                        trackcount = trackcount+1;
                    end
                end
            end
        end
    elseif length(selectracks)==1
        tracklist={};
        events = struct2cell(selectracks)';
        trackcount = 1;
        tracklist{end+1,1} = {events{1,2}, events{1,3},
 events{1,4},events{1,5}};
    else
        trackcount = 0;
    end

    resultprompt = [num2str(trackcount) ' tracks were found. How do
 want to proceed?'];
    charanswer = questdlg(resultprompt,'Vizualization options'...
        ,'give me a random cell','give me all cells','give me all
 cells');
    switch charanswer
        case 'give me a random cell'
            randomnumber = ceil(rand(1)*size(tracklist,1));
            cellid = tracklist{randomnumber,1}{1,3};
            cellpath = [tracklist{randomnumber,1}{1,2} '\Cell'
 num2str(cellid)];
            path = tracklist{randomnumber,1}{1,2};
            image = [tracklist{randomnumber,1}{1,2} '.tif'];
            xml = [tracklist{randomnumber,1}{1,2}...
                '\Cell' num2str(tracklist{randomnumber,1}{1,3}) '\'
 tracklist{randomnumber,1}{1,1} '_Tracks.xml'];
            toilist=[];
            for z=1:size(tracklist,1)
               if strcmp(tracklist{z,1}{1,1},tracklist{randomnumber,1}
{1,1})&&tracklist{z,1}{1,3}==tracklist{randomnumber,1}{1,3}
                    toilist=[toilist; tracklist{z,1}{1,4}];
               end
```

```
            end

 overlayprinttxt(image,xml,toilist,clipZ,scaleT,cellpath,spotsize,cellid)
                for t = 1:size(toilist,1)
                  roadmapfile = [cellpath...
                       '\' num2str(toilist(t,1)) '_Roadmap.csv'];
                    roadmap = struct2table(mksqlite('select * from
 Events where Subcell = ? and Path = ? and TrackID = ?',...
                        cellid, path, toilist(t,1)));
                    writetable(roadmap,roadmapfile);
                end

        case 'give me all cells'
            k=1;
        while (k < size(tracklist,1))
                cellid = tracklist{k,1}{1,3};
                cellpath = [tracklist{k,1}{1,2} '\Cell'
 num2str(cellid)];
                path = tracklist{k,1}{1,2};
                image = [tracklist{k,1}{1,2} '.tif'];
                xml = [tracklist{k,1}{1,2}...
                    '\Cell' num2str(tracklist{k,1}{1,3}) '\'
 tracklist{k,1}{1,1} '_Tracks.xml'];
                toilist=[tracklist{k,1}{1,4}];
               for z=k+1:size(tracklist,1)
                   if strcmp(tracklist{z,1}{1,1},tracklist{k,1}
{1,1})&&tracklist{z,1}{1,3}==tracklist{k,1}{1,3}...
                            && z < size(tracklist,1)
                        toilist=[toilist; tracklist{z,1}{1,4}];
                   else
                       k=z;
                       break
                   end
               end

 overlayprinttxt(image,xml,toilist,clipZ,scaleT,cellpath,spotsize,cellid)
                for t = 1:size(toilist,1)
                   roadmapfile = [cellpath...
                        '\' num2str(toilist(t,1)) '_Roadmap.csv'];
                    roadmap = struct2table(mksqlite('select * from
 Events where Subcell = ? and Path = ? and TrackID = ?',...
                        cellid, path, toilist(t,1)));
                    writetable(roadmap,roadmapfile);
                end
           end

    end

   case 'Database Properties'
        properties = mksqlite('select * from Properties');
        evttype = mksqlite('select distinct Description from Events');
        evtype = struct2cell(evttype)';
        evtype = [evtype cell(size(evtype,1),1)];
        for i=1:size(evtype,1)
```

```
            evcount = struct2cell(mksqlite('Select count(*) from
 Events where Description = ?', evtype{i,1}));
            evtype(i,2) = evcount(1,1);
        end
end
```

Close the Database

```
mksqlite('close');
```

Published with MATLAB® R2019b

Table of Contents


```
function
 overlayprinttxt=overlayprinttxt(image,xml,toilist,clipZ,scaleT,path,spotsize,cell

%This function takes an Image path, the corresponding Trackmate XML, a
 list
%of tracks of interest, the dimensionality information for trackmate
 and an
%outputpath to print the toi
import java.util.HashMap
import ij.*
import fiji.plugin.trackmate.*
import fiji.plugin.trackmate.detection.*
import fiji.plugin.trackmate.features.*
import fiji.plugin.trackmate.features.track.*
import fiji.plugin.trackmate.tracking.*
import fiji.plugin.trackmate.visualization.hyperstack.*
%addpath 'D:\fiji-win64\Fiji.app\scripts'
```

fixed properties

```
bgmasksize = 1.5;
```

Code pt. I loading data

```
img = bfopen(image);
omeMeta = img{1, 4};
[tracks, metadata]=importTrackMateTracks(xml, clipZ, scaleT);
stackSizeX = omeMeta.getPixelsSizeX(0).getValue; % image width, pixels
stackSizeY = omeMeta.getPixelsSizeY(0).getValue; % image height,
 pixels
stackSizeZ = omeMeta.getPixelsSizeZ(0).getValue; % number of Z slices
stackSizeC = omeMeta.getPixelsSizeC(0).getValue; % number of channels
stackSizeT = omeMeta.getPixelsSizeT(0).getValue; % number of T slices
voxelSizeX = double(omeMeta.getPixelsPhysicalSizeX(0).value()); % in
 #m
voxelSizeY = double(omeMeta.getPixelsPhysicalSizeY(0).value()); % in
 #m
if omeMeta.getPixelsPhysicalSizeZ(0)
    voxelSizeZ = double(omeMeta.getPixelsPhysicalSizeZ(0).value()); %
 in #m
end
```

```
dimension=2;
if omeMeta.getPixelsPhysicalSizeZ(0)
    dimension=3;
end
pixelspotsize=ceil(spotsize/((voxelSizeX+voxelSizeY)/2));%always
 rounds up the spotsize that it is rather bigger than smaller
```

Not enough input arguments.

Error in overlayprinttxt (line 18)
img = bfopen(image);

make overlay images

```
ovl=zeros(size(img{1,1}{1,1},2),size(img{1,1}
{1,1},1),size(img{1,1},1)/stackSizeC);
ovl=uint16(ovl);
for i=1:size(toilist,1)
    thetrack=tracks{toilist(i,1),1};
    for k=1:size(thetrack,1)
        rois=ROIandDonut(round(thetrack(k,2)/voxelSizeX),
 round(thetrack(k,3)/voxelSizeY), pixelspotsize,
 bgmasksize,stackSizeX,stackSizeY);
        for g=1:length(rois{1,2})
            ovl(rois{1,2}(g,1),rois{1,2}(g,2),thetrack(k,1)+1) =
 65535;
        end
        txtposition = [max(rois{1,2}(:,2)),max(rois{1,2}(:,1))];
        ovl(:,:,thetrack(k,1)+1) =
 rgb2gray(insertText(ovl(:,:,thetrack(k,1)+1), txtposition,
 num2str(toilist(i,1)),...
            'TextColor', 'White',...
            'FontSize', 10,...
            'BoxOpacity', 0));
    end
end
```

Write the mask Tiff

```
t = Tiff([path '/trackoutput.tif'],'w8');
ovl=uint16(ovl);
ovl = imrotate(ovl,270);
ovl=flip(ovl,2);
for i=1:size(ovl,3)


t = Tiff([path '/trackoutput.tif'],'a');

tagstruct.ImageLength = size(ovl,1);
tagstruct.ImageWidth = size(ovl,2);
tagstruct.Photometric = Tiff.Photometric.MinIsBlack;
tagstruct.SampleFormat = Tiff.SampleFormat.UInt;
tagstruct.Compression = Tiff.Compression.None;
```

```
tagstruct.BitsPerSample = 16;
tagstruct.SamplesPerPixel = 1;
tagstruct.RowsPerStrip = 1;
tagstruct.PlanarConfiguration = Tiff.PlanarConfiguration.Chunky;
tagstruct.Software = 'MATLAB';
t.setTag(tagstruct);


t.write(ovl(:, :, i));

t.close();
end
overlayprinttxt = ['overlay for cell ' num2str(cellid) ' was printed
 in ' path ' as trackoutput.tif']
```

Published with MATLAB® R2019b

```
function querysorter = qrysort(evtlist)
%This function sorts the result from a query on a Triss Database into
 a
%cell array.
evtlist=struct2cell(evtlist)';
events = sortrows(evtlist, [2 4 5]);
querysorter={};
imagecount=0;
trackcount=0;
for i=1:length(events)
    if ~any(strcmp(querysorter,events{i,2}))
        querysorter{end+1,1}=events{i,2};
        querysorter{size(querysorter,1),3}=events{i,3};
        imagecount=size(querysorter,1);
        querysorter{imagecount,2}={};
        querysorter{imagecount,2}{end+1,1}=events{i,4};
        cellcount=size(querysorter{imagecount,2},1);
        querysorter{imagecount,2}{cellcount,2}={};
        querysorter{imagecount,2}{cellcount,2}{end+1,1}=events{i,5};
        trackcount=size(querysorter{imagecount,2}{cellcount,2},1);
        querysorter{imagecount,2}{cellcount,2}{trackcount,2}={};
        querysorter{imagecount,2}{cellcount,2}{trackcount,2}{end
+1,1}=events{i,1};
        querysorter{imagecount,2}{cellcount,2}{trackcount,2}
{end,2}=events{i,10};
    elseif ~ismember(events{i,4},querysorter{imagecount,2}
{cellcount,1})
        imagecount=size(querysorter,1);
        querysorter{imagecount,2}{end+1,1}=events{i,4};
        cellcount=size(querysorter{imagecount,2},1);
        querysorter{imagecount,2}{cellcount,2}={};
        querysorter{imagecount,2}{cellcount,2}{end+1,1}=events{i,5};
        trackcount=size(querysorter{imagecount,2}{cellcount,2},1);
        querysorter{imagecount,2}{cellcount,2}{trackcount,2}={};
        querysorter{imagecount,2}{cellcount,2}{trackcount,2}{end
+1,1}=events{i,1};
        querysorter{imagecount,2}{cellcount,2}{trackcount,2}
{end,2}=events{i,10};
    elseif ~ismember(events{i,5},querysorter{imagecount,2}
{cellcount,2}{trackcount,1})
        imagecount=size(querysorter,1);
        cellcount=size(querysorter{imagecount,2},1);
        querysorter{imagecount,2}{cellcount,2}{end+1,1}=events{i,5};
        trackcount=size(querysorter{imagecount,2}{cellcount,2},1);
        querysorter{imagecount,2}{cellcount,2}{trackcount,2}={};
        querysorter{imagecount,2}{cellcount,2}{trackcount,2}{end
+1,1}=events{i,1};
        querysorter{imagecount,2}{cellcount,2}{trackcount,2}
{end,2}=events{i,10};
    else
        imagecount=size(querysorter,1);
        cellcount=size(querysorter{imagecount,2},1);
```

```
        trackcount=size(querysorter{imagecount,2}{cellcount,2},1);
        querysorter{imagecount,2}{cellcount,2}{trackcount,2}{end
+1,1}=events{i,1};
        querysorter{imagecount,2}{cellcount,2}{trackcount,2}
{end,2}=events{i,10};
    end
end
```

```
Not enough input arguments.

Error in qrysort (line 4)
evtlist=struct2cell(evtlist)';
```

Published with MATLAB® R2019b

Code 3:
Spatial colocalization analysis

Spatial Colocalization Analysis

General Info

This script takes two images as input and creates a heatmap which is supposed to highlight the areas in the image where the two channels colocalize. The idea behind the script is to normalize both channels to relative intensities and then compare the pixel values for both channels. For this, the pixel values are interpreted as a vector (int_channel_A, int_int_channel_B). In a classical 2D coordinate system this vector starts at (0,0) and has two properties: Length and Angle. The higher the intensities in the channels,the greater the length of the vector and the closer the angle is to 45° the more similar is the relative brightness in both channels. This tool calculates the heatmap intensity of each pixel by calculating the length of the vector and multiply it by y=1-(|cos(x)-sin(x)|), whereby y = 0 at angles of 0° and 90° and y = 1 at the 45° angle.
grafik.png
By this multiplication the pixels increase in brightness the more similar their relative intensities in the two channels and are darker the more dissimilar their relative intensities are. This tool is especially designed to show spatial relation between colocalizing pixels. It is of limited use to determine the biological relevance of the colocalization because it highlights areas just based on the similarities of their relative intensities.

How to use this skript

0) You may need to install at least the tifffile library if you already use anaconda3

1) Copy two one channel tiffs in the input folder in the directory of this notebook.

2) Run all the boxes from the skript.

3) Save resulting figure.

In [1]:
```
from mpl_toolkits import mplot3d
%matplotlib inline
import numpy as np
import sys
from matplotlib import pyplot as plt
import tifffile as tff
import os
import zipfile
```

In [2]:
```
if not 'workbookDir' in globals():
    workbookDir = os.getcwd()
os.chdir(workbookDir)
inputpath = workbookDir+'/Input/' #This is the default input path. Make sure you have only two single channel tiffs in this folder
plt.rcParams['figure.figsize'] = [60/2.54, 40/2.54] #Change this if you want to change the output figure size
```

In [8]:
```
#Here the two tiffs are loaded and copied into a single array. The data is normalized
on the maximum value
#In the end the array shape and pictures are shown for verification.
i=0
for file in os.listdir(inputpath):
    img = tff.imread(inputpath+file)
    img = np.stack((img,)*1, axis=-1)
    X = np.array(img).astype(np.int)
    maxi = np.max(X)
    X = np.true_divide(X,maxi)

    if i==0 :
        array = X
    else :
            array = np.concatenate((array, X), axis=2)
    i=i+1
plt.figure(figsize=(5, 5))
plt.imshow(array[:,:,0], cmap="cubehelix")
plt.figure(figsize=(5, 5))
plt.imshow(array[:,:,1], cmap="cubehelix")
print(array.shape)
```

```
(269, 269, 2)
```

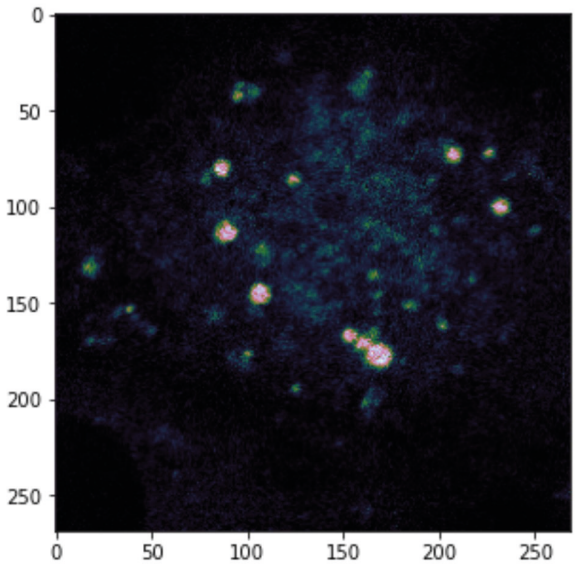

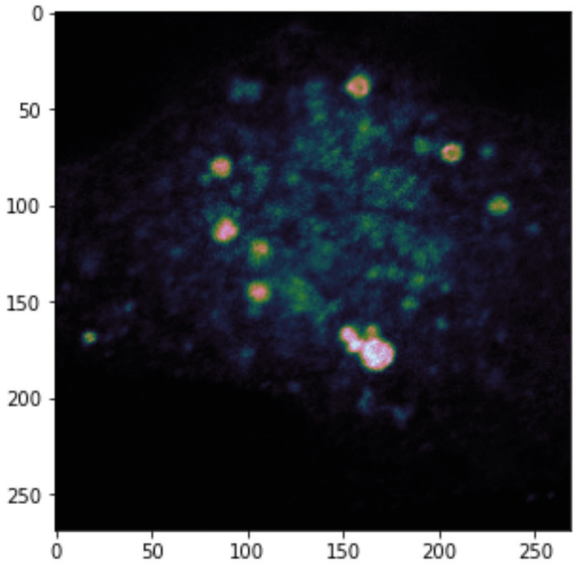

In [9]:
```
# Here the calculations are done. Via pythagoras the ctmap is generated with the vect
or lengths. Cosmaps and Sinmaps are
# created by calculating the angle of the vector to the x-axis.
# Finally the colmap is generated by the formula described above in the general info
section.
sqarray = array**2
ctmap = sqarray[:,:,0]+sqarray[:,:,1]
ctmap = ctmap**0.5
cosmap = np.divide(array[:,:,0], ctmap, out=np.zeros_like(array[:,:,0]), where=ctmap!
=0)
sinmap = np.divide(array[:,:,1], ctmap, out=np.zeros_like(array[:,:,1]), where=ctmap!
=0)
colmap = ctmap*(1-abs(cosmap-sinmap))
plt.imshow(colmap, cmap="cubehelix")
plt.clim(0,1)
#plt.imshow(ctmap, cmap="cubehelix") #This command will show the ct-map with the just
the vector lengths
plt.colorbar()
```

Out[9]: <matplotlib.colorbar.Colorbar at 0x1b008ea1c40>

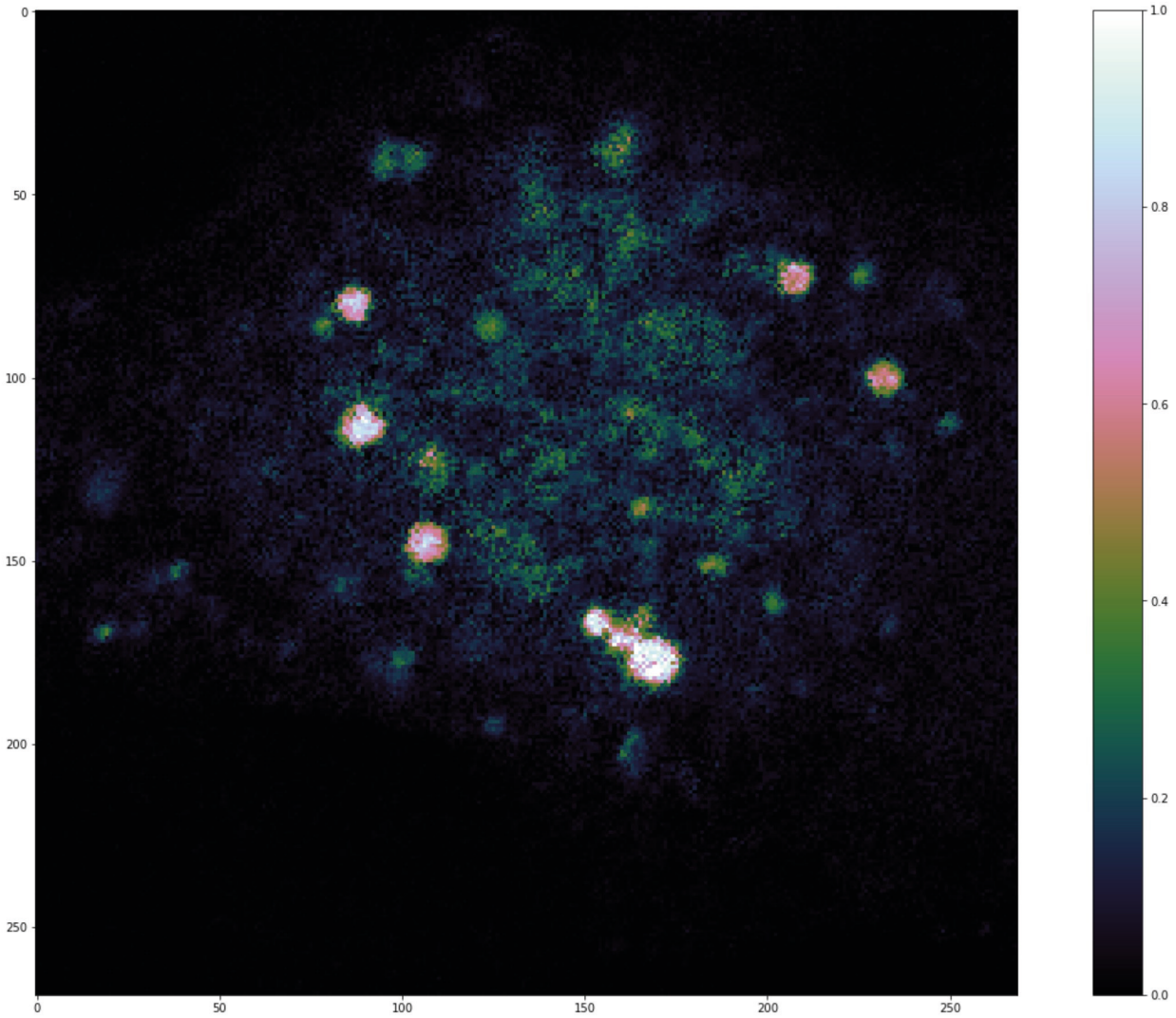

In [6]:
```
#This plot will give you a 3D visualization of the colmap data.
fig = plt.figure()
ax = plt.axes(projection='3d')
xl=np.linspace(0,len(colmap[1,:])-1,len(colmap[1,:]))
yl=np.linspace(0,len(colmap[:,1])-1,len(colmap[:,1]))
print(np.shape(xl))
print(np.shape(yl))
print(np.shape(colmap))
X,Y = np.meshgrid(xl,yl)
ax.plot_surface(X,Y,colmap,cmap='inferno')
ax.set_xlabel('x')
ax.set_ylabel('y')
ax.set_zlabel('coloc');
ax.view_init(60, 35)
```

```
(131,)
(131,)
(131, 131)
```

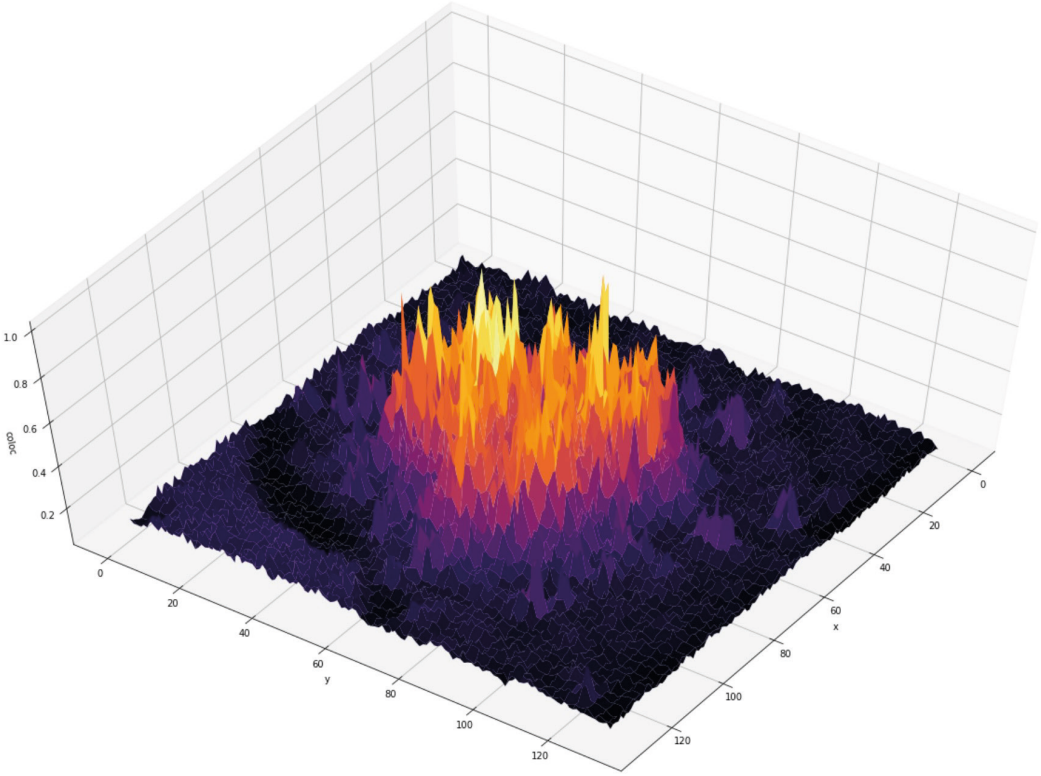

In [ ]:

11 Acknowledgements

Firstly, I want to thank my supervisors, Jens Bosse, Kay Grünewald and Rudolph Reimer, for their support, guidance and advice that made this work possible. Also, I want to thank Timothy Soh for his day-to-day guidance and support in the experimental work in the lab. Moreover, I want to thank all current, former and associated members of the Bosse group for helpful and inspiring discussion, collaboration and fun times inside and outside the lab.

I also want to thank all people who contributed to this work by providing reagents, protocols and helpful advice: Christian Sinzger and Kerstin Sampaio for their short notice, almost next-day sending of HCMV-Merlin virus stocks during a stressful manuscript revision process. Carola Schneider for support with her invaluable expertise in electron microscopy. Wolfram Brune and his lab members (especially Giada Frascaroli, Jiajia Tang and Elena Muscolino) for providing expertise, material, tips and tricks about HCMV virology. Big thanks also go out to everyone who critically read this dissertation and provided all the helpful feedback on how to improve this work.

Moreover, I want to thank the organizations, who funded this research. I am grateful to the Studienstiftung des deutschen Volkes for their financial support and the opportunities for exchange with other fellows from different fields. Also, I want to thank the Wellcome trust, who funded the big grant, in which my little project was embedded.

Finally, I want to thank my family and my girlfriend, Julia, without whose endless support I could not imagine being where I am now.

Thank you!

12 Statement of Authorship

I hereby declare on oath that this doctoral dissertation is written independently and solely by my own based on the original work of my PhD and has not been used other than the acknowledged resources and aids. The submitted written version corresponds to the version on the electronic storage medium. I declare that the present dissertation was prepared maintaining the Rules of Good Scientific Practice of the German Research Foundation and it has never been submitted in the present form or similar to any other University or board of examiners. | Hiermit versichere ich an Eides statt, die vorliegende Dissertation selbst verfasst und keine anderen als die angegebenen Hilfsmittel benutzt zu haben. Die eingereichte schriftliche Fassung entspricht der auf dem elektronischen Speichermedium. Ich versichere, dass diese Dissertation nicht in einem früheren Promotionsverfahren eingereicht wurde.

Hamburg 25.07.2022

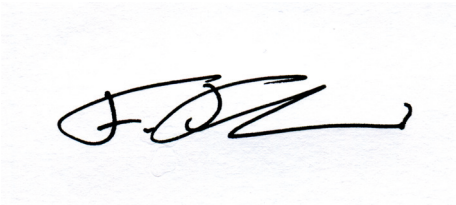

(Felix Johannes Flomm)